

December 2017

# Design of Tribologically Enhanced Polymeric Materials for Biomedical Applications

Allen Osaheni  
Syracuse University

Follow this and additional works at: <https://surface.syr.edu/etd>

 Part of the [Engineering Commons](#)

## Recommended Citation

Osaheni, Allen, "Design of Tribologically Enhanced Polymeric Materials for Biomedical Applications" (2017). *Dissertations - ALL*. 836.  
<https://surface.syr.edu/etd/836>

This Dissertation is brought to you for free and open access by the SURFACE at SURFACE. It has been accepted for inclusion in Dissertations - ALL by an authorized administrator of SURFACE. For more information, please contact [surface@syr.edu](mailto:surface@syr.edu).

## ABSTRACT

Anytime two surfaces are in normal contact, accompanied by tangential motion, there is potential for deterioration of one or both surfaces. Gradual wear, or the removal of surface material, is typically an undesirable event. Therefore, the need for lubrication arises to minimize the amount of shear stress that develops between opposing surfaces. This reduction in shear stress is characterized by the coefficient of friction (COF). Friction is one of the primary subjects of interest in tribology, the science of the friction and wear of articulating surfaces.

A number of fascinating tribological systems can be found in nature. One example which has drawn a considerable interest is articular cartilage. This smooth white tissue lines the articulating surfaces of our joints and sustains a tremendous amount of stress while maintaining smooth joint motion and low COF. The low COF exhibited by articular cartilage is unmatched by any man-made material. The phenomenal tribological properties of this biphasic material are attributed to a combination of a unique boundary lubrication mechanism and its ability to support interstitial fluid pressurization

This dissertation details the synthesis and characterization of novel tribologically enhanced polymeric materials which show great potential for several biomedical applications. Design of these material relied on the use of biomimetic tribological mechanisms. The overarching characterization described in this investigation provides valuable insight into the physical and mechanical characteristics of these unique materials.

# DESIGN OF TRIBOLOGICALLY ENHANCED POLYMERIC MATERIALS FOR BIOMEDICAL APPLICATIONS

by

Allen O. Osaheni

B.S., Mechanical Engineering, Clarkson University, 2009  
M.S., Mechanical & Aerospace Engineering, Syracuse University, 2013

Dissertation

Submitted in partial fulfillment of the requirements for the degree of  
Doctor of Philosophy in Mechanical & Aerospace Engineering.

Syracuse University

December 2017

Copyright © Allen O. Osaheni  
All Rights Reserved

## ACKNOWLEDGEMENTS

First and foremost, I would like to thank Dr. Michelle Blum for giving me the opportunity to be her first PhD student. I appreciate the freedom you gave me in pursuing such an interdisciplinary body of work. From day one you demonstrated eagerness to help me in any way you could. Thank you for being so approachable in times of distress. I would also like to thank Dr. Patrick Mather for adopting me into his research group and providing me with the tools and technical guidance that have allowed me to achieve much of this work. The opportunity to work and learn from you and your group members have been invaluable in my maturing as a researcher.

I would also like to thank Dr. Wenyang Pan for introducing me to polymer chemistry, Dr. Ivan Gitsov for his assistance with ATRP method development, Dr. Sally Prash for her assistance preparing custom glassware, Dr. Katie Cadwell for allowing me to use her lab's viscometer, Drs. Ariel Ash-Shakoor and Eric Finkelstein for their assistance with cytotoxicity method development/characterization, Gabe Smolnycki and Ryan Olson for the role they played in the design of the six degree of freedom tribometer, and Tim Breen, Bill Dossert, and Dick Chave for their assistance in the design and fabrication of a number of the custom devices which have made much of this work possible.

Thank you, Kristin Shapiro, Linda Manzano, Karen Low, Kathy Datthyn-Madigan, and Lynore de la Rosa for your assistance processing purchase orders, reimbursements, room reservations, and general assistance navigating the graduate program. I would also like to thank undergraduate students Robin Ramos, Leah Anderson, Shirley Zhang, Emily Lindberg, Norma Bachman, Kyle Wade, Kaeli O'Connor, Stephanie Hernandez, and Katherine Lindsley, for their contribution to experimental method develop, sample preparation, and characterization.

Finally, I would the thank my wife Courtney as well as my parents for their love, support, and encouragement. I would not have made it this far without you!

## TABLE OF CONTENTS

<b>List of Figures.....</b>	<b>x</b>
<b>List of Tables.....</b>	<b>xvii</b>
<b>Chapter 1: Introduction.....</b>	<b>1</b>
1.1 Preface.....	1
1.2 Structure and Physiology of Articular Cartilage.....	2
1.2.1 Collagen.....	3
1.2.2 Proteoglycans.....	5
1.3 Tribology of Synovial Joints.....	6
1.3.1 Conventional Regimes of Lubrication.....	7
1.3.2 Multimode Lubrication in Synovial Joints.....	8
1.3.3 Interstitial Lubrication.....	10
1.3.4 Weeping Lubrication.....	11
1.3.5 Hydration Lubrication.....	12
1.3.6 Cartilage Boundary Lubricants.....	14
1.3.7 Synergistic Boundary Lubrication.....	16
1.4 Cartilage Repair Options and Their Deficiencies.....	17
1.4.1 Stimulation of Underlying Bomed.....	18
1.4.2 Transplantation of Healthy Cartilage.....	19
1.4.3 Tissue Engineering Scaffolds.....	21
1.5 Development of Tribologically Enhanced Polymeric Materials.....	22
1.5.1 Structure of Poly Vinyl Alcohol Hydrogels.....	23
1.5.2 Cast Dried Freeze Thaw Hybrid Gels.....	24

1.5.3 Fiber Reinforced Hydrogels.....	26
1.5.4 PVA-HA Hydrogels.....	28
1.5.5 PVA-PVP Blends.....	29
1.5.6 Boundary Lubricant Functionalized Hydrogels.....	30
1.6 Dissertation Scope.....	32
<b>Chapter 2: Synthesis &amp; Characterization of Low Friction Zwitterionic Hydrogel Blend.....</b>	<b>35</b>
2.1 Introduction.....	36
2.2 Hydrogel Fabrication.....	36
2.2.1 Materials.....	36
2.2.2 Neat PVA-H Fabrication.....	36
2.2.3 Polymerization of MEDSAH.....	37
2.2.4 PVA PMEDSAH Blend Fabrication.....	37
2.3 Hydrogel Characterization.....	38
2.3.1 Fourier Transform Infrared Spectroscopy with Attenuated Total Reflection (FTIR-ATR).....	38
2.3.2 Wide Angle X-ray Scattering (WAXS).....	39
2.3.3 Equilibrium Water Content (EWC).....	39
2.3.4 Water Contact Angle.....	40
2.3.5 Surface Roughness (Rq).....	40
2.3.6 Confined Compression.....	41
2.3.7 Tensile Testing.....	41
2.3.8 Tribological Characterization.....	42
2.3.9 Cytotoxicity.....	43



2.3.9.1 Sample Preparation.....	43
2.3.9.2 Cellular Assay.....	44
2.3.9.3 Cytotoxicity Analysis.....	44
2.3.10 Statistical Analysis.....	45
2.4 Results.....	45
2.4.1 Hydrogel Blend Preparation.....	45
2.4.2 Surface Composition.....	45
2.4.3 Physical Characterization.....	46
2.4.4 Mechanical Characterization.....	50
2.4.5 Tribological Characterization.....	51
2.4.6 Cytotoxicity.....	53
2.5 Discussion.....	54
2.6 Conclusion.....	59
<b>Chapter 3: Effects of Lubricant Chain Length on the Mechanics and Tribology of Zwitterionic Hydrogel Blends.....</b>	<b>60</b>
3.1 Introduction.....	60
3.2 Hydrogel Fabrication Method.....	61
3.2.1 Materials.....	61
3.2.2 Boundary Lubricant Synthesis & Hydrogel Fabrication.....	61
3.3 Characterization Methods.....	62
3.3.1 Viscosity Average Molecular Weight.....	62
3.3.2 Boundary Lubricant Diffusion.....	63
3.3.3 Rate Controlled Hertzian Indentation.....	64
3.3.4 Small Angle X-Ray Scattering.....	66
3.3.5 Differential Scanning Calorimetry.....	67
3.3.6 Scanning Electron Microscopy.....	67

3.3.7 Tribo-Rheometry.....	67
3.3.8 Statistical Analysis.....	69
3.4 Results.....	69
3.4.1 Viscosity Average Molecular Weight.....	69
3.4.2 Boundary Lubricant Diffusion.....	70
3.4.3 Rate Controlled Hertzian Indentation.....	71
3.4.4 Physical Characterization.....	73
3.4.5 Tribo-Rheometry.....	75
3.5 Discussion.....	76
3.5 Conclusion.....	80
<b>Chapter 4: Synthesis and Characterization of Zwitterionic Polymer Brush Functionalized Polymer Brush Functionalized Hydrogels with Ionic Responsive Coefficient of Friction.....</b>	<b>82</b>
4.1 Introduction.....	82
4.2 Hydrogel Fabrication Method.....	83
4.2.1 Materials.....	83
4.2.2 PVA-H Fabrication.....	84
4.2.3 Zwitterionic Polymer Brush Functionalization.....	84
4.3 Characterization Methods.....	85
4.3.1 Fourier Transform Infrared Spectroscopy with Attenuated Total Reflection (FTIR-ATR).....	85
4.3.2 Coefficient of Friction.....	86
4.3.3 Water Contact Angle.....	87
4.3.4 Surface Roughness.....	87
4.3.5 Surface Microstructure.....	87
4.3.6 Mechanical Characterization.....	88
4.3.7 Bulk Physical Characterization.....	88
4.3.8 Cell Viability.....	89
4.3.9 Statistical Analysis.....	90

4.4 Results.....	90
4.4.1 Surface Composition.....	90
4.4.2 Coefficient of Friction.....	91
4.4.3 Physical Surface Characterization.....	93
4.4.4 Mechanical Characterization.....	94
4.4.5 Bulk Physical Characterization.....	95
4.4.6 Cytotoxicity.....	97
4.5 Discussion.....	98
4.6 Conclusion.....	101
<b>Chapter 5: Mechanics and Tribology of Electrospun Low Friction Polyurethane Fibermats.....</b>	<b>103</b>
5.1 Introduction.....	103
5.2 Fibermat Manufacturing Method.....	105
5.2.1 Materials.....	105
5.2.2 PMEDSAH Synthesis.....	105
5.2.3 Fibermat Fabrication.....	106
5.3 Characterization Methods.....	107
5.3.1 Scanning Electron Microscopy.....	107
5.3.2 Tribo-Rheometry.....	107
5.3.3 Tensile Testing.....	108
5.3.4 X-Ray Scattering.....	109
5.3.5 Boundary Lubricant Retention.....	109
5.3.6 Statistical Analysis.....	110
5.4 Results.....	110
5.4.1 Fibermat Microstructure.....	110
5.4.2 Tensile Properties.....	113
5.4.3 Coefficient of Friction.....	115
5.4.4 Boundary Lubricant Retention.....	117
5.5 Discussion.....	119

5.6 Conclusion.....	124
<b>Chapter 6: Conclusions and Future Directions.....</b>	<b>125</b>
6.1 Summary and Conclusions.....	125
6.2 Future Directions.....	131
6.2.1 Synthesis and Characterization of PMPC PVA Blends.....	132
6.2.2 Nanometer Scale Characterization of Tribological Performance.....	133
6.2.3 Self-Replenishing Zwitterionic Brush Functionalized Hydrogels.....	136
6.2.4 Characterization of Hydrogel Performance Under Physiologically Relevant Conditions.....	138
6.2.5 Multiscale Modelling of Hydrogel Tribological Performance.....	140
6.2.6 Mechanically and Tribologically Enhanced Low Friction, Low Fouling Nanofibrous Composites.....	141
6.2.7 Continuum Modelling of Low Friction, Low Fouling Nanofibrous Composites.....	142
<b>Appendix A: Design of a Pin on Disc Tribometer for Surface Wear Characterization.....</b>	<b>143</b>
A.1 Introduction.....	143
A.2 Position Control.....	144
A.3 Force Transduction.....	145
A.4 Load Cell Calibration.....	146
A.5 Friction Force Measurement.....	147
<b>Appendix B: Design of a Six Degree of Freedom Tribometer for Surface Wear Characterization.....</b>	<b>152</b>
B.1 Introduction.....	152
B.2 Description of Motion.....	149
B2.1 Anterior-posterior and medial-lateral displacement.....	150
B2.2 Flexion-extension and adduction-abduction.....	151
B2.3 Distraction-compression.....	152
B2.6 Stepper Motor Selection.....	154
B.3 Digital Motion Control.....	157
B.4 Force Transduction.....	159

B4.1 Load Cell Platform.....	160
B4.2 Load Cell Data Acquisition.....	161
B4.3 Load Cell Calibration.....	159
B4.4 Force Transduction Calibration Results.....	162
B.5 Conclusion.....	164
<b>Appendix C: Characterization of Cartilage Surface Wear Using High Performance Liquid Chromatography.....</b>	<b>165</b>
C.1 Introduction.....	165
C.2 Materials.....	165
C.3 Calibration Curve.....	166
C.4 Wear Particle Extraction.....	166
C.5 Derivatization.....	166
C.6 High Performance Liquid Chromatography Measurement.....	172
<b>Appendix D: Use of Tribologically Enhanced Hydrogels for Repair of Focal Chondral Defects.....</b>	<b>168</b>
D.1 Introduction.....	168
D.2 Experimental Methods.....	169
D.3 Results.....	170
D.4 Conclusions & Future Directions.....	171
<b>Appendix E: Design of a Device for in situ Characterization of Deformation Induced Changes in Polymer Microstructure Under Uniaxial Tension.....</b>	<b>172</b>
E.1 Introduction.....	172
E.2 Device Design.....	173
E.3 Conclusion.....	174
<b>References.....</b>	<b>175</b>
<b>Vita.....</b>	<b>205</b>

<b>Figure 1.1</b> – (a) Illustration of the six primary joints found in humans. (b) Illustration of the primary structures found in the knee joint. This joint behaves like a complex hinge.....	2
<b>Figure 1.2</b> – Schematic illustration of the hierarchal structure of collagen [17].....	3
<b>Figure 1.3</b> – Schematic illustration of the cell distribution and collagen fiber orientation within articular cartilage [19].....	4
<b>Figure 1.4</b> – Schematic illustration of the various components of proteoglycan aggregation found in articular cartilage.....	5
<b>Figure 1.5</b> – (a) Typical Stribeck curve showing variation in COF as a function of Gumbel number. $G_u \approx (\text{speed} \times \text{viscosity})/\text{load}$ . (b) Wear rates generally associated with the various regimes of lubrication.....	7
<b>Figure 1.6</b> – The gait cycle can be divided into the stance phase (weight-bearing) and swing phase (non-weight bearing) Stance face consists of three intermediate steps: heel strike, mid stance, and toe off [26].....	9
<b>Figure 1.7</b> – Illustration of fluid load support in a biphasic material.....	11
<b>Figure 1.8</b> – Illustration of (a) fluid film formation promoted by weeping lubrication as proposed by McCutchen [30]. (b) Tribological hydration as proposed by Moore & Burris [28].....	12
<b>Figure 1.9</b> - Schematic illustration of a surface force balance. Distance between mica sheets is measured via optical fringes produced by the light passing through the sheets. Piezoelectric tube (PZT) illustrates bending induced when opposing sectors experience equal and opposite potentials. Shear force is measured through the bending of the vertical leaf springs (S1). This results in a change in capacitance at G which can be measured to $\pm 2\text{\AA}$ . In a similar manner, the horizontal leaf-spring (S2), measures normal forces. [48].....	13
<b>Figure 1.10</b> – (a) Illustration of the dipole nature of water and the formation of hydration shells around ions. (b) Illustration of the repulsion experience by adjacent hydration shells [4].....	14
<b>Figure 1.11</b> – Schematic illustration of (a) phospholipid bilayers and (b) the chemical structure of a single phospholipid molecule.....	16
<b>Figure 1.12</b> – Illustration of the steps involves in cartilage repair via micro-fracture. (1) Damaged cartilage is removed. (2) Holes are drilled to stimulate bleeding from the subchondral bone. (3) Regeneration of fibrocartilage [82].....	19
<b>Figure 1.13</b> – Illustration of the steps involved in a typical OATS procedure.....	20

<b>Figure 1.14</b> – Illustration of the steps involved in a typical ACI procedure. (1) Surgeon harvests a full thickness cartilage biopsy (2) Biopsy is sterilized and (3) enzymatically digested to isolate chondrocytes. (4) Chondrocyte population is expanded over several weeks and then (5) seeded onto a scaffold. (6) Implant is then transferred in a sterile container to the surgeon and (7) used to repair the defect often via the use of fibrin glue [82].....	20
<b>Figure 1.15</b> - Photograph of PVA hydrogels prepared via (a) freeze thawing, (b) cast drying, and (c) freeze thaw cast dry hybrid [6].....	25
<b>Figure 1.16</b> - Summary of the major finding regarding improvement of the tribological properties of PVA hydrogels via variation in permeability. (a) Cross-section of hydrated FT-CD hybrid gel. (b) Representative COF vs time plots (tests were run in saline). (c) Fluid flow immediately after loading. (d) Von Mises stress after 292 s. (e) Interstitial fluid pressure after 292 s.....	26
<b>Figure 1.17</b> – Summary of the major findings regarding the strengthening of PVA-H through fiber reinforcement. (a) Illustration of the method used to achieve good interfacial adhesion. (b) Neat UHMWPE fiber after fiber pull out. (c) Surface treated UHMWPE fiber after fiber pullout. (d) Effects of surface treatment on interfacial shear strength. (e) Effects of surface treatment on maximum force.....	28
<b>Figure 1.18</b> – Illustration of the proposed boundary lubrication mechanism where a layer of water (a) interfaces with a hydrophobic boundary lubricant layer (b) which is functionalized to a crosslinked hydrogel (c).....	32
<b>Figure 2.1</b> – Schematic depicting the polymerization of MESDSAHA.....	37
<b>Figure 2.2</b> - Schematic of hydrogel fabrication procedure: (a) Structure of PVA and a cartoon depiction of PMEDSAHA, (b) Illustration of heating PVA-PMEDSAHA solution, (c) Hydrogel crosslinking and (d) Final product.....	38
<b>Figure 2.3:</b> Illustration of the (a) confined compression and (b) tribo-rheometry experimental setup.....	41
<b>Figure 2.4</b> - Representative images of neat and blended hydrogels following solvent casting and freeze thaw cycles.....	45
<b>Figure 2.5</b> - Representative FTIR-ATR spectra of the neat and tribologically enhanced hydrogels displaying the ester peak characteristic of MEDSAHA.....	46
<b>Figure 2.6</b> - (top) representative WAXS patterns for dry and hydrated neat PVA-H and PVA PMEDSAHA blends: (i, iv) neat PVA-H; (ii, v) 3% PVA-PMEDSAHA blend; (iii, vi) 25% PVA-PMEDSAHA blend. Below are representative WAXS profiles for: (a) dry, and (b) hydrated PVA-PMEDSAHA blends.....	49

<b>Figure 2.7</b> - Characterization of (a) compressive modulus of the hydrogel discs used in the COF experiments (b) compressive modulus of the hydrogel discs compared to hydrogels fabricated as films and (c) Young's modulus for neat and blended hydrogels (n = 5, *p < 0.05 with neat PVA-H, ANOVA).....	51
<b>Figure 2.8</b> – (a) Friction data for hydrogels with increasing PMEDSAH concentrations (n = 5, *p < 0.05 with neat PVA-H, ANOVA). (b) Representative plots of COF vs time for the neat and blended material over the course of 6 h experiments.....	52
<b>Figure 2.9</b> - Cytocompatibility of L929 cells in extracts generated from (a) Neat PVA hydrogel and hydrogel samples with 3% or 25% PMEDSAH, (b) PMEDSAH dissolved in media at various concentrations. Data is representative of the mean cell viability ( $\pm$ SD) for three material samples, assessed in three cell-based assays.....	53
<b>Figure 2.10</b> - Schematic showing the boundary lubrication mechanism fostered by the zwitterionic polymer at the surface and with interstitial mobility within the crosslinked hydrogel.....	55
<b>Figure 3.1</b> – Schematic illustration of the experimental setup used for measuring the viscosity of the aqueous polymer solutions.....	63
<b>Figure 3.2</b> - Scheme illustrating the test conditions for characterizing passive boundary lubricant diffusion.....	64
<b>Figure 3.3</b> - Scheme illustrating the test conditions for characterizing pressure driven boundary lubricant elution.....	64
<b>Figure 3.4</b> - Schematic illustration of the test conditions for indentation testing.....	66
<b>Figure 3.5</b> - Schematic illustration of the test conditions for measuring coefficient of friction.....	68
<b>Figure 3.6</b> - Effects of synthesis parameters on boundary lubricant molecular weight.....	69
<b>Figure 3.7</b> - Effect of boundary lubricant molecular weight on boundary lubricant diffusion (left) and elution (right).....	70
<b>Figure 3.8</b> Representative contact model fit for indentation (left) and stress relaxation(right) experiments.....	71
<b>Figure 3.9</b> - Effects of boundary lubricant molecular weight and boundary lubricant content on hydrogel contact modulus.....	71
<b>Figure 3.10</b> - Hertzian biphasic theory contact model fit for neat PVA and 25 wt% PVA PMEDSAH blends.....	72



<b>Figure 3.11</b> - Hydrogel degree of crystallinity determined through differential scanning calorimetry (left) and representative thermograms (right) for neat PVA compared to a 25 wt% PMEDSAH blend.....	73
<b>Figure 3.12</b> - SEM micrographs of the surface microstructure of neat PVA-H (top) and PVA PMEDSAH hydrogel blends (bottom).....	74
<b>Figure 3.13</b> - SEM micrographs illustrating the porosity of neat PVA (top) and 25 wt% PMEDSAH blends (bottom).....	74
<b>Figure 3.14</b> - Frictional behavior of neat PVA hydrogels and PVA PMEDSAH blends against glass with PMEDSAH molecular weight ranging from 50 – 825 kDa (left). Representative COF vs time curves for hydrogels articulating against glass a 1 rad/s (right).....	75
<b>Figure 3.15</b> - Sensitivity of power law diffusion model.....	76
<b>Figure 3.16</b> - Sensitivity of HBT contact model developed by Moore and Burris {{19 Moore, AC 2015}}.....	78
<b>Figure 4.1</b> - (a) Scheme illustrating the functionalization of ATRP initiator $\alpha$ -bromoisobutyryl bromide to the surface of a dehydrated PVA-H. (b) Chemical structure of the surface of a PMEDSAH brush functionalized PVA-H. (c) Chemical structure of a PMPC brush functionalized PVA-H.....	84
<b>Figure 4.2</b> - Schematic illustration of the test conditions for measuring hydrogel coefficient of friction against (a) glass and (b) stainless steel.....	85
<b>Figure 4.3</b> - Schematic illustration of the test conditions for contact modulus, $E_c$ and (b) a representative experiment curve fit.....	87
<b>Figure 4.4</b> - Representative FTIR-ATR spectra displaying the effects of catalyst content on hydrogel surface chemistry for both the PMEDSAH (left) and PMPC (right) functionalization reactions.....	90
<b>Figure 4.5</b> - Coefficient of friction (COF) behavior of neat PVA compared to initiator and zwitterionic polymer brush functionalized hydrogels tested against glass in both DI water and 0.2 M aqueous sodium chloride.....	91
<b>Figure 4.6</b> - Coefficient of friction (COF) behavior of neat PVA compared to initiator and zwitterionic polymer brush functionalized hydrogels tested against stainless steel in both DI water and 0.2 M aqueous NaCl.....	92
<b>Figure 4.7</b> - Water contact angle of neat PVA compared to initiator and zwitterionic polymer brush functionalized hydrogels.....	93
<b>Figure 4.8</b> - Representative SEM images of the surface microstructure following initiator and brush functionalization.....	93

<b>Figure 4.9</b> - Average contact modulus of (left) neat PVA-H compared to brush functionalized PVA-H and (right) bovine articular cartilage [30].....	94
<b>Figure 4.10</b> - SEM micrographs illustrating porosity of neat PVA-H compared to rehydrated PVA-H.....	95
<b>Figure 4.11</b> - Representative WAXS patterns for neat and rehydrated PVA-H.....	96
<b>Figure 4.12</b> - Viability of L929 cells in extracts generated from neat and surface modified hydrogels. Extract containing 0.1% SDS was used as a negative control.....	97
<b>Figure 5.1</b> - Schematic illustration of the fibermat manufacturing method.....	107
<b>Figure 5.2</b> - Schematic illustration of the test configuration used to measure fibermat coefficient of friction against glass with an AR-G2 rheometer.....	108
<b>Figure 5.3</b> - Representative scanning electron micrographs of fibermats composed of (a) neat Pellethane (b) neat PMEDSAH minutes after electrospinning (c) neat PMEDSAH after 24 h on lab bench (d) 50:50 Pellethane PMEDSAH blend (e) 75:25 Pellethane PMEDSAH blend (f) Blend containing 75% 50 kDa PMEDSAH.....	111
<b>Figure 5.4</b> - Representative 1D WAXS patterns of hydrated fibermats containing 0 and 50 wt% PMEDSAH compared to neat PMEDSAH.....	112
<b>Figure 5.5</b> - Representative 2D WAXS (top) and SAXS (bottom) patterns of hydrated fibermats containing 0 and 50 wt% PMEDSAH compared to neat PMEDSAH.....	112
<b>Figure 5.6</b> - Effect of PMEDSAH content on (a) Young's modulus, (b) ultimate stress, (c) ultimate strain, and (d) toughness. Means that do not share a letter are significantly different.....	114
<b>Figure 5.7</b> - Representative stress-strain plots of composite fibermats with PMEDSAH content ranging from 0 -75 wt% tested in 20 °C DI water.....	114
<b>Figure 5.8</b> - (a) Effect of PMEDSAH on average coefficient of friction. (b) Representative COF vs time curves.....	116
<b>Figure 5.9</b> - (a) Average coefficient of friction of functionally graded fibermats compared to neat Pellethane and the 50 wt% PMEDSAH blend. (b) Representative COF vs time curves.....	116
<b>Figure 5.10</b> - (a) Boundary lubricant depletion of composite fibermats with PMEDSAH content ranging from 0-75 wt% immersed in 0.2 M aqueous NaCl stored on a shaker table at 37 °C. (b) Average COF of composite fibermats after immersion in incubator for up to 7 days.....	118
<b>Figure 5.11</b> - SEM images displaying changes in fibermat morphology after being immersed in 0.2 M aqueous NaCl stored on a shaker table at 37 °C for up to 7 days.....	119

<b>Figure 6.1</b> - (a) Illustration of the primary components of a typical AFM system [236]. (b) SEM images of an AFM cantilever with a 10 $\mu\text{m}$ diameter glass sphere attached [36] and a (c) tapered cantilever tip.....	135
<b>Figure 6.2</b> – Scheme illustrating the cross-sectional design of the rigid probe normal and tangential force transducer.....	135
<b>Figure 6.3</b> – Topographical maps and representative cross sections of thermos-responsive poly(N-isopropylacrylamide) (PNIPAM) brushes grafted on gold at (a) 31 and (b) 36 $^{\circ}\text{C}$ [237].....	136
<b>Figure 6.4</b> – Schematic illustration of the primary components of an HPLC system.....	140
<b>Figure A.1</b> – Custom designed electromechanical 1D reciprocating pin on disc tribometer.....	143
<b>Figure A.2</b> – Example pin on disc test configuration supported by the tribometer.....	145
<b>Figure A.3</b> – Test configuration used for friction force load cell calibration.....	146
<b>Figure A.4</b> – Representative results from (a) friction force and (b) crosstalk calibration.....	147
<b>Figure A.5</b> – Representative friction force vs time trace for a stainless steel spherical indenter tip articulating against a neat PVA hydrogel in DI water.....	147
<b>Figure B.1</b> - Upper assembly supporting anterior-posterior and medial-lateral displacement control.....	151
<b>Figure B.2</b> - Detail of flexion-extension and valgus-varus motion control assembly.....	152
<b>Figure B.3</b> - Detail of vertical displacement control system.....	153
<b>Figure B.4</b> - Assembled and exploded view of the internal-external rotation system.....	153
<b>Figure B.5</b> - Block diagram illustrating component involved in position control and load cell data acquisition.....	155
<b>Figure B.6</b> - Interpolated experimental data and Fourier series representation of the kinematics of the human tibiofemoral joint during a single gait cycle for (a) flexion-extension, (b) abduction-adduction, (c) internal-external rotation, (d) medial-lateral displacement, (e) compression-distraction, and (f) anterior-posterior displacement.....	156
<b>Figure B.7</b> – Sensor plate design.....	158
<b>Figure B.8</b> - Normal force load cell calibration detail.....	159
<b>Figure B.9</b> - Friction force load cell calibration detail.....	160

**Figure B.10** – Representative results from (a) normal, (b) tangential, and (c) crosstalk characterization.....161

**Figure D.1** – Illustration of the proposed surgical procedure where (1) zwitterionic boundary lubricant molecules are grafted on to a hydrogel blend resulting in a (2) self-replenishing boundary lubricant enhanced material which (3) following implantation restores mechanical and tribological performance of an intact joint.....165

**Figure D.2** – Photograph of (a) the experimental test setup used for gait simulation [243] and (b) a hydrogel plug implanted in a human femoral condyle.....166

**Figure D.3** – Average contact pressures from various areas within the knee joint in intact joints compared to joints containing a hydrogel plug implant.....167

**Figure E.1** – Schematic illustration of the x-ray stretcher design.....171

<b>Table 2.1</b> - EWC and water contact angle data for PVA-H with increasing PMEDSAH content.....	47
<b>Table 3.1</b> – Effects of synthesis parameters on boundary lubricant molecular weight.....	69
<b>Table 3.2</b> – Proportionality constant and release exponent for diffusion power law.....	70
<b>Table 3.3</b> - Material properties determined through curve fitting HBT contact model to experimental data.....	72
<b>Table 3.4</b> - Hydrogel degree of crystallinity determined enthalpy of melting.....	74
<b>Table 4.1</b> – Hydrogel COF against glass.....	92
<b>Table 4.2</b> – Hydrogel COF against stainless steel.....	93
<b>Table 4.3</b> – Water contact angle results.....	94
<b>Table 4.4</b> Physical characterization results.....	96
<b>Table 4.5</b> – Cytotoxicity test results.....	98
<b>Table 5.1</b> – Tensile properties of composite fibermats with PMEDSAH content ranging from 0 – 75 wt% tested in 20 °C DI water.....	115
<b>Table 5.2</b> – Average coefficient of friction of composite fibermats with PMEDSAH content ranging from 0 – 75 wt% tested against glass in 20 °C DI water.....	116
<b>Table 5.3</b> – Average coefficient of friction of functionally graded composite fibermats compared to neat Pellethane and the 50 wt% PMEDSAH blends.....	117
<b>Table 5.4</b> - Normalized mass of composite fibermats with PMEDSAH content ranging from 0 -75 wt% immersed in 0.2 M aqueous NaCl stored on a shaker table at 37 oC for up to 7 days.....	118
<b>Table 5.5</b> - Average coefficient of friction of composite fibermats with PMEDSAH content ranging from 0 -75 wt% immersed in 0.2 M aqueous NaCl stored on a shaker table at 37 °C for up to 7 days.....	119
<b>Table B.1</b> - Calculated position, velocity, and acceleration range of the tibiofemoral joint during walking.....	150
<b>Table B.2</b> – Stepper motor capacity and Nanotec part number for each degree of freedom.....	154
<b>Table B.3</b> - Calculated position, velocity, and acceleration range of the tibiofemoral joint during walking.....	156

## CHAPTER 1: INTRODUCTION

### 1.1 Preface

Tribology, the study of the friction and wear behavior of articulating surfaces, is an extremely broad and interdisciplinary field involving theories based in solid and fluid mechanics as well as chemistry and material science. In addition to the traditional applications for which the science of tribology emerged to address (i.e. the design of bearings, shafts, oil based lubricants, and other machine components) the subject extends to a wide range of other mechanical systems including brushing teeth, ice skating, and operation of articulating joints [1,2]. One natural tribological system that has fascinated tribologists for decades is articulating joints, most notably, articular cartilage. To date, no man-made material has been shown to exhibit comparable tribological performance to that of articular cartilage [3,4]. This research investigation examines the design and characterization of novel synthetic materials towards mimicry of the impressive tribological properties displayed by articular cartilage.

The remainder of this section will detail relevant background information which provided the conceptual foundation for this investigation. First the structure and tribological properties of articular cartilage will be detailed, followed by a discussion of cartilage repair options and their deficiencies. Chapter 1 will conclude by reviewing some recent approaches which have been employed in the design of tribologically enhanced polymeric materials followed by an overview of the specific objectives of this dissertation.

## 1.2 Structure & Physiology of Articular Cartilage

Synovial joints are the most common type of joint in the human body and are subjected to a wide variety of loading conditions as illustrated in Figure 1.1a [5]. Often these joints must provide smooth articulation while being subjected to loads that are several times one's body weight. For this reason, synovial joints are equipped with a variety of structures to allow them to successfully function (Figure 1.1b). Of these structures, one that has long intrigued tribologists is articular cartilage.

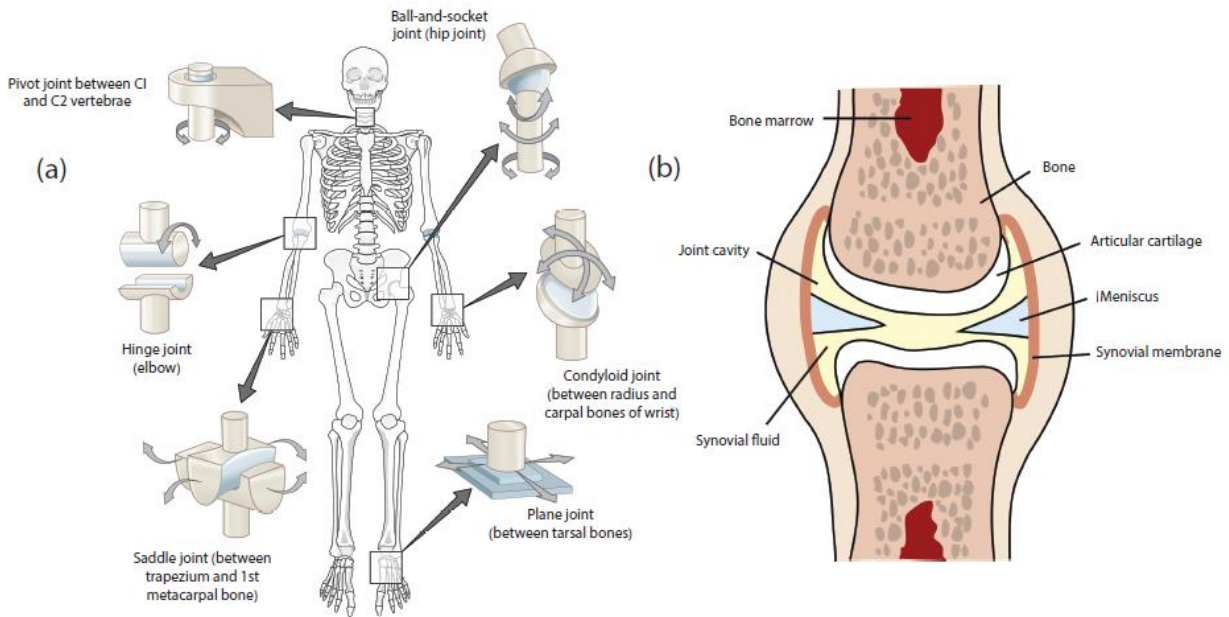


**Figure 1.1** – (a) Illustration of the six primary joints found in humans. (b) Illustration of the primary structures found in the knee joint. This joint behaves like a complex hinge.

Articular cartilage is the smooth white tissue which covers the articulating surfaces of synovial joints. It supports smooth motion by reducing friction and distributing stress between the opposing bone surfaces. This soft tissue is quite hydrated, with water content generally ranging from 60 – 80 wt%. The solid phase is composed primarily of type II collagen (50 – 75 wt %) and proteoglycans (20 – 30 wt %). The hierarchical structure of articular cartilage dictates its unique

properties which support healthy function [6]. The following subsections detail further the structure and physiology of articular cartilage.

### 1.2.1 Collagen

Collagen is the most abundant protein in the human body. This long, fibrous, macromolecule serves a similar role as that of the steel rods found in reinforced concrete or the carbon fibers in thermoplastics. They provide our tissue with its mechanical strength [7]. Long amino acid chains containing sequences of glycine (GLY), proline (PRO), and hydroxyproline (HYP) serve as the primary building block of collagen molecules. These polypeptide chains form triple helix structures known as  $\alpha$ -chains which are about 1.5 nm in diameter and 280 - 300 nm in length. The rod-like structures aggregate to form larger substructures as illustrated in Figure 1.2 which ultimately form collagen fibers which are 50 -300  $\mu\text{m}$  in diameter and can easily be seen via light microscopy [5].

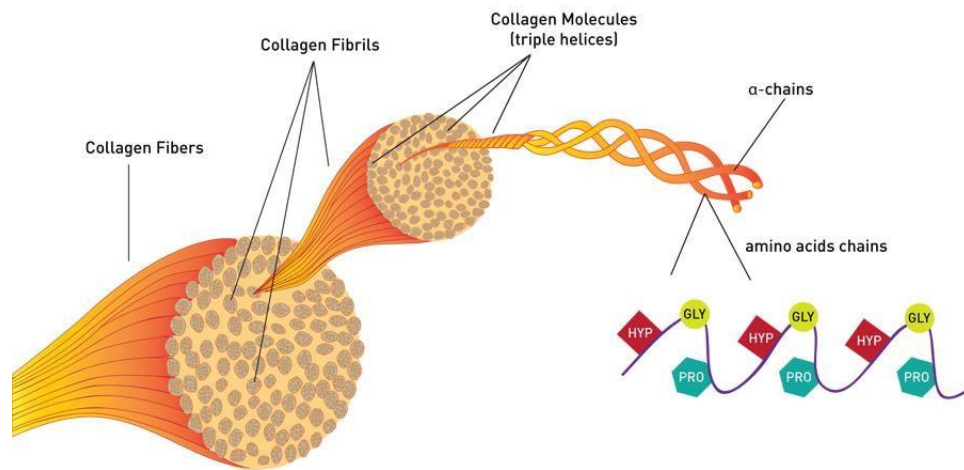


**Figure 1.2** – Schematic illustration of the hierarchal structure of collagen [8].

Although there are 29 known types of collagen, Types I, II, III, make up 80 - 90% of the human body. Of these types of collagen, Type I is the most abundant as it is the primary component



of skin, tendons, vasculature, ligaments, and bone. The next most abundant type of collagen is Type II which is found in articular and hyaline cartilage [5,9]. The fibrous network provides cartilage with its tensile strength and aids in containing the proteoglycan aggregates found in articular cartilage. The alignment of these fibers exists in a manner that provides optimal tribological function and can be classified by three distinct regions: the deep zone, middle zone, and superficial tangential zone (Figure 1.3). The deep zone lays closest to the underlying bone and contains a dense array of fibers oriented normal to the underlying bone. The middle zone is less dense and contains most of the proteoglycans and fluid contained in the tissue. Here fibers are randomly oriented. This zone is understood to play a significant role in load dissipation and acts as a reservoir for the lubricating fluid. Finally, the superficial tangential zone contains a dense array of collagen fibers oriented parallel to the underlying bone. This region contains the highest collagen content and is organized in a manner ideal for sustaining high levels of shear stress [6].

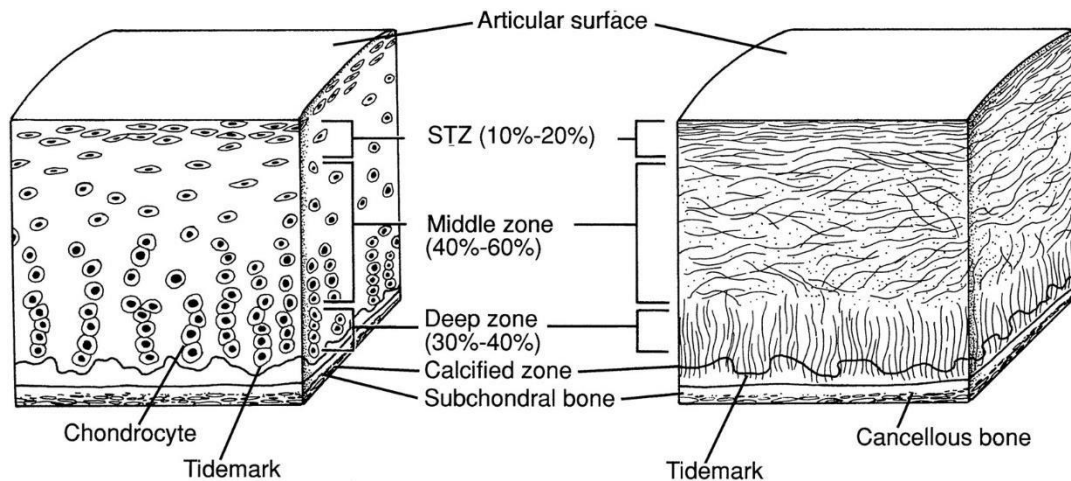


**Figure 1.3** – Schematic illustration of the cell distribution and collagen fiber orientation within articular cartilage [10].

### 1.2.2 Proteoglycans

Proteoglycans are a class of bio-macromolecules that provide articular cartilage with its high-water content and compressive strength due to their hydrophilic properties. Substructures of these molecules consist of a glycosaminoglycan-protein complex which forms a bottle brush like structure. Glycosaminoglycan (GAGs) are a special class of polysaccharides which contain repeating, negatively charged disaccharide units. The GAGS found in cartilage are chondroitin and keratin sulphate. These negatively charged subunits covalently associate with a core protein known as aggrecan which links to another GAG chain made up of hyaluronate repeat units. The overall structure of these bio-macromolecules is illustrated in Figure 1.4. Due to negatively charged groups found on the GAG's that make up proteoglycans, these structures strongly attract water, another polar molecule. Proteoglycan's strong affinity for water, coupled with collagen fibers which restrict swelling, play an essential role in providing cartilage with its excellent tribological properties [11].

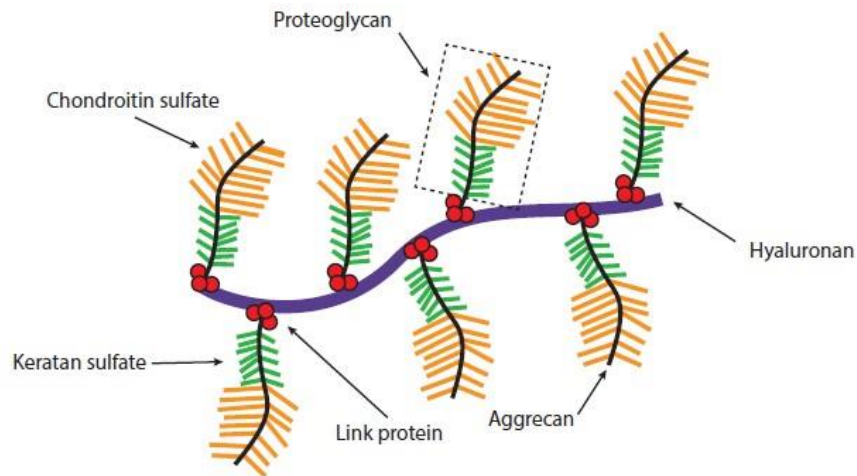


**Figure 1.4** – Schematic illustration of the various components of proteoglycan aggregation found in articular cartilage

### *1.2.3 Cellular Composition*

Articular cartilage has a relatively low cell density with chondrocytes, the resident cell type, making up about 2% of the total tissue volume [6]. These cells are nourished by the diffusion of nutrients found in the synovial fluid during joint movement and are understood to exhibit very little interaction with one another [9]. Chondrocytes have been shown to respond to mechanical loads, hydrostatic pressure, and the mechanical properties of the surrounding tissue [12-14]. Although chondrocytes are responsible for the synthesis and maintenance of articular cartilage, their low cell density and low propensity towards replication limits cartilage regeneration [10,15].

### **1.3 Tribology of Synovial Joints**

Synovial joints are a complex tribological system which operates under several different modes of lubrication depending on the magnitude of the applied load and the rate of articulation [16]. Generally, lubrication phenomena are characterized by one of four distinct regimes: hydrodynamic, elastohydrodynamic, mixed, and boundary lubrication (Figure 1.5). In transitioning from hydrodynamic to boundary lubrication, the effects of the lubricating fluid, most notably dynamic viscosity, become negligible. Instead the properties of surface asperities and nanometer scale films dictate coefficient of friction (COF). COF or  $\mu$  is a dimensionless parameter defined as the ratio of friction force to normal force [17].

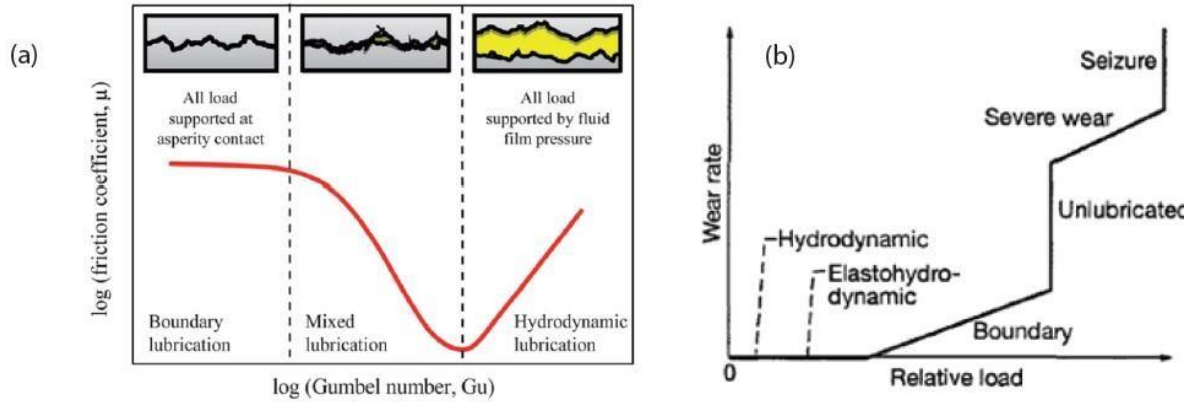


**Figure 1.5** – (a) Typical Stribeck curve showing variation in COF as a function of Gumbel number.  $G_u \approx (\text{speed} \times \text{viscosity})/\text{pressure}$ . (b) Wear rates generally associated with the various regimes of lubrication.

### 1.3.1 Conventional Regimes of Lubrication

In hydrodynamic lubrication (HL) the opposing solid surfaces do not come in direct contact due to the presence of thick fluid films. Generally, the thickness of these films is greater than 1  $\mu\text{m}$ . Of the four primary lubrication regimes, the loads experience in HL are generally the lowest. Here, normal applied loads are dissipated by the pressurization of these fluid films and as a result, little to no elastic deformation of the opposing solid surfaces is observed. Since the opposing surfaces are completely separated by the fluid film, sliding resistance is very low. Consequently, wear rates are lowest in HL making this the best-case scenario in terms of tribological performance.

In elastohydrodynamic lubrication (EHL), the magnitude of the normal loads reaches a level that results in significant elastic deformation of one or both opposing surfaces. Although the opposing surfaces are still separated by a fluid film, EHL is generally accompanied by an increase in coefficient of friction compared to HL [17].

When fluid films become thin enough for some asperity contact to occur, contacting pairs are said to be in the mixed lubrication regime. While in boundary lubrication (BL) the effects of

the bulk properties lubricating fluid become negligible. This is generally the case when surfaces are subjected to high loads, low sliding speeds, and/or low lubricant viscosity. In BL, friction is governed by the physical and chemical properties of nanometer scale films that form at the interface of the opposing surfaces. Due to the significant increase in solid asperity contact, BL represents the most destructive lubrication regime. Therefore, the presence of molecules which function as boundary lubricants is imperative for minimizing surface wear [17].

### *1.3.2 Multimode Lubrication in Synovial Joints*

The conventional regimes of lubrication provide tribologists with a reasonable understanding of the phenomena at work in the articulation of traditional machine elements such as pistons, bearings and gears. On the other hand, a comprehensive theory which explains the phenomena at work in the lubrication of biological systems such as synovial joints is still a work in progress. Although there are tribological mechanisms that are still the subject to debate, there are a handful of phenomena that are generally believed to occur, to some extent, in normal joint motion. These phenomena can be described by using normal gait as a model. Note that a gait cycle can be divided into two phases: stance phase and swing phase (Figure 1.6). It is likely that fluid films form during the swing phase and are exuded during extended periods in stance phase. Stance phase can be divided further into three intermediate steps: heel strike, mid stance, and toe off. There is a general consensus that lubricating films become pressurized during heel strike and are gradually dissipated as the joint transitions from EHL during heel strike to BL at toe off [2].

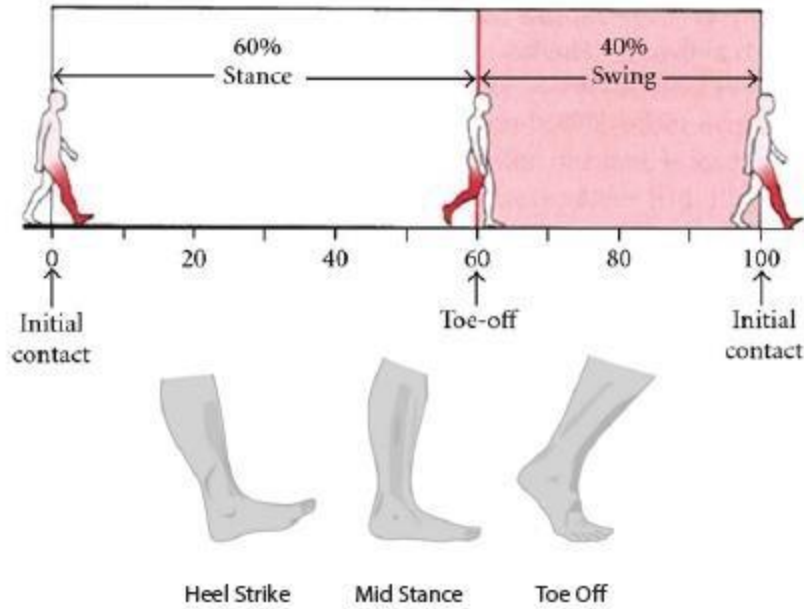


**Figure 1.6** – The gait cycle can be divided into the stance phase (weight-bearing) and swing phase (non-weight bearing) Stance face consists of three intermediate steps: heel strike, mid stance, and toe off [18].

Load bearing synovial joints are subjected to loads ranging from 1.5 – 10 times a person’s body weight. This corresponds to contact stresses as high as 2 – 12 MPa. Even under these harsh conditions, articulating joints can maintain coefficients of friction as low as 0.03. This is due to the excellent tribological properties of articular cartilage. Although this material has a very limited potential for self-repair, it withstands millions of cycles per year often for most one’s lifespan [6]. There are a number of theories explaining how this is possible [2,3,16,19,20]. Hypotheses regarding the mechanisms involved in cartilage lubrication have been used to develop mathematical models, which in turn can be validated or refuted through experiments. The following sections briefly review the theoretical framework behind the tribological mechanisms of articular cartilage.

### 1.3.3 Interstitial Lubrication

Due to its high-water content and low permeability, articular cartilage is often modelled as a biphasic material. The solid phase is treated as an elastic, incompressible material while the fluid phase is assumed to be incompressible and inviscid [21]. The biphasic nature of this tissue promotes a unique lubrication mechanism often referred to as interstitial lubrication (IL). McCutchen and his colleagues were some of the first to highlight the role of IL in cartilage lubrication. Their findings were first reported in the early 1960's [22]. This theory claims that the pressurization of the interstitial fluid contained within cartilage is attributed to the tissue's low coefficient of friction (Figure 1.7). The concept was supported by their experimental results where they observed a gradual increase in COF over time when cartilage was articulated against glass. McCutchen and his colleagues' observations suggested that under compression, the fluid phase supports most of the load, minimizing the load transfer to the solid phase. As the fluid pressure subsides, due to fluid exudation, the load on the solid phase increases resulting in the gradual increase in COF. This mindset served as the foundation for several theoretical analyses involving articular cartilage, most notably Mow's linear biphasic theory [21]. Comparison between experimental results and theoretical predictions based on Mow's linear biphasic theory have displayed good agreement in stress relaxation, creep, and dynamic loading [16,21,23,24]. This supports the validity of the interstitial lubrication mechanism hypothesized by McCutchen. An in-depth discussion of the theoretical models and experimental validation is beyond the scope of this manuscript. Some key players in the progression of this research include Gerard Ateshian [16], Duncan Dowson [2], Van C. Mow [21], and David Burris [20].

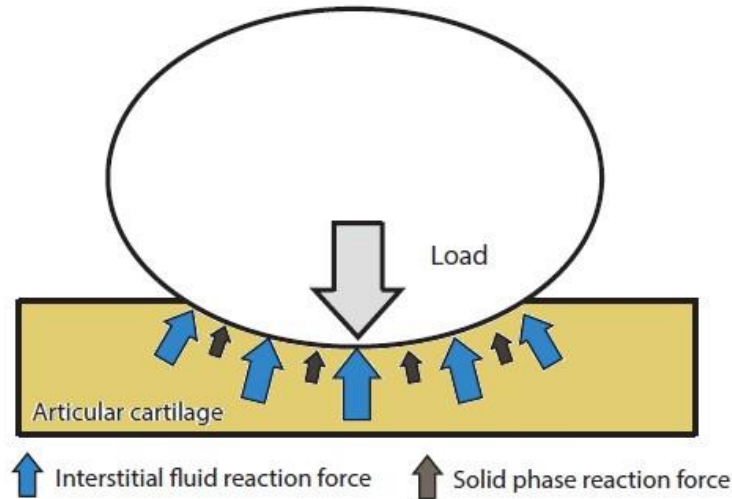


**Figure 1.7** – Illustration of fluid load support in a biphasic material

#### 1.3.4 Weeping Lubrication

In addition to IL, McCutchen also proposed a second possible lubrication mechanism, weeping lubrication (WL). This concept was later investigated from the point of view of continuum mechanics by Mow and Ling [25]. In WL, McCutchen et al postulated that when articular cartilage is subjected to compression synovial fluid is exuded from the bulk tissue, promoting hydrodynamic lubrication. Weeping is used to personify the exudation of fluid from the bulk to the surface of the tissue.

This theory was initially received well as it provides an intuitive explanation for the time dependent friction response associated with experimental results, however it was frequently contested by Dowson and his colleagues [26,27]. The opposition argued that WL violated conservation of linear momentum. Also, theoretical investigations based on the porous media theories suggest that any fluid found between bearing surfaces will flow into the cartilage [28-32]. This contradicts McCutchen's notion that WL promoted the formation of thick films between articulating surfaces. In fact, results from a number of studies indicate that synovial fluid trapped



between articulating surfaces are subject to a filtration like process as they are imbibed by the cartilage tissue [33-35]. Through this process hyaluronic acid, a boundary lubricant found in synovial fluid, is entangled by the cartilage matrix enhancing the lubricious nature of the cartilage surface. This process is referred to as boosted lubrication or tribological rehydration (Figure 1.8).

Although WL most likely does not occur in the way described by McCutchen, it is possible that tribological rehydration may be at work. In tribological rehydration, a paradigm recently proposed and investigated by Moore and Burris., cartilage weeping is followed by pressure driven recovery of interstitial fluid, and a replenishing of boundary lubricant molecules and interstitial fluid [20].

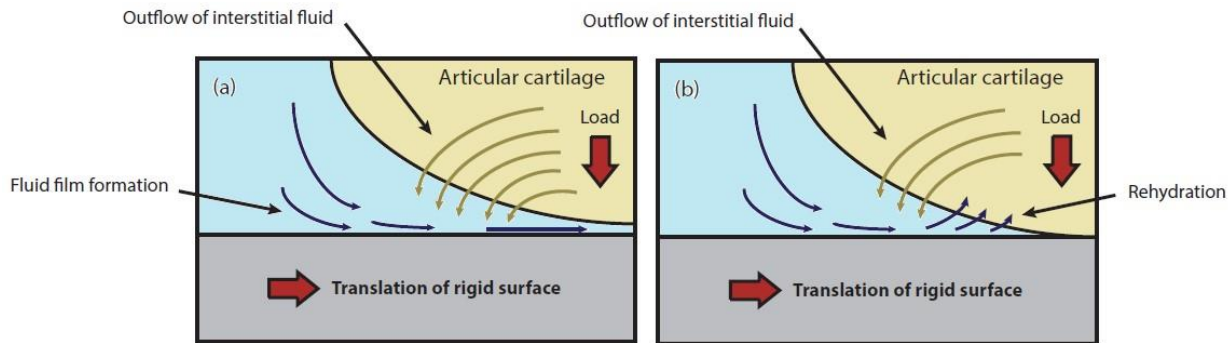


**Figure 1.8** – Illustration of (a) fluid film formation promoted by weeping lubrication as proposed by McCutchen [22]. (b) Tribological hydration as proposed by Moore & Burris [20]

### 1.3.5 Hydration Lubrication

Although the bulk properties of articular cartilage play a significant role in dictating tribological performance, it is also important to consider the role of boundary lubrication. Scanning probe methods using atomic force microscopy or surface force balances provide an excellent platform for analysis of molecular scale phenomena such as boundary lubrication [3,36]. Surface force balances (SFBs) have been utilized by a number of researchers at Israel's Weizmann Institute

of Science to do a great deal of fundamental research on the physics of interacting surfaces [3,37-39]. These devices can measure shear and normal forces with extreme accuracy (Figure 1.9). The resolution of SFB measurements has been reported to exceed that of conventional scanning probe methods such as atomic force microscopy and friction force microscopy by a factor of 5,000 – 10,000 [40]. The high degree of accuracy in displacement control and force measurement coupled with extreme surface flatness makes the SFB an excellent tool for direct characterization of the mechanical properties of nanometer scale films (Figure 1.9).

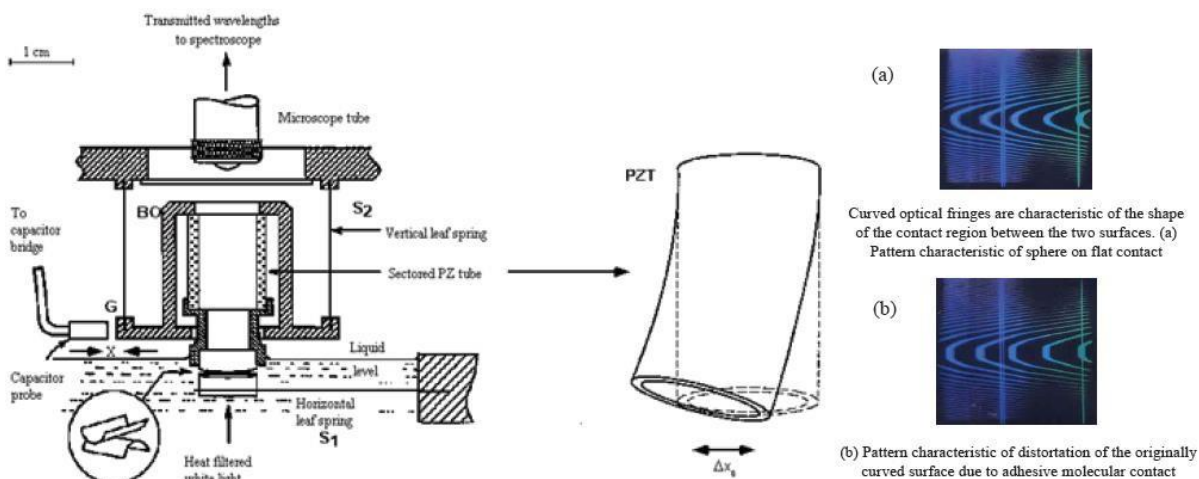


**Figure 1.9** - Schematic illustration of a surface force balance. Distance between mica sheets is measured via optical fringes produced by the light passing through the sheets. Piezoelectric tube (PZT) illustrates bending induced when opposing sectors experience equal and opposite potentials. Shear force is measured through the bending of the vertical leaf springs (S1). This results in a change in capacitance at G which can be measured to  $\pm 2\text{\AA}$ . In a similar manner, the horizontal leaf-spring (S2), measures normal forces. [40]

When studying the behavior organic solvents with a SFB, investigators observed an abrupt, reversible increase in viscosity resulting in solid-like behavior when films were compressed to thicknesses less than  $\sim 7$  molecular layers. Films compressed to this degree exhibited a seven to eight order of magnitude increase in viscosity. This is attributed to the transition from a loosely layered fluid phase to much more ordered solid phase [38]. Conversely, water was observed to maintain its bulk fluidity all the way down to a single monolayer. This unique behavior is attributed

to the fact that the liquid phase of water is denser than the solid phase. Therefore, as surfaces are pressed together the densification of the confined water suppresses the propensity towards solidification resulting in maintenance of fluidity all the way down to a single monolayer [37]. Due to the strong dipole nature of water it is understood to form strongly bound hydration layers around charged species (Figure 1.10). The presence of charged species surrounded by these hydration shells has since been found to result in an extremely efficient boundary lubrication mechanism acting as molecular scale ball bearings [39]. This mechanism has since been referred to as hydration lubrication and is attributed to the low coefficient of friction observed in articular cartilage within the boundary lubrication regime [3,4].

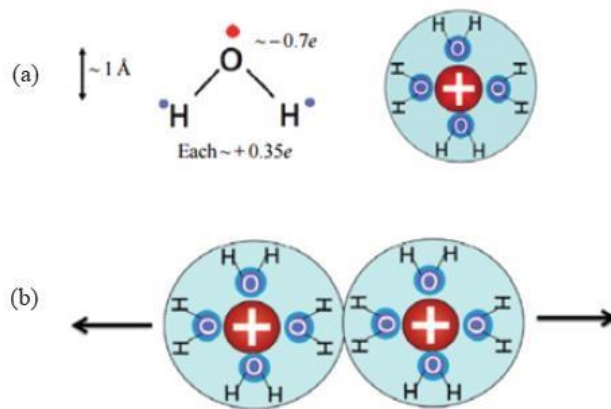


**Figure 1.10** – (a) Illustration of the dipole nature of water and the formation of hydration shells around ions. (b) Illustration of the repulsion experience by adjacent hydration shells [4]

### 1.3.6 Cartilage Boundary Lubricants

As noted earlier, the performance of articular cartilage within the boundary lubrication (BL) regime is of interest due to the high levels of friction and wear experienced compared to the other regimes of lubrication. In BL, friction and wear are minimized via the presence of nanometer scale films which form between the articulating surfaces. There are three distinct components

found in synovial joints which are all understood to act as a boundary lubricant: hyaluronan [2,41-43], lubricin [44-47], and surface active phospholipids [48-51].

Hyaluronan, often referred to as hyaluronic acid (HA), is a linear polysaccharide, more specifically a GAG, composed of hyaluronate repeat units. These anionic biomacromolecules are present in a wide range of human tissue, namely: connective, epithelial, and neural tissue. HA is also present in articular cartilage and synovial fluid [42]. While the exact function of this compound in synovial joints is still not fully understood, studies have shown that it exhibits both mechanical and biological utility. HA content is understood to dictate the viscosity of synovial fluid and has also been shown to maintain cartilage cell health by minimizing oxidative stress and inflammation [42]. Although HA plays a significant role in promoting healthy joint function, a number of studies have shown that HA alone does not act as a boundary lubricant [3,52,53].

Lubricin is a special class of proteoglycan and is often referred to as proteoglycan 4. This mucinous glycoprotein is found in both synovial fluid and the superficial tangential zone (STZ) of articular cartilage and is secreted by synovial fibroblasts and chondrocytes in the STZ. Lubricin is also a major component of menisci and tendons. In synovial joints lubricin is found in both the soluble and surface bound state. It is understood to ionically bind to macromolecules found in the STZ [44,45]. Studies have shown that Lubricin alone does aid in reducing friction in the boundary lubrication regime; however, Lubricin alone does not promote BL comparable to that observed in natural joints [46].

Phospholipids are a class of small amphiphilic molecules consisting of a hydrophilic phosphate head linked to two hydrophobic fatty acid tails. In aqueous environments, these molecules readily self-assemble into zwitterionic lipid bilayers (Figure 1.11). This behavior is due to their amphiphilic nature [54]. In addition to synovial joints, phospholipids also make up a large

portion of the composition of cell membranes and have been identified as the boundary lubricant at work in the frictionless sliding of lungs during breathing [55,56]. In synovial joints, phospholipid bilayers have been shown to adsorb onto the surface of articular cartilage. These adsorbed bilayers are often referred to as surface active phospholipids (SAPL) [48,49,57]. Although the BL mediated by SAPL is not fully understood, there are a handful of theories which describe the mechanisms at work. It is possible that the bilayers can easily slide past one another or absorb shear energy via deformation within the bilayer. A number of studies have also shown that these structures act as boundary lubricants due to the strong attachment of water molecules to the phosphate heads promoting hydration lubrication [4,58-60]. Even though SAPL are understood to act as a boundary lubricant in some way, reports have indicated that on their own, SAPL are not able to provide BL comparable to what is observed in natural joints [3].

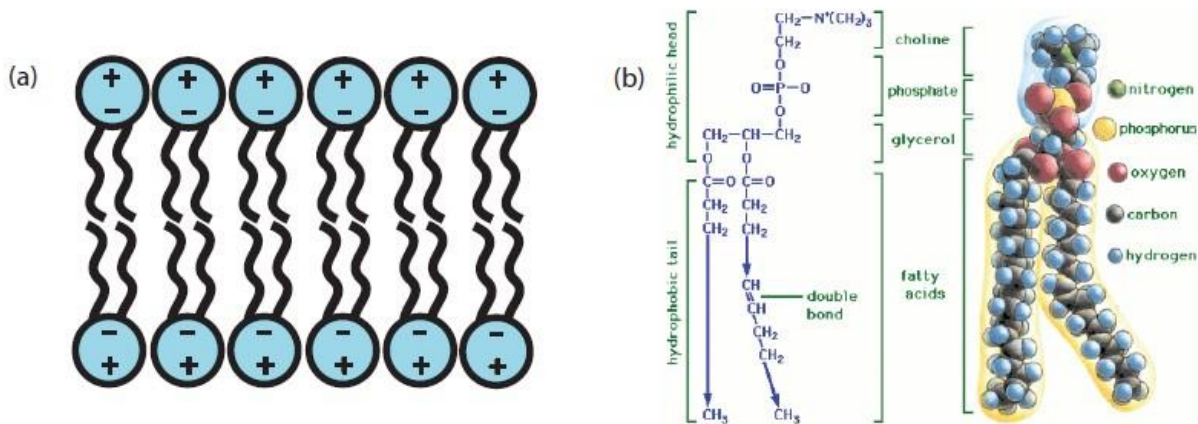


**Figure 1.11** – Schematic illustration of (a) phospholipid bilayers and (b) the chemical structure of a single phospholipid molecule

### 1.3.7 Synergistic Boundary Lubrication

Although, lubricin, hyaluronan, and surface-active phospholipids, are all synonymous with boundary lubrication in articular cartilage, synergistic interaction between all three is necessary

for the maintenance of COF as low as 0.001 when the tissue is subjected to stresses as high as 10 MPa. This paradigm was recently proposed by Jacob Klein and his colleagues following results obtained from direct measurement of this phenomena using a SFB [3]. The results of this study in conjunction with previous investigations regarding cartilage boundary lubrication [46,54,60,61], points to a convincing model which explains how these three boundary lubricants work together to promote hydration lubrication.

Surfaces bearing HA alone have been found to exhibit poor boundary lubrication, with COF on the order of 0.3 [3]. This may be due to poor hydration of the HA subunits. HA is understood to attach to the surface of articular cartilage via entanglement with collagen and/or known interaction with lubricin found in the STZ [46]. Surface bound HA is also understood to complex with zwitterionic phospholipids which are found within the tissue and the synovial fluid which it is immersed in [59,60]. The presence of these zwitterionic groups promotes the formation of hydration shells which have been shown to provide excellent boundary lubrication properties [4,58].

#### **1.4 Cartilage Repair Options & Their Deficiencies**

While articular cartilage exhibits friction and wear properties far superior to any man-made material, wear and irreversible damage is inevitable. Due to its low cell density and avascular nature, articular cartilage has a very limited potential for self-repair. Thus, the presence of defects as small as 2-4 mm rarely heal resulting in degradation of the surrounding tissue and exposure of underlying bone [62]. This process is understood to forebode the onset of osteoarthritis [10]. Symptoms associated with this debilitating condition include chronic pain and limited mobility. Although there are a number of treatment options available to attempt to restore healthy joint

function, particularly in load bearing joints, none are recognized as a comprehensive solution and often require total or partial replacement of the joint [63-65]. Joint replacement is extremely undesirable for a younger, more active population due to the invasive nature of the surgery and the limited service life of these implants. This section will review some of the treatment options that are currently available for knee joint cartilage repair as well as their deficiencies.

#### *1.4.1 Stimulation of Underlying Bone*

As noted earlier in this chapter, articular cartilage is relatively thin (2 – 5 mm) and masks the surfaces of our bones. Unlike cartilage, bone has much more pronounced vasculature and a significantly larger cell density [5]. For this reason, bone exhibit great potential for self-repair. In the late 1950's, Pridie conceived the idea of taking advantage of the bioactivity of the underlying bone in articulating joints [66-68]. This was achieved by stimulating subchondral bone via an approach often referred to as micro-fracture or subchondral drilling (Figure 1.12). By drilling into the bone surgeons induce bleeding and blood clot formation. The tissue generated via this method is known as fibrocartilage [65]. Fibrocartilage is the primary component of intervertebral discs and the meniscus of the knee.

Although fibrocartilage resembles healthy articular cartilage, it has a much lower proteoglycan content (1 – 3% dry weight compared to 20-30% in hyaline cartilage). It also has a slightly lower water content [9]. For this reason, the lubricative properties of this tissue are inferior to that of the natural tissue particularly in boundary lubrication. Success of micro-fracture is limited to individuals younger than the age of forty [69] due to the need for expedient generation of new tissue. Although micro-fracture results in improved joint functionality in the short term, 60 – 80% of the time in patient under the age of 40 it is not a comprehensive solution [70-74]. Inferior

tribological properties have been shown to result in resurgence of osteoarthritic symptoms after several years [74].

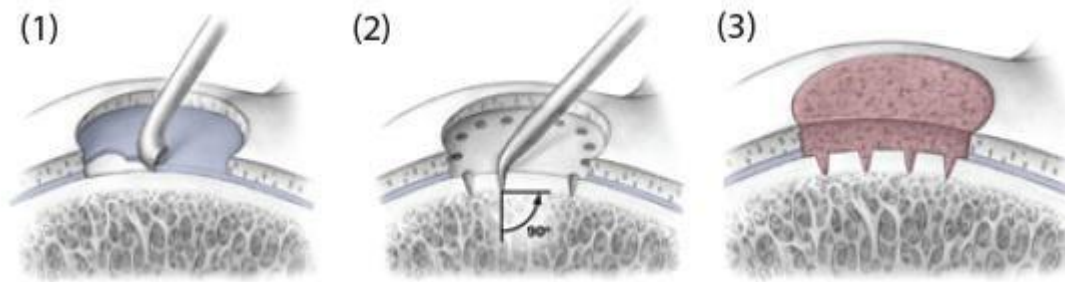


**Figure 1.12** – Illustration of the steps involved in cartilage repair via micro-fracture. (1) Damaged cartilage is removed. (2) Holes are drilled to stimulate bleeding from the subchondral bone. (3) Regeneration of fibrocartilage [75].

#### 1.4.2 Transplantation of Healthy Cartilage

An alternative approach, conceived in the early 90's for articular cartilage repair involves the transplantation of healthy cartilage from low weight bearing regions of the joint [76-78]. This surgical procedure is generally referred to as osteochondral autograft transplantation or OATS (Figure 1.13). Again, success of this approach is limited to relatively young patients (under the age of 50 [79]) due to the same reasons as micro-fracture. Historically, osteochondral autografting has been more popular in Japan and Europe compared to in the United States [63]. The major shortcoming of this technique is that the surgeon is impairing the viability of one area of the joint to repair another. Also, the relocated tissue is generally thinner and geared towards less severe loading, limiting its capability for maintaining healthy function after implantation. Finally, the scarce availability of tissue for this application restricts this technique to the repair of defects that are relatively small [80].



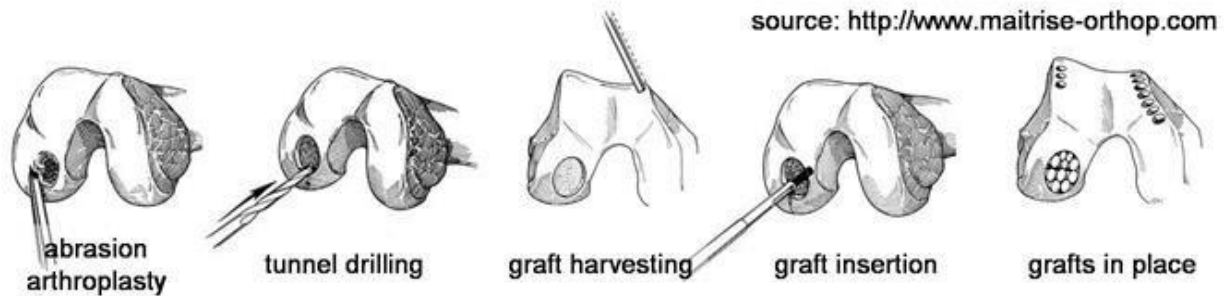


**Figure 1.13** – Illustration of the steps involved in a typical OATS procedure

An adaptation to this technique known as autologous chondrocyte implantation (ACI) was first introduced in 1994 by Brittberg [81]. Here small amounts of cartilage tissue are explanted and its chondrocytes are cultured and expanded. The cells are then introduced to the defect either with a periosteal flap or a collagen based matrix. One major shortcoming of this procedure compared to micro-fracture is that it is more complicated and expensive and requires two surgeries than one. Although short term clinical success is good (65 – 85% success), results from 5 and 15 year clinical trials suggest that ACI does not provide any advantages over microfracture [63,82].

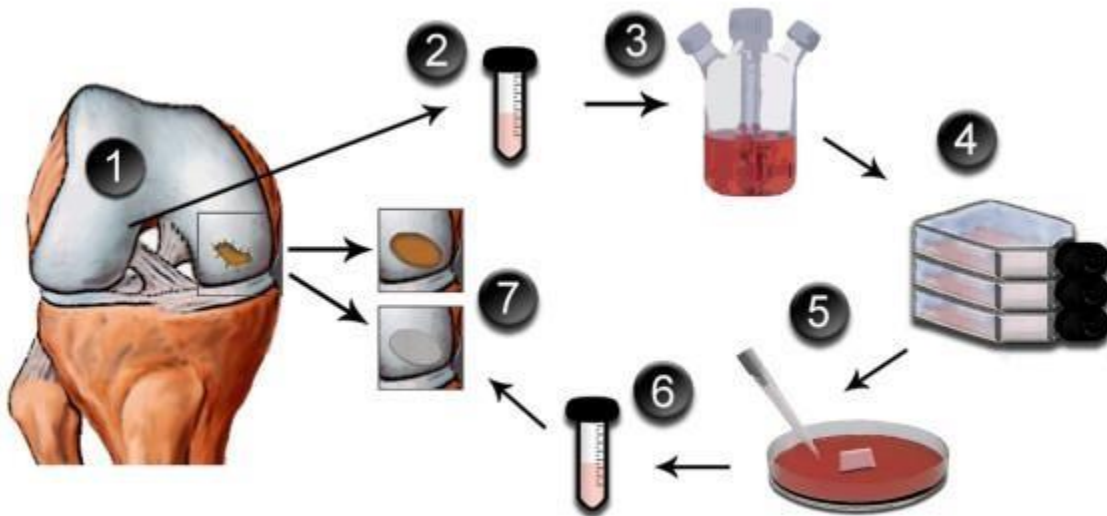


**Figure 1.14** – Illustration of the steps involved in a typical ACI procedure. (1) Surgeon harvests a full thickness cartilage biopsy (2) Biopsy is sterilized and (3) enzymatically digested to isolate chondrocytes. (4) Chondrocyte population is expanded over several weeks and then (5) seeded onto a scaffold. (6) Implant is then transferred in a sterile container to the surgeon and (7) used to repair the defect often via the use of fibrin glue [75]

### 1.4.3 Tissue Engineering Scaffolds

Tissue engineering (TE) involves the regeneration of natural tissue either *in vitro*, *in vivo*, or through use of both platforms. Although clinical success of this strategy in articular cartilage repair in humans remains elusive, recent findings show that this approach has great potential [63,64,83]. Restoration of articular cartilage can be achieved either completely *in vivo* or through the introduction of a medium which induces cartilage regeneration or *in vitro* via the fabrication of a scaffold suitable for supporting tissue growth. Research striving to push this technology forward focuses on optimization of the procurement of cells [84-87], release of chondrogenic signaling molecules [88-90], and scaffold development [91-94].

The ideal scaffold for cartilage repair should possess mechanical and tribological properties comparable to that of natural tissue. In addition, scaffolds should allow for the infiltration of cells and gradually degrade as natural tissue is generated [63]. Both natural and synthetic materials have been considered for use in this application. The advantage of using natural materials, i.e. materials found in the body is that they are inherently biocompatible and able to interact with the cells they house. Some of the materials that have been considered for this application include silk fibroin [7,95], alginate [96,97], agarose [13,14], and hyaluronan [98,99]. The drawback is that the mechanical and tribological properties of natural materials that have been considered thus are generally inferior to healthy mature articular cartilage. Also, the ability to tune the properties of these materials is limited. On the other hand, synthetic materials allow for much more control over mechanical and tribological properties as well as the degradation behavior. The drawback of synthetic based scaffolds is poor bioactivity and in some cases, poor biocompatibility. Synthetic materials which have been considered for use in articular cartilage repair include: poly (vinyl alcohol) [100], poly (2-hydroxyethyl methacrylate) [101], and poly (vinyl pyrrolidone) [102]. Use

of composite systems comprised of both natural and synthetic constituents has also shown great potential [94,103].

While tissue engineering of natural cartilage is recognized as the ideal method for cartilage repair, tissue engineering solutions are still many years away from producing practical *in vivo* solutions for cartilage growth [16].

### **1.5. Development of Tribologically Enhanced Hydrogels**

Polymers take a wide variety of forms depending on an array of factors such as: temperature, hydration, molecular weight, and monomer structure. Hydrogels are a class of polymers which have shown a great deal of promise for biomedical applications due to their inherent biomimetic properties. These gels are highly hydrophilic due to the presence of water-solubilizing groups such (i.e.  $-\text{SO}_3\text{H}$ ,  $-\text{COOH}$ ,  $-\text{OH}$ , and  $-\text{CONH}-$ ) but remain insoluble due to their crosslinked structure. These crosslinks can be formed via chain entanglement, dipole-dipole interactions, and/or covalent bonds. Mechanical and physical properties are dictated by chemical composition and crystal structure. The similarity in structure and mechanics between hydrogels and articular cartilage has been noted as early as 1973 by Bray and Merrill [104,105].

Due to their unique structure, hydrogels exhibit a significant degree of swelling when immersed in aqueous solution. Their high water content results in viscoelastic deformation comparable to what is observed in a wide range of natural tissue [106-109]. The biphasic nature of these materials allows for the promotion of interstitial lubrication. Therefore, considerable effort has gone into the development of hydrogels suitable for articular cartilage repair as well as many other medical applications (i.e. contact lenses, nucleus pulposis replacement, drug delivery, wound dressing, vascular grafts, and meniscal repair) [100]. A number of different types of

hydrogels have been considered for use as artificial cartilage some of which include: poly 2-hydroxyethyl methacrylate [101,110], agarose [13,14], silk fibroin [7,111], poly vinyl alcohol [112-114], and poly ethylene glycol [115]. Despite their promise for a wide range of medical technology, use of hydrogels in load bearing applications is severely limited due to inferior tribological properties [110,116,117]. Of the wide range of polymers which can be used to form hydrogels poly vinyl alcohol hydrogels have received a significant amount of attention due to their biocompatibility, high mechanical strength, and tunable physical and mechanical properties [100,102,112,118].

### *1.5.1 Structure of Poly Vinyl Alcohol Hydrogels*

Poly vinyl alcohol hydrogels (PVA-H) are one of the first types of hydrogels to be studied for articular cartilage repair and their development for this application as well as a number of other applications has been ongoing since the early 1970's [104]. PVA-H are an attractive option for a cartilage-like materials due to their mechanical strength, biocompatibility, and tunable physical and mechanical properties. The fabrication of PVA-H based biomaterials has been developed and characterized extensively over the decades [118-122].

PVA has a relatively simple structure and is synthesized via the hydrolysis of poly vinyl acetate (PVAc). PVAc is produced via free radical polymerization of vinyl acetate with polydispersity indices ranging from 2 – 2.5 in most commercial grades. The degree of hydrolysis has been shown to influence solubility and crystallizability of PVA. This is due to the hydrophobic nature of the acetate groups and the weakening of hydrogen bonds between polymer chains [119].

PVA can be crosslinked via a variety of means. In chemical crosslinking, the use of a crosslinking agents such as glutaraldehyde, acetaldehyde or formaldehyde results in the

formation of chemical bonds between polymer chains. One shortcoming associated with this type of approach is the fact that many crosslinking agents are toxic requiring extensive purification for use in biomedical applications. An alternative approach for PVA-H fabrication utilizes the formation of physical crosslinks through crystallite formation. Formation of physical crosslinks is achieved by subjecting aqueous PVA solutions to a series of freeze-thaw cycles (FTC). Each successive FTC is understood to increase the prevalence and stability of the crystallites. In addition to avoiding the use of potentially toxic crosslinking agents physically crosslinked hydrogels generally provide high mechanical strength and elasticity compared to those formed by chemical or irradiative means [119].

Despite the potential PVA-H have shown for several biomedical applications, their success in load bearing applications such as articular cartilage repair is severely limited due to inferior friction and wear properties compared to the natural tissue. The remainder of this section will review some of the most recent efforts to enhance the tribological properties of these biomaterials.

### *1.5.2 Cast Dried-Freeze Thaw Hybrid Gels*

As noted earlier, interstitial lubrication, is understood to play a major role in the tribological performance of articular cartilage. The effectiveness of this lubrication mechanism on biphasic materials is governed by the material's permeability and aggregate modulus. The permeability of physically crosslinked PVA-H can be tuned relatively easily through variation in the fabrication method. In addition to the freeze thaw (FT) method, PVA-H can also be formed via cast drying (CD). CD gels are formed by simply casting PVA in an aqueous solution and then storing the solution in air until it solidifies. Unlike gels fabricated via FT crosslinking, CD gels are understood to have a uniform network structure [116]. This postulation is supported by the transparency of

CD gels compared to FT gels (Figure 1.15) Gel permeability has been shown to be two orders of magnitude less than FT gels approaching levels more comparable to articular cartilage [113].

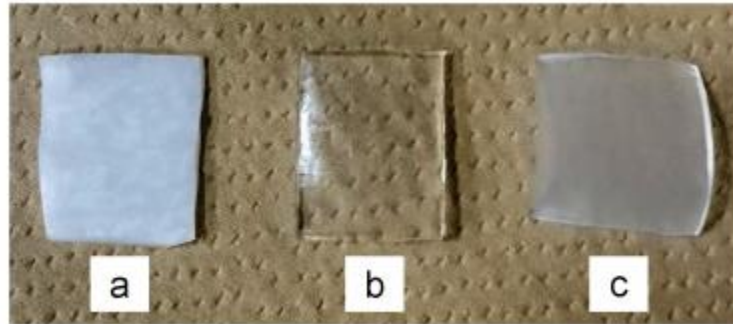


**Figure 1.15** - Photograph of PVA hydrogels prepared via (a) freeze thawing, (b) cast drying, and (c) freeze thaw cast dry hybrid [116]

Recently the Suzuki group of Yakihamma National University characterized the mechanical and tribological properties of CD and FT gels as well as laminated hybrid gels consisting of a CD layer on top of a FT layer (Figure 1.16a) [113,116,123]. The hybrid gels were found to exhibit superior friction and wear properties compared to the CD and FT gels (Figure 1.16b) [113,116]. Results from their biphasic finite element models produced comparable COF values and time dependent behavior. These models indicated that the hybrid gels maintain improved tribological performance by maintaining fluid pressurization while still providing support for fluid flow (Figure 1.16c-e). They postulated that these properties contribute to the low levels of von Mises stress in the solid phase which allows for less wear and friction compared to the CD and FT gels. Although hybrid gels appear to be a promising method for improving the tribological properties of PVA-H to date all tribological tests have been performed on the lower end of what would be experienced in vivo [124]. Performance against natural cartilage is also yet to be investigated.

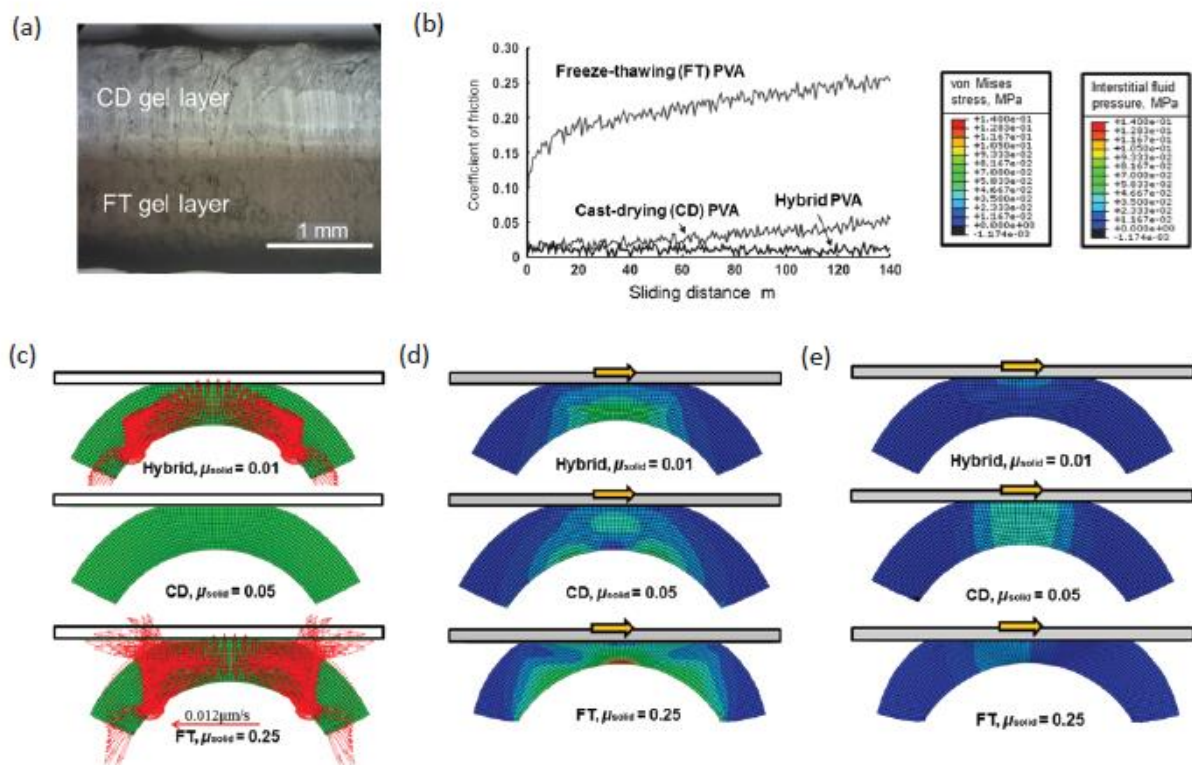


**Figure 1.16** - Summary of the major finding regarding improvement of the tribological properties of PVA hydrogels via variation in permeability. (a) Cross-section of hydrated FT-CD hybrid gel. (b) Representative COF vs time plots (tests were run in saline). (c) Fluid flow immediately after loading. (d) Von Mises stress after 292 s. (e) Interstitial fluid pressure after 292 s.

### 1.3.3 Fiber Reinforced Hydrogels

Tribological performance of PVA-H have also been enhanced by reinforcing the hydrogel matrix with high strength fibers. Recently, Giuseppe Palmese's group from Drexel University reported the mechanical and physical properties of PVA hydrogels reinforced with polypropylene (PP) and ultrahigh molecular weight polyethylene (UHMWPE) [125]. The stiffest gel reported in this investigation contained 29 vol% UHMWPE and displayed a tensile modulus of  $258.1 \pm 40.1$  MPa. Hydrogels without reinforcement displayed a tensile modulus of  $0.23 \pm 0.02$  MPa. With fiber reinforcement, Hollaway et al. was able to prepare PVA-H with tensile properties comparable to natural fibrous tissue.

More recent efforts by the Palmese group have focused on improving interfacial adhesion between UHMWPE fibers and the PVA matrix [126]. Inherently this interfacial adhesion is poor due to the hydrophobic nature of UHMWPE. In order to overcome this problem, Hollaway et al. developed a novel chemical grafting method where aldehyde groups were functionalized to the surface of UHMWPE fibers. The authors expect these aldehyde groups to form acetal bridges between the fibers and the hydroxyl groups of PVA (Figure 1.17a). Results from fiber pull out experiments indicate that the chemically grafted fibers promote a significant increase in interfacial shear stress from  $11.5 \pm 2.9$  kPa in the neat material to  $256.4 \pm 64.3$  kPa in the fiber reinforced (Figure 1.17d). Unlike untreated fiber, the surface functionalized fibers displayed signs of cohesive failure with a significant amount PVA adhered to the fiber after pullout (Figure 1.17c). This suggest successful optimization of the interfacial adhesion. Thus, fiber reinforcement appears to be a promising method for imparting biomimetic anisotropy to PVA-H. The effects of fiber reinforcement on tribological performance is a subject that has not yet been investigated.



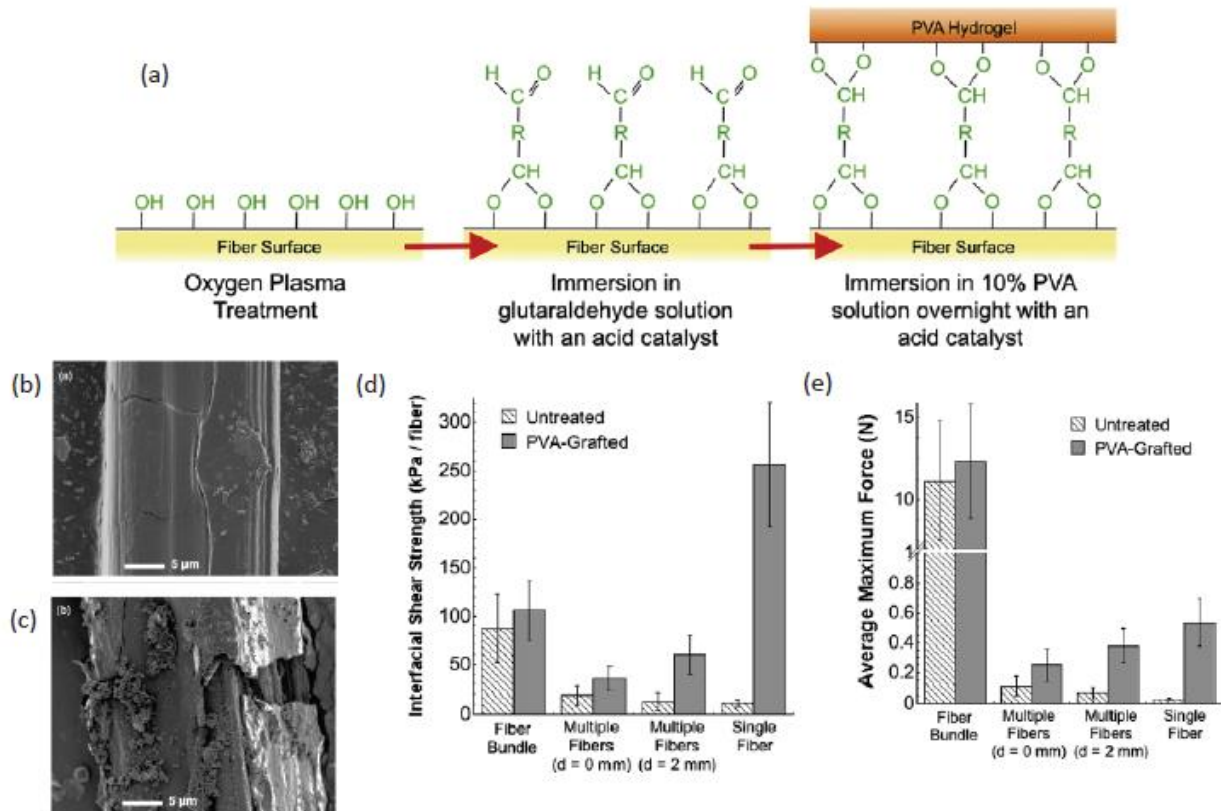


**Figure 1.17** – Summary of the major findings regarding the strengthening of PVA-H through fiber reinforcement. (a) Illustration of the method used to achieve good interfacial adhesion. (b) Neat UHMWPE fiber after fiber pull out. (c) Surface treated UHMWPE fiber after fiber pullout. (d) Effects of surface treatment on interfacial shear strength. (e) Effects of surface treatment on maximum force.

### 1.3.4 PVA- HA Hydrogels

In addition to fiber reinforcement, another popular approach for enhancing the tribological properties of PVA-H involves the incorporation of hydroxyapatite (HA) nanocrystals. HA is understood to provide bone with its strength and rigidity as it is the primary component of the mineral phase and makes up 70% of the tissue's total mass [9]. In addition to its inherent rigidity and biocompatibility, HA is understood to be bioactive. Therefore, in addition to providing hydrogels with mechanical strength, the incorporation of synthetic HA is also expected to promote osteointegration a process that is unlikely to occur if a neat PVA-H was implanted.

The fabrication and characterization of PVA-HA blends has been a popular subject of investigation over the past decade [112,127,128]. The fabrication of PVA-HA composites with HA content ranging from 1.5 – 7.5 wt% HA has been shown to result in a significant increase in the mechanical strength in both tension and compression [129]. This enhancement is accompanied by a slight change in COF (both slight increases and slight decreases have been observed), a slight decrease in equilibrium water content, and a significant decrease in strain to failure. Hydrogel wear resistance has been to increase with increasing HA content however there is a relatively narrow threshold where this is true. Above this threshold value the dispersion of the HA particles is inhibited resulting in the formation of larger particles which contribute to abrasive wear. The threshold value has been shown to range from 2 – 4 wt% depending on the hydrogel fabrication method [128].

### *1.3.5 PVA-PVP Blends*

Often the mechanical, physical, and tribological properties of hydrogels can be tuned via the fabrication of miscible blends. A popular polymer of choice for blending with PVA is poly vinyl pyrrolidone (PVP) [102,130-132]. PVP is a biocompatible hydrogel which has been considered for a number of biomedical applications such as soft contact lenses [133], tissue adhesives , and wound dressings [134,135]. These blends can be fabricated by simply mixing the PVP with PVA prior to solvent casting [136]. The initial motivation behind the fabrication of PVA-PVP blends was to enhance network stability thorough inter-polymer complexation [137].

Katta et. al was the first to report on the tribological properties of PVA/PVP blends [136]. Since then, investigators have reported that mechanical strength of the hydrogel blends appears to be highest when PVP content is at 1 wt% [102]. The authors postulate this may be due to the promotion of some sort of secondary interaction between the two polymers. The addition of PVP

has also been shown to cause a progressive increase in EWC and significant reduction in COF. However, the COF of these blends is still an order of magnitude higher than that of natural cartilage (even when the hydrogels are lubricated by bovine serum) [102,136].

### *1.3.6 Boundary Lubricant Functionalized Hydrogels*

Although many investigators have developed methods for improving mechanical strength of hydrogels, few have addressed the importance of boundary lubrication. As noted earlier, the service life of materials is dictated by its performance in boundary lubrication. Good boundary lubrication will also minimize wear of opposing surfaces. Blum et al. were the first to report the functionalization of organic boundary lubricants to the surface of PVA-H [114]. To date, the boundary lubricants that have been investigated include lauroyl chloride ( $C_{12}$ ) and stearyl chloride ( $C_{18}$ ) [117].

Functionalization of these hydrophobic boundary lubricants was achieved via nucleophilic acyl substitution. In this reaction, the acid chloride associated with the boundary lubricant ( $C_{12}$  or  $C_{18}$ ) were linked to the polymer backbone via ester bonds [138]. Characterization of the friction and wear properties of these biomaterials was performed in DI water under boundary lubrication conditions to facilitate worst case scenario condition with respect to friction and wear. Results from these experiments suggest that the functionalization of fatty acid boundary lubricants promotes boundary lubrication when hydrocarbon chain length is low [117]. This conclusion was made since the hydrogels functionalized to  $C_{12}$  yielded a significant decrease in COF compared to the neat material while hydrogels functionalized to  $C_{18}$  displayed a significant increase in COF. Since  $C_{12}$  and  $C_{18}$  are very small molecules compared to the PVA backbone, reduction in COF was also found to be heavily depended on the amount of functionalization [114,139].

In addition to quantifying COF Blum et al. assessed the wear characteristics of BLF hydrogels against steel and natural cartilage compared to that of neat PVA [117]. The pressures administered during these experiments were comparable to what would be experienced in vivo. Characterization of the surface of cartilage plugs articulating against neat PVA revealed fraying and pitting on the cartilage surface. While fraying was also observed on the surface of cartilage articulating against BLF hydrogels, its severity was noticeably lower. Overall C<sub>12</sub> functionalized hydrogels displayed the best tribological performance.

The authors postulated that the tribological properties promoted by C<sub>12</sub> and C<sub>18</sub> were attributed to their hydrophobicity which promotes the formation of interfacial aqueous films (Figure 1.18) [139]. In addition, the linear nature of these molecules allows for close packing on the hydrogel surface resulting in a brush like structure which minimizes shear stress in sliding contact. The poor tribological properties exhibited by C<sub>18</sub> grafted hydrogels suggests that there is a critical range above which hydrocarbon chain length has a negative effect. Although the boundary lubricant functionalized hydrogels prepared by Blum et al. exhibited improved tribological performance compared to the neat material. These properties still fell short of the natural tissue. Use of a boundary lubrication mechanism which mimics those exhibited by natural cartilage is expected to provide improved boundary lubrication.

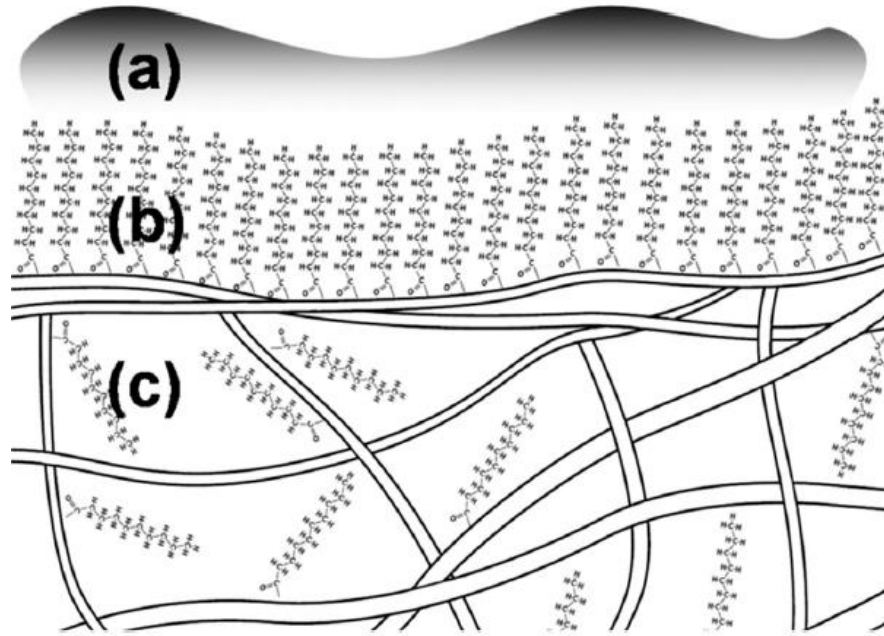


**Figure 1.18** – Illustration of the proposed boundary lubrication mechanism where a layer of water (a) interfaces with a hydrophobic boundary lubricant layer (b) which is functionalized to a crosslinked hydrogel (c)

## 1.6 Dissertation Scope

The primary objective of this investigation was to develop and examine novel biomimetic approaches for enhancing the tribological properties of polymeric materials with potential for use in medical applications. The methods described deal with two classes of polymeric materials: hydrogels and thermoplastic polyurethanes. This involved the design and execution of a variety of experimental methods as well as the implementation of previously established empirical and analytical models. An outline of the contents discussed in this dissertation is provided below:

Chapter 2 describes the design and characterization of a novel tribologically enhanced hydrogel blend. Synthesis of the biomimetic boundary lubricant was achieved through free radical polymerization of the zwitterionic monomer [2-(methacryloyloxy) ethyl] dimethyl-(3-sulfopropyl) ammonium hydroxide) (MEDSAH). The resulting polymer, PMEDSAH, was subsequently blended with poly vinyl alcohol (PVA) to form a zwitterionic hydrogel blend. In addition to

describing the method developed for fabricating this biomimetic material, the effect of PMEDSAH on coefficient of friction, compressive modulus, and physical properties such as microstructure, water content, and surface tension were also reported. Finally, assessment of potential for use as a tissue engineering scaffold was achieved via cytotoxicity experiments.

In Chapter 3 the examination of the effects of boundary lubricant molecular weight on the mechanics tribology, and diffusive properties of PVA-PMEDSAH hydrogel blends is described. The boundary lubrication behavior is described within the context of a theoretical surface repulsion-adsorption model. Indentation experiments within the context of Hertzian biphasic theory were used to characterize the effects of boundary lubricant on interstitial fluid load support. In addition, boundary lubricant mobility within the hydrogel matrix and physical characterization involving scanning electron microscopy, x-ray scattering, and differential scanning calorimetry are also discussed.

Chapter 4 describes the synthesis and characterization of novel biomimetic surface modified PVA hydrogels. Synthesis of these materials was achieved through surface initiated polymerization of the boundary lubricant molecules. In addition to the validation of surface chemistry, ionic responsive coefficient of friction, mechanics, surface tension, and cytotoxicity were also characterized and reported.

In addition to hydrogels, thermoplastic polyurethanes represent a second class of polymers which could benefit from the biomimetic boundary lubricants described in chapters 2 – 4. Chapter 5 describes the development and characterization of a novel method for preparing tribologically enhanced thermoplastic polyurethanes. The chapter describes the versatile fabrication method as well as potential clinical applications which could benefit from the supplemental functionalities of the boundary lubricant.

Like most academic research investigations, the work is never truly complete and should not end with this dissertation. Chapter 6 summarizes the findings and conclusions of this dissertation and provides detailed insight into future directions which could stem from this body of work.

## CHAPTER 2: SYNTHESIS AND CHARACTERIZATION OF LOW FRICTION ZWITTERIONIC HYDROGEL BLENDS

### 2. 1 Introduction

Zwitterionic molecules are net-neutral, but possess both positive and negative charges in close proximity to one another [140]. The charged regions associated with these molecules allows them to interact with water through electrostatic attraction [141]. Due to their unique behavior, zwitterionic based systems have been investigated for a number of applications including use as hydrogel implants [142,143,143,144], electrostatic ion chromatography [145], low fouling substrates [146-148], and microfluidic devices [149]. Recently, zwitterionic polymers have been shown to act as an efficient boundary lubricant [4,58]. This behavior is attributed to the formation of hydration shells surrounding the charged components of zwitterionic chains promoting a mechanism known as hydration lubrication [4,150].

Although several methods have been developed to enhance the mechanical properties of PVA hydrogels, few have addressed their poor performance in boundary lubrication compared to that observed by natural tissue such as articular cartilage. Based on the known boundary lubrication mechanisms exhibited by articular cartilage and the biomimetic structure of zwitterionic polymers it was postulated that synthesizing a zwitterionic polymer and blending it with PVA to form a zwitterionic hydrogel blend would result in a significant reduction in coefficient of friction. The work discussed in this chapter details the results of this investigation and their implications through the synthesis and characterization of hydrogels formed from PVA blended with zwitterionic polymer: [2-(methacryloyloxy) ethyl] dimethyl-(3-sulfopropyl) ammonium hydroxide) or PMEDSAH.



## 2.2 Hydrogel Fabrication Method

### 2.2.1 Materials

Polyvinyl alcohol (PVA, 99% hydrolyzed) with a reported average molecular weight of 130,000 g/mol was purchased from Sigma-Aldrich (St. Louis, MO). The monomer [2-(methacryloyloxy) ethyl] dimethyl-(3-sulfopropyl) ammonium hydroxide) (MEDSAH), solvent N, N-dimethylformamide (DMF) and initiator 2, 2'-azobisisobutyronitrile (AIBN) were also obtained from Sigma-Aldrich. All chemicals were used as received.

### 2.2.2 Neat PVA-H Fabrication

Neat PVA-H were prepared by solvent casting a 40 wt% (m/v) mixture of PVA and deionized (DI) water. The mixture was heated at 90 °C in an isothermal oven (Fisher Scientific, Waltham, MA) for 6 h resulting in a viscous, transparent solution. Stirring was not used during solvent casting due to the high viscosity of the solution and propensity towards bubble formation.

Following solvent casting, samples were subjected to four freeze-thaw cycles where samples were frozen at -80 °C for 30 min and then allowed to thaw at room temperature for 30 min. Freezing was achieved by submerging sample in an ice bath containing dry ice and acetone. This cyclic freeze-thaw process is understood to reinforce the hydrogel structure through formation of crystalline regions, the concentration of these crystalline regions increasing with each successive freeze-thaw cycle [151]. Following the freeze thaw process, samples were submerged in DI water for at least 48 h to ensure they reached equilibrium swelling.

### 2.2.3 Polymerization of MEDSAH

The zwitterionic polymer, PMEDSAH, was prepared through the free radical polymerization of MEDSAH initiated by AIBN under nitrogen in a 60:40 volume ratio of DMF:DI water solution containing 6.7 wt% MEDSAH and a 100:1 monomer to initiator mass ratio (58.78:1 mole ratio). The reaction was performed at 65 °C for 6 h at which point the precipitated product was harvested.

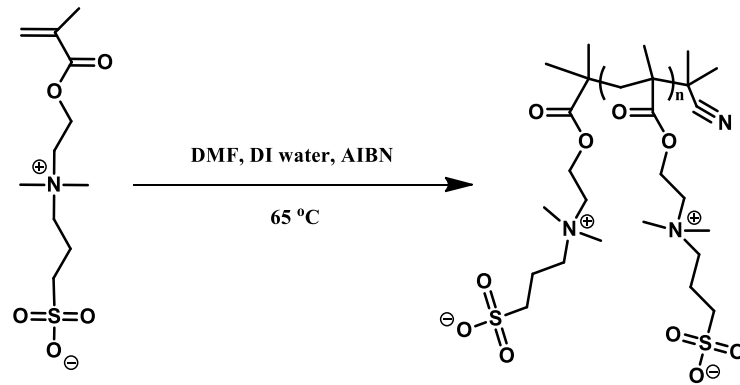


**Figure 2.1** – Schematic depicting the polymerization of MEDSAH

### 2.2.4 PVA-PMEDSAH Blend Fabrication

The hydrogel blends were fabricated by initially preparing a 40 wt% (m/v) mixture of PVA to DI water with PMEDSAH contents ranging from 1– 30 wt% relative to PVA. PMEDSAH was dissolved in DI water via the assistance of a Vortex-Genie 2 mixer (Scientific Industries Inc., Bohemia, NY) The mixtures were heated at 90 °C for 6 h resulting in a viscous solution. Each solution was then subjected to four freeze-thaw cycles where samples were frozen at -80 °C for 30 min and then allowed to thaw at room temperature for 30 min. Following the freeze-thaw process, samples were submerged in DI water for at least 48 h to allow for equilibrium swelling to be

reached. All samples were fabricated in the form of 12 mm diameter discs that were each nominally 5 mm thick. The hydrogel fabrication process is summarized in Figure 2.2.

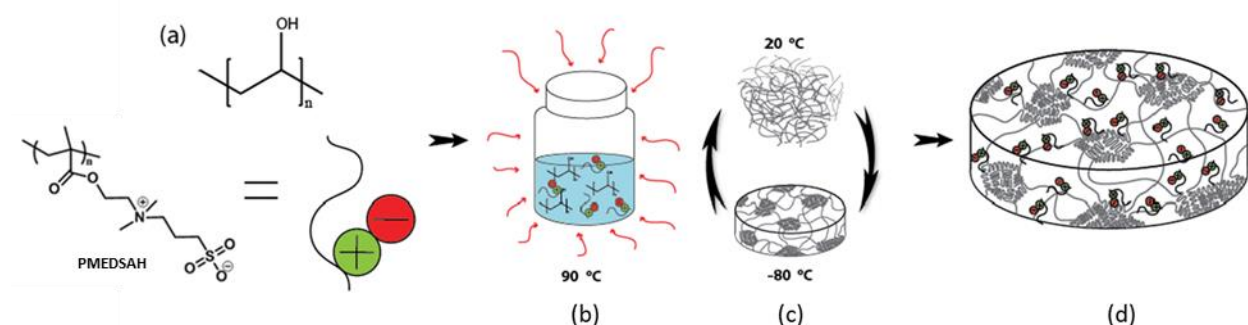


**Figure 2.2** - Schematic of hydrogel fabrication procedure: (a) Structure of PVA and a cartoon depiction of PMEDSAH, (b) Illustration of heating PVA-PMEDSAH solution, (c) Hydrogel crosslinking and (d) Final product.

## 2.3 Hydrogel Characterization

### 2.3.1 Fourier Transform Infrared Spectroscopy with Attenuated Total Reflection (FTIR-ATR)

FTIR-ATR was used to quantitatively evaluate the chemical composition of the neat PVA and zwitterionic blend samples with a PerkinElmer AutoIMAGE FTIR-ATR microscope (PerkinElmer Inc., Waltham, MA). Neat PVA and zwitterionic blends were placed in contact with a highly reflective germanium crystal. An infrared beam was directed towards the crystal where it reflected off the sample surface and internal faces of the crystal, producing evanescent waves. A portion of this wave energy was absorbed by the sample at wavelength that depends on the chemical composition, while the remaining energy was received by a detector [152]. Absorbance spectra were collected over a range of 450-4000  $\text{cm}^{-1}$ .

### 2.3.2 Wide Angle X-ray Scattering (WAXS)

WAXS experiments were conducted to ascertain the crystalline microstructure of the neat and blended material in both dry and hydrated states. For this purpose, a Rigaku S-MAX3000 pinhole camera system was utilized, with a Micromax-007HF rotating anode source operating with Cu K $\alpha$  emission ( $\lambda = 1.5406$ ), voltage of 40 kV and current of 20 mA. Wide-angle scattering patterns were collected at a sample-detector distance of 117 mm, as calibrated using corundum (NIST SRM 676a) with Fujifilm image plates (CR HR-V) and a Raxia-Di Image Plate reader at a scan resolution of 100  $\mu\text{m}$ . An exposure time of 600 s was used for all samples. Samples were prepared for WAXS by slicing the 5 mm thick disks into  $\sim 1$  mm thick films. Wet samples were maintained in their fully hydrated form by being stored in separate glass vials containing DI water. Samples were mounted in an unconstrained form on the Rigaku sample tray for x-ray scattering analysis. Dry samples were mounted without containment as a film while hydrated samples were contained within a capsule prepared from Kapton $^{\circledR}$  tape. 1D WAXS patterns were plotted as intensity versus the detector angle ( $2\theta$ ).

### 2.3.3 Equilibrium Water Content (EWC)

Hydrogels were submerged in DI water until equilibrium conditions were reached and the equilibrium hydrated mass ( $m_w$ ) was recorded. Samples were then placed in a vacuum oven (Isotemp Vacuum Oven, Fisher Scientific), until equilibrium was reached and the equilibrium dehydrated mass ( $m_d$ ) was recorded. EWC was computed by calculating the percent difference between the masses of the hydrated and dehydrated samples [114].

$$EWC = \frac{m_w - m_d}{m_w} \quad (2.1)$$

### 2.3.4 Water Contact Angle

Hydrophilicity was evaluated with a ramé–hart advanced goniometer (ramé–hart instruments co., Succasunna, NJ). Here, contact angle was estimated via the shadow method where a high-resolution image of an ultrapure water droplet (EMD Millipore, Billerica, MA) was analyzed via the ramé–hart’s DROPimage Advanced™ software version 2.4.07.

### 2.3.5 Surface Roughness ( $R_q$ )

Surface roughness was quantified with a 3D digital microscope (HIROX KH-8700 Digital Microscope, HIROX-USA, Inc. Hackensack, NJ). Z-stack images were attained from a 100 x 100  $\mu\text{m}$  field of view with a 1  $\mu\text{m}$  z-step. The surface profile obtained through this approach was then used to compute the RMS roughness using equation 2.

$$R_q = \sqrt{\frac{1}{n} \cdot \sum_{i=1}^n (z_i - \bar{z})^2} \quad (2.2)$$

Where  $z_i$  is the individual height measurements over the length of the sample space,  $n$  represents the number of height measurements taken, and  $\bar{z}$  is the mean value of the individual height measurements [1]. Although there are a number of other methods for measuring surface roughness (including stylus profilometry and atomic force microscopy), non-contact optical profilometry (NOP) has been shown to produce accurate profile measurements when objective lens magnification is greater than 40 [153]. Given the simplicity of NOP compared to contact profilometry methods, it is often the method of choice for measuring hydrogel surface roughness when friction experiments are performed on the macro scale [7,154].

### 2.3.6 Confined Compression

Elastic compressive modulus was determined by performing confined compression experiments using an AR-G2 rheometer (TA Instruments, New Castle, DE) with an 8-mm diameter flat punch. Confinement was achieved by placing samples in a blind-tapped hole of diameter equal to that of the hydrogels (Figure 4.3a). Samples were loaded axially to 10% strain at a strain rate of 10  $\mu\text{m/s}$ , held at 10% strain for 1 minute following compression, and then unloaded at 10  $\mu\text{m/s}$  while monitoring the normal force. Elastic compressive modulus was obtained from the average slope of the initial linear portion of stress-strain curve produced during the unloading step (1-5% strain).

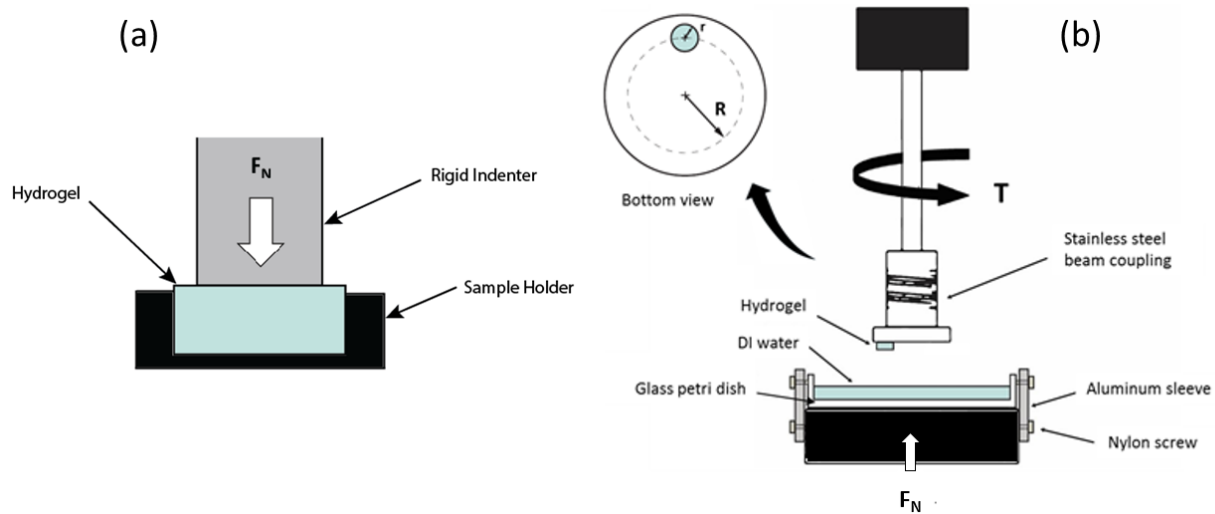


**Figure 2.3:** Illustration of the (a) confined compression and (b) tribo-rheometry experimental setup

### 2.3.7 Tensile Testing

Young's modulus was determined by performing tensile tests on  $2.27 \pm 0.27$  mm thick dog-bone shaped hydrogel films (ASTM Standard D636-03 Type IV, reduced in size four-fold).

For tensile testing, a Model 100P Universal Testing Machine equipped with a Biobath chamber and 5.6 lbf load cell was utilized (TestResources, Inc, Shakopee, MN). Fully hydrated samples were submerged in saline solution at 37 °C for the duration of the test. For each test, samples were preloaded to 0.1 N before being strained at strain rates ranging from 50 – 166  $\mu\text{m/s}$  to 10% strain. Modulus was calculated from the average slope over the entire range of the stress-strain curve (0 – 10% strain).

### *2.3.8 Tribological Characterization*

Observation of the short-term and long-term friction coefficients was performed using an AR-G2 rheometer (TA Instruments) using similar methods to other researchers [155,156]. Disc-shaped hydrogel samples were press fit into an adapted tribo-rheometry accessory (TA Instruments, Figure 2.3b) serving as the upper plate. The lower contacting surface was a glass petri dish. A glass petri dish was selected to provide repeatable, low surface roughness. The normal pressure experimental parameter was set at an average of 0.2 MPa. Since the sliding velocity varies along the radial direction, the midpoint of the sample was adopted for velocity calculations ( $R = 12 \text{ mm}$ ). This relatively high pressure coupled with a constant and relatively slow angular velocity of 0.065 rad/sec was maintained in order to minimize hydrodynamic effects [29,113]. The torque ( $T$ ) was measured for a period spanning 5 min to 6 h. In developing an expression for COF we assumed a uniform normal pressure acting over the sample surface. Thus, pressure was expressed as normal force per unit area. The torque that develops the frictional force on the sample was approximated as the measured torque divided by the distance from the center of the rotational axis

to the midpoint of the sample surface. Given the definition of COF, the ratio of shear force to normal force, COF was calculated using equation 3.

$$\mu = \frac{T}{F_N \cdot R} \quad (2.3)$$

### 2.3.9 Cytotoxicity

#### 2.3.9.1 Sample Preparation.

PVA-PMEDSAH hydrogels prepared as described earlier were cut into pieces approximately 1-2 mm thick while hydrated followed by complete drying. For determination of cytocompatibility, an extract-based method was employed, based on ISO10993-5 and ISO 10993-12. To make extracts, dry hydrogel material was weighed out so each sample had 0.1g/mL extraction media. Materials were extracted in DMEM-F12 (Invitrogen, Carlsbad, CA) supplemented with 10% Fetal Bovine Serum (Atlanta Biologicals, Norcross, GA) and 11% glutamine-penicillin-streptomycin (Invitrogen, Carlsbad, CA). Next, hydrogel samples were rehydrated in extraction media for 72 h until equilibrium was reached. Samples were then sterilized by exposure to ultraviolet light (UV) for 2 h. For extraction, sterile samples were placed in vials with an appropriate amount of media based on the dry mass, sealed and placed on a shaker at 37 °C, 60 rpm for 48 h. Following the extraction, media was removed from the sample, to a new tube and frozen at -80 °C until the cell assay. To test the cytocompatibility of PMEDSAH, samples were prepared as previously described, and made into a dry powder which was sterilized by UV as above, and dissolved directly in extraction media (PMEDSAH/media) and allowed to shake at 37 °C for 48 h. As a control, extraction media was allowed to shake at 37 °C for 48 h without sample.



### 2.3.9.2 Cellular Assay

L929 mouse fibroblasts (American Type Culture Collection, Manassas, VA) were used for this assay, as this cell line is commonly employed for cytotoxicity assays. Cells were grown in the aforementioned media using standard cell culture procedures. L929 mouse fibroblasts were seeded at 25,000 cells/cm<sup>2</sup> in a 96-well plate. The cells were allowed to attach and spread on the plate for 24h at which point media was removed and replaced with samples or controls as prepared above. As a negative control, 0.1% sodium dodecyl sulphate (SDS) [157], was made in control media. Following a 24 h incubation, extracts and control media were removed, and replaced with 1/10 volume of CCK-8 solution (Cell Counting Kit-8, Dojindo Molecular Technologies, Inc., Rockville, MD) which is metabolized by viable cells, turning the media an orange color. This solution was incubated with the cells for 4 h, followed by absorbance reading on a plate reader at 450 nm.

### 2.3.9.3 Cytotoxicity Analysis

Extracts were prepared from three individual material syntheses as well as three batches of PMEDSAH/media. For the cellular assay, all samples were tested in triplicate. For each assayed batch of material, the mean absorbance was determined for each sample. This absorbance was made relative to the media control, set to 100%. A value greater than 70% viability was an indication of cytocompatibility. The mean percent viability between the three assays was calculated and from this statistical difference between samples was determined.

### 2.3.10 Statistical Analysis

All statistical analyses were conducted with Minitab 17 (Minitab Inc., State College, PA). One way ANOVA with a significance level  $\alpha = 0.05$  was performed for comparison between the neat and blended material.

## 2.4 Results

### 2.4.1 Hydrogel Blend Preparation

Fabrication of hydrogels via the methods described earlier resulted in a robust hydrogel at all PMEDSAH contents. A slight increase in opacity was observed following the freeze-thaw process. Also, the formation of micron scale pores was observed throughout the bulk material at all levels however the prevalence of these pores generally increased with PMEDSAH content (Figure 2.4).

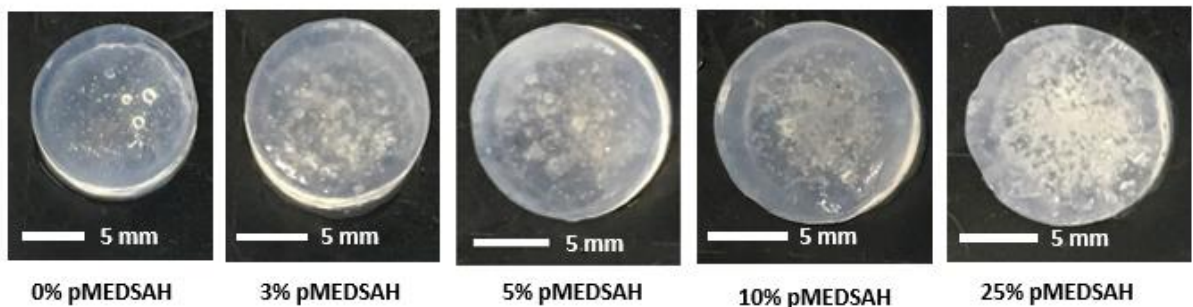


**Figure 2.4** - Representative images of neat and blended hydrogels following solvent casting and freeze thaw cycles

### 2.4.2 Surface Composition

Fourier transform infrared spectroscopy with attenuated total reflectance FTIR-ATR was used to determine if the zwitterionic polymer remained within the material and was present on the surface after being equilibrated in DI water. The infrared (IR) absorption spectra of neat PVA

hydrogels displayed a broad peak spanning 3500 – 3200  $\text{cm}^{-1}$ , characteristic of a hydroxyl (O–H) stretching vibration (Figure 2.5). The peaks spanning 3000 – 2850  $\text{cm}^{-1}$  and 1350-1470  $\text{cm}^{-1}$  are indicative of alkyl (–CH) stretching and bending vibrations. Compared to the IR spectra produced by the neat material, the PVA-PMEDSAH blends display a distinct peak spanning 1735 – 1750  $\text{cm}^{-1}$  characteristic of carbonyl (C=O) stretching. In addition, we no longer observe the peak spanning 3000 – 2850  $\text{cm}^{-1}$  characteristic of an alkyl stretching vibration [156]. These results suggest that PMEDSAH remains present on the surface of our hydrogels even after being equilibrated in DI water for several days.

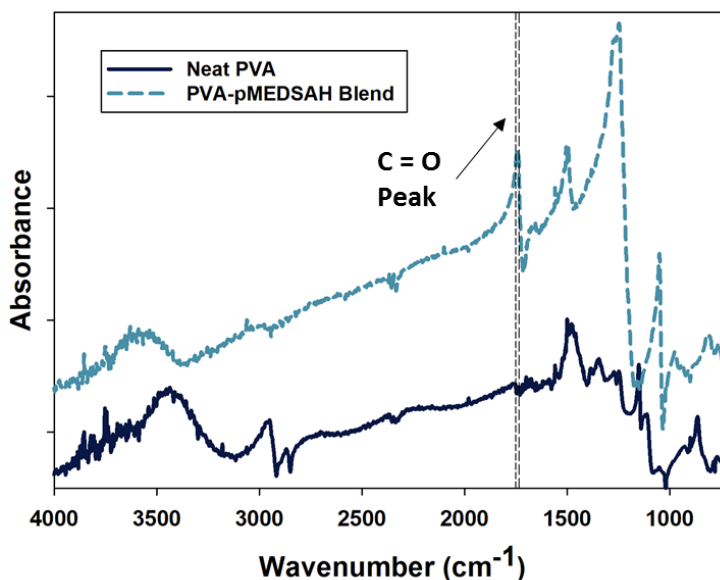


**Figure 2.5** - Representative FTIR-ATR spectra of the neat and tribologically enhanced hydrogels displaying the ester peak characteristic of MEDSAH.

### 2.4.3 Physical Characterization

The hydrophilicity and swelling behavior of the hydrogels was characterized through measurements of contact angle and equilibrium water content. Results in Table 2.1 show that PVA hydrogels with PMEDSAH contents ranging from 1 – 30 wt% relative to PVA did not yield a significant change in either of these parameters. An average water content of  $71.83 \pm 1.51\%$  was

observed regardless of the PMEDSAH content. This result falls within the mid-range of reported values for hydrogels fabricated with high molecular weight PVA [139]. A similar result was observed in our water contact angle measurements where contact angle ranged from 32 – 42° with no apparent trend or significant difference as PMEDSAH content was increased from 1 – 30 wt% relative to PVA. These measurements are within the standard range for PVA hydrogels [158].

**Table 2.1** - EWC and water contact angle data for PVA-H with increasing PMEDSAH content.

%PMEDSAH	EWC (%)	$\theta$ (deg.)
0	72 ± 1	36 ± 4
1	74 ± 1	32 ± 4
3	74 ± 0.4	32 ± 7
5	71 ± 1	40 ± 12
10	70 ± 1	32 ± 5
15	71 ± 1	36 ± 5
20	69 ± 1	32 ± 1
25	74 ± 1	42 ± 7
30	72 ± 0.4	38 ± 5

The potential for changes to hydrogel microstructure brought about by blending PVA with PMEDSAH was assessed via WAXS of both dry and fully hydrated samples. The WAXS profile produced by dehydrated PVA-H yielded diffraction peaks at  $2\theta$  angles of 11.4° (w), 19.3° (s), 23.0° (shoulder), 27.7° (w), 31.5° (w), and 40.3° (s) (w = weak, s = strong). These diffraction peak positions correspond to the monoclinic unit cell structure of crystallized PVA [159,160].

Diffraction patterns produced from fully hydrated PVA-H yielded an amorphous halo accompanied by a single diffraction ring at  $2\theta = 19.4^\circ$  (very close to the dry hydrogel). A low angle peak characteristic of the Kapton® window was also evident. The strongest peaks in both cases correspond to a  $d$ -spacing of 4.59 Å. Although hydrogels prepared in this investigation were formed from solutions that were significantly more concentrated than other studies that have

evaluated PVA-H microstructure via WAXS, these results agree quite well with results from the low wt% gels [160,161]. WAXS experiments were also performed on PVA-PMEDSAH blends at the 3% and 25% PMEDSAH levels to assess whether trends observed in terms of elastic compressive modulus (discussed below) were attributed to changes in the hydrogel microstructure. In comparing the profiles from Figure 2.6b we do not observe any changes in the WAXS patterns, indicating that the blended material continues to diffract x-rays in a similar manner compared to the neat material. This suggests that PMEDSAH does not alter the hydrogel microstructure at either of these levels.

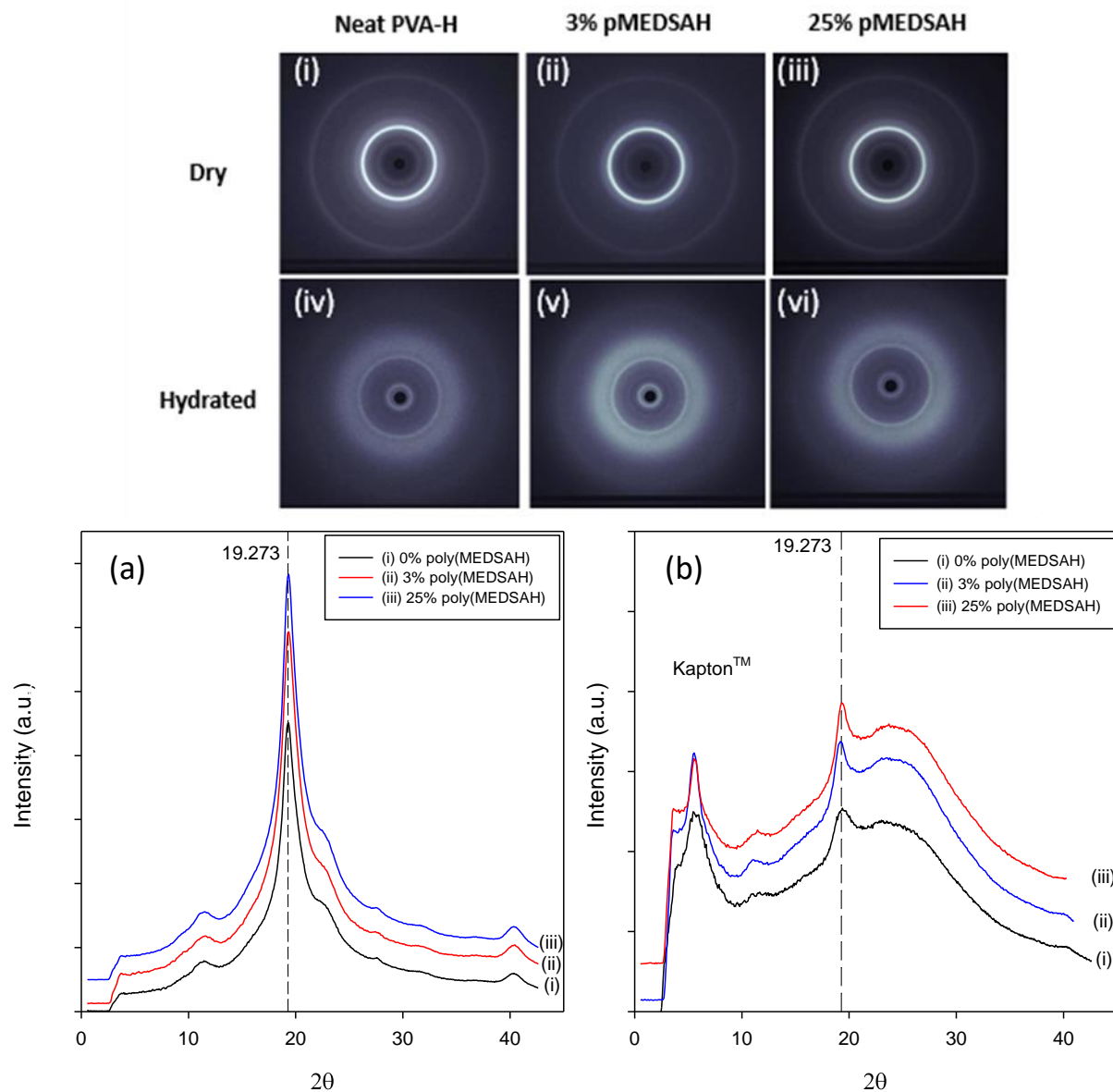


**Figure 2.6** - (top) representative WAXS patterns for dry and hydrated neat PVA-H and PVA-PMEDSAH blends: (i, iv) neat PVA-H; (ii, v) 3% PVA-PMEDSAH blend; (iii, vi) 25% PVA-PMEDSAH blend. Below are representative WAXS profiles for: (a) dry, and (b) hydrated PVA-PMEDSAH blends.

#### 2.4.4 Mechanical Characterization

Results from the confined compression experiments (Figure 2.7a, 2.7b) show that blending PVA with as much as 30 wt% PMEDSAH does not diminish the compressive stiffness of the hydrogel matrix. Rather than observing a steady decline in compressive modulus as PMEDSAH content was increased, we consistently observed a peak in modulus at 3% PMEDSAH that is statistically higher ( $p < 0.05$ ) than that of the neat material. This peak at the 3% level was followed by a slight but steady decrease as PMEDSAH content was increased further, though never dropping below  $1.38 \pm 0.39$  MPa. The confined compressive modulus of neat PVA was found to be  $1.92 \pm 0.26$  MPa which is within the reported range for neat PVA-H [114,139,162]. Compressive modulus for the blended material containing 1 – 30 wt% PMEDSAH ranged from  $2.66 \pm 0.34$  MPa to  $1.38 \pm 0.39$  MPa.

Tensile tests were performed on hydrogel films to determine if the peak compressive modulus observed at 3 wt% PMEDSAH also exists in tension. Results from these experiments showed that this was not the case (Figure 2.7c). Instead, as PMEDSAH content was increased, we observed a trending decrease in Young's modulus at a  $166 \mu\text{m/s}$  strain rate, and no apparent trend at a  $50 \mu\text{m/s}$  strain rate. Confined compression tests were also performed on hydrogel films of the same thickness as required for tensile testing to determine if the fabrication process to yield thinner freeze-thaw gels, itself, influenced the trend we observed on the thicker gels used for the friction experiments. Results from these experiments revealed a slight decrease in compressive modulus across the board; however, a similar trend was observed (Figure 2.7b) for the two thicknesses.

We did find that that blending PVA with PMEDSAH appears to increase the elastic nature of the hydrogel matrix (Figure 7c). An increase in the strain rate from  $50 \mu\text{m/s}$  to  $166 \mu\text{m/s}$  yielded

a significant increase in the apparent Young's modulus of the neat PVA-H films ( $p < 0.05$ ); however, this viscoelastic behavior appears to be suppressed as PMEDSAH content is increased. The relative change in Young's Modulus in response to the strain rate ranged from 48% in the neat material to 2% in the 25% PMEDSAH blends.

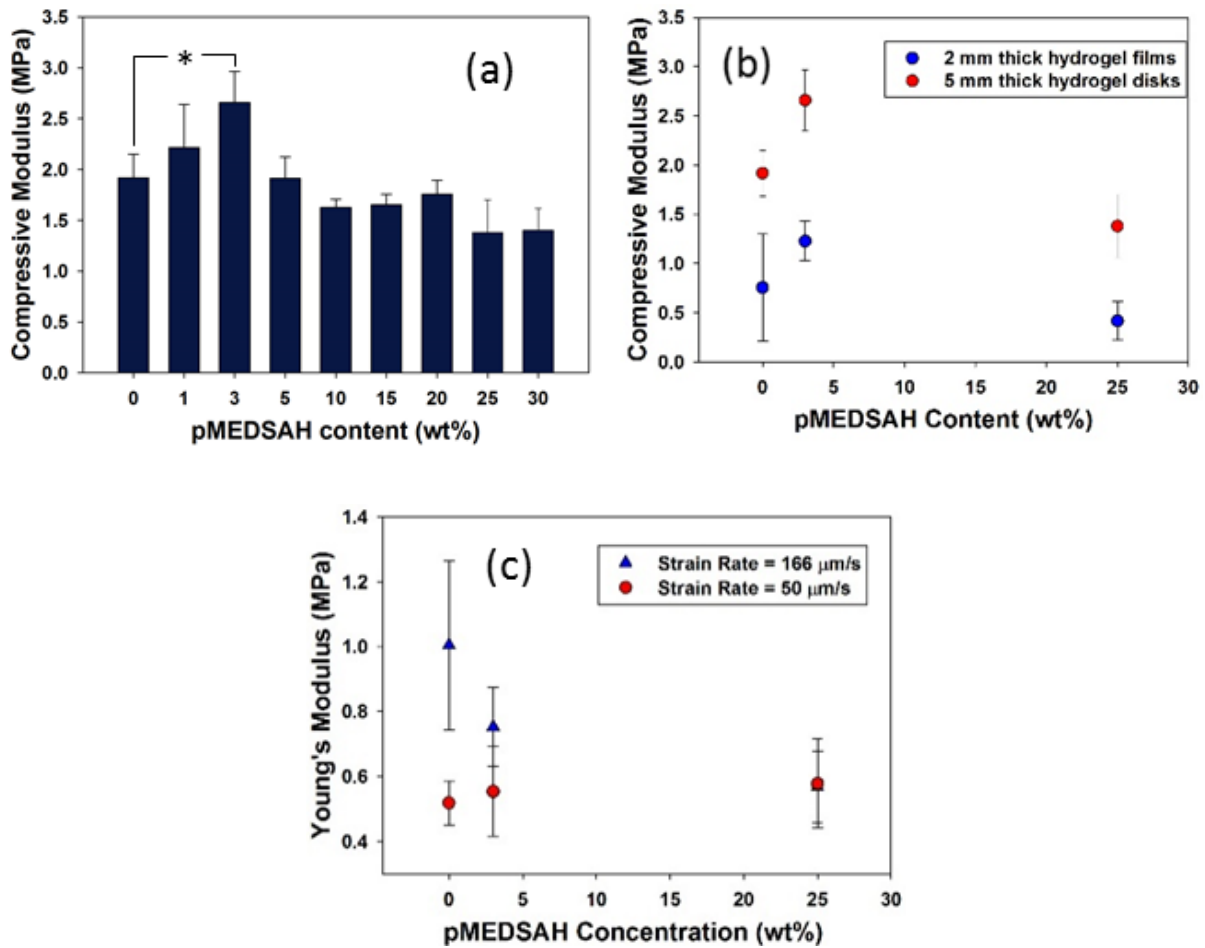


**Figure 2.7** - Characterization of (a) compressive modulus of the hydrogel discs used in the COF experiments (b) compressive modulus of the hydrogel discs compared to hydrogels fabricated as films and (c) Young's modulus for neat and blended hydrogels ( $n = 5$ ,  $*p < 0.05$  with neat PVA-H, ANOVA).



#### 2.4.5 Tribological Characterization

Comparison between neat PVA-H and the zwitterionic blends revealed that blending PVA with PMEDSAH resulted in a significant reduction in average COF (Figure 2.8). This significant decrease in COF was observed with as little as 3 wt% PMEDSAH relative to PVA. With 5% PMEDSAH a saturation point appears to be reached in terms of reducing COF. Average COF decreases from  $0.136 \pm 0.015$  for the neat material down to  $0.024 \pm 0.009$  at the 5% level. The lowest coefficient of friction was observed for 30 wt% PMEDSAH which displayed a COF of  $0.019 \pm 0.003$ .

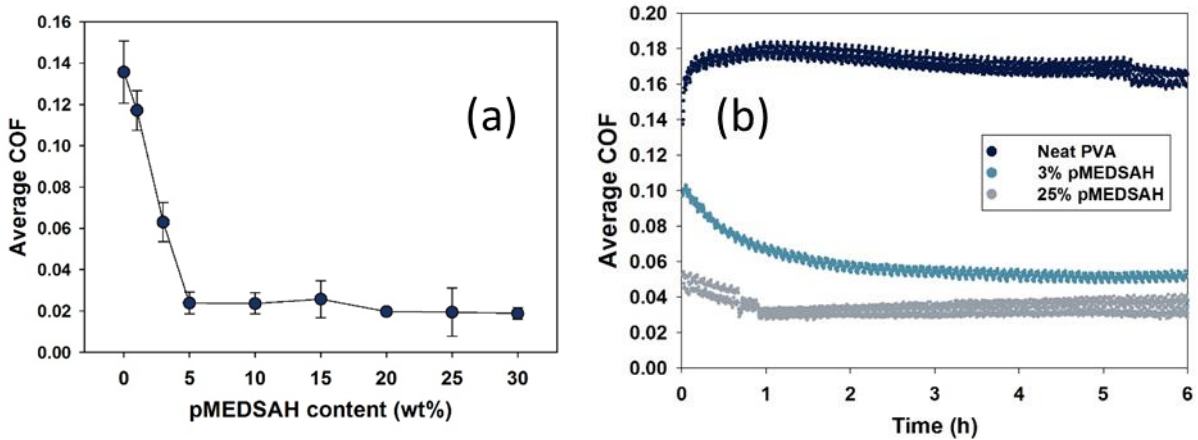


**Figure 2.8** – (a) Friction data for hydrogels with increasing PMEDSAH concentrations ( $n = 5$ ,  $*p < 0.05$  with neat PVA-H, ANOVA). (b) Representative plots of COF vs time for the neat and blended material over the course of 6 h experiments

Six-hour friction experiments were performed to investigate the stability of the lubricative properties observed in our five-minute experiments. Results in Figure 2.8b show that the significant reduction observed in our five-minute experiments were maintained over a 6 h period. In addition, the blends displayed a steady decrease in COF over the first 1 – 2 h of the experiment before reaching a steady value. On the other hand, neat PVA-H generally displayed a steady increase in COF over the first hour of the experiment before reaching a steady value.

When evaluating the tribological properties of any material, surface roughness is an important parameter to consider. Characterization of the surfaces of hydrated neat and blended material via 3D digital microscopy yielded RMS values ranging from  $0.36 \pm 0.25 \mu\text{m}$  to  $0.66 \pm 0.48 \mu\text{m}$  with no apparent trend or significant difference as PMEDSAH content was increased. Based on this result we postulate that the significant reduction in coefficient of friction can be attributed to hydration lubrication brought about by the zwitterionic polymer rather than a change in surface topography.

#### 2.4.6 Cytotoxicity

Cytocompatibility of PMEDSAH was assessed by dissolving the weight percentage of PMEDSAH associated with each blend level and incubating for 48 h. When L929 cells were cultured in the PMEDSAH, it was determined that at all PMEDSAH concentrations, the cells are highly viable (Figure 2.9a). Higher levels of PMEDSAH resulted in a trend towards lower viability which, however, was not statistically significant. In a similar study, neat PVA and PVA-PMEDSAH blends were found to be cytocompatible (Figure 2.9b), with viability levels well above the 70% threshold indicative of cell viability. These data demonstrate that our materials are cytocompatible, and lay the ground work for future work with the materials in cellular environments as substrates for cell culture as well as for implant studies where the materials are in contact with body tissues.

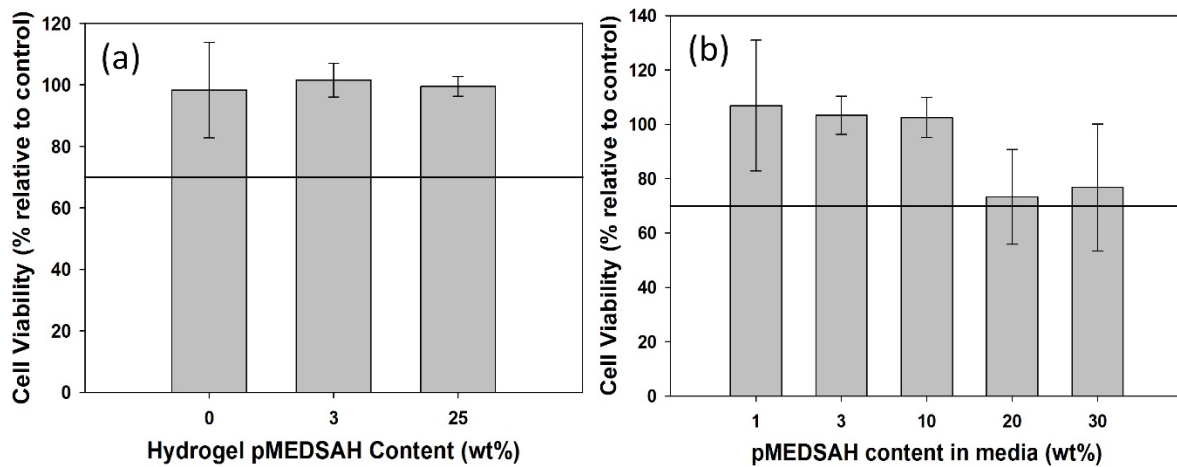


**Figure 2.9** - Cytocompatibility of L929 cells in extracts generated from (a) Neat PVA hydrogel and hydrogel samples with 3% or 25% PMEDSAH, (b) PMEDSAH dissolved in media at various concentrations. Data is representative of the mean cell viability ( $\pm$ SD) for three material samples, assessed in three cell-based assays.

## 2.5 Discussion

A novel material was prepared by blending zwitterionic polymer, PMEDSAH, with PVA, a widely used biocompatible hydrogel. Freeze-thaw PVA-H was selected as the base polymer of choice due to its well-established biocompatibility, low protein absorption [120] and mechanical strength [107,108]. In addition, these hydrogels have been approved by the FDA for use as drug delivery systems, contact lenses, membranes, and orthopedic devices [100]. Other biomedical applications of PVA-H include artificial cornea [163], vascular grafts [164], and nucleus pulposus replacement [132].

The data displayed in Figures 2.8 show that the addition of as little as 5% PMEDSAH results in as much as an 80% reduction in COF. We postulate that this result can be attributed to hydration shells forming around the charged groups on the PMEDSAH; namely the negatively charged sulfur trioxide group ( $\text{SO}_3^-$ ) and the positively charged quaternary ammonium group ( $\text{NR}_4^+$ ). Due to their dipole, water molecules are strongly attracted to the charged groups on

PMEDSAH resulting in the formation of molecular scale H<sub>2</sub>O films on the hydrogel surface [165]. Unlike non-associating liquids which exhibit solid-like properties under high pressures, these hydration films can maintain their fluidity providing a fluid-like response under high pressure. This yields a reduction in the development of shear stress between the opposing surfaces and a decrease in coefficient of friction [4].

Although further investigations are needed to fully understand this mechanism to design and possibly control a hydrogel material with a very efficient boundary lubrication system, the results observed in this investigation indicate that blending PMEDSAH with PVA significantly enhances the materials lubricity through hydration lubrication, depicted schematically in Figure 2.10. While predicting the thickness of interfacial fluid films was not the primary focus of this investigation, Grubin's formula is a useful tool for estimating the minimum film thickness [166]. Despite the relative simplicity of such methods, more recent analytical and numerical investigations have demonstrated their utility and accuracy [167,168]. Given equation 2.4, the dynamic viscosity of the lubricant,  $\eta$ , the contact load,  $w$ , sliding speed,  $u$ , as well as the compressive modulus,  $E$ , and radius,  $R$ , of the hydrogel, the minimum film thickness was found to be 17 nm.

$$h_{min} = R \cdot \left( \frac{2.8 \cdot \eta \cdot u}{E \cdot R} \right)^{0.65} \cdot \left( \frac{w}{E \cdot R} \right)^{-0.21} \quad (2.4)$$

This is well below the root mean square roughness of the opposing surfaces, indicating that the surfaces are articulating within the boundary lubrication regime. The true film thickness is likely lower since the Grubin formula assumes that the articulating surfaces are impermeable. Like articular cartilage, hydrogels are permeable, in fact recent investigations have revealed that such these materials are unable to maintain fluid films under physiological scale loads [16,20]. Film

thickness could also be characterized experimentally through in situ observation of Newton's fringes [169].

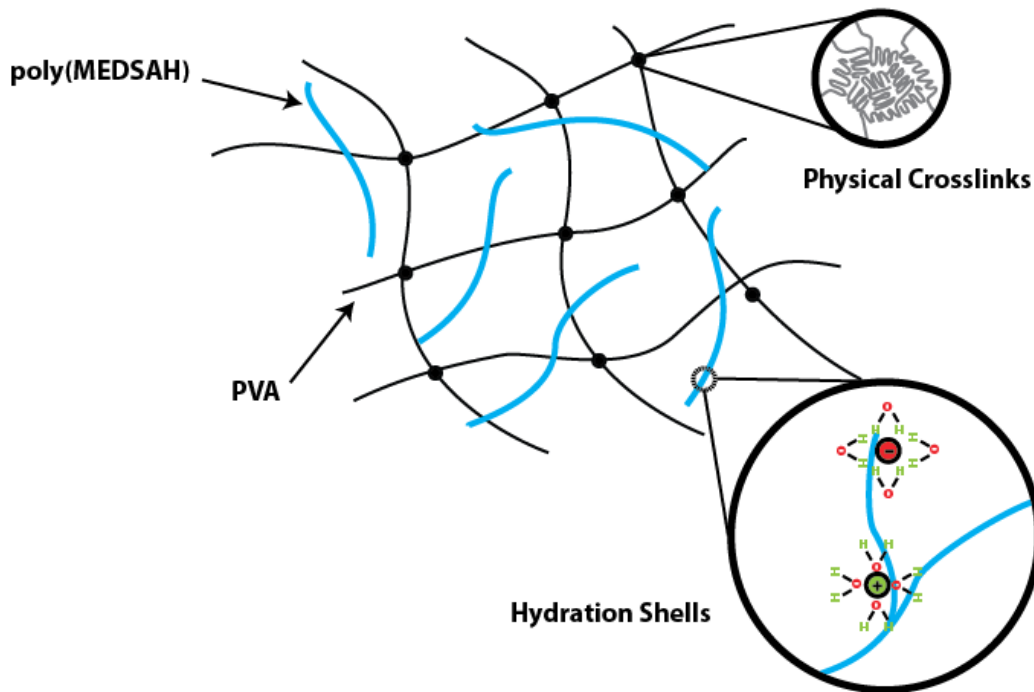


**Figure 2.10** - Schematic showing the boundary lubrication mechanism fostered by the zwitterionic polymer at the surface and with interstitial mobility within the crosslinked hydrogel.

Results from the confined compression and tensile experiments showed that the reduction in COF can be achieved without significant compromise to the mechanical properties of the neat material (Figure 2.7). Resistance to compressive loading is attributed to the modulus of the solid matrix as well as the hydrogel's ability to provide interstitial fluid load support. By using the slope of the stress-strain curve obtained from the unloading step of the test, the confounding effects of interstitial fluid load support are mitigated and direct measurement of the modulus of the solid matrix can be achieved. Results reveal that modulus of the hydrogels is finite when tested in

confined compression. Although incompressibility is a common simplifying assumption in the characterization of hydrogels, this result reveals that the material is not truly incompressible. Mechanical strengthening of freeze-thaw PVA hydrogels is understood to be dictated by the formation of physical crosslinks [151]. At low concentrations, blending PVA with PMEDSAH appears to result in stiffer hydrogels, possibly due to a secondary interaction between the two polymers [102]. When PMEDSAH content exceeded 3 wt% we observed a trending decrease for both tensile and compressive deformations. We postulate that above this threshold concentration, PMEDSAH may inhibit the formation of physical crosslinks between PVA molecules, resulting in the observed decrease in mechanical stiffness. Crosslinking capability affects the volume fraction of water present in the hydrogel which, in turn, alters the rigidity of the system reflected in the measured elastic modulus. Nevertheless, results from our physical characterization did not reveal any significant changes or trends in equilibrium water content (Table 2.1) or hydrogel crystallinity (Figure 2.6). The amorphous halo evident in diffraction patterns from hydrated samples which are absent in the dry material are likely attributed to swollen amorphous PVA or free water. Crosslinking capability affects the volume fraction of water present in the hydrogel which in turn alters the rigidity of the system, ultimately determining the hydrogel stiffness. Equilibrium water content (Table 2.1) remained unchanged, and hydrogel crystallinity suggesting that the changes in physical crosslinking may occur at constant overall crystallinity.

Results from our physical characterization also suggests that the PMEDSAH molecules freely diffuse within the hydrogel matrix, but do not directly affect its mechanical properties. This mechanism also appears to be at work in our friction experiments where, unlike in the neat material where we observe a steady increase in COF followed by a plateau, blends containing 3% and 25% displayed a steady *decrease* in COF over time, followed by a plateau. This behavior may be caused

by the gradual elution of PMEDSAH from the bulk to the surface of the hydrogel, an area of current inquiry.

One major area of potential for these zwitterionic blends is in the repair of focal chondral defects. Numerous researchers have considered PVA-H as a synthetic implant to repair articular cartilage damaged by injury or disease [100,110,113,114,120,162]. Considerable effort has gone into characterizing and improving PVA-H mechanical stability [102,170-173]. Thus PVA-H is considered to have suitable tensile and compressive mechanical properties to be able to function as a cartilage or meniscus implant. Although these PVA-H successfully replicate the fluid pressurization mechanism exhibited by the natural tissue, they often fail to replicate surface boundary lubrication mechanisms brought about by proteoglycan-synovial fluid interactions [123]. Investigations that have sought to improve the tribological properties of PVA-H include the fabrication of PVA-polyvinyl pyrrolidone blends, and surface functionalization of a hydrophobic boundary lubricant molecule [102,114]. Based on the results of this study, blending PVA with PMEDSAH appeared to result in a very effective approach for enhancing the tribological properties of PVA hydrogels while preserving desirable mechanical properties comparable to the neat material.

There were several limitations identified in this study. One limitation is that COF is not a singular value. Friction measurements are strongly dependent on experimental parameters, specifically, the nature of the two opposing surfaces and the lubricating fluid [17,174]. For hydrogels, the polymer content effects friction. Hydrogels with a high polymer content generally exhibit stiffer surface properties and lower water contents. As a result, heightened effects of surface asperities and the reduction in fluid available to lubricate the surface promote the generation of shear resulting in higher coefficients of friction [136].

Considering test parameters for hydrogels, COF can be increased by increasing load, because depth of contact increases due to hydrogels viscoelasticity [175], an area unexplored in our study. The sliding velocity can also affect COF, namely, a slow sliding speed may be manifested as a high COF due to the surface deforming at the same rate as the sliding speed, providing a large contact area. A fast sliding velocity often yields a low COF because the deformation rate of the gel lags behind the slider leading to small contact area and depth. Finally, the mechanical and chemical properties of the lubricant play an important role in dictating COF. High viscosity lubricants often yield low COF at a low sliding speeds since the fluid is not easily displaced, leading to an increase in fluid film thickness. Also, if a lubricant is able to interact with the contacting surfaces this gives rise to a low COF because molecules in lubricant do not permeate into the gel, leading to a thicker fluid film [175]. Water was used as the lubricant to highlight the hydration lubrication mechanism associated with zwitterionic polymers and also minimize viscous effects. However, since COF values can be varied based on details of the experimental setup, the emphasis for COF data should be placed on the relative magnitudes between the groups rather than in their absolute values.

Although this investigation does provide evidence that blending PVA with PMEDSAH results in the production of a low friction hydrogel, the effects of molecular weight have not yet been investigated. We postulate that changing the molecular weight of the boundary lubricant may have a significant effect on the mechanics and tribology of these biomaterials. This will be the subject of a future investigation. In addition, chemical characterization of the tribologically enhanced hydrogels was limited to FTIR-ATR. Conformation of the boundary lubricant structure should be characterized further via NMR spectroscopy. This will also be included in our assessment of the effects of molecular weight.



Another limitation in testing was that contact angle measurements are influenced by roughness. Caution was taken so that impurities during processing were minimized, but for hydrogels, deviations in surface roughness can range significantly [163,176,177]. The nominal surface roughness of the hydrogels was found to be around 0.51  $\mu\text{m}$ , which is satisfactory for biomedical applications. For example, if this material was used as a cartilage implant, these values are on the order of roughness that has been reported for articular cartilage, which can range from 0.1 to 1  $\mu\text{m}$  [178].

Finally, this study only considered constant sliding motion at the lower end of physiologically relevant loads. Tests were performed this way intentionally, so as to maintain boundary lubrication conditions throughout the experiments [17]. Future testing needs to explore loading and sliding situations that are physiologically relevant to specific applications. For example, hydrogels could be articulated against cartilage in both rolling and sliding motion to study the friction and wear of the natural and synthetic counter-faces.

## 2.6 Conclusion

This investigation describes enhancement of the tribological properties PVA-H by incorporation of a zwitterionic polymer that served as a boundary lubricant embedded within the hydrogel matrix. With a relatively simple solvent casting and freeze-thaw processes, PVA-PMEDSAH blends were successfully prepared. Chemical, physical, mechanical and tribological analysis was performed to analyze the structure-property relationships. The results showed a dramatic reduction in COF with as little as 5 wt% PMEDSAH, while maintaining cytocompatibility, mechanical and physical properties comparable to the neat material. This novel

approach provides a promising platform for further investigation of enhancing the boundary lubricant properties of hydrogels for use in biomedical applications.

## CHAPTER 3: EFFECTS OF LUBRICANT CHAIN LENGTH ON THE MECHANICS AND TRIBOLOGY OF ZWITTERIONIC HYDROGEL BLENDS

### 3.1 Introduction

Results discussed in Chapter 2 indicate that blending PVA with PMEDSAH results in significant reduction in coefficient of friction while maintaining comparable physical and mechanical properties to the neat material. While the compression experiments described previously are useful for relative comparisons between sample types, the reported compressive modulus is not a true material property. Material properties of biphasic materials such as hydrogels and articular cartilage can be ascertained through the application of an analytical model. Such models allow investigators to relate controllable mechanical test conditions to material properties which in turn can be used to predict behavior which may not be measurable directly (i.e. stress and fluid load support).

In articular cartilage, compressive loading results in pressurization of the fluid contained within the collagenous matrix. This behavior is attributed to the high-water content (~80%) and low permeability ( $\sim 1.8 \times 10^{-3} \text{ mm}^4/\text{N}\cdot\text{s}$ ) of articular cartilage. In addition to minimizing stress on the solid phase of the tissue, experimental reports have revealed that as fluid load support subsides, coefficient of friction increases by as much as 2 orders of magnitude [20]. These insights have motivated the investigation described in this chapter, which uses an analytical model, recently developed by Moore and Burriss to characterize the mechanics of articular cartilage, to investigate the effects of PMEDSAH molecular weight on interstitial fluid load support.

Given the high-water content of PVA-H and PMEDSAH's solubility in water it was hypothesized that compressive loading may cause the boundary lubricant to be eluted to the surface of the hydrogels as a result of pressure driven flow. This type of behavior would be valuable for a

self-replenishing tribological system. Both passive and pressure driven diffusion experiments were performed to access the feasibility of this hypothesis and to investigate the effect of boundary lubricant molecular weight on the diffusive kinetics of the blend. In addition to diffusion experiments and characterization of fluid load support, this chapter will also detail the effects of boundary lubricant molecular weight on COF vs sliding speed behavior and hydrogel microstructure to provide additional insight into the identification of critical factors for the design of a tribologically enhanced polymeric system.

## 3.2 Hydrogel Fabrication Method

### 3.2.1 Materials

2,2'-Azobis(2-methylpropionamide) dihydrochloride (AAPH), [2-(methacryloyloxy ethyl] dimethyl-(3-sulfopropyl) ammonium hydroxide) (MEDSAH), sodium chloride, and polyvinyl alcohol (PVA, 99% hydrolyzed) with a reported average molecular weight of 130,000 g/mol were purchased from Sigma-Aldrich (St. Louis, MO). All chemicals were used as received. Deionized water was obtained from a Synergy® Water Purification System (Merk Millipore, Billerica, MA).

### 3.2.2 Boundary Lubricant Synthesis and Hydrogel Fabrication

The zwitterionic polymer poly(MEDSAH), hereafter PMEDSAH, was prepared by free radical polymerization initiated by AAPH under nitrogen in a DI water solution with a monomer concentration of 0.25 M. The ratio of monomer to initiator molar concentration,  $[M_0]/[I_0]$ , spanned from 65 – 400 to achieve a wide range of molecular weights. The reactions were performed at 65 °C for 6 h at which point the polymer was harvested with a Busci Rotovapor® R-210 rotary

evaporator (Buchi Analytical Inc, New Castle, DE) at 60 °C for 1 h. The harvested polymer was subsequently ground to a fine powder and dried at -30 in.Hg in an Isotemp Vacuum Oven (Fisher Scientific, Hampton, NH) at room temperature for 24 h.

Hydrogels were fabricated via a similar method to what was described in our previous manuscript [179]. First a prescribed amount of PMEDSAH was dissolved in 0.2 M aqueous NaCl and then mixed with PVA to achieve 40 wt% (m/v) PVA relative to solvent. The mixtures were then heated at 90 °C for 6 h and the subjected to four freeze thaw cycles where samples were frozen at -80 °C for 0.5 h and then thawed at room temperature for 0.5 h. All samples were fabricated in the form of 12 mm diameter discs that were each nominally 5 mm thick.

### 3.3 Characterization Methods

#### 3.3.1 Viscosity Average Molecular Weight

Given the previously reported Mark-Houwink parameters for PMEDSAH (at 21 °C in 0.2 M aqueous NaCl),  $a = 0.4071$ , and  $k = 2.06 \times 10^{-3}$ , intrinsic viscosity measurements for aqueous boundary lubricant solutions were used to calculate the viscosity average molecular weight [180]. Viscosity measurements were performed with a m-VROC™ viscometer (RheoSense, San Ramon, CA). Stock solutions with 3.5 g/dL polymer concentration were subsequently diluted with 0.2 M aqueous NaCl to 14 g/dL. Measurements were performed in triplicate and viscosity was measured at five different concentrations for a given molecular weight. Relative viscosity,  $\eta_r$ , was computed from the measured solution viscosity  $\eta$ , and the solvent viscosity,  $\eta_s$  and can be expressed as  $\eta_r = \eta/\eta_s$ . Specific viscosity ( $\eta_{sp}$ ) can be expressed as  $\eta_{sp} = \eta_{rel} - 1$ . Intrinsic viscosity was calculated by linear extrapolation to zero concentration ( $c = 0$ ) of reduced viscosity,  $\eta_{red} =$

$\eta_{sp}/c$ , and inherent viscosity,  $\eta_{inh} = \ln \eta_r/c$  in accordance with the Huggins and Kraemer equations [181].

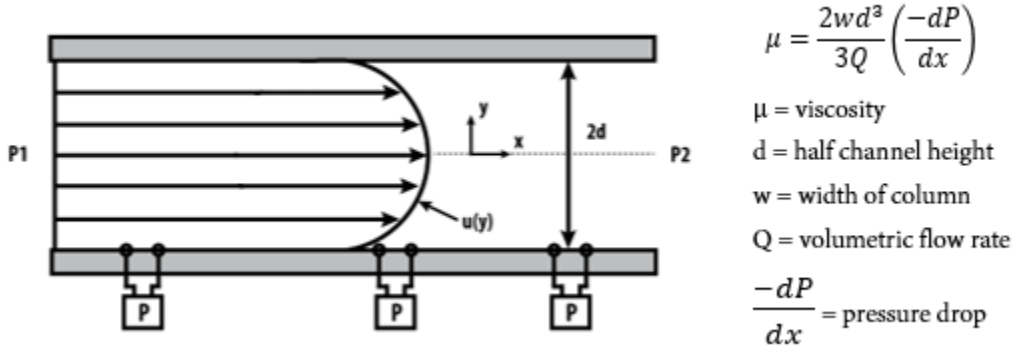


**Figure 3.1** – Schematic illustration of the experimental setup used for measuring the viscosity of the aqueous polymer solutions.

### 3.3.2 Boundary Lubricant Diffusion

The m-VROC™ viscometer (RheoSense, San Ramon, CA) was also used to measure the diffusive properties of PMEDSAH within the PVA-H matrix. For passive diffusion experiments, 1 mL of 0.2 M aqueous NaCl was added to the surface of hydrogels immediately after the final freeze thaw cycle (Figure 3.2). Samples were stored on a shaker table in a 37 °C incubator and viscosity of the supernatant was measured at time points ranging from 1-12 days. After constructing a calibration curve for solution viscosity versus polymer concentration, the amount of polymer that had diffused out of the hydrogel could be computed. Analysis of the passive diffusion kinetics was performed with an empirical power law model developed by Peppas et al [182,183]:

$$\frac{M_t}{M_\infty} = Kt^n \quad (3.1)$$

PMEDSAH elution was characterized by indenting the surface of the hydrogel with a 6.35 mm diameter stainless steel spherical indenter tip attached to a AR-G2 rheometer (TA Instruments, New Castle, DE) as illustrated in Figure 3.3. Indentation was performed at 18 °C after passive

diffusion had subsided. Samples were indented by as much as 30% of the sample thickness at an indentation rate of 10  $\mu\text{m/s}$  and then held for 1 minute before the load was released and the supernatant collected.

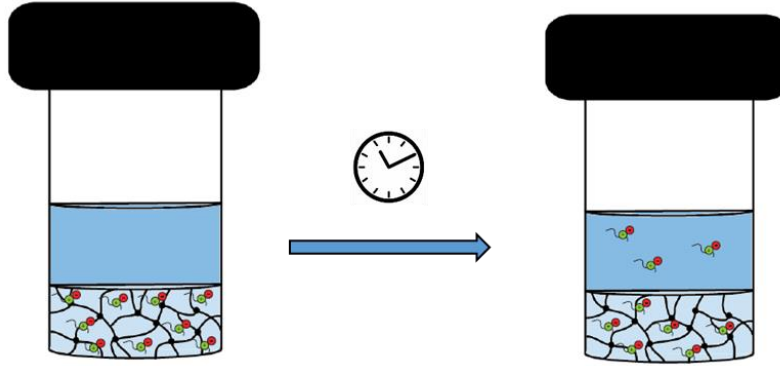


**Figure 3.2** - Scheme illustrating the test conditions for characterizing passive boundary lubricant diffusion

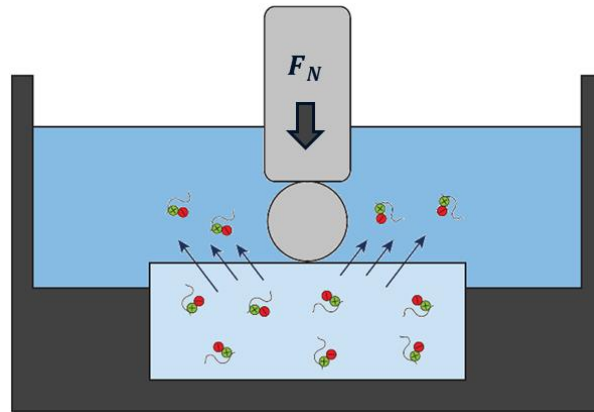


**Figure 3.3** - Scheme illustrating the test conditions for characterizing pressure driven boundary lubricant elution

### 3.3.3 Rate Controlled Hertzian Indentation

The effects of PMEDSAH molecular weight on the mechanics of the zwitterionic hydrogel blends were characterized within the context of Hertzian biphasic theory (HBT). These experiments stem from an analytical solution to the Hertzian contact problem for a biphasic semi-infinite half space derived by Moore and Burris [184]. This method allows us to compute four material properties: effective contact modulus,  $E_c$ , equilibrium contact modulus,  $E_{c0}$ , tensile

modulus,  $E_t$ , and permeability,  $k$  [185]. All experiments were performed with an AR-G2 rheometer (TA Instruments, New Castle, DE) with a 6.25 mm diameter stainless steel spherical indenter tip (Figure 3.4). As detailed previously [185], effective contact modulus, a function of normal force,  $F_N$ , probe radius,  $R$ , and penetration depth,  $\delta$ , is defined as:

$$E_c = \frac{3}{4} F_N R^{-0.5} \delta^{-1.5} \quad (3.2)$$

Effective contact modulus was computed at indentation rates,  $\dot{\delta}$ , ranging from 0.1 – 100  $\mu\text{m/s}$  in randomized order. Equilibrium contact modulus,  $E_{c0}$ , was computed via stress relaxation experiments. A previously described approximate solution was fit to the experimental load-relaxation data allowing us to compute  $E_{c0}$  [186]. The relaxation data was fit using equation 3.

$$F_N(t) = \sum_{i=0}^3 B_i e^{-t/\tau_i} \quad (3.3)$$

Given the indentation ramp time,  $t_R$ , and the ramp correction factors given as:

$$RCF_i = \frac{\tau_i}{t_R} (e^{t_R/\tau_i} - 1), i = 1,2,3 \quad (3.4)$$

The material parameters,  $C_i$ , for a given displacement,  $\delta$ , can be expressed as:

$$C_0 = \frac{B_0}{\delta^{3/2} (8\sqrt{R}/3)} \quad (3.5)$$

and

$$C_i = \frac{B_i}{(RCF_i) \delta^{3/2} (8\sqrt{R}/3)}, i = 1,2,3 \quad (3.6)$$

Given material parameters,  $C_i$ , and the radius of the indenter tip,  $R$ , contact modulus expressed as:

$$C_i = \frac{B_i}{(RCF_i) \delta^{3/2} (8\sqrt{R}/3)} \quad (3.7)$$

was used as an additional constraint on the optimization function by using it fit the indentation curve. Equilibrium contact modulus was expressed as:



$$E_{c0} = \frac{3}{2} C_0 \quad (3.8)$$

Given  $E_{c0}$  and  $E_c(\delta)$ , a non-linear least squared curve fit algorithm was applied to equation 3 to compute permeability,  $k$ , and tensile modulus  $E_t$  for a given sample type. All tests were performed in DI water at room temperature.

$$E_c = \frac{E_0}{1 - \left( \frac{E_t}{E_t + E_0} \frac{\delta R}{\delta R + E_0 k} \right)} \quad (3.9)$$

Given  $E_c, E_{c0}, E_t$ , and  $k$  for a given sample type the fluid load fraction,  $F'$  can be expressed as:

$$F' = \left( \frac{E_t}{E_t + E_{c0}} \right) \left( \frac{\delta R}{\delta R + E_{c0} k} \right) \quad (3.10)$$

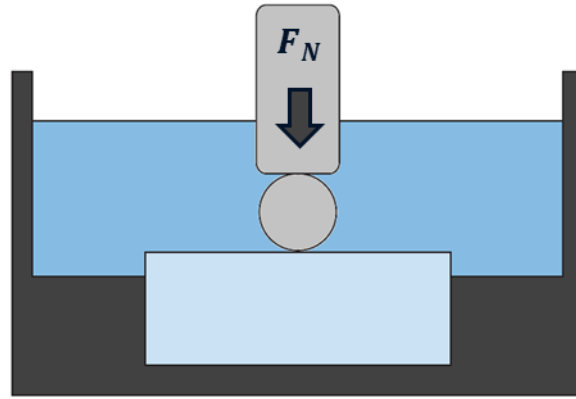


**Figure 3.4** - Schematic illustration of the test conditions for (left) indentation testing

### 3.3.4 Small Angle X-Ray Scattering

Small-angle X-ray scattering (SAXS) was performed to investigate how PMEDSAH influenced long range molecular order of the hydrogel matrix. Experiments were conducted with a Rigaku SMAX 3000 Pinhole SAXS instrument operating at 45 kV and 0.88 mA producing Cu

K $\alpha$  X-ray radiation ( $\lambda = 1.5405 \text{ \AA}$ ) at a sample-detector distance of 1550 mm. Hydrogels were cut into 1 mm thick films and encapsulated in Kapton<sup>®</sup> tape prior to being placed in the X-ray chamber under ambient pressure. Kapton<sup>®</sup> windows were used to isolate the chamber from the evacuated source and detector tubes. 1D SAXS patterns were plotted as intensity,  $I$ , vs scattering vector,  $q$ .

### 3.3.5 Differential Scanning Calorimetry

The effects of PMEDSAH on hydrogel crystallinity was characterized via differential scanning calorimetry (Q200 TA Instruments, New Castle, DE). Specimens obtained from the center of the neat and 25 wt% PMEDSAH hydrogels were hermetically sealed inside stainless-steel pans and heated at 10 °C/min under flowing nitrogen atmosphere from 40 to 250 °C. Hydrogel degree of crystallinity was calculated via the ratio of the heat of fusion,  $\Delta H$ , of the hydrogel (normalized for the solid mass) and the reported enthalpy of melting for 100% crystalline PVA  $\Delta H_c$  [187-189].

### 3.3.6 Scanning Electron Microscopy

A JEOL JSM-5600 Scanning Electron Microscope (SEM) was used to study the microstructural morphology and surface topography of the zwitterionic hydrogel blends. Samples were frozen for at least 12 h in a -80 °C freezer and then lyophilized with a Labconco FreeZone 2.5 Plus (Labconco, Kansas City, MO). Following lyophilization, all samples were sputter coated with gold via a Desk II Sputter Coater (Denton Vacuum LLC, Moorestown, NJ) for 45 s prior to SEM. Both surfaces and cross sections were imaged at an acceleration voltage of 8 kV.

### 3.3.7 Tribo-Rheometry

The effects of boundary lubricant molecular weight on coefficient of friction were characterized with an AR-G2 rheometer (TA Instruments, New Castle, DE). Disc-shaped

hydrogels were press fit into an adapted tribo-rheometry accessory which served as the upper geometry. The lower contacting surface was a glass petri dish filled with DI water (Figure 3.5). Hydrogels were subjected to average contact pressure of 0.1 MPa and were rotated at angular velocities ranging from 0.1 to 5 rad/s in randomized order. The rheometer operation under position control rather than force control. To minimize the effects of stress relaxation samples were unloaded before changing angular velocity. All PVA PMEDSAH blends contained 10 wt% PMEDSAH. Given the measured normal force,  $F_N$ , torque,  $T$ , and the hydrogel offset radius,  $R$ , coefficient of friction was calculated using the following equation:

$$\mu = \frac{T}{F_N \cdot R} \quad (3.11)$$

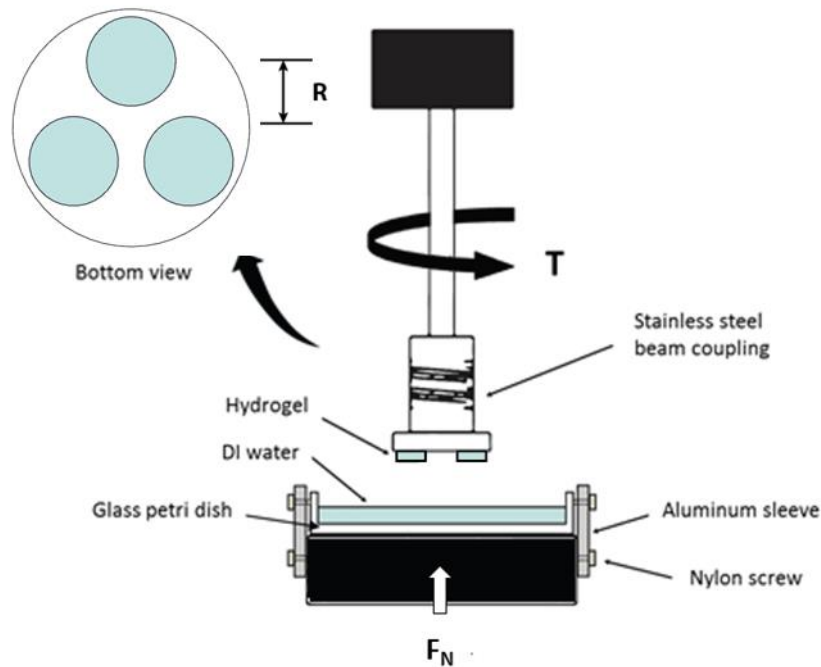


**Figure 3.5** - Schematic illustration of the test conditions for measuring coefficient of friction

### 3.3.8 Statistical Analysis

All statistical analyses were conducted with Minitab 17 (Minitab Inc., State College, PA). One way ANOVA with a significance level  $\alpha = 0.05$  was performed for all hypothesis testing.

## 3.4 Results

### 3.4.1 Viscosity Average Molecular Weight

The boundary lubricant chain length or viscosity average molecular weight was determined through intrinsic viscosity measurements and the Mark-Houwink parameters for PMEDSAH (at 21 °C in 0.2 M aqueous NaCl). Viscosity measurement result reveal a trending increase in boundary lubricant molecular weight with decreasing initiator concentration relative to monomer concentration (Figure 3.6). Diffusion, indentation, and friction experiments were performed with PMEDSAH molecular weight ranging from 50 – 825 kDa (Table 3.1).

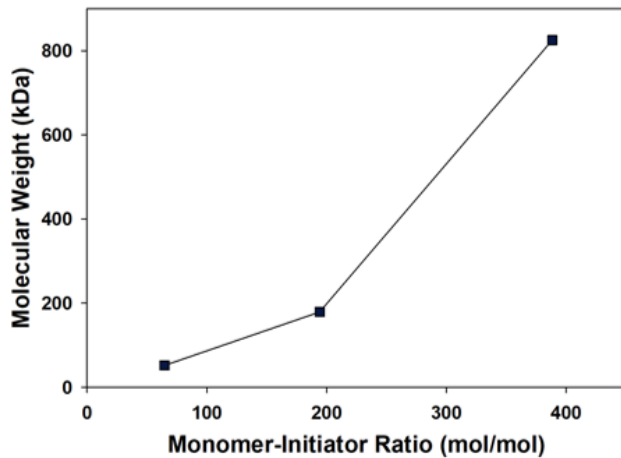


**Table 3.1** - Effects of synthesis parameters on boundary lubricant molecular weight

Monomer-Initiator Ratio [mol/mol]	Molecular Weight [g/mol]
64.72	52,525
194.16	179,641
388.32	825,064

**Figure 3.6** - Effects of synthesis parameters on boundary lubricant molecular weight

### 3.4.2 Boundary Lubricant Diffusion

Diffusion of PMEDSAH was characterized by immersing hydrogels in aqueous NaCl and measuring changes in supernatant viscosity. An empirical power law model was used to characterize the diffusive properties of PMEDSAH within the PVA hydrogel matrix. Use of the power law resulted in a satisfactory fit of the experimental data with coefficient of determination ranging from 0.59 – 0.71 (Figure 3.7). This characterization method revealed a trending increase in diffusion coefficient with increasing PMEDSAH molecular weight and a trending decrease in the release exponent (Table 3.2). Measurement of supernatant viscosity following hydrogel indentation revealed an apparent increase in PMEDSAH release when the boundary lubricant molecular weight was  $\leq 180$  kDa (Figure 3.7).

**Table 3.2** - Proportionality constant and release exponent for diffusion power law

<b>Mv</b>	<b>K</b>	<b>n</b>	<b>R<sup>2</sup></b>
50	0.15	0.85	0.71
180	0.20	0.75	0.59
825	0.61	0.27	0.62

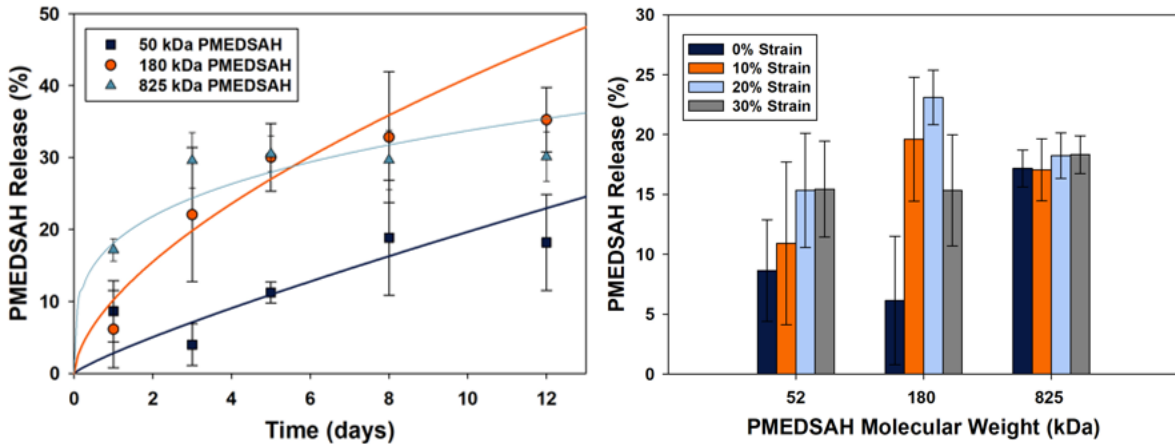


**Figure 3.7** - Effect of boundary lubricant molecular weight on boundary lubricant diffusion (left) and elution (right)

### 3.4.3 Rate Controlled Hertzian Indentation

Fitting experimental indentation and stress relaxation data via Hertz contact theory a numerical approximation resulted in an excellent fit with coefficient of determination very close to 1 in all cases (Figure 3.8). Result did not reveal any apparent trends regarding the effects of boundary lubricant molecular weight on hydrogel contact modulus however regardless of BL molecular weight a trending increase in contact modulus was observed as PMEDSAH content increased. In all cases blending PVA with 25 wt% PMEDSAH resulted in a statistically significant increase in hydrogel contact modulus (Figure 3.9). As displayed in Figure 3.10, application of Hertzian biphasic theory revealed that the contact model provided a satisfactory fit of the experimental data with coefficient of determination between 0.58 – 0.91). The blends provided the best fit with  $0.76 < R^2 < 0.91$ . Based on the contact model fit increasing PMEDSAH molecular weight results in an order of magnitude decrease in hydrogel permeability (Table 3.3).

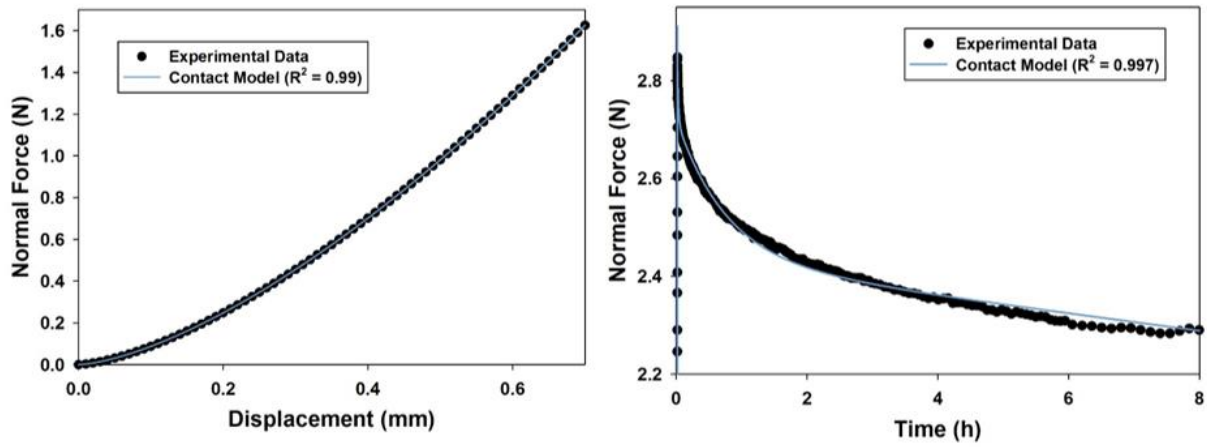


Figure 3.8 Representative contact model fit for indentation (left) and stress relaxation(right) experiments

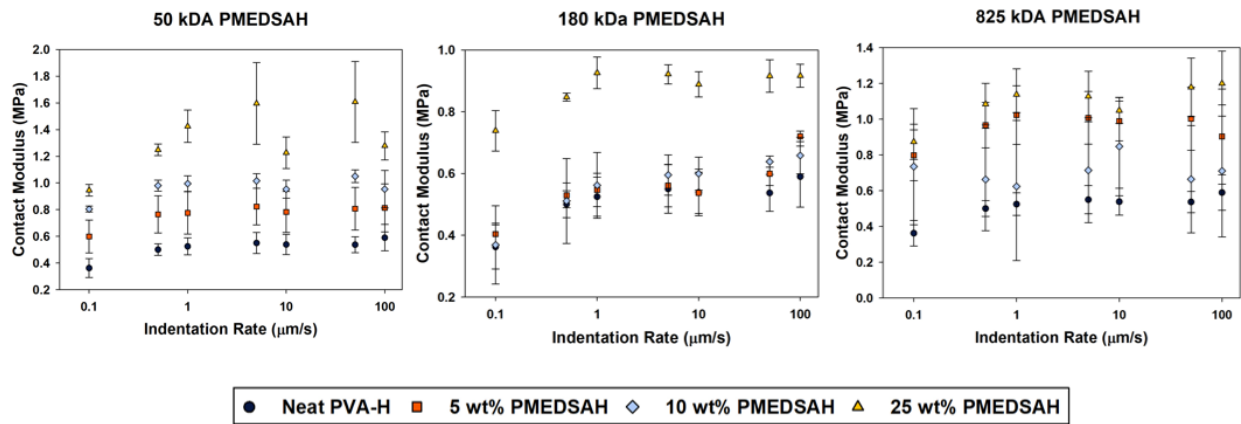


Figure 3.9 - Effects of boundary lubricant molecular weight and boundary lubricant content on hydrogel contact modulus

Table 3.3 - Material properties determined through curve fitting HBT contact model to experimental data

Sample	$E_{c0}$ (MPa)	$k$ (mm <sup>4</sup> /Ns)	$E_t$ (MPa)
Neat PVA	0.41	3.58	0.14
50 kDa Blend	0.70	0.36	0.75
180 kDa Blend	0.35	0.16	0.57
825 kDa Blend	0.38	0.15	0.77

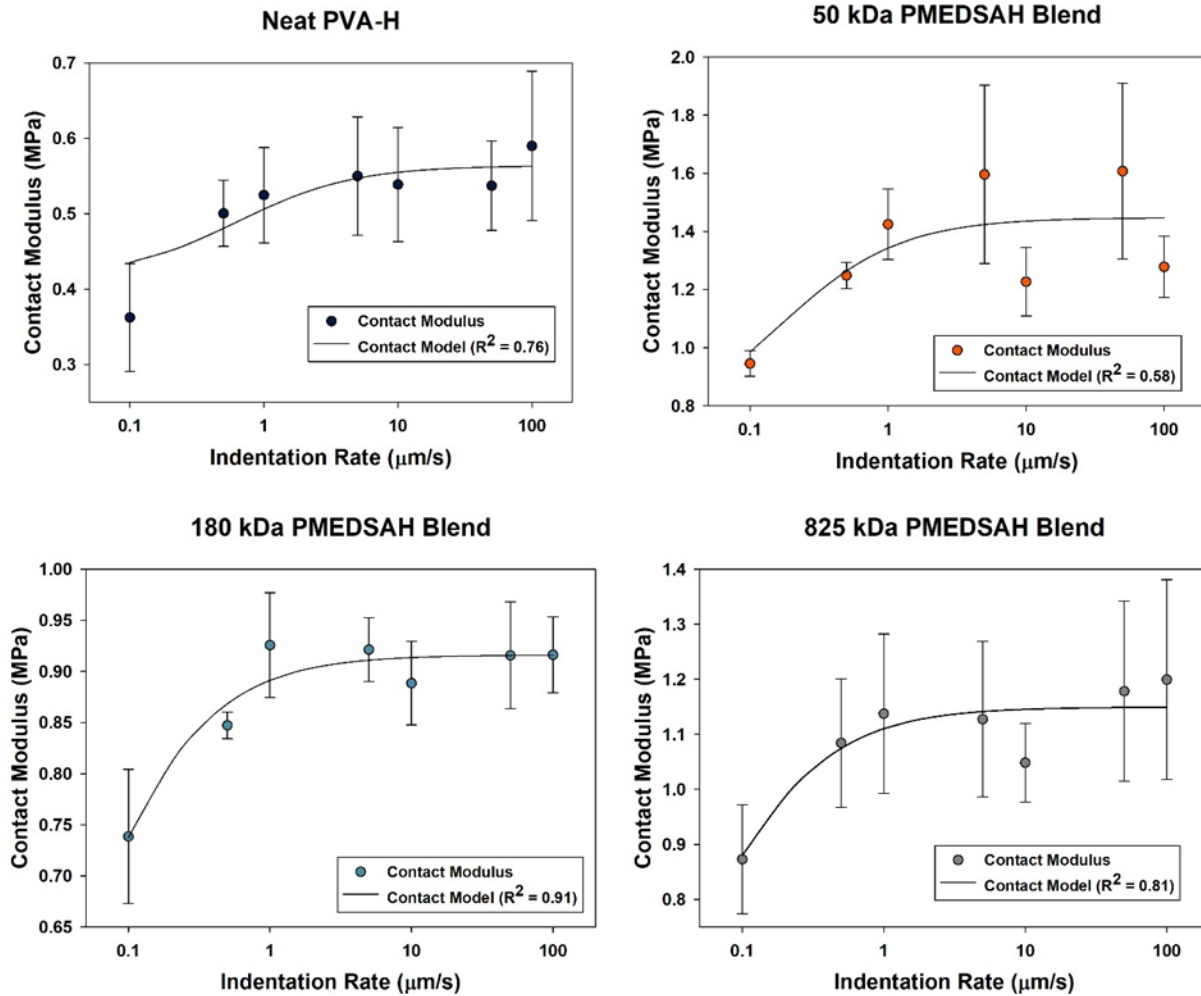


Figure 3.10 - Hertzian biphasic theory contact model fit for neat PVA and 25 wt% PVA PMEDSAH blends

### 3.4.4 Physical Characterization

Blending PMEDSAH with PVA did not appear to influence small angle x-ray diffraction.

The processing method did result in a statistically significant change in bulk crystallinity based on



the entropy of melting measurements performed with DSC (Figure 3.11). Neat PVA hydrogels displayed an average degree of crystallinity of  $38.5 \pm 5.0\%$  compared to the 25 wt% blend which displayed an average degree of crystallinity of  $50.9 \pm 5.0\%$  (Table 3.3). Low magnification (as low as X100) imaging via SEM revealed the presence of PMEDSAH on both the surface and through the cross section of the hydrogel (Figure 3.12). Bulk hydrogel porosity is apparent at magnification greater than X950 however there is no distinct difference apparent porosity between neat PVA and blends containing 25 wt% PMEDSAH. Hydrogel pores sizes were heterogeneously distributed with diameters ranging from single micron to nanometer scale (Figure 3.13).

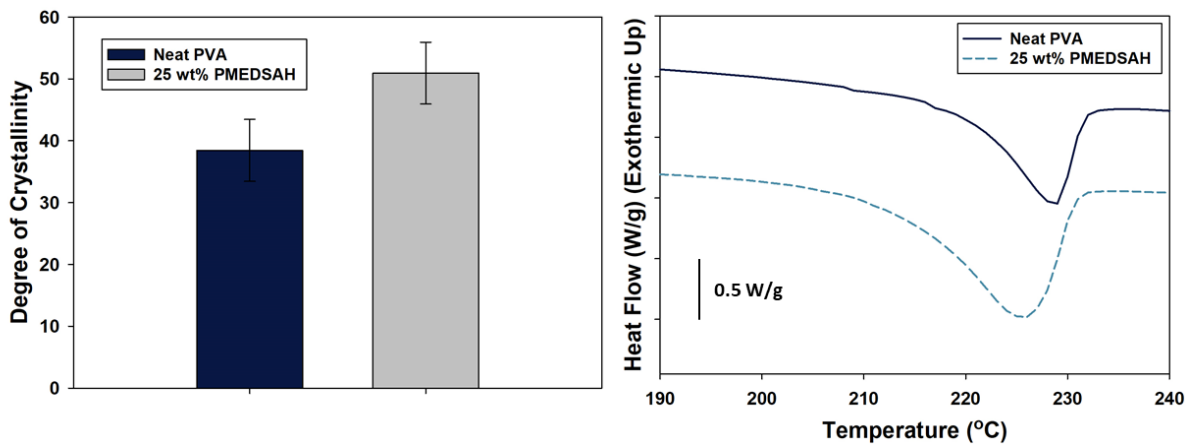


**Figure 3.11** - Hydrogel degree of crystallinity determined through differential scanning calorimetry (left) and representative thermograms (right) for neat PVA compared to a 25 wt% PMEDSAH blend

**Table 3.4** - Hydrogel degree of crystallinity determined enthalpy of melting

Sample	Degree of Crystallinity
Neat PVA	$38.5 \pm 5.0$
25 wt% PMEDSAH	$50.9 \pm 5.0$

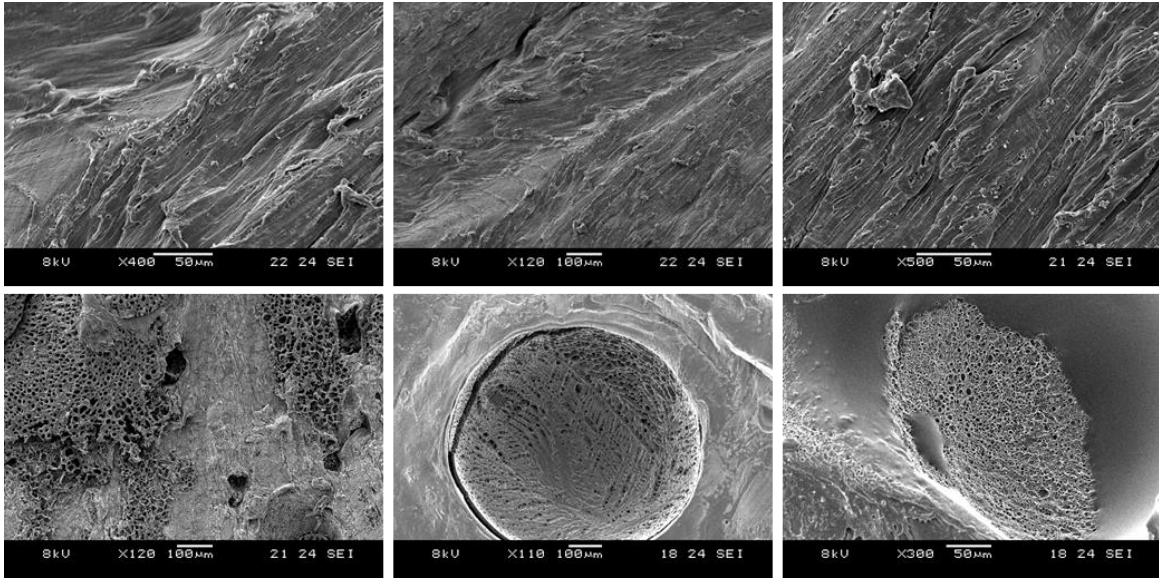


**Figure 3.12** - SEM micrographs of the surface microstructure of neat PVA-H (top) and PVA-PMEDSAH hydrogel blends (bottom)

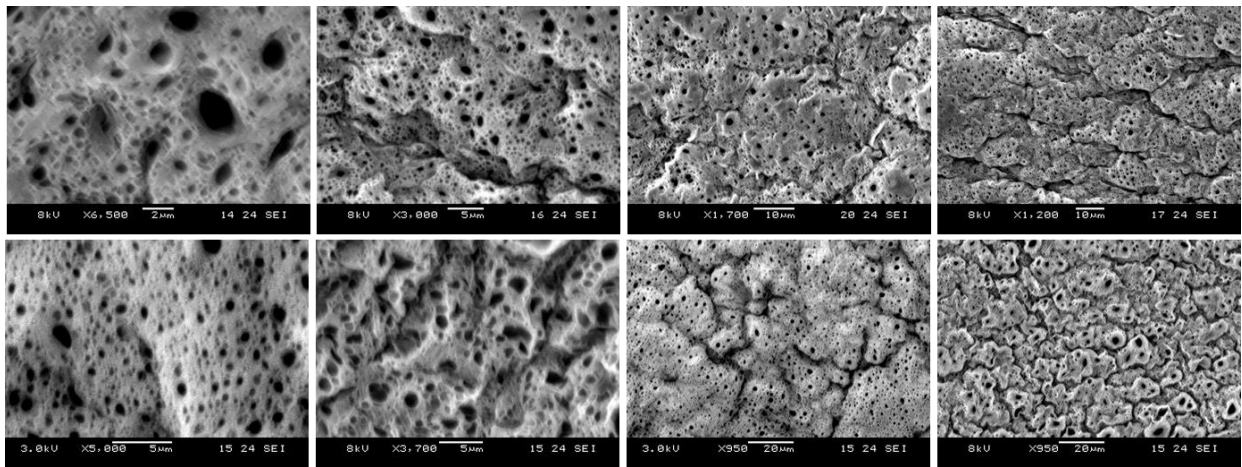


**Figure 3.13** - SEM micrographs illustrating the porosity of neat PVA (top) and 25 wt% PMEDSAH blends (bottom)

### 3.4.5 Tribo-Rheometry

Hydrogels were tested against glass in DI water at angular velocities ranging from 0.1 – 5 rad/s to characterize the effect of PMEDSAH molecular weight on hydrogel COF vs sliding speed. Neat PVA displayed a trending increase in average COF from 0.04 to 0.14 when angular velocity is increased from 0.1 – 1 rad/s. This is followed by a trending decrease in COF as angular velocity

is increased from 1 rad/s to 5 rad/s (Figure 3.14). The blends display very different behavior with a trending increase in COF as angular velocity increases. While there is no statistically significant difference between COF vs time for 50 and 180 kDa PMEDSAH the blend containing 825 kDa PMEDSAH displayed a statistically significant increase in COF compared to the lower molecular weight blends. All blends displayed a statistically significant decrease in COF compared to neat PVA at 1 rad/s.

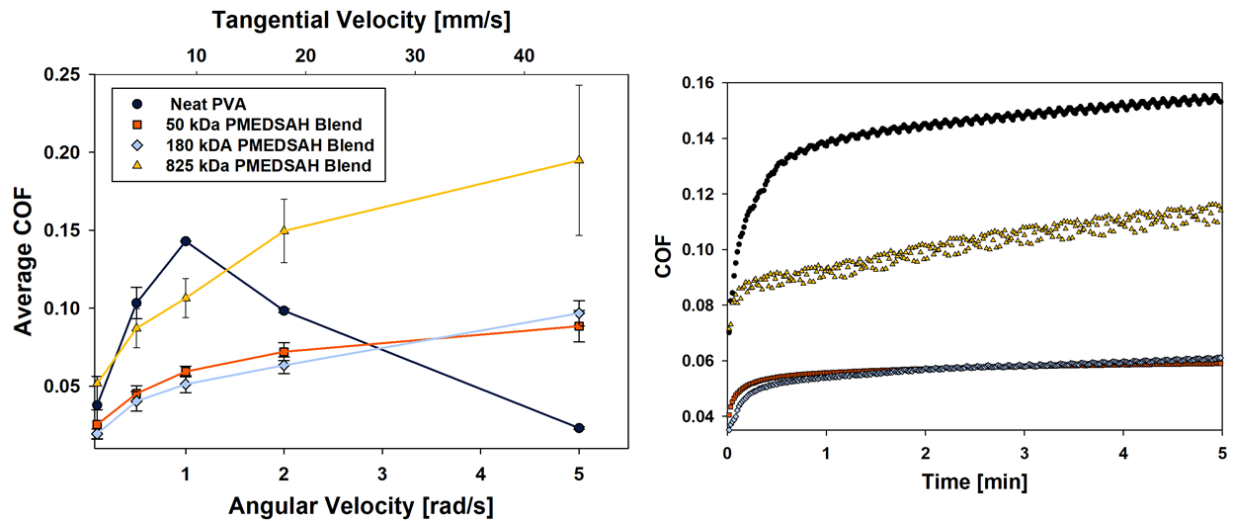


**Figure 3.14** - Frictional behavior of neat PVA hydrogels and PVA PMEDSAH blends against glass with PMEDSAH molecular weight ranging from 50 – 825 kDa (left). Representative COF vs time curves for hydrogels articulating against glass at 1 rad/s (right)

### 3.5. Discussion

Previously we have shown that PMEDSAH is an effective boundary lubricant which can be used to reduce hydrogel COF through the fabrication of PVA PMEDSAH zwitterionic hydrogel blends. Since hydrogels are permeable (consisting of about 80% water [179]) and the zwitterionic boundary lubricant is soluble in water, we postulated that the boundary lubricant may be susceptible to diffusion within the hydrogel matrix. Results from passive diffusion experiments

revealed a trending increase in diffusion coefficient,  $K$ , with increasing PMEDSAH molecular weight and a trending decrease in  $n$ .

While the empirical power law model used for this investigation is not suitable for predicting complex diffusive phenomena it does provide a quantitative analog to diffusion coefficient and the exponent  $n$  defines the release mechanism. When  $n = 0.5$  the model is equivalent to the approximation of the exact solution to Fick's second law for thin films [183]. Sensitivity analysis was performed to access how  $K$  and  $n$  influenced the release curve (Figure 3.15). Each term has a unique effect with  $K$  acting as a proportionality constant increasing the magnitude of the rate of release without influencing the general shape of the curve. On the other hand,  $n$  significantly influences the shape of the release curve with  $n > 0.5$  the curve resembles a burst release where  $n < 0.5$  approaches a linear increase in release with time.

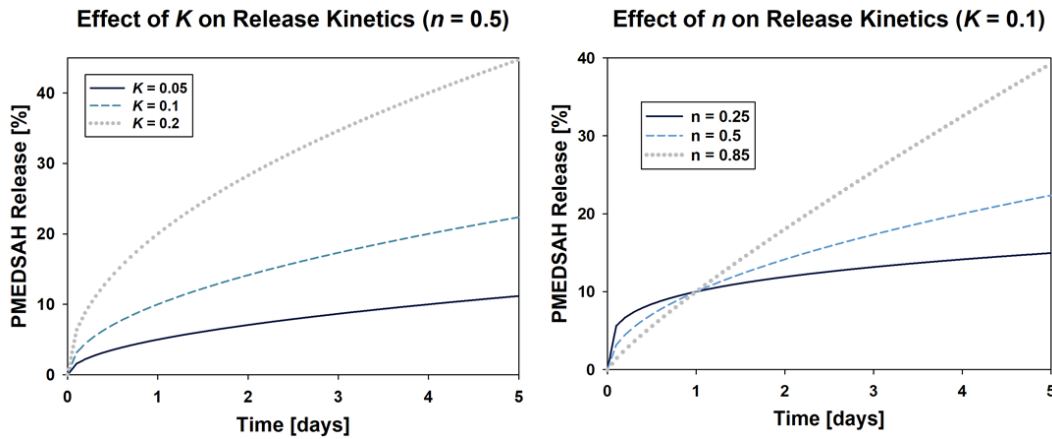


Figure 3.15 - Sensitivity of power law diffusion model

The release kinetics of 825 kDa PMEDSAH resembles a burst release of boundary lubricant. Increasing polymer molecular weight is understood to result in an increase in hydrodynamic radius therefore we postulate the higher molecular weight boundary lubricant is more susceptible to rejection from the hydrogel matrix during the freeze thaw process. PMEDSAH elution results indicate that the boundary lubricant is susceptible to elution when its molecular

weight is less than 180 kDa. We postulate that due to the large hydrodynamic radius of 825 kDa PMEDSAH, there is a higher concentration of polymer toward the outside of the matrix causing the initial significant increase in PMEDSAH release compared to the lower molecular weight blends. Following the initial burst release, PMEDSAH release appears to reach a steady value faster than the lower molecular weight blends. Boundary lubricant mobility is desirable for a tribologically enhanced hydrogel with pressure driven flow carrying solubilized boundary lubricant from the bulk material towards the surface. A number of theoretical and experimental investigations involving the mechanics of biphasic materials such as articular cartilage supports the feasibility of this lubrication mechanism [20,190].

Indentation testing revealed a trending increase in hydrogel contact modulus with increasing PMEDSAH content. The 25 wt% blends displayed a statistically significant increase in contact modulus compared to neat PVA at all molecular weights. There was no apparent trend in the effect of PMEDSAH molecular weight on hydrogel contact modulus. Application of the HBT contact model is ideal for characterizing biphasic materials because it allows for prediction of fluid load support behavior which is critical to tribological performance. Results reveal that blending PVA with PMEDSAH results in an order of magnitude decrease in permeability and as much as an 80% increase in tensile modulus. HBT reveals that a decrease in permeability and an increase in tensile modulus are ideal for improving fluid load support. Hertzian biphasic theory provides a constitutive relation which predicts fluid load support behavior following the determination of measurable material properties. Application of this theory revealed that the boundary lubricant enhances the hydrogels ability to provide interstitial fluid load support by as much as 69%. This behavior may be due to structural remodeling of the hydrogel matrix due to the presence of the zwitterionic polymer or electrostatic interaction between PMEDSAH and water molecules. The

later mechanism is understood to describe the role of proteoglycans and other polar molecules found in articular cartilage. Characterization of the sensitivity of this contact model reveals that each term has an independent effect on the model prediction (Figure 3.16). An increase in permeability and/or tensile modulus result in an increase in contact modulus strain rate dependence.

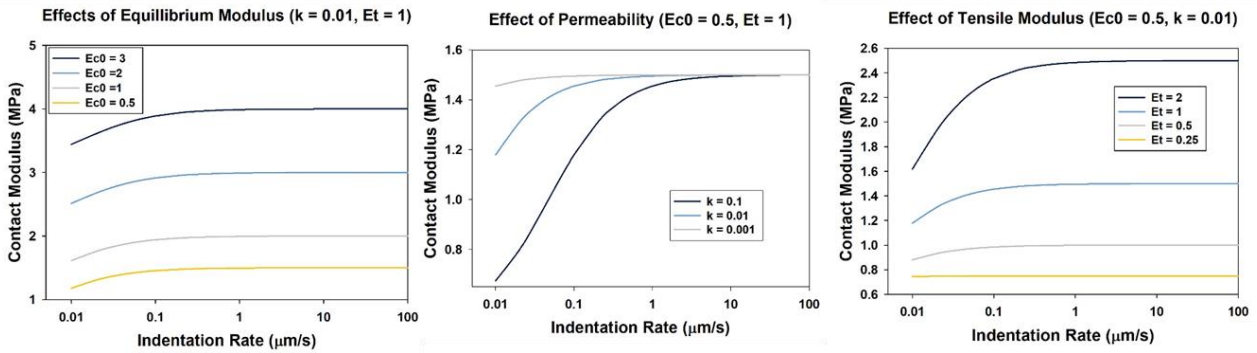


**Figure 3.16** - Sensitivity of HBT contact model developed by Moore and Burris [185]

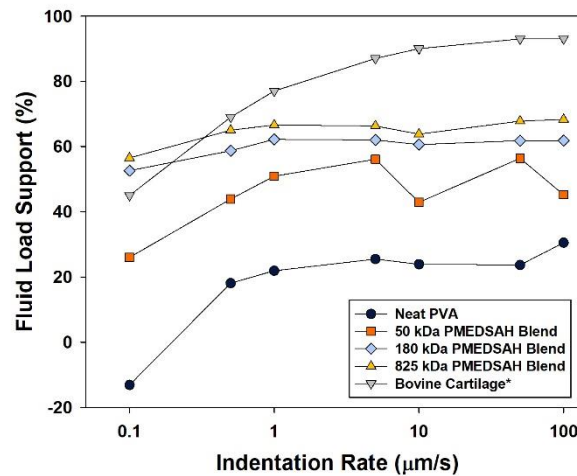


**Figure 3.17** – Effect of boundary lubricant molecular weight on interstitial fluid load support compared to bovine cartilage result obtained by Moore and Burris via application of Hertzian biphasic theory [185].

SEM was performed to investigate whether blending PVA with PMEDSAH resulted in distinct changes in hydrogel porosity. Results revealed no apparent changes in porosity. Another possible explanation for the trending increase in contact modulus with and increase PMEDSAH

content is the formation of ionic crosslinks between PMEDSAH molecules. SAXS was performed to investigate this hypothesis but result did not reveal any apparent changes in hydrogel diffraction patterns. DSC revealed a statistically significant increase in hydrogel crystallinity in 25 wt% PMEDSAH blends compared to the neat material. Like the theta-gel method developed by Ruberti and Braithwaite, we postulate that water has a higher affinity for PMEDAH than PVA resulting in the formation of stiffer, more crystalline hydrogels. Since water has a higher affinity for PMEDSAH than PVA PVA molecules are understood to be more susceptible to hydrogel bonding and crystalline formation during solvent casting can freeze thaw processing [191,192].

Unlike many solid materials, hydrogel COF is not a constant. Instead it depends on several factors including contact pressure, interfacial interactions, bulk lubricant properties, and sliding speed. As initially reported by JP Gong and her colleagues, hydrogel friction behavior can be described as repulsive or attractive [174]. Under repulsive conditions COF vs sliding speed behavior resembles the relationship between shear stress and shear rate in Couette flow. This behavior occurs when the interaction between the hydrogel and the solid substrate is weaker than that of the solvent and the COF behavior is dictated by the viscosity of the solvent. On the other hand, COF behavior of surfaces with an attractive interaction display a trending increasing in COF with sliding velocity followed by a steady decrease following a critical velocity. This steady decrease in COF with increasing velocity is followed by a transition into hydrodynamic lubrication.

PVA is understood to have an attractive interaction with glass [193]. Given the hydration lubrication paradigm developed by Klein and his colleagues, we postulated that blending PVA with PMEDSAH would hinder the attractive interaction between PVA and the glass [4]. The friction test results we observed support this hypothesis. PVA displays COF vs sliding speed

resembling what has been reported in the literature while the zwitterionic blends display COF vs time behavior which resembles what one would expect for a material with a repulsive interaction. We also observed the COF of 825 kDa PMEDSAH is significantly higher than the lower molecular weight blends. Since increasing PMEDSAH molecular weight increases hydrodynamic radius we postulate that the increase in COF for the highest molecular weight blend is attributed to an increase in the viscosity of the aqueous lubricating layer between the hydrogel and the glass surface. All hydrogels display COF vs time behavior resembling what has been reported for articular cartilage tested under stationary contact [20]. Under such conditions a steady increase in coefficient of friction is observed as fluid load support subsides.

### **3.6 Conclusion**

This investigation sought to investigate the effects of PMEDSAH's molecular weight on the mechanics, tribology and diffusive properties of zwitterionic hydrogel blends. Results revealed that the PMEDSAH is mobile within the hydrogel matrix however this mobility is heavily influenced by the molecular weight of the boundary lubricant. This property is ideal for long term low friction applications as a reservoir of lubricant is contained within the matrix which can be eluted to the surface through pressure driven interstitial fluid flow. The presence of PMEDSAH was also found to enhance the hydrogel's ability to provide biomimetic interstitial fluid load support. This result is attributed to electrostatic interaction between the boundary lubricant and DI water rather than macroscale remodeling. We postulate that the unique properties of the novel biomimetic hydrogel fabrication approach described in this manuscript are suitable for a wide range of medical applications including articular cartilage repair, guide wire coatings, and soft contact lenses.



## CHAPTER 4: SYNTHESIS AND CHARACTERIZATION OF ZWITTERIONIC POLYMER BRUSH FUNCTIONALIZED HYDROGELS WITH IONIC RESPONSIVE COEFFICIENT OF FRICTION

### 4.1 Introduction

Fundamental studies on the behavior of surfaces bearing grafted polymers, often referred to as polymer brushes, has been a subject of interest in the scientific community since the early 1980's. [194-196] The polymer chains which form these structures are tethered on one end to a surface through a chemical bond while the other end is free. These nanometer scale features promote a relatively fluid interface between articulating surfaces, making them an effective boundary lubricant. [197,198] More recently, rigid surfaces bearing zwitterionic polymer brushes have been shown to promote even lower coefficients of friction due to hydration lubrication coupled with the inherent friction reducing properties of the polymer brushes. [58,199] Hydrophilic polymer brushes have also been shown to reduce hydrodynamic drag in microfluidic devices by promoting slip. [200] This behavior may explain the nature of blood flow through capillaries. [201]

Based on the findings that have been detailed in chapters 2 and 3 along with previously reported investigations on the behavior of zwitterionic polymer brushes, it was postulated that the tribological performance and biomimetic nature of hydrogels could be improved through the functionalization of zwitterionic polymer brushes. Although many studies have investigated the physical, biochemical, and tribological properties of surfaces bearing zwitterionic polymer brushes. To the best of our knowledge none have reported the synthesis or synergistic effects of grafting zwitterionic polymer brushes on a biphasic material capable of supporting fluid load

support on the order of articular cartilage. Instead, these studies have been limited to rigid substrates such as gold, silicon, and mica. [39,202,203]

This chapter details the synthesis and characterization of two unique types of polymer brush functionalized hydrogels. The zwitterionic polymers of choice included poly[2-(methacryloyloxy) ethyl dimethyl-(3-sulfopropyl) ammonium hydroxide] (PMEDSAH) and poly(2-methacryloyloxyethyl phosphorylcholine) (PMPC). In addition, the surface properties of these novel hydrogels were characterized via infrared (IR) spectroscopy, contact angle goniometry and scanning electron microscopy (SEM). The impact of brush functionalization on the mechanics and tribological properties will also be reported within the context of Hertzian contact theory and friction experiments. Finally, cytotoxicity towards L929 fibroblast cells was investigated to assess the feasibility of this processing method for materials intended for tissue engineering applications.

## **4.2 Hydrogel Fabrication Method**

### *4.2.1 Materials*

Polyvinyl alcohol (PVA, 99% hydrolyzed) with a reported average molecular weight of 130,000 g/mol,  $\alpha$ -bromoisobutyryl bromide (BB), N-methyl-2-pyrrolidone (NMP), [2-(methacryloyloxy) ethyl] dimethyl-(3-sulfopropyl) ammonium hydroxide) (MEDSAH), 2-methacryloyloxyethyl phosphorylcholine (MPC), 2,2,2-trifluoroethanol, copper(I) chloride, and 2,2'-bipyridyl were purchased from Sigma-Aldrich (St. Louis, MO). All chemicals were used as received.

#### 4.2.2 PVA-H Fabrication

Neat PVA-H was prepared following a prior report with modifications [151]. Solutions were first prepared by solvent casting a 40 wt% (m/v) mixture of PVA and deionized (DI) water. The mixture was heated at 90 °C in an isothermal oven (Fisher Scientific, Waltham, MA) for 6 h resulting in a viscous, transparent solution. Stirring was not done during solvent casting due to the high viscosity of the solution and propensity to bubble formation. Following solvent casting, samples were subjected to four freeze-thaw cycles where samples were frozen at -80 °C for 30 min and then allowed to thaw at room temperature for 30 min. This cyclic freeze-thaw process is understood to reinforce the hydrogel structure through formation of crystalline regions, the concentration of these crystalline regions increasing with each successive freeze-thaw cycle. Following the freeze thaw process, samples were immersed in DI water for at least 48 h to ensure they reached equilibrium swelling.

#### 4.2.3 Zwitterionic Polymer Brush Functionalization

Fully hydrated PVA-H were immersed in ethanol for 48 h followed by 24 h in a vacuum oven at room temperature at -100 kPa (Isotemp Vacuum Oven, Fisher Scientific). ATRP initiator functionalization was achieved by immersing dehydrated PVA-H in NMP containing 0.4 M bromoisobutryl bromide at 50 °C for 1 h resulting in BB-PVA-H (Figure 1a). Polymerization of MEDSAH and MPC was achieved under identical reaction conditions. The effects of synthesis parameters on brush functionalization and coefficient of friction were characterized by varying catalyst content between 0.01 – 0.04 M and monomer content between 0.09 – 0.35 M. In all cases 5 mL test glass vessels containing dehydrated BB-PVA-H with catalyst CuCl and ligand 2,2'-bipyridyl, and monomer MPC or MEDSAH were degassed under nitrogen prior to the addition of



### 4.3.2 Coefficient of Friction

Coefficient of friction,  $\mu$ , was measured against glass and stainless steel with an AR-G2 rheometer (TA Instruments Inc., New Castle, DE). To measure coefficient of friction against glass, three 12 mm disc shaped hydrogels were press fit into an adapted tribo-rheometry accessory and articulated against a glass petri dish (Figure 4.3a). Samples were subjected to an average contact pressure of 0.1 MPa and translated at an average velocity of 3.5 mm/s. Given measurement of applied torque,  $T$ , and normal force  $F_N$ , the average  $\mu$  was calculated by equation 4.1. Friction tests were performed in 18 °C DI water and 0.2 M aqueous NaCl.

$$COF = \frac{T}{F_N \cdot R} \quad (4.1)$$

To measure coefficient of friction against steel, hydrogels were confined in a bath containing 18 °C DI water and 0.2 M aqueous NaCl. Samples were subjected to an average contact pressure of 0.4 MPa with a 20-mm diameter stainless steel parallel plate (TA Instruments Inc., New Castle, DE) at an angular velocity of 1 rad/s. Under these test conditions, the applied torque overcomes coefficient of friction over velocity ranging from 0 –  $\omega R$  (where  $R$  is the radius of the hydrogel). Investigations from Gong and her colleagues have revealed that hydrogel coefficient of friction is linearly proportional to the total contact area,  $A$ , and velocity [193,204]. Given this assumption, friction force per unit area,  $f$ , at radial position,  $r$ , and angular velocity,  $\omega$ , can be expressed as:

$$f = A\omega r \quad (4.2)$$

Given friction force per unit area, the total friction force can be expressed as:

$$F = \int_0^R 2\pi r f dr = \frac{2}{3}\pi A\omega R^3 \quad (4.3)$$

Similarly, the total torque can be expressed as:

$$T = \int_0^R 2\pi r f r dr = \frac{\pi}{2} A \omega R^4 \quad (4.4)$$

Solving equation 4.3 for  $A\omega$  as a function of  $F$  and  $R$  and substituting that equation into 4.4, an approximation for the total friction force as a function of applied torque and the radius of the hydrogel can be expressed as:

$$F = \frac{4T}{3R} \quad (4.5)$$

Noting that coefficient of friction is defined as the ratio to total friction force to normal force, the coefficient of friction is expressed as:

$$COF = \frac{4T}{3F_N R} \quad (4.6)$$

This is a commonly used approach for using normal force and torque measurements obtained from a rheometer to calculate COF [205-207]

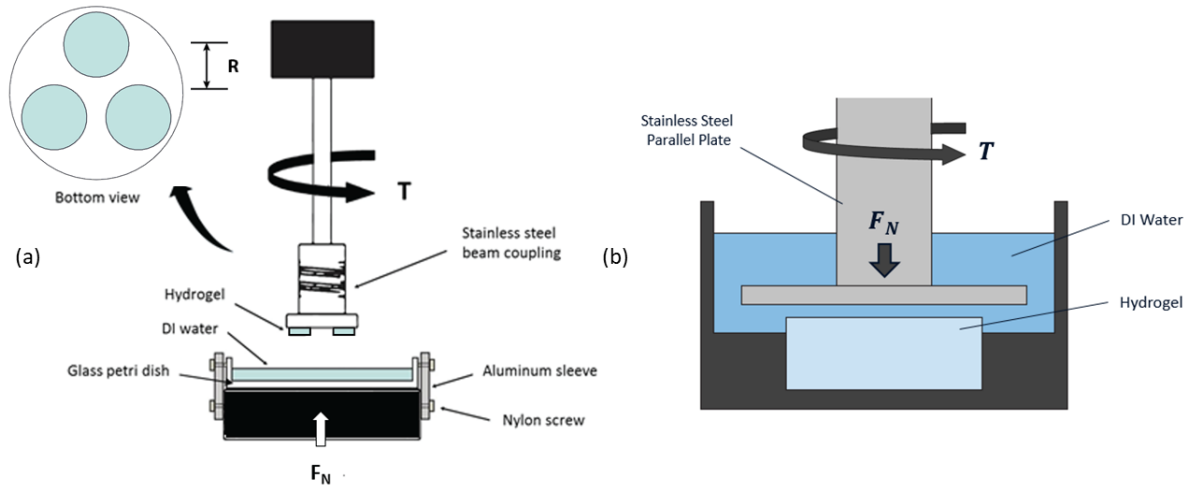


**Figure 4.2** - Schematic illustration of the test conditions for measuring hydrogel coefficient of friction against (a) glass and (b) stainless steel

### 4.3.3 Water Contact Angle

Hydrophilicity was characterized with a ramé–hart advanced goniometer (ramé–hart instruments co., Succasunna, NJ). Water contact angle was measured via the sessile drop method

where a high-resolution image of an ultrapure water droplet (EMD Millipore, Billerica, MA) was analyzed via the ramé-hart's DROPimage Advanced™ software version 2.4.07.

#### 4.3.4 Surface Roughness ( $R_q$ )

Surface topography was measured with a P-17 stylus profiler (KLA-Tencor Corp., Milpitas, CA). The surface profile obtained through this approach was used to compute the RMS roughness using equation 4.3.

$$R_q = \sqrt{\frac{1}{n} \cdot \sum_{i=1}^n (z_i - \bar{z})^2} \quad (4.3)$$

Where  $z_i$  is the individual height measurements over the length of the sample space,  $n$  represents the number of height measurements taken, and  $\bar{z}$  is the mean value of the individual height measurements. [1]

#### 4.3.5 Surface Microstructure

A JEOL JSM-5600 Scanning Electron Microscope (SEM) was used to study the microstructural morphology and degree of polymer brush functionalization. Samples were frozen for at least 12 h in a -80 °C freezer and then lyophilized with a Labconco Benchtop Freeze Dryer (Labconco Corp, Kansas City, MO). Following lyophilization, all samples were sputter coated with gold for 45 s prior to imaging with SEM. Both surface and cross section were imaged with an acceleration voltage of 8 kV.

#### 4.3.6 Mechanical Characterization

Mechanical characterization was performed within the context of Hertz contact theory with an AR-G2 rheometer (TA Instruments Inc., New Castle, DE). Hydrogels were confined in a bath containing 18 °C DI water and were indented with a 6.35 mm diameter indenter at 10 μm/s (Figure

4.3). A nonlinear least squares optimization function was used to fit the contact model to the experimental data using equation 4.4.

$$F_N = \frac{4}{3} E_c R^{0.5} \delta^{1.5} \quad (4.4)$$

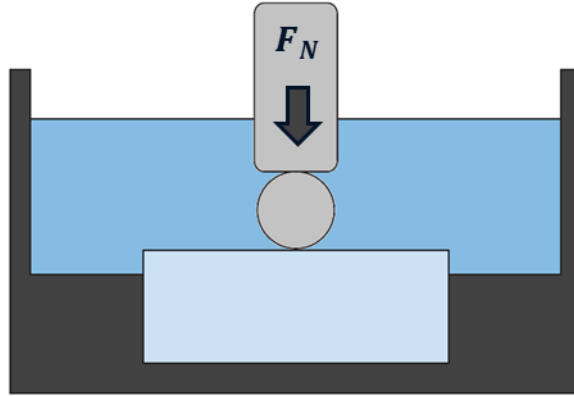


**Figure 4.3** - Schematic illustration of the test conditions for contact modulus,  $E_c$  and (b) a representative experiment curve fit

#### 4.3.7 Bulk Physical Characterization

Brush functionalization required fabrication of a neat PVA hydrogel followed by dehydration, brush functionalization, and rehydration. The effects of this processing method on the bulk microstructure was characterized via differential scanning calorimetry (Q200 TA Instruments, New Castle, DE). Specimens obtained from the center of the PVA hydrogel were hermetically sealed inside stainless-steel pans and heated at 10 °C/min under flowing nitrogen atmosphere from 40 to 250 °C. Hydrogel degree of crystallinity was calculated via the ratio of the heat of fusion,  $\Delta H$ , of the hydrogel (normalized for the solid mass) and the reported enthalpy of melting for 100% crystalline PVA  $\Delta H_c$ . [187-189]



WAXS experiments were conducted to investigate the effects of the dehydration rehydration process on the crystalline microstructure of the neat material. For this purpose, a Rigaku S-MAX3000 pinhole camera system was utilized, with a Micromax-007HF rotating anode source operating with Cu K $\alpha$  emission ( $\lambda = 1.5406$ ), voltage of 40 kV and current of 20 mA. Wide-angle scattering patterns were collected at a sample-detector distance of 117 mm, as calibrated using corundum (NIST SRM 676a) with Fujifilm image plates (CR HR-V) and a Raxia-Di Image Plate reader at a scan resolution of 100  $\mu\text{m}$ . Samples were prepared for WAXS by slicing the 12 mm diameter disks into  $\sim 1$  mm thick films followed by containment within a capsule prepared from Kapton<sup>®</sup> tape. 1D WAXS patterns were plotted as intensity versus the detector angle ( $2\theta$ ).

Hydrogel equilibrium water content (EWC) was determined via a previously described method. [179] To summarize, EWC was computed by calculating the percent difference between the masses of the fully hydrated and dehydrated materials.

#### 4.3.8 Cell Viability

Cytotoxicity towards L929 mouse fibroblasts (American Type Culture Collection, Manassas, VA) was characterized in accordance with ISO 10993-5 and ISO 10993-12 via a previously described method. [179] Briefly, hydrogels prepared as described earlier were cut into pieces approximately 1-2 mm<sup>3</sup> and sterilized by exposure to ultraviolet light (UV) for 2 h. For extraction, sterile samples were placed in vials with an appropriate amount of media based on the dry mass, sealed and placed on a shaker at 37 °C, 60 rpm for 48 h.

Cells were grown in DMEM-F12 (Invitrogen, Carlsbad, CA) supplemented with 10% Fetal Bovine Serum (Atlanta Biologicals, Norcross, GA) and 11% glutamine-penicillin-streptomycin (Invitrogen, Carlsbad, CA) using standard cell culture procedures. L929 mouse fibroblasts were seeded at 25,000 cells/cm<sup>2</sup> in a 96-well plate. The cells were allowed to attach and spread on the

plate for 24h at which point media was removed and replaced with extracts or controls as prepared above. As a negative control, 0.1% sodium dodecyl sulphate (SDS) [157], was made in control media. Following a 24 h incubation, extracts and control media were removed, and replaced with 1/10 volume of CCK-8 solution (Cell Counting Kit-8, Dojindo Molecular Technologies, Inc., Rockville, MD) which is metabolized by viable cells, turning the media an orange color. This solution was incubated with the cells for 4 h, followed by absorbance reading on a plate reader at 450 nm.

#### *4.3.9 Statistical Analysis*

All statistical analyses were conducted with Minitab 17 (Minitab Inc., State College, PA). One way ANOVA with a significance level  $\alpha = 0.05$  was performed for all hypothesis testing.

## **4.4 Results**

### *4.4.1 Surface Composition*

Fourier transform infrared spectroscopy with attenuated total reflectance FTIR-ATR was performed after initiator and brush functionalization to verify that the desired surface chemistry had been achieved. Representative IR spectra are illustrated in Figure 4.4. Successful ATRP initiator surface functionalization was verified based on the distinct peak spanning 1735 – 1750  $\text{cm}^{-1}$  characteristic of carbonyl (C=O) stretching. Following PMEDSAH brush functionalization a distinct peak spanning 1030 – 1060  $\text{cm}^{-1}$  characteristic of the sulfoxide group of the zwitterionic polymer PMEDSAH. Following PMPC brush functionalization distinct peaks at 1100  $\text{cm}^{-1}$  and 970  $\text{cm}^{-1}$  which are characteristic of molecular scale vibrations associated with the P=O and P-O-C containing functional groups of PMPC [156]. A trending decrease in the magnitude of the

absorbance peaks indicative of brush functionalization was observed when catalyst concentration was decreased from 0.01 – 0.04 M.

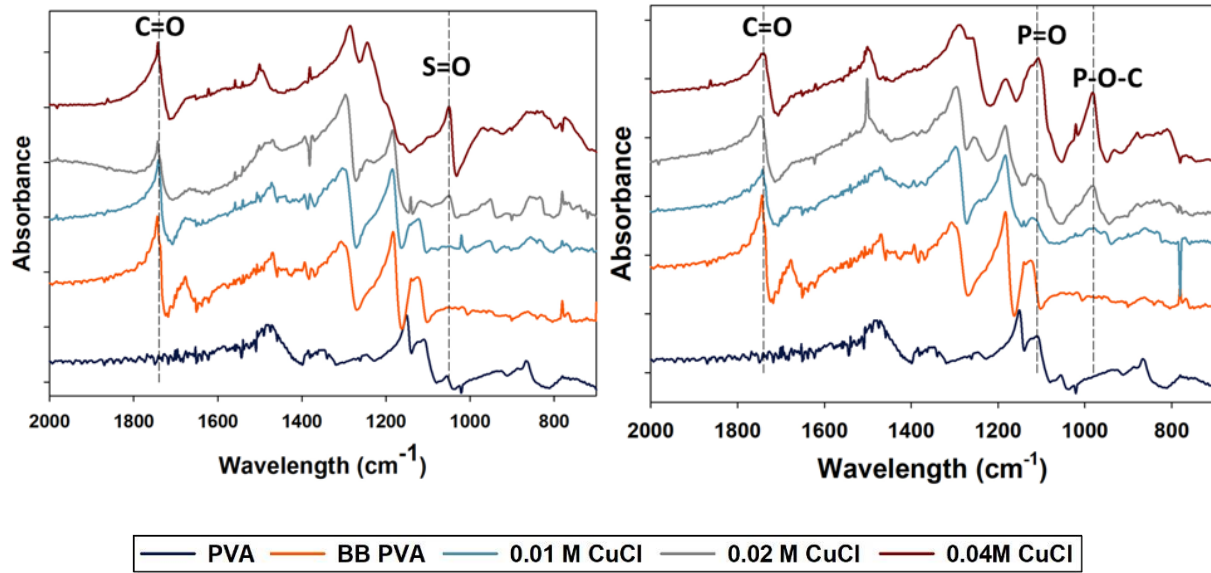


**Figure 4.4** - Representative FTIR-ATR spectra displaying the effects of catalyst content on hydrogel surface chemistry for both the PMEDSAH (left) and PMPC (right) functionalization reactions

#### 4.4.2 Coefficient of Friction

Measurement of hydrogel COF against glass lubricated by DI water and aqueous NaCl revealed that brush functionalization results in significant changes in hydrogel COF (Figure 4.5). Both PMEDSAH-PVA and neat PVA displayed statistically significant, reversible, ionic responsive coefficient of friction behavior. Results reveal as much as a 35% reduction in average COF when articulating surfaces were lubricated by aqueous NaCl rather than DI water. Solvent salinity does not appear to have a significant effect on COF of the initiator functionalized material (BB PVA) or PMPC brush functionalized PVA (PMPC PVA). PMEDSAH-PVA lubricated by DI

water displayed the highest average COF,  $0.35 \pm 0.06$  while PMPC PVA lubricated by DI water displayed the lowest average COF,  $0.07 \pm 0.02$ .

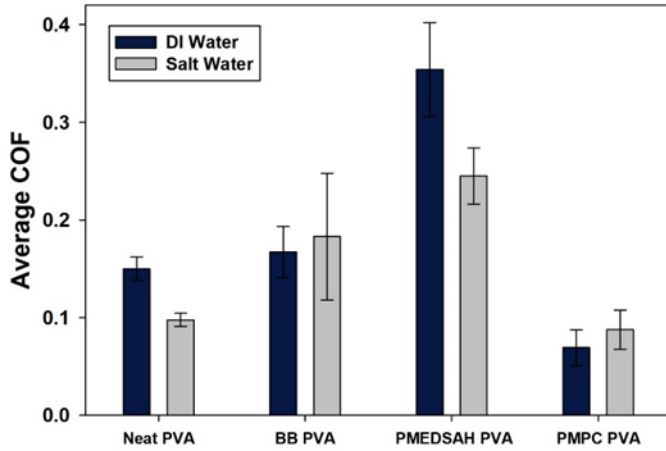


**Table 4.1** - Hydrogel COF against glass

Sample	DI Water	Salt Water
Neat PVA	$0.15 \pm 0.01$	$0.10 \pm 0.007$
BB PVA	$0.17 \pm 0.03$	$0.18 \pm 0.06$
PMEDSAH PVA	$0.35 \pm 0.05$	$0.24 \pm 0.03$
PMPC PVA	$0.07 \pm 0.02$	$0.08 \pm 0.02$

**Figure 4.5** - Coefficient of friction (COF) behavior of neat PVA compared to initiator and zwitterionic polymer brush functionalized hydrogels tested against glass in both DI water and 0.2 M aqueous sodium chloride

Measurement of hydrogel COF against stainless lubricated by DI water and aqueous NaCl revealed that brush functionalization results in a significant change in hydrogel COF, but ionic responsive COF was not observed (Figure 4.6). Neat PVA lubricated by DI water displayed the highest COF,  $0.36 \pm 0.09$  and both PMPC and PMEDSAH brush functionalized hydrogels displayed a statistically significant reduction in average coefficient of friction compared to the neat material. PMPC PVA lubricated by DI water displayed the lowest average COF,  $0.08 \pm 0.05$ .

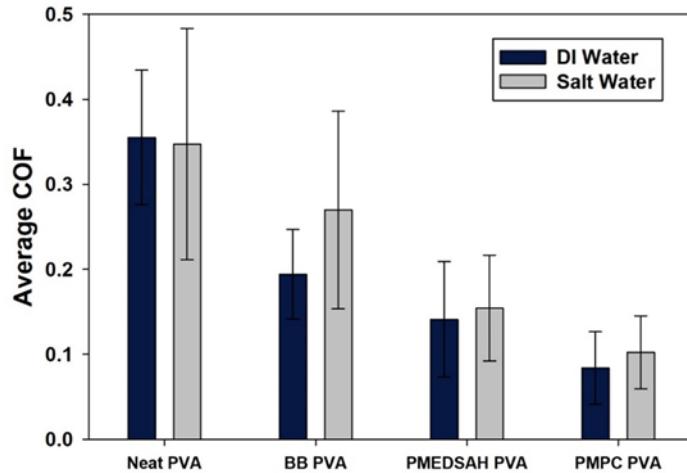


**Table 4.2** - Hydrogel COF against stainless steel

Sample	DI Water	Salt Water
Neat PVA	0.36 ± 0.08	0.35 ± 0.14
BB PVA	0.19 ± 0.05	0.26 ± 0.12
PMEDSAH PVA	0.14 ± 0.07	0.15 ± 0.06
PMPC PVA	0.08 ± 0.04	0.1 ± 0.04

**Figure 4.6** - Coefficient of friction (COF) behavior of neat PVA compared to initiator and zwitterionic polymer brush functionalized hydrogels tested against stainless steel in both DI water and 0.2 M aqueous NaCl

#### 4.4.3 Physical Surface Characterization

Water contact angle experiments revealed that initiator functionalization results in a statistically significant increase in water contact angle following initiator functionalization (Figure 4.7). This significant increase in water contact angle is maintained after brush functionalization with both PMEDSAH and PMPC.

Initiator and brush functionalization did not result in a significant increase in hydrogel surface roughness but SEM imaging revealed distinct changes to the surface microstructure at magnification as low as X200 (Figure 4.8).

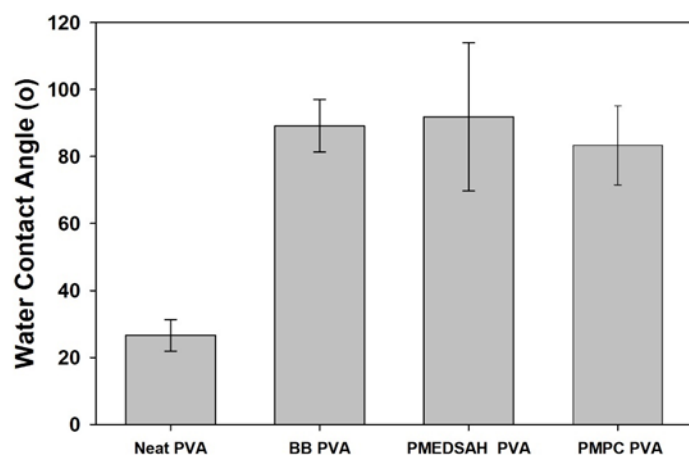


**Table 4.3** - Water contact angle results

Sample	DI Water
Neat PVA	26.7 ± 4.7
BB PVA	89.2 ± 7.8
PMEDSAH PVA	91.8 ± 22.1
PMPC PVA	83.3 ± 11.8

**Figure 4.7** - Water contact angle of neat PVA compared to initiator and zwitterionic polymer brush functionalized hydrogels

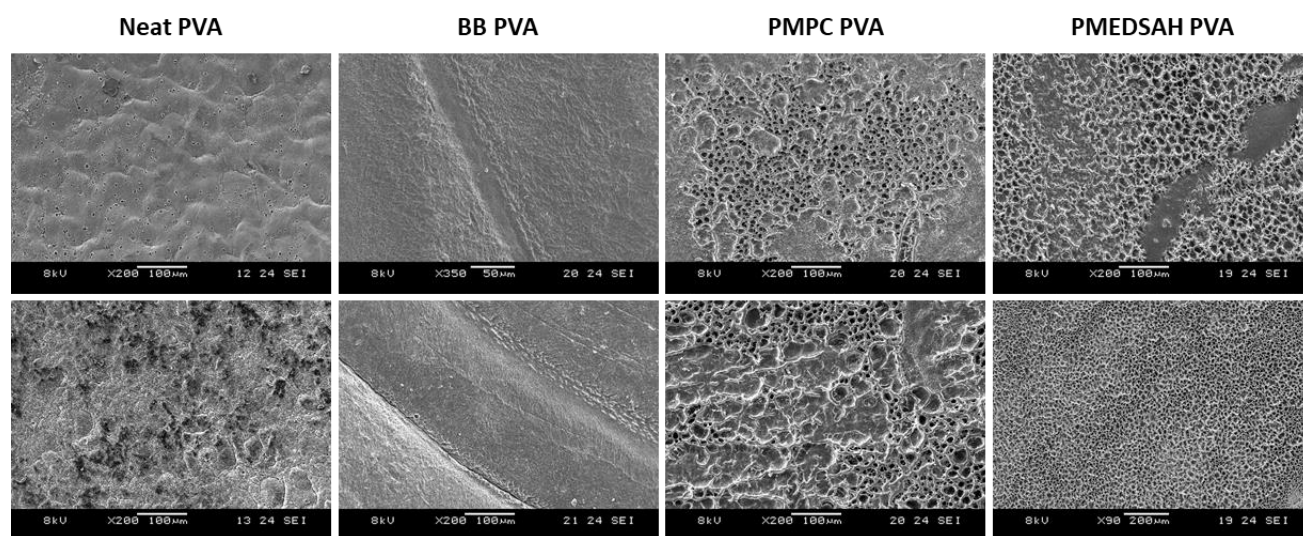


**Figure 4.8** - Representative SEM images of the surface microstructure following initiator and brush functionalization

#### 4.4.4 Mechanical Characterization

Mechanical indentation via indentation experiments revealed that the brush functionalized hydrogels maintained comparable mechanical properties to the neat material (Figure 4.9). The brush functionalized hydrogels display an increase in strain rate dependence on contact modulus, however the degree of strain rate dependence is still significantly lower than what has been reported

for articular cartilage [185]. Both brush functionalizing chemistries result in an increase. The increase in contact modulus of PMPC brush functionalized hydrogels is statistically significant. Brush functionalization required fabrication of a neat PVA hydrogel followed by dehydration, brush functionalization, and rehydration. Indentation results revealed that this processing method resulted in a significant increase in hydrogel contact modulus as shown in Table 4.4.

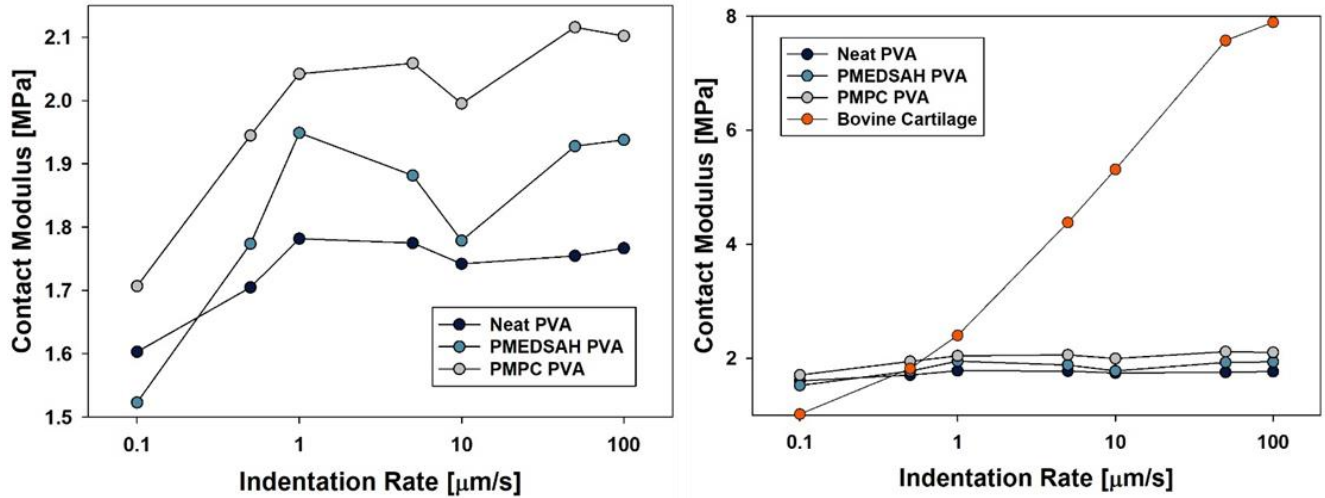


**Figure 4.9** - Average contact modulus of (left) neat PVA-H compared to brush functionalized PVA-H and (right) bovine articular cartilage [30]

#### 4.4.5 Bulk Physical Characterization

Enthalpy of melting measurements performed via differential scanning calorimetry (DSC) revealed that the dehydration-rehydration processing method did not result in a significant change in hydrogel degree of crystallinity (Table 4.4). The processing method did result in a statistically significant decrease in equilibrium water content (EWC). Following the initial solvent casting process, hydrogels were found to have an EWC of  $78.7 \pm 2.0\%$ . After the dehydration and subsequent rehydration, hydrogels were found to have an EWC of  $68.5 \pm 1.7\%$ . A 30% decrease in average volume was also observed following the dehydration rehydration process.

SEM imaging revealed that the dehydration and subsequent rehydration of PVA hydrogels resulted a qualitative increase in porosity homogeneity (Figure 4.10). In addition to being

qualitatively more homogeneous in size compared to the neat material, the pores present in the rehydrated gels were generally significantly more densely packed than the neat material. Results from the WAXS experiments (Figure 4.10) revealed that both neat and rehydrated hydrogels display diffraction rings at  $2\theta = 19.4^\circ$  which corresponding to a d-spacing of 4.59 Å. Low angle peaks characteristic of the Kapton® window was also evident. The magnitude of the diffraction peak characteristic of PVA's monoclinic unit cell was more distinct following rehydration.

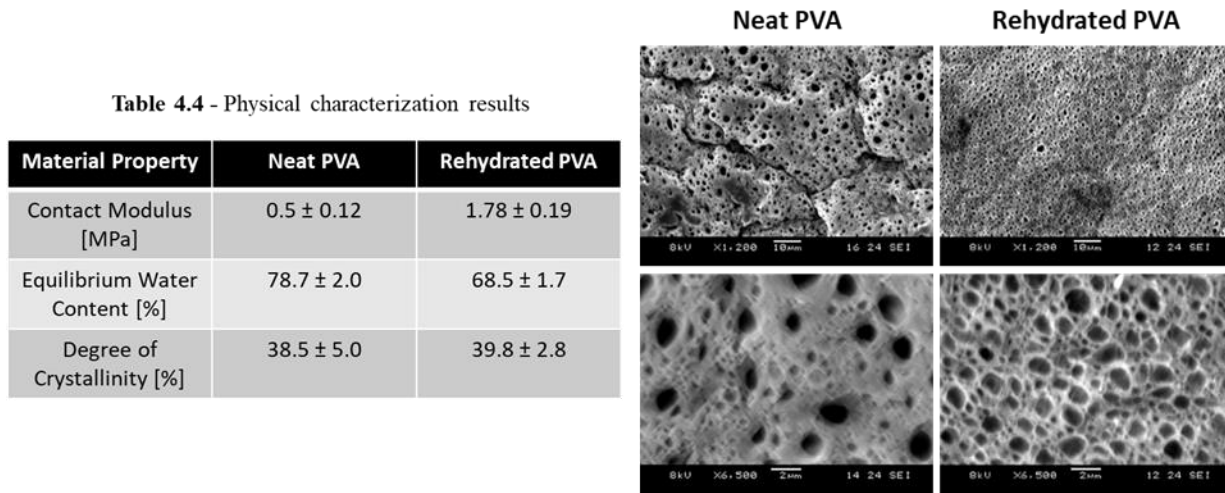


**Figure 4.10** - SEM micrographs illustrating porosity of neat PVA-H compared to rehydrated PVA-H



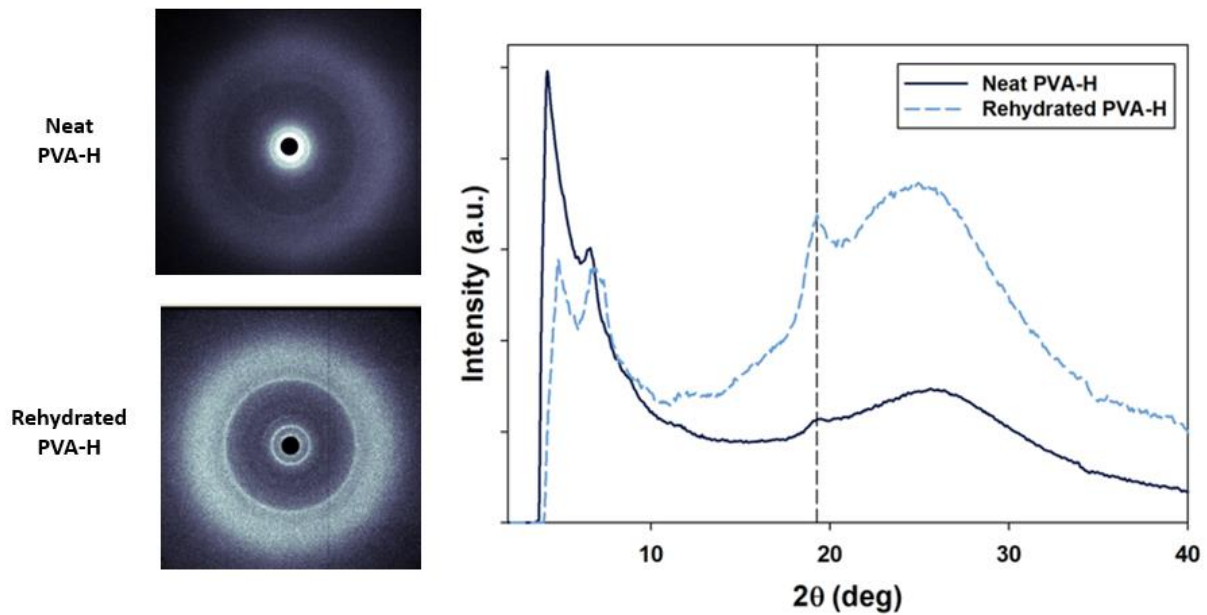


**Figure 4.11** - Representative WAXS patterns for neat and rehydrated PVA-H

#### 4.4.6 Cytotoxicity

Cytocompatibility was determined for the neat PVA, initiator, and brush functionalized hydrogels after reaching an equilibrium swelling volume. L929 cells were incubated with media extracts of each sample and exhibited high metabolic activity. In comparison to cells incubated with DMEM-F12 media, all hydrogels exhibited high cytocompatibility with an average viability above the 70% viability threshold. No statistically significant differences were observed among the group with the one exception being the SDS negative control (Figure 12).

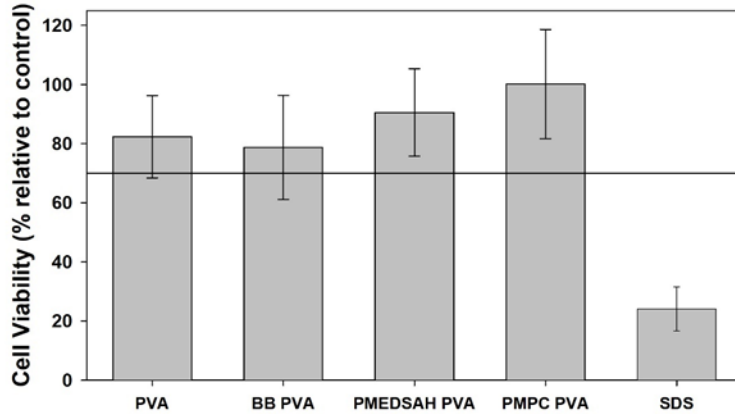


**Table 4.5 - Cytotoxicity test results**

Sample	Viability [%]
Neat PVA	82.3 ± 13.9
BB PVA	78.7 ± 17.6
HC PMEDSAH	90.5 ± 14.8
HC PMPC	100.2 ± 18.4
SDS	24.1 ± 7.4

**Figure 4.12 - Viability of L929 cells in extracts generated from neat and surface modified hydrogels. Extract containing 0.1% SDS was used as a negative control.**

## 4.5 Discussion

Under boundary lubrication conditions, friction and wear behavior is dictated by molecular scale interactions between the opposing articulating surfaces. Effective boundary lubricants reduce COF and surface wear by hindering attractive interactions between articulating surfaces. Neat PVA has a weak attractive interaction with glass under aqueous conditions due to electrostatic interactions between the negatively charged glass substrate and the hydrogel's hydroxyl groups. [193] The significant reduction in neat PVA COF caused by the addition of salt ions is attributed to electrostatic screening hindering association between the glass and the hydroxyl groups. PMEDSAH brush functionalized PVA exhibits similar ionic responsive behavior indicating that the zwitterionic polymer is associating with the glass substrate. The significant increase in COF of PMEDSAH-PVA compared to neat PVA is likely due to larger electrostatic interactions between the positively charged quaternary ammonium group ( $\text{NR}_4^+$ ) of PMEDSAH brushes and the negative glass counter face.

Unlike PMPC, chain conformation of sulfobetaines such as PMEDSAH has been shown to be heavily influenced by the ionic strength of the solvent. [208-210] In low ionic strength aqueous

solutions, these polymers assume a collapsed configuration due to a high degree of inter and intra molecular interactions caused by the presence of opposite charges within a single repeat unit. Immersion in high ionic strength solution results in electrostatic screening of self-association, causing the polymer chains to assume an extended or stretched conformation. Self-association prevents the zwitterionic polymer from attracting water molecule and is undesirable for achieving effective boundary lubrication through hydration lubrication. [211] In contrast, the polymer chain conformation of phosphorylcholine containing zwitterions such as PMPC has been shown to be significantly less sensitive to by the ionic strength of the solvent. [208,210] The high affinity of phosphorylcholine groups for water is understood to be responsible for the unique behavior of PMPC brushes and is expected to keep the polymer from being attracted to the negatively charged glass substrate. Results observed in the friction tests performed against glass support this hypothesis as PMPC-PVA gels did not exhibit ionic responsive COF and displayed significantly lower coefficient of friction against glass. We postulate that hydration of the PMPC molecules likely resulted in net repulsion between the articulating surfaces. The structure of PMPC brushes resemble that of the zwitterionic phosphatidylcholine lipids present which are understood to play a central role in excellent boundary lubrication properties of articular cartilage. [3] This is yet another example of how biomimicry is a valuable design approach.

The lack of ionic responsiveness among samples tested against stainless steel indicates a reduction in the degree of electrostatically driven association between the polymer chains and the solid substrate. Under these test conditions both the PMEDSAH and PMPC brush functionalized hydrogels displayed a statistically significant reduction in COF compared to the neat material. This is an indication that the ionic responsive behavior observed when hydrogels were tested against glass was likely due to PMEDSAH brush association with the negatively charged glass rather than

inter or intra chain association. Without electrostatic attraction between the opposing substrates the zwitterionic polymer can better attract water molecules resulting in a net repulsive interaction and a low shear strength interface due to the formation of hydration shells around the charged regions of the zwitterionic brushes. Overall the results observed in this investigation reveal that PMPC is a more versatile and effective boundary lubricant than PMEDSAH. We hypothesize that this is due to PMPC's higher affinity for water making PMPC brushes less susceptible to association with molecules other than water.

Indentation test results revealed that brush functionalization yielded an increase in viscoelasticity and average contact modulus. Analysis of the compressive behavior of biphasic materials predicted by Hertzian biphasic theory reveals that an increase in viscoelasticity is accompanied by an increase in the degree of fluid pressurization that the material can support. [184,185] This behavior can be caused by an increase in matrix tensile modulus or a decrease in permeability. We hypothesize that the statistically significant increase in contact modulus and viscoelasticity of PMPC-PVA compared to neat PVA is caused by the high affinity of water molecules for the phosphorylcholine groups of the surface bound PMPC resulting in a decrease in surface permeability. This behavior is expected to result in improved tribological performance due to enhancement of interstitial fluid load support.

The dehydration rehydration process resulted in more than a 250% increase in contact modulus. This statistically significant increase in stiffness was accompanied by a 10% decrease in EWC and a 30% decrease in volume. DSC experiments were performed to determine if the change in compressive stiffness and EWC were attributed to a change in the hydrogel's degree of crystallinity. Results revealed that the average degree of crystallinity for rehydrated PVA was 1% higher than neat PVA samples. The magnitude of the diffraction peak characteristic of PVA's

monoclinic unit cell was more distinct following rehydration. This may be an indication of an increase in the size of the crystalline regions. [212,213] Characterization of hydrogel surface microstructure through SEM reveals a significant degree of microstructural remodeling following dehydration and rehydration. We hypothesize that the solvent dehydration process results in the formation of regions with increasing polymer richness and packing density of the polymer chains. This increase in packing density facilitates hydrogel bonding leaving less polymer chains susceptible to attracting water. As a result, we have a lower EWC and an increase in compressive modulus.

While this investigation does provide valuable insight into the mechanics and tribology of this novel tribologically enhanced material, there are some limitations. For use in biomedical applications such as articular cartilage repair, it will be important to characterize the tribological properties of these hydrogels under physiological scale loads and using physiologically relevant lubricating fluids such as phosphate buffered saline (PBS). It would also be interesting to investigate the thickness of the brush layer and identify possible correlations between coefficient of friction and fluid load support and brush thickness. Brush thickness of surface modified hydrogels could be estimated via the use of a chemical mask to yield patterned initiator and brush functionalization followed atomic force microscopy as demonstrated by Wei et al. [211]

#### **4.6 Conclusion**

This investigation sought to investigate the effects of coupling the tribological benefits of interstitial fluid load support with biomimetic boundary lubrication. This was achieved through the fabrication of novel zwitterionic polymer brush functionalized PVA hydrogels. Results indicate that brush functionalization has a significant effect on COF. In addition to resulting in as much as an 78 % reduction in COF, brush functionalization resulted in a decrease in apparent

permeability which is desirable for increasing interstitial fluid load support. The hydrogel processing method was also found to have a significant influence on the mechanical and physical properties of the material both of which are expected to result in significant enhancement to tribological performance. Overall this cytocompatible approach provides a unique investigation of the tribological properties of a novel biomimetic materials. It also provides a versatile method for surface modification of soft biphasic materials contain hydroxyl groups.

## CHAPTER 5: MECHANICS AND TRIBOLOGY OF ELECTROSPUN LOW FRICTION POLYURETHANE FIBERMATS

### 5.1 Introduction

Electrospinning is versatile method for manufacturing non-woven micro-nanofibrous materials. This is achieved by using a high voltage electrostatic field and pressure driven fluid flow to draw small diameter polymer threads from a conductive solution to a grounded or negatively charged collector. With the correct balance between surface tension and applied voltage, continuous fibers can be formed and collected in random or aligned configurations [214]. While the conceptual framework has existed since the 1930's, investigations involving this unique material fabrication method have been increasing in popularity for many reasons [215]. First, it has a wide range of applications ranging from tissue engineering and wound dressings, to fuel cells and filtration devices [216-220]. Also, due to electrospinning's unparalleled operational simplicity, manufacturing can be scaled up relatively easily through the addition of multiple spinnerets. This characteristic also allows sets of insoluble materials to be electrospun simultaneously to achieve homogeneous or functionally graded composites benefitting from the unique properties of each of the materials it is composed of.

Zwitterionic polymers are a class of materials which are net neutral but possess positive and negative charges in close proximity to one another. Because of their unique structure, zwitterionic polymers are hygroscopic due to their electrostatic attraction to water. This strong attraction is understood to explain why zwitterionic polymers are effective boundary lubricants [4]. In addition to being superhydrophilic and providing low friction, zwitterionic molecules also provide strong resistance to bacterial adhesion, protein adsorption, and cell attachment; traits which are often desirable in the design of materials for biomedical applications [218,221]. While zwitterionic polymers do possess some attractive characteristics, they inherently do not have good

mechanical properties and are unstable under aqueous conditions gradually dissolving due to their hydrophilicity even at high molecular weights [180].

Thermoplastic polyurethanes are characterized as synthetic, thermoplastic, elastomeric, linear block copolymers consisting of hard and soft segments. This class of materials are attractive for several areas within academic research and product development since they are susceptible to a wide range of processing methods and their properties can be significantly altered by varying monomer type, block ratio, or molecular weight of the macromolecule [181]. While thermoplastic polyurethanes have suitable mechanical properties for diverse applications including footwear, textiles, inflatables, and casings, their use for medical applications is often limited due to their inability to prevent nonspecific protein adsorption. Protein adsorption is undesirable for medical implants as it is understood to initiate an inflammatory response from the body resulting in platelet adhesion and thrombosis [222].

The investigations described in Chapters 2-3 demonstrated the effectiveness of zwitterionic sulfobetaine, PMEDSAH, in reducing coefficient of friction of poly vinyl alcohol hydrogels through the fabrication of solvent casted polymer blends [179]. Given PMEDSAH's lubricious properties in addition to its low fouling antimicrobial characteristics coupled with the mechanical properties of a thermoplastic polyurethanes, we postulated that the resulting composite material would be suitable for several medical applications including wound dressings, fibrous tissue repair, and stent coatings. This chapter presents a novel and versatile method for the fabrication of low friction elastomeric fibermats. In addition to measuring changes in coefficient of friction we investigated the effects of PMEDSAH content on tensile properties as well as the long-term stability of PMEDSAH within the fibrous matrix under aqueous conditions. Pellethane®, was the



thermoplastic polyurethane of choice for this investigation however these methods could be extended to other TPU's given the appropriate electrospinning solvent.

## 5.2 Fibermat Manufacturing Method

### 5.2.1 Materials

N,N-dimethylformamide (DMF), tetrahydrofuran (THF), 2,2'-azobis(2-methylpropionamide) dihydrochloride (AAPH), 2,2,2-trifluoroethanol (TFE), and [2-(methacryloyloxy) ethyl] dimethyl-(3-sulfopropyl) ammonium hydroxide (MEDSAH), were obtained from Sigma-Aldrich (St. Louis, MO). Pellethane® 5863-80A was obtained from Lubrizol (Wickliffe, OH). All chemicals were used as received.

### 5.2.2 PMEDSAH Synthesis

Synthesis of the zwitterionic polymer PMEDSAH was achieved via free radical polymerization of MEDSAH initiated by AAPH under nitrogen in a DI water solution with a monomer concentration of 0.25 M. Reactions were performed at monomer to initiator molar concentration,  $[M_0]/[I_0]$ , spanning 65 - 400. The reactions were performed at 65 °C for 6 h at which point the polymer was harvested with a Busci Rotovapor® R-210 rotary evaporator (Buchi Analytical Inc, New Castle, DE) at 60 °C for 1 h. The harvested polymer was subsequently ground to a fine powder and dried at -30 in.Hg in an Isotemp Vacuum Oven (Fisher Scientific, Hampton, NH) at room temperature for 24 h. Viscosity average molecular weight was determined via intrinsic viscosity measurements and the previously reported Mark-Houwink parameters for PMEDSAH (at 21 °C in 0.2 M NaCl) [180].

### 5.2.3 Fibermat Fabrication

Pellethane® electrospinning solutions were prepared by dissolving 10 wt% polymer in 60:40 volume ratio tetrahydrofuran-dimethylformamide solution. PMEDSAH electrospinning solutions were prepared by dissolving 10 wt% polymer in trifluoroethanol. Dissolution of both polymers was achieved in screw cap glass vials sealed with Parafilm M (Bemis Company, Neenah, WI) at room temperature assisted by a magnetic stir bar for at least 12 h. Following polymer dissolution, electrospinning solutions were loaded into 20 mL Norm-Ject® plastic syringes attached to a stainless-steel 21G BD PrecisionGlide™ hypodermic needle with a blunt tip (Becton Dickinson, Franklin Lakes, NJ). Syringes were driven with KDS 100 syringe pumps (KD Scientific Inc., Holliston, MA) at volumetric flow rates ranging from 1 – 3 mL/h. Both syringes were positioned horizontally on either side of a rotating, translating grounded mandrel (Figure 1). The distance between both syringe needles and the mandrel was 14 cm. PMEDSAH was electrospun at 17 kV while Pellethane® was electrospun at 12 kV. All fiber mats were fabricated within a custom designed humidity controlled box at 40% relative humidity. Following electrospinning, fiber mats were dried at room temperature in a vacuum oven (Isotemp Vacuum Oven, Fisher Scientific) for at least 24 h to remove any residual solvent.

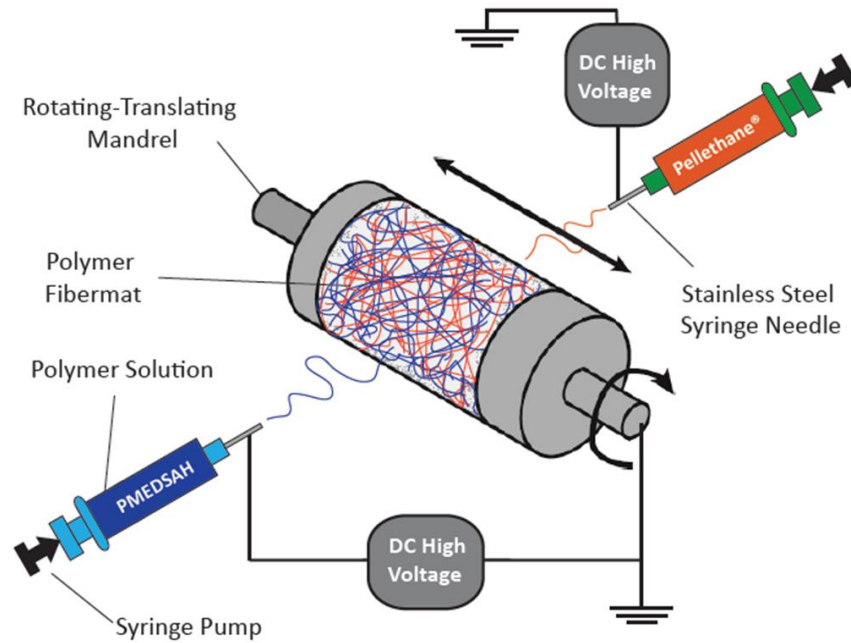


**Figure 5.1** - Schematic illustration of the fiber mat manufacturing method

## 5.3 Characterization Methods

### 5.3.1 Scanning Electron Microscopy

A JEOL JSM-5600 Scanning Electron Microscope (SEM) was used to characterize the fiber morphology of fiber mats with PMEDSAH content ranging from 0 – 100 wt%. Following electrospinning and drying, square samples were cut from their parent fiber mat using a razor blade. Sputter coating with gold via a Desk II Sputter Coater (Denton Vacuum LLC, Moorestown, NJ) was performed for 45 s. All samples were imaged at an acceleration voltage of 8 kV and a working distance ranging from 20 – 30 mm.

### 5.3.2 Tribo-Rheometry

The effects of PMEDSAH content on fiber mat coefficient of friction was characterized with an AR-G2 rheometer (TA Instruments, New Castle, DE). Pairs of 7 x 7 mm fiber mat squares

were firmly affixed to an adapted tribo-rheometry accessory with double sided tape (Figure 5.2). The opposing contacting surface was a glass petri dish containing deionized water. Fiber mats were subjected to an average contact pressure of 0.04 MPa and were rotated at an angular velocity of 1 rad/s. Given the measured normal force,  $F_N$ , torque,  $T$ , and fiber mat offset radius,  $R$ , coefficient of friction was calculated using the following equation:

$$\mu = \frac{T}{F_N \cdot R} \quad (5.1)$$

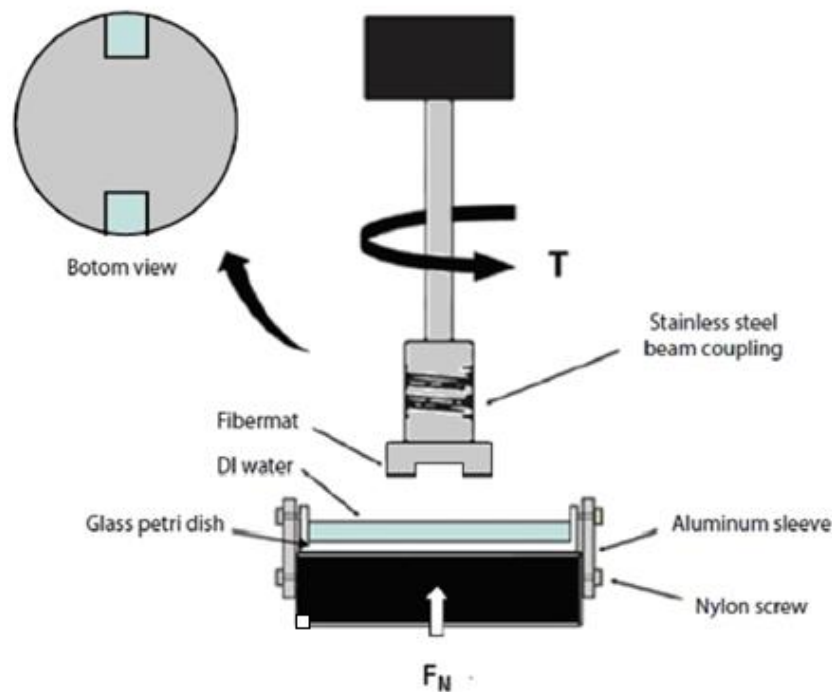


**Figure 5.2** - Schematic illustration of the test configuration used to measure fiber mat coefficient of friction against glass with an AR-G2 rheometer

### 5.3.3 Tensile Testing

Tensile testing was performed on dog-bone shaped fiber mats (ASTM Standard D636-03 Type IV, reduced in size four-fold) to determine the effects of PMEDSAH content on Young's modulus, ultimate stress, ultimate strain, and fracture toughness. All tests were performed with a

model 100P Universal Testing Machine equipped with a Biobath chamber and 5.6 lbf load cell was (TestResources, Inc, Shakopee, MN). Fully hydrated samples were immersed in DI water at 20 °C for the duration of the test. For each experiment, samples were preloaded to 0.1 N before being stretched at 50  $\mu\text{m/s}$ . Young's modulus was calculated from the slope of the engineering stress vs strain curve from 0-10% strain. Toughness was characterized by computing the area under the engineering stress strain curve.

#### *5.3.4 X-Ray Scattering*

X-ray scattering experiments were performed to elucidate relations between polymer microstructure and mechanical properties. Experiments were conducted with a Rigaku SMAX 3000 Pinhole SAXS instrument operating at 45 kV and 0.88 mA producing Cu  $K\alpha$  X-ray radiation ( $\lambda = 1.5405 \text{ \AA}$ ) at a sample to SAXS detector distance of 1550 mm. Wide-angle scattering patterns were collected at a sample-detector distance of 117 mm, as calibrated using corundum (NIST SRM 676a) with Fujifilm image plates (CR HR-V) and a Raxia-Di Image Plate reader at a scan resolution of 100  $\mu\text{m}$ . Fiber mats saturated in DI water were encapsulated in Kapton<sup>®</sup> tape prior to being placed in the X-ray chamber under ambient pressure. Kapton<sup>®</sup> windows were used to isolate the chamber from the evacuated source and detector tubes. 1D WAXS patterns were plotted as intensity versus the detector angle ( $2\theta$ ).

#### *5.3.5 Boundary Lubricant Retention*

Fiber mats were immersed in 0.2 M aqueous sodium chloride for up to 7 days to characterize the long-term stability of PMEDSAH within the fiber mat matrix. Vessels were stored in a 37 °C C24 Benchtop Incubator Shaker (New Brunswick Scientific, Enfield, CT) rotating at 60 rpm. In

addition to measuring changes in mass, the effects of boundary lubricant depletion on fiber mat coefficient of friction was also characterized using the tribo-rheometry setup described earlier.

### 5.3.6 Statistical Analysis

All statistical analyses were conducted with Minitab 17 (Minitab Inc., State College, PA). One way ANOVA with a significance level  $\alpha = 0.05$  was performed for all hypothesis testing.

## 5.4. Results

### 5.4.1 Fiber mat Microstructure

Characterization of fiber morphology was achieved with scanning electron microscopy (Figure 5.3). The electrospinning conditions used for this investigation results in an isotropic microstructure with randomly oriented fibers. Neat Pellethane fiber mats maintained an average fiber diameter of about 2  $\mu\text{m}$ . Fibers were consistently smooth with no evidence of bead formation. When left in ambient lab conditions, PMEDSAH fiber mats gradually transitioned from a fiber mat to a brittle, transparent film. Composite fiber mats with 180 kDa PMEDSAH did not exhibit any film formation when sample were stored at ambient lab conditions. PMEDSAH fibers appear to have an average fiber diameter of about 500 nm. Dual spinning with 50 kDa PMEDSAH resulted in electrospaying rather than fiber production desired for electrospinning. PMEDSAH film is evident throughout the matrix suspended by Pellethane fibers.

While wide angle x-ray scattering experiments did reveal a distinct diffraction peak at  $2\theta$  angles spanning 10 – 20° with neat PMEDSAH, this peak was not apparent in the blends containing 50 wt% PMEDSAH (Figure 5.4). Low angle peaks characteristic of the Kapton® window were also evident. Neither neat Pellethane, PMEDSAH, nor the 50:50 blend yielded small angle

diffraction (Figure 5.5). Again, a low angle peak characteristic of the Kapton® window was observed.

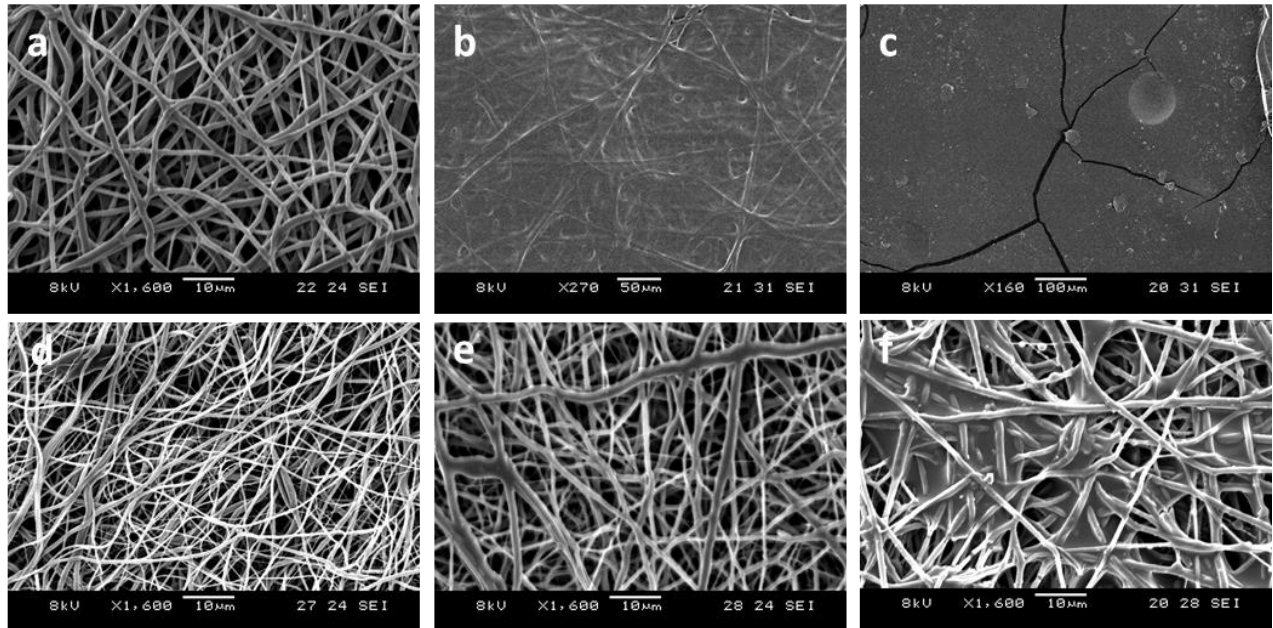


**Figure 5.3** - Representative scanning electron micrographs of fiber mats composed of (a) neat Pellethane (b) neat PMEDSAH minutes after electrospinning (c) neat PMEDSAH after 24 h on lab bench (d) 50:50 Pellethane PMEDSAH blend (e) 75:25 Pellethane PMEDSAH blend (f) Blend containing 75% 50 kDa PMEDSAH

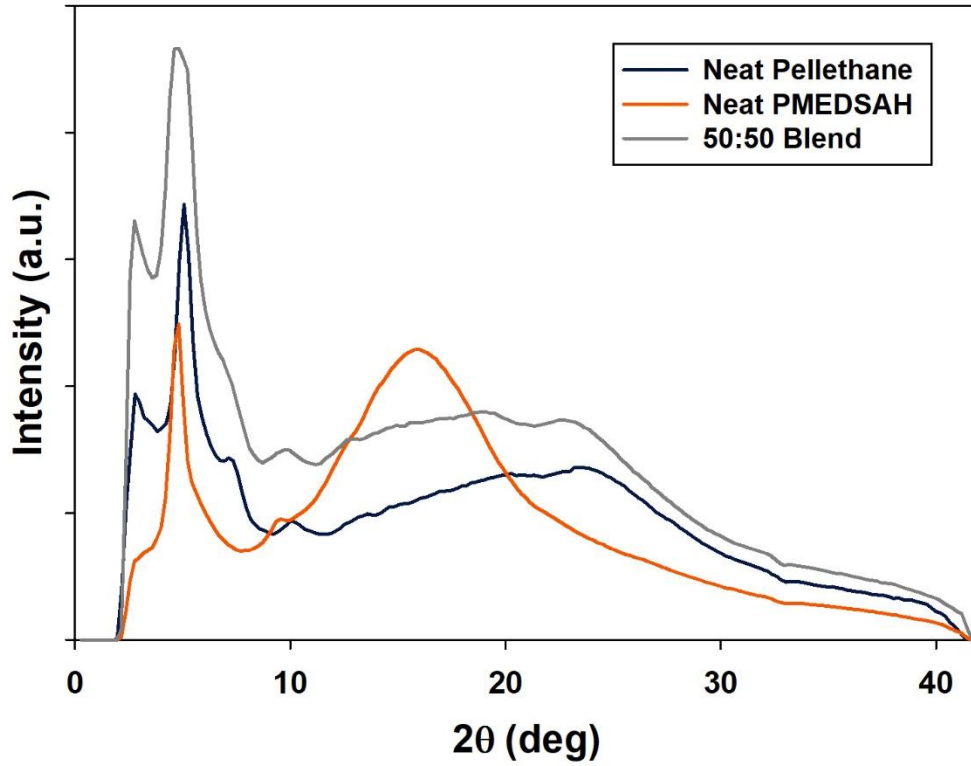


Figure 5.4 - Representative 1D WAXS patterns of hydrated fibermats containing 0 and 50 wt% PMEDSAH compared to neat PMEDSAH

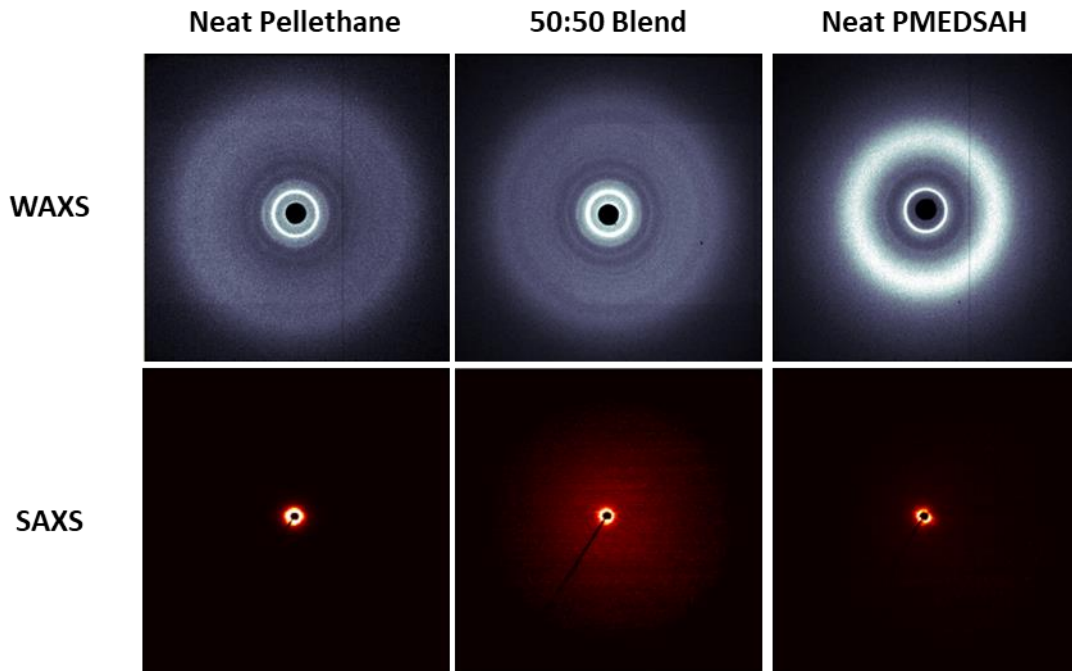


Figure 5.5 - Representative 2D WAXS (top) and SAXS (bottom) patterns of hydrated fibermats containing 0 and 50 wt% PMEDSAH compared to neat PMEDSAH



#### 5.4.2 Tensile Properties

Fibermat tensile properties were characterized with dogbone specimens immersed in DI water at approximately 20 °C (Figure 5.6). Increasing PMEDSAH content resulted in a trending decrease in Young's Modulus. PMEDSAH content  $\geq 50$  wt% resulted in a significant decrease in Young's Modulus. PMEDSAH content did not have a significant effect on ultimate stress when PMEDSAH content was less than 75 wt%. Also, PMEDSAH did not yield a significant effect on strain to failure however the highest average ultimate strain was observed in fibermats containing 50 wt% PMEDSAH. A significant change in toughness was not observed in any of the blends compared to neat Pellethane however fibermats containing 50 wt% PMEDSAH displayed the highest average toughness. Representative stress strain plots for each sample type are presented in Figure 5.7. The mean and standard deviation for each test parameter are provided in Table 5.1.

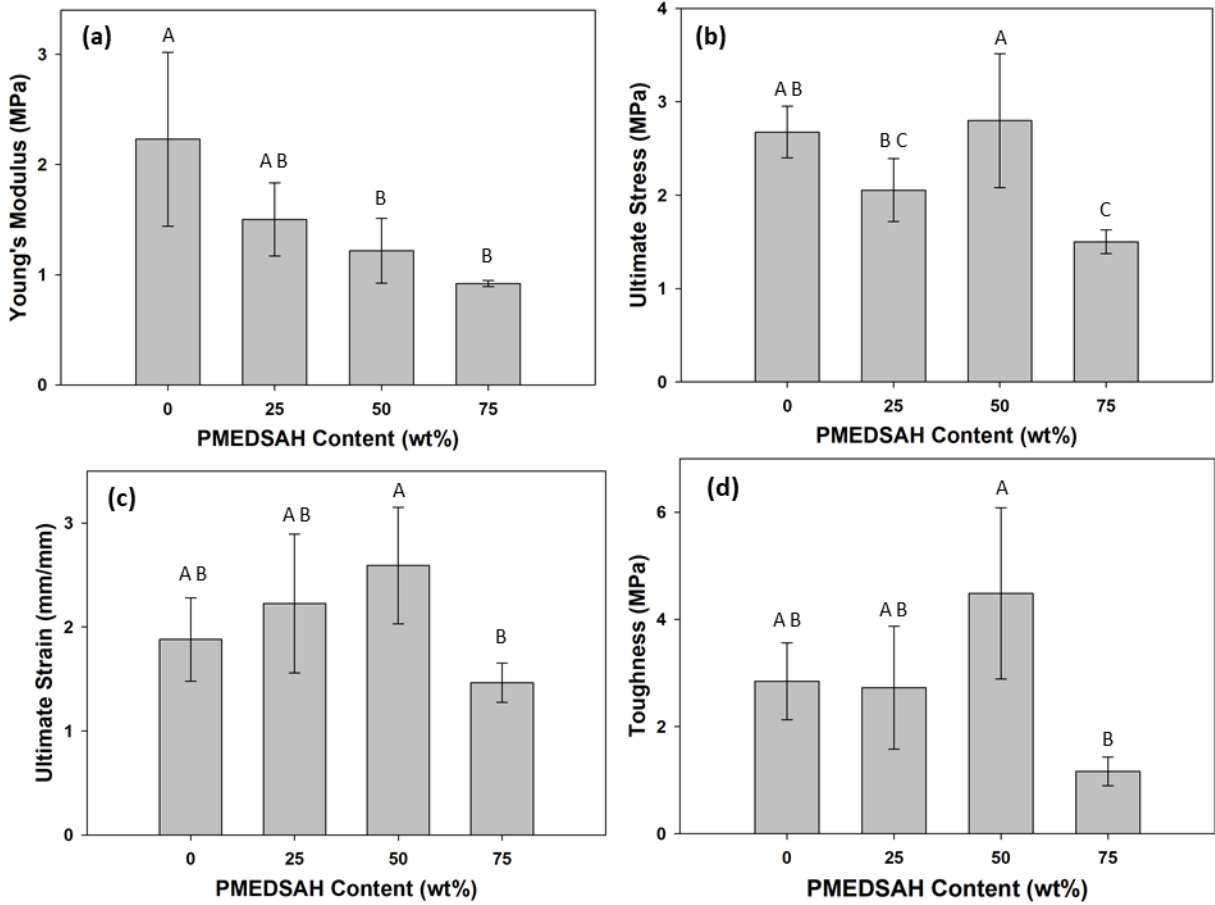


Figure 5.6 - Effect of PMEDSAH content on (a) Young's modulus, (b) ultimate stress, (c) ultimate strain, and (d) toughness. Means that do not share a letter are significantly different

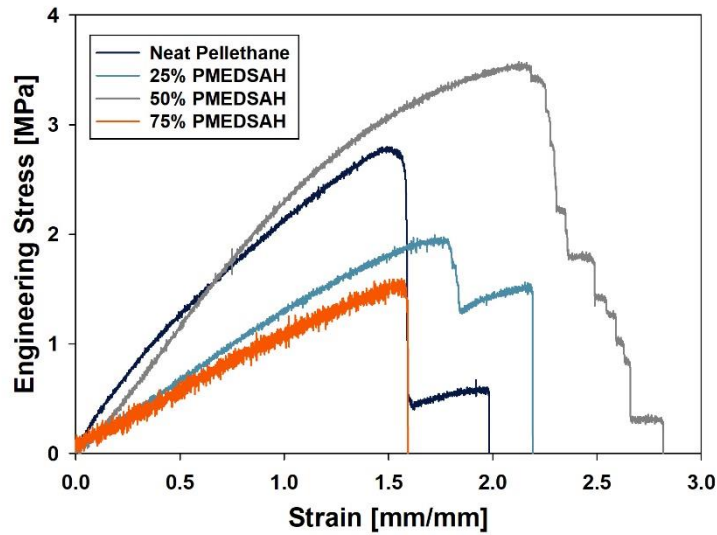


Figure 5.7 - Representative stress-strain plots of composite fiber mats with PMEDSAH content ranging from 0 -75 wt% tested in 20 °C DI water

**Table 5.1** – Tensile properties of composite fibermats with PMEDSAH content ranging from 0 – 75 wt% tested in 20 °C DI water

PMEDSAH Content (wt%)	Young's Modulus (MPa)	Ultimate Stress (MPa)	Ultimate Strain (mm/mm)	Toughness (MPa)
0	2.23 ± 0.79	2.68 ± 0.28	1.88 ± 0.40	2.85 ± 0.72
25	1.50 ± 0.33	2.05 ± 0.34	2.23 ± 0.67	2.72 ± 1.15
50	1.22 ± 0.29	2.80 ± 0.72	2.59 ± 0.56	4.48 ± 1.60
75	.92 ± 0.03	1.50 ± 0.13	1.46 ± 0.19	1.16 ± 0.27

#### 5.4.3 Coefficient of Friction

Coefficient of friction between fibermats and glass with DI water as the lubricating fluid was characterized with a rheometer. Results revealed that PMEDSAH resulted in a significant reduction in coefficient of friction with as little as 25 wt% PMEDSAH. Blends containing 50% PMEDSAH displayed the highest reduction in average coefficient of friction yielding a 70% reduction (Table 5.2). With fibermats containing PMEDSAH, a steady decrease in coefficient of friction is observed during the first 10-15 seconds of the test before reaching equilibrium, neat Pellethane fibermats typically took 3-4 minutes to reach an apparent asymptote (Figure 5.8).

In addition to manufacturing composite fibermats with homogeneous blending through the thickness, functionally graded fibermats were also prepared with a neat Pellethane base followed by simultaneous spinning of PMEDSAH and Pellethane and finally a neat PMEDSAH layer. Both the PMEDSAH and Pellethane sides of the functionally graded fiber mat displayed significantly lower coefficient of friction than neat Pellethane fibermats (Figure 5.9). The Pellethane side of the gradient fiber mat displayed the lowest average coefficient of friction which was more than 80% lower than that of the neat material (Table 5.3).

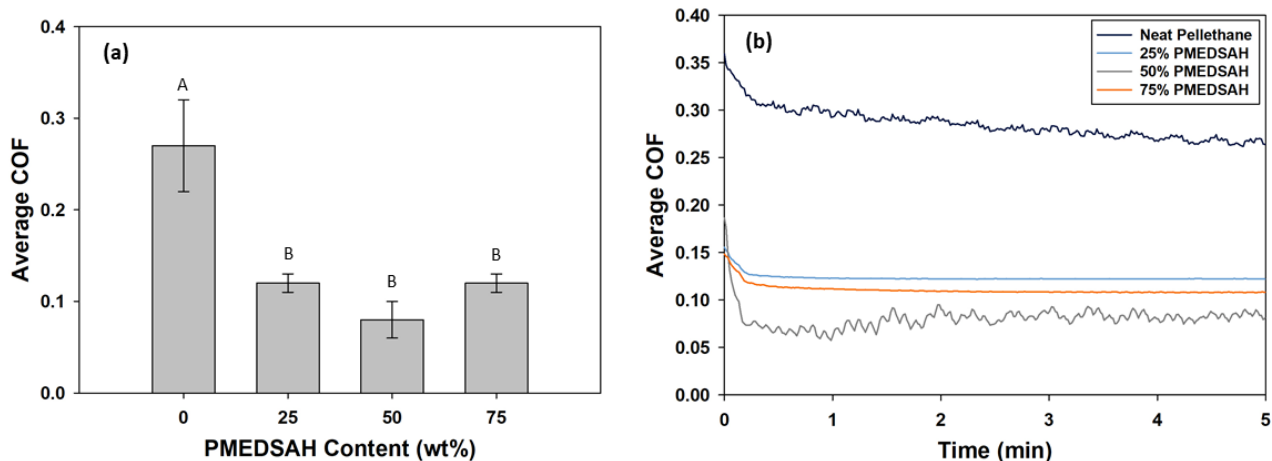


Figure 5.8 - (a) Effect of PMEDSAH on average coefficient of friction. (b) Representative COF vs time curves.

Table 5.2 – Average coefficient of friction of composite fibermats with PMEDSAH content ranging from 0 – 75 wt% tested against glass in 20 °C DI water

PMEDSAH Content [%]	Average COF
0	0.27 ± 0.05
25	0.12 ± 0.01
50	0.08 ± 0.02
75	0.12 ± 0.01

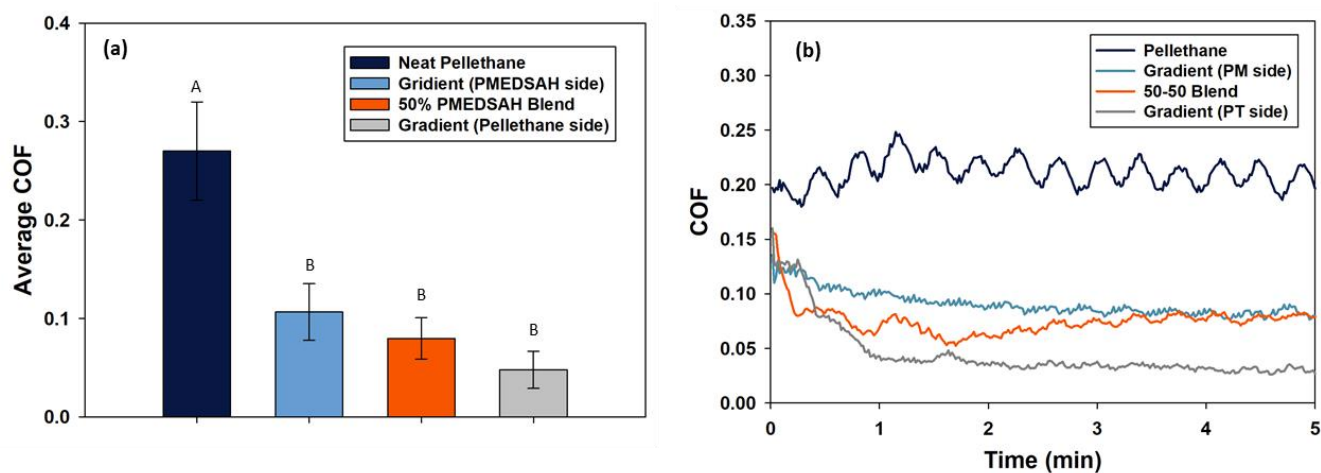


Figure 5.9 - (a) Average coefficient of friction of functionally graded fibermats compared to neat Pellethane and the 50 wt% PMEDSAH blend. (b) Representative COF vs time curves.

**Table 5.3** – Average coefficient of friction of functionally graded composite fibermats compared to neat Pellethane and the 50 wt% PMEDSAH blends

Sample	Average COF
Neat Pellethane	0.27 ± 0.05
Gradient (PMEDSAH side)	0.11 ± 0.03
50 wt% PMEDSAH Blend	0.08 ± 0.02
Gradient (Pellethane side)	0.05 ± 0.02

#### 5.4.4 Boundary Lubricant Retention

Fibermats were immersed in DI water and stored in a 37 °C shaker table for up to 7 days to characterize how well PMEDSAH was retained within the matrix. Unlike the neat Pellethane fibermats, the composite materials displayed a significant decrease in mass after as little as 24 hours (Figure 5.10). No significant decrease in mass was observed after 24 h regardless of initial PMEDSAH content. While a trending increase in mass loss was observed with increasing PMEDSAH content, initial PMEDSAH content did not have a significant effect on the relative amount of boundary that was retained in the fibermat. Instead blends retained an average of 45% of the initial boundary lubricant content (Table 5.4).

All blends maintained an average coefficient of friction that was significantly lower than that of neat Pellethane even after being immersed in DI water stored in a 37 °C shaker table for 7 days. The fibermat containing 75 wt% PMEDSAH displayed the lowest average coefficient of friction after 7 days however no significant difference in average coefficient of friction among the blends was observed (Table 5.5).

Scanning electron microscopy revealed no apparent change in fiber morphology of neat Pellethane fibermats after being immersed in DI water for as long as 7 days (Figure 5.11). In fibermats containing 180 kDa PMEDSAH film formation was observed after as little as 24 h.

PMEDSAH was still visible on the surface of the fibermat after as long as 7 days. In fibermats containing 50 kDa PMEDSAH, the boundary lubricant is present in the form of a film rather than fibers. PMEDSAH appears to be completely depleted from the surface of the gel after as little as 24 h.

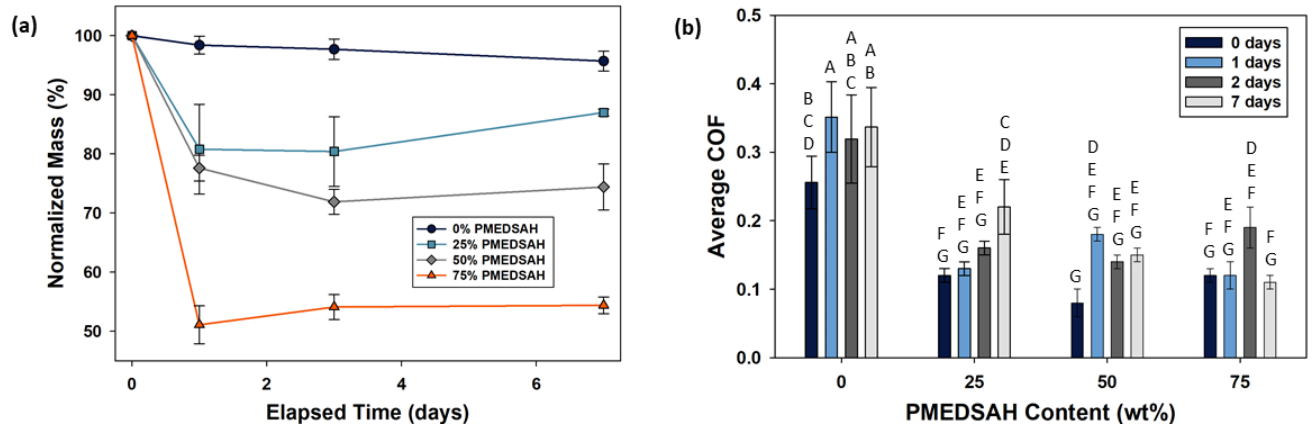


**Figure 5.10** - (a) Boundary lubricant depletion of composite fibermats with PMEDSAH content ranging from 0-75 wt% immersed in 0.2 M aqueous NaCl stored on a shaker table at 37 °C. (b) Average COF of composite fibermats after immersion in incubator for up to 7 days.

**Table 5.4** - Normalized mass of composite fibermats with PMEDSAH content ranging from 0 -75 wt% immersed in 0.2 M aqueous NaCl stored on a shaker table at 37 oC for up to 7 days

Elapsed Time (days)	Normalized Mass (wt%)			
	0% PMEDSAH	25% PMEDSAH	50% PMEDSAH	75% PMEDSAH
1	98.4 ± 1.5	80.8 ± 7.6	77.6 ± 2.2	51.1 ± 3.2
3	97.7 ± 1.7	80.4 ± 5.9	71.9 ± 2.1	54.1 ± 2.1
7	95.7 ± 1.7	87 ± 0.6	74.4 ± 3.9	54.4 ± 1.4

**Table 5.5** - Average coefficient of friction of composite fiber mats with PMEDSAH content ranging from 0 -75 wt% immersed in 0.2 M aqueous NaCl stored on a shaker table at 37 °C for up to 7 days

Elapsed Time (days)	Coefficient of Friction			
	0% PMEDSAH	25% PMEDSAH	50% PMEDSAH	75% PMEDSAH
0	0.27 ± 0.05	0.12 ± 0.01	0.08 ± 0.02	0.12 ± 0.01
1	0.35 ± 0.05	0.13 ± 0.01	0.18 ± 0.01	0.12 ± 0.02
3	0.32 ± 0.06	0.16 ± 0.01	0.14 ± 0.01	0.19 ± 0.03
7	0.34 ± 0.06	0.22 ± 0.04	0.15 ± 0.01	0.11 ± 0.01

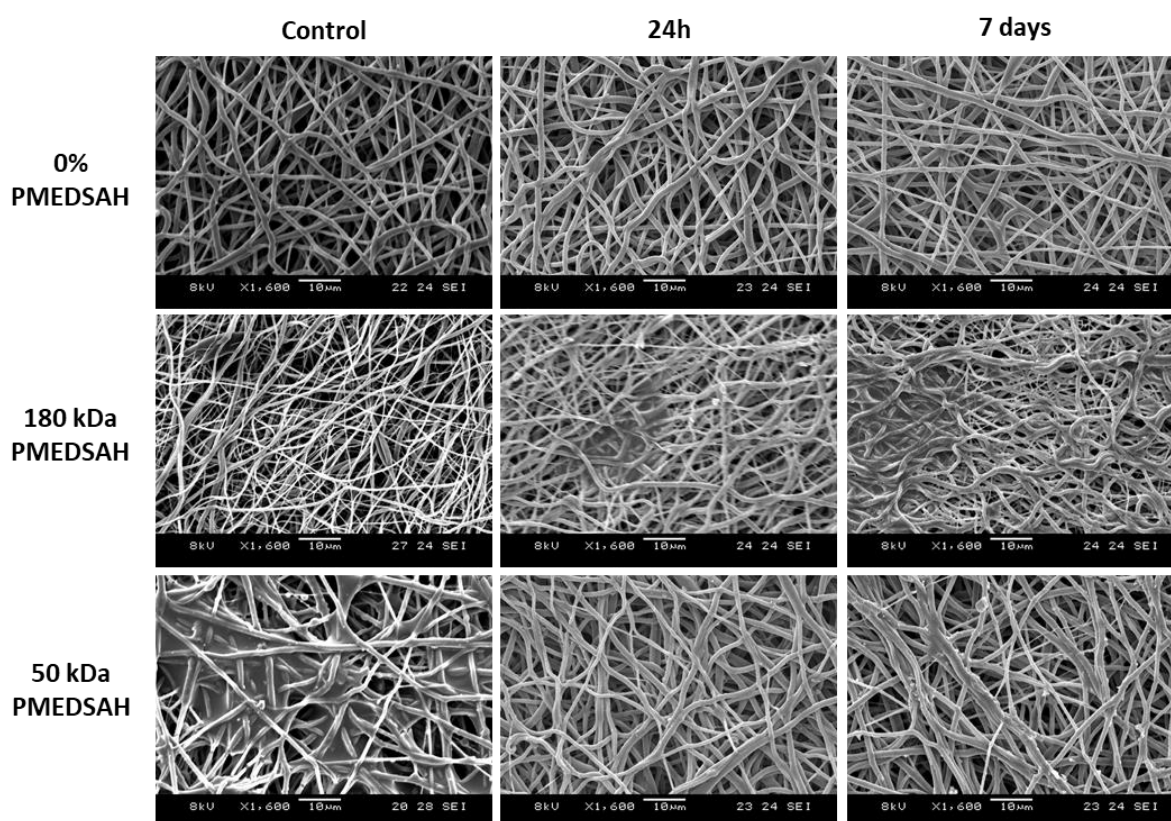


**Figure 5.11** - SEM images displaying changes in fiber mat morphology after being immersed in 0.2 M aqueous NaCl stored on a shaker table at 37 °C for up to 7 days

## 5.5 Discussion

It is well understood that the morphology of micro-nanometer scale fibers produced via electrospinning depends of a number of factors including applied voltage, solvent conductivity, viscosity, collector distance, etc. [223]. In this investigation PMEDSAH was electrospun at two

different molecular weights, 50 kDa and 180 kDa. The former resulted in immediate film formation while the later produced fibers despite having the same solution concentration. This result is attributed to a significant decrease in chain entanglement resulting in a decrease in solution viscosity [224]. Without a proper balance between viscosity and surface tension smooth fibers cannot be maintained and instead beads of droplets are produced [225]. Due to the hygroscopic nature of the zwitterionic polymer, neat PMEDSAH fibermats gradually turned into brittle films as moisture absorbed from the atmosphere dissolved the fibers. On the other hand, PMEDSAH fibers electrospun simultaneously with Pellethane did not form films under ambient lab conditions. This behavior is attributed to the hydrophobicity of the Pellethane fibers.

As noted in the introduction section, one useful functionality of zwitterionic polymers is their strong resistance to bacterial adhesion, protein adsorption, and cell attachment as demonstrated by Lalani and Liu [218]. On their own, electrospun PMEDSAH fibermats do not have suitable mechanical properties for use as a wound dressing however, blending the polymer with a TPU such as Pellethane produced a material which retained comparable elasticity to that of the neat elastomer. Electrospun membranes impart several other useful functionalities for use as wound dressings including good conformability, high surface area, and gas permeability[226,227]. The hygroscopic nature of PMEDSAH is also ideal for maintaining a moist wound environment which has been shown to accelerate epithelialization [228].

Although Pellethane fibermats displayed the highest average Young's modulus, blends containing 50 wt% PMEDSAH displayed the highest average ultimate stress, strain, and toughness. We postulated that this behavior may be due to interchain association between boundary lubricant molecules as this behavior is well documented in literature concerning PMEDSAH [202,208]. Changes associated with fibermat microstructure were characterized via x-



ray scattering however results did not reveal any new diffraction patterns in the blends indicative of changes in short or long-range order as a result of association between the zwitterionic side groups. Characterization of neat PMEDSAH did reveal a broad diffraction ring spanning  $10 - 20^\circ$ . This behavior may be evidence of interchain association between PMEDSAH molecules resulting in an increase in toughness.

Zwitterionic polymers are understood to be effective boundary lubricants due to their unique net neutral but locally charged structure. These characteristics cause zwitterionic molecules to electrostatically attract water, a polar molecule and excellent boundary lubricant, resulting in a mechanism known as hydration lubrication [4,229]. Tensile testing revealed that PMEDSAH resulted in a trending decrease in Young's modulus with increasing boundary lubricant content therefore in addition to investigating whether or no dual electrospinning was an effective method for producing low friction TPU's, the effect of PMEDSAH content on coefficient of friction was also characterized. Results revealed that increasing PMEDSAH content from 25 – 75 wt% did not result in a significant change in coefficient of friction. In fact, fibermats containing 50 wt% PMEDSAH displayed the lowest average coefficient of friction among the homogeneous composite blends.

In addition to forming composite fibermats with homogeneous polymer composition through the thickness, electrospinning is a suitable method for fabricating functionally graded materials. We hypothesized that this approach would result in an elastomer with high coefficient of friction on the Pellethane rich side, and low coefficient of friction on the PMEDSAH rich side. Instead we observed that the Pellethane rich side displayed the lowest average coefficient of friction than any of the other sample types. PMEDSAH is soluble in water therefore we hypothesize that Pellethane plays a role in retaining the boundary lubricant on the surface. Due to

the hydrophilicity and permeability of the fibermat, the boundary lubricant is likely diffusing from the PMEDSAH rich side to the Pellethane rich side. The gradual decrease in COF of observed in the COF vs time behavior of the Pellethane side of the gradient fibermat supports this hypothesis as COF steadily decreases from 0.15 before reaching an asymptote at 0.04. This behavior could be mitigated by preparing a thicker Pellethane rich region. Another possible explanation is that increasing PMEDSAH content past a certain level results in an increase in the viscosity of the fluid boundary layer at the interface between the articulating surfaces.

One of the primary limitations of the material used for this investigation is that the boundary lubricant is soluble in water and is gradually depleted while the fibermat is immersed in aqueous conditions. Regardless of initial boundary lubricant content, composite fiber mats retained about 45% of their initial boundary lubricant content. Fresh solvent was substituted to maintain perfect sink conditions and promote Fickian diffusion however result indicate that after about 24 hours, passive diffusion of PMEDSAH out of the fibermat ceases. Fiber mat thickness may be a limiting factor. Another limitation is the solvent used for the degradation study. Phosphate buffered saline or PBS would provide more physiologically relevant osmotic pressure resulting in more accurate representation of how the material would behave *in vivo*.

While passive boundary lubricant depletion may be undesirable for use of zwitterionic composite fiber mats intended for use as a permanent implant, these properties may be idea for wound dressing applications where a reservoir of antimicrobial would be available to replenish the wound site. PMEDSAH depletion could be mitigated via co-polymerization with a hydrophobic polymer. The low fouling properties of PMEDSAH may also be useful for stent coatings where the base material which provide mechanical properties suitable for the stent coating suffers from poor resistance to fouling and poor hemocompatibility. Antimicrobial properties of the composite

fibermat could be improved further through impregnation with silver ions, a well-known antimicrobial agent as demonstrated by Lanani and Liu [218]. Composite fibermats are expected to be susceptible to efficient Ag ion impregnation through ionic attraction between  $Ag^+$  and the anionic  $SO_3^-$  groups of PMEDSAH.

As noted earlier, composite materials similar to the one discussed in this investigation also show great potential for use as a synthetic ligament or tendon. Previous investigations have revealed the importance of boundary lubrication on the performance of ligaments and tendons which are subjected to a high degree of shear during normal operation. Examples include the Achilles tendon, rotator cuff tendons, as well as ligaments in the ankle and wrist. This is evidenced by the presence of lubricin a well-known boundary lubricant both on the surface and between the collagen fiber bundle which make up the tissue [230,231]. Reported values reveal that the mechanical properties of the fibrous tissue these composite fibermats seek to mimic have Young's moduli ranging from 100 – 800 MPa [232-234]. Although Pellethane clearly falls short of the mechanical performance of the natural tissue, the versatility of the fabrication method described herein allows for substitution of alternative TPU's such as polycaprolactone (PCL). Mechanical properties could be enhanced further by attaining fiber alignment. This can be achieved by increasing the rotational speed of the electrospinning collector or introducing an auxiliary electric field [235,236]. The resulting anisotropic fibrous microstructure more closely resembles that of natural tissue and has also been shown to influence ECM production of human fibroblasts and differentiation of stem cells [237-239]. Young's modulus and ultimate tensile strength could also be enhanced through the addition of polylactic acid (PLA) fibers [240].

While zwitterionic polymers such as PMEDSAH do inhibit nonspecific protein adsorption and cell attachment due to their high hydration, previous investigations have demonstrated that

cell attachment and proliferation can be achieved through the introduction of growth factors and peptides such as Arginylglycylaspartic acid (RGD) [241,242]. Based on these findings we postulate that a composite fiber mat consisting of PMEDSAH, PCL, PLA, and the appropriate adhesion proteins and growth factor would result in a material suitable for repair and regeneration of ligaments and tendons.

## 5.6 Conclusion

This chapter describes the design and characterization of a composite fiber mat consisting of the zwitterionic polymer PMEDSAH and thermoplastic polyurethane Pellethane. Fiber mats were prepared via dual electrospinning. Results revealed that this approach results in a significant reduction in coefficient of friction while maintaining comparable mechanical properties to the neat fiber mat. Results also reveal that the zwitterionic polymer can enhance fiber mat toughness and ultimate strain. While the investigation does have limitations, it presents a versatile platform for the design of composite biomaterials for many biomedical applications including wound dressings, cardiovascular stent coatings, and ligament/tendon repair.

## CHAPTER 6: CONCLUSIONS AND FUTURE DIRECTIONS

### 6.1 Summary and Conclusions

From fish fins driving wind turbine design, to lotus leaves motivating the development of self-cleaning surfaces, there are countless examples of technological advances which have drawn inspiration from nature. This dissertation provides yet another illustration of the utility of biomimicry for innovation in engineering. Drawing inspiration from recent insights into the tribological mechanisms employed by articular cartilage, this dissertation presents and examines three novel approaches for the design of tribologically enhanced polymeric materials.

Chapter 2 described the synthesis and characterization of a novel tribologically enhanced hydrogel systems. This was achieved through the synthesis of the biomimetic boundary lubricant, PMEDSAH, which was blended with PVA to form a low friction hydrogel blend. The presence of the boundary lubricant on the surface of the gel was confirmed through ATR-FTIR. The reduction in coefficient of friction was attributed to hydration lubrication, a relatively new paradigm proposed by Jacob Klein. Hydration lubrication was recently identified as the underlying mechanism behind the phenomenal tribological properties exhibited by articular cartilage. In addition to providing a significant reduction in coefficient of friction, this fabrication method resulted in comparable mechanical and physical properties to the neat material. The zwitterionic blend was also found to be cytocompatible towards L929 fibroblast cells despite the toxic initiator and solvents that were used for boundary lubricant synthesis. In summary, this chapter provided a versatile method for the fabrication of low friction hydrogels with potential for use for a wide range of medical applications including guide wire coatings, contact lenses as well as meniscus and articular cartilage repair.

The coefficient of friction vs time behavior described in Chapter 2, as well as the solubility of the zwitterionic boundary lubricant in aqueous solvents motivated the hypothesis that the zwitterionic blends may support a self-replenishing lubrication system. It is also well understood that the behavior of polymers depends heavily on their molecular weight. Chapter 3 provided a detailed investigation into the effects of boundary lubricant molecular weight on the mechanics, tribology, and diffusive properties of the hydrogel blends. The reported results support hypotheses regarding the effect of boundary lubricant molecular weight on diffusive kinetics, interstitial fluid load support, and coefficient of friction.

Results from the diffusion experiments revealed that the boundary lubricant is mobile within the hydrogel matrix however boundary lubricant molecular weight influences diffusivity. This is attributed to the increase in hydrodynamic radius associated with increasing molecular weight. The investigation also revealed that PMEDSAH is susceptible to pressure driven elution when the boundary lubricant molecular weight is below 180 kDa. This is a necessary characteristic for a self-replenishing lubrication system, providing storage of lubricant within the bulk of the material which can be eluted to the surface; very much like the boosted lubrication mechanism of articular cartilage proposed by McCutchen.

As noted in Chapter 1, interstitial fluid load support is understood to play a central role in the tribological performance of articular cartilage. By implementing Hertzian biphasic theory, an analytical model recently developed by Moore and Burris, the effects of boundary lubricant molecular weight on fluid load support was characterized through a series of indentation tests. Results from these experiments revealed that in addition to acting as a boundary lubricant, PMEDSAH increases the hydrogels capacity to provide interstitial fluid load support. This

behavior may be due to electrostatic attraction of PMEDSAH towards water molecules or structural remodeling of the hydrogel matrix resulting in a decrease in porosity and permeability.

No evidence of distinct changes to hydrogel porosity was evident through SEM imaging, however it is possible that these morphological changes may have occurred at length scales above the resolution of the JEOL microscope. The increase in crystallinity observed in PVA-PMEDSAH blends supports the notion that the boundary lubricant results in a decrease in molecular scale permeability. Previous investigations have revealed that an increase in fluid load support is a valuable trait for tribologically enhanced materials as it is expected to result in improved resistance to surface wear.

The investigation described in Chapter 3 also sought to address the hypothesis that the reduction in coefficient of friction reported in Chapter 2 was attributed to hydration lubrication and not a change in bulk mechanics such as interstitial fluid load support. PVA is understood to have an attractive interaction with glass. If hydration lubrication was promoted by PMEDSAH it was hypothesized that the COF vs sliding speed behavior of the blends would resemble that of a repulsive interaction rather than an attractive one. Results from these experiments supported the hypothesis that hydration lubrication causes the observed reduction in coefficient of friction. This is a valuable characteristic for the development of materials for articular cartilage repair. While it is important to implant a material that can withstand the rigorous loading experience by articulating joints such as the knee, it is essential to ensure that wear of the opposing cartilage surface does not occur. Adhesive wear is one of the primary modes of surface wear and may be mitigated through hydration lubrication.

Given the significant reduction in coefficient of friction observed when PMEDSAH was blended with PVA to form a zwitterionic hydrogel blend, it was postulated that grafting a

zwitterionic polymer to the surface of a hydrogel would result in enhanced tribological performance. While the behavior of zwitterionic polymer brushes has been a subject of interest in the literature over the past decade, to the best of our knowledge no report has presented the synthesis or tribological characterization of hydrogels bearing zwitterionic polymer brushes. Chapter 4 presents the synthesis and characterization of novel brush functionalized hydrogels bearing PMEDSAH brushes and PMPC brushes. Successful surface modification was verified through ATR-FTIR.

The effect of solvent and the articulating substrate on coefficient of friction was consistent with what was postulated given the known tribological behavior of PMEDSAH and PMPC brushes. The findings support the hypothesis that PMPC is a more versatile and effective boundary lubricant due to its high attraction to water compared to PMEDSAH. As a result, PMPC brushes are less susceptible to interchain association which inhibits the polymer's ability to attract water molecules and promote hydration lubrication. It is interesting to note that the zwitterionic entities more closely mimic those found in natural tribological systems such as synovial joints, providing yet another example of the value of biomimicry.

Hydrogel surface characterization via scanning electron microscopy and water contact angle experiments revealed that brush functionalization may be optimized further to achieve more surface coverage. Given the hydrophilicity of PMEDSAH and PMPC it was postulated that surface modified hydrogels would display a water contact angle as low or lower than that of the neat material. Instead water contact angle experiments revealed that brush functionalized hydrogels displayed a significant increase in water contact angle. A significant increase in water contact angle was observed following initiator functionalization suggesting that the presence of unreacted initiator on the surface of the hydrogel may be contributing to the hydrophobic behavior observed



in the brush modified gels. Characterization of hydrogel surface morphology revealed additional evidence of brush formation with distinct micron scale surface features which were not observed on the surface of the neat or initiator functionalized hydrogels. These images also reveal areas where brush functionalization may not have occurred.

Chapter 4 also examined the effects of brush functionalization on the compressive properties of the hydrogel and its ability to provide interstitial fluid load support. Results revealed that brush functionalization resulted in an increase in the hydrogels ability to promote interstitial fluid load support as evidenced by the increase in strain rate dependence on contact modulus. This behavior supports the hypothesis proposed in Chapter 3 that the zwitterionic boundary lubricant may be influencing hydrogel permeability due electrostatic interaction between the polar functional groups of the zwitterionic polymer and water. PMPC is understood to have a higher affinity for water than PMEDSAH therefore it was postulated that if permeability was influenced by the boundary lubricant's affinity for water, then PMPC brush functionalized hydrogels would display a higher average contact modulus than PMEDSAH brush functionalized hydrogels. Indentation test results observed and reported in Chapter 4 support this hypothesis. Although the compressive properties of the brush functionalized hydrogels are within the reported range for natural articular cartilage, their stain rate dependence is significantly lower indicating that the ability to provide interstitial fluid load support is still inferior to that of the natural tissue.

Hydrogel surface modification through atom transfer radical polymerization required the hydrogels to be completely dehydrated during the reaction. The process of dehydrating and rehydrating the material resulted in a dramatic increase in contact modulus accompanied by a relatively small decrease in equilibrium water content and no change in bulk crystallinity. Characterization of porosity via SEM revealed a distinct change in porosity indicating that

macroscale remodeling occurred during the dehydration process. This process is likely due to plastic deformation of the polymer matrix resulting in a change in permeability and compressive modulus. While this was an unanticipated result, it provides an additional method for enhancing the tribological and load bearing characteristics of freeze-thaw PVA hydrogels. The compressive stiffness of freeze thaw PVA hydrogels can be enhanced by increasing the molecular weight of the polymer, the concentration in solution, or the number of freeze thaw cycles. While each of these approaches have an additive effect on increasing hydrogel stiffness, they each have their limits. Increasing polymer molecular weight and or concentration does result in stiffer gels, however increasing these parameters past a critical point results in inhibits gel formation and ease of processing. Increasing freeze thaw cycles has also been shown to increase compressive stiffness and bulk crystallinity however the relative increase in these properties decreases with each successive freeze thaw cycle. Therefore, dehydration and rehydration provides an additional method for enhancing the tribological and load bearing properties of PVA hydrogels.

Many of the proposed applications for the material presented in Chapter 4 involve contact with cells or tissue. Given the toxic solvents and catalysts that were used to perform the surface modification cytotoxicity experiments were performed to as a preliminary measure to assess the feasibility of the use of these materials for medical applications. Results from these experiments revealed that the surface modified hydrogels maintain the cytocompatibility of the neat material and support additional investigations into the use of this material for biomedical applications.

In addition to articular cartilage the hydration lubrication paradigm is understood to be applicable to many other tribological systems found in nature. One such system is that of fibrous tissue such as ligaments and tendons. Chapter 5 sought to investigate the effects of hydration lubrication on thermoplastic polyurethanes through the development of novel low friction

composite polyurethane fibermats. This was achieved through electrospinning. Results revealed that a significant reduction in coefficient of friction comparable to the reduction observed in the PVA hydrogels could be achieved while maintaining comparable mechanical properties to that of the neat fibermat. This approach also allowed for more precise control over the distribution and concentration of boundary lubricant on the surface of the material allowing for the fabrication and characterization of functionally graded fibermats. Results from this investigation provided additional insight into the mobility of solubilized PMEDSAH within a solid matrix and provides insight into a novel approach for the fabrication of low friction polymeric materials suitable for several medical applications which the hydrogel platform described previously would not be suitable. In addition to providing low friction Chapter 5 also highlight additional functionalities imparted by zwitterionic polymers due to their superhydrophilicity supporting the use of the fabrication method described for the design of wound dressings and cardiovascular stent coatings.

Overall this dissertation presents three novel approaches for the fabrication of tribologically enhanced materials for medical application. In addition to detailing the methods developed to prepare these materials, experiments coupled with previously developed analytical, empirical, and conceptual models were used to provide valuable insight into the physical and mechanical characteristics of these unique materials.

## **6.2 Future Directions**

Like most research investigations, this body of work has some limitations. It does however provide an excellent foundation for several new experimental and analytical investigations. Pursuit of these investigations will provide novel insights which is expected to further development of innovative polymeric based medical device solutions and biomimetic technology. The remainder of this chapter provides detailed recommendations for future investigations.

### 6.2.1 Synthesis and Characterization of PMPC PVA Blends

Results reported in Chapter 4 as well as previous investigations involving the behavior of zwitterionic polymer brushes indicate that PMPC brushes are less susceptible to interchain association than PMEDSAH due to their strong attraction to water. The increase in average contact modulus compared to PMEDSAH brush functionalized hydrogels supports the hypothesis that electrostatic attraction may decrease water permeability and increase the hydrogel's ability to provide interstitial fluid load support. PMPC also more closely resembles the chemical structure of the boundary lubricants found in natural tribological systems such as articular cartilage. These insights motivate the synthesis and characterization of PMPC PVA blends.

The similarity in the chemical structure between the monomer MPC and MEDSAH, namely their methacrylate functional group, allow PMPC to be synthesized via free radical polymerization using a similar method as what was described in Chapters 3. Improved control over molecular weight and polydispersity can be achieved by performing the synthesis at a lower temperature or by preparing a mixture of ethanol and water rather than just water. This is expected to result in a reduction in chain transfer and a slower more controlled reaction. Following synthesis of PMPC via free radical polymerization blends can be fabricated via similar solvent casting and freeze thaw methods to what has been described in Chapters 2 and 3. One drawback of investigations involving the use of PMPC as oppose to PMEDSAH is its significantly higher cost of the MPC monomer compared to MEDSAH. Currently MPC is available for purchase from Sigma Aldrich for about \$21/g as oppose to MEDSAH which is available for as little as \$0.57/g. The first reported method for synthesizing MPC was published by Ishihara et al back in 1989,

however the cost of the precursors does not result in any monetary savings even if one achieved 100% yield.

Following the preparation of PMPC PVA blends, which would be a novel material, several interesting hypotheses could be investigated. (1) Given PMPC's strong affinity for water compared to PMEDSAH it would be interesting to address the postulation that PMPC PVA blends will exhibit lower coefficient of friction than PMEDSAH PVA blends. (2) Given the solubility of PMPC under aqueous conditions an investigation into the diffusive characteristics of PMPC compared to PMEDSAH would also be of interest. (3) Finally, given PMPC's strong affinity for water compared to PMEDSAH it would be reasonable to postulate that PMPC blends would display an improved capacity for interstitial fluid load support compared to PMEDSAH. This behavior could be investigated within the context of Hertzian biphasic theory through a similar method to what was described in Chapter 3. Characterization of this behavior would also provide insight into the effect of electrostatic interactions on water permeability. An investigation such as the one described in this section would be of great interest to the readership of several peer reviewed materials science journals including *Acta Biomaterialia*, *Materials Science and Engineering: C*, and *Polymer*.

### 6.2.2 Nanometer Scale Characterization of Tribological Performance

As noted in Chapter 1, interstitial fluid load support significantly influences coefficient of friction in biphasic materials such as hydrogels and articular cartilage. One of the primary objectives of the investigation described in this dissertation was improve tribological performance under boundary lubrication conditions. While the tribo-rheometry experiments described revealed that interfacial interactions were influencing friction, bulk properties such as modulus, crystallinity, and interstitial fluid load support may have influenced the observed friction behavior.

One way to isolate the confounding effects of bulk material properties on surface friction behavior is with the use of nanomechanical test methods such as atomic force microscopy.

Performing nanometer scale experiments introduces significant challenges in terms of sample preparation since these methods can only be successfully implemented with surfaces which are very flat. In addition, due to the small length scales involved in such experiments appropriate measures must be taken to isolate the instrument from exterior noise such as building vibrations. Due to these limitations samples prepared using the solvent casting method described in this investigation are not suitable for nanomechanical testing. One approach for overcoming this challenge would be to prepare a polymer solution for solvent casting as described previously and dip coat a rigid flat substrate such as a glass slide.

Measuring coefficient of friction could be achieved with an atomic force microscope equipped with a photodiode capable of recording cantilever twisting in addition to bending as illustrated in Figure 6.1. The complications associated with AFM because of its dependence on the use of compliant probes could be illuminated with a rigid probe and a more isolated displacement transducer such as the Hysitron TriboScope (Hysitron, Inc, Eden Prairie, MN). Instead of relying on cantilever beam deflection, these probes are coupled with capacitive displacement transducers as illustrated in Figure 6.2. A displacement of the center plate corresponds to a change in voltage which can be used to calculate normal as low as 1 nN and tangential forces as low as 3  $\mu$ N.

A nanometer scale investigation of the pressure dependent and sliding speed dependent friction behavior of blends compared to brush functionalized hydrogels containing PMEDSAH and PMPC would be of great interest to readership of *Langmuir*. Given the results observed and discussed in this dissertation, brush functionalized hydrogels are expected to display lower

coefficient of friction than blends and surfaces bearing PMEDSAH are expected to display higher coefficient of friction than PMPC when tested under aqueous conditions.

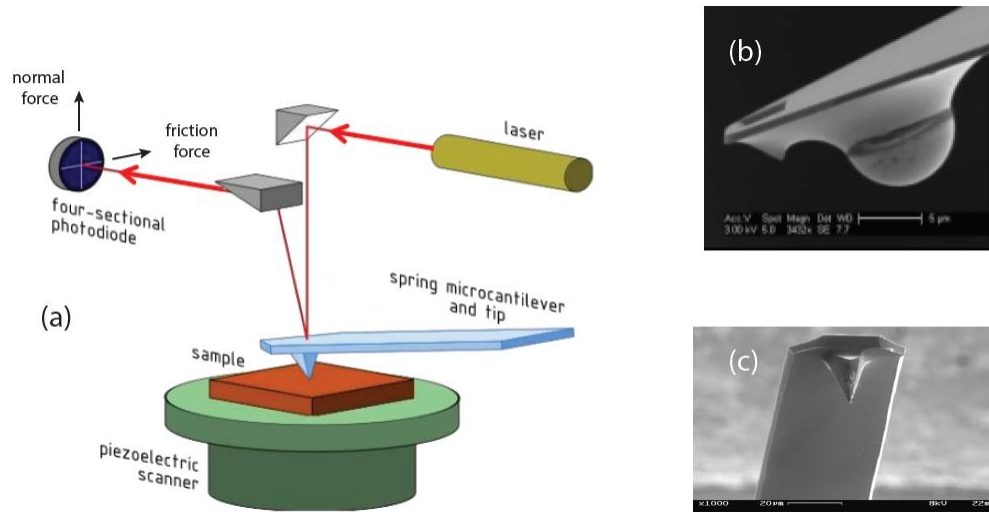


**Figure 6.1** - (a) Illustration of the primary components of a typical AFM system [243]. (b) SEM images of an AFM cantilever with a 10  $\mu\text{m}$  diameter glass sphere attached [36] and a (c) tapered cantilever tip.

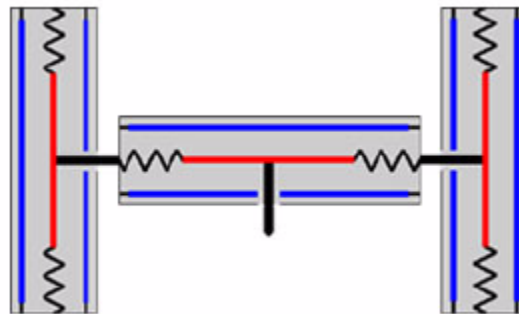


**Figure 6.2** – Scheme illustrating the cross-sectional design of the rigid probe normal and tangential force transducer

In addition to measuring coefficient of friction, the effects of synthesis parameters and solvent on brush layer thickness would be provide valuable insight toward the design of tribologically enhanced PVA-H. This could be accessed through tapping mode AFM. Brush layer thickness is understood to be a fundamental structural parameter which plays a significant role in boundary lubrication behavior. Some investigators have characterized brush thickness based on compression profiles however this approach is expected to be less accurate on a soft substrate such

as a hydrogel compared to a more rigid substrate like gold or silicon. An alternative approach would involve creating patterned brush layers (Figure 6.3) via microcontact printing of the initiator layer or performing initiator functionalization in the presence of a patterned mask.

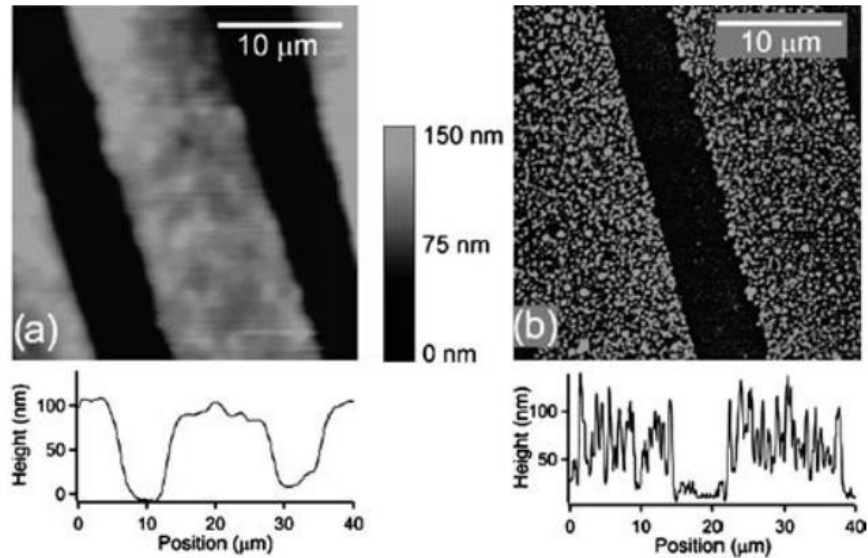


**Figure 6.3** – Topographical maps and representative cross sections of thermos-responsive poly(N-isopropylacrylamide) (PNIPAM) brushes grafted on gold at (a) 31 and (b) 36 °C [244]

### 6.2.3 Self-Replenishing Zwitterionic Brush Functionalized Hydrogels

This dissertation introduced two novel methods for the fabrication of tribologically enhanced hydrogels. Each of these methods have been shown to enhance tribological performance through unique physical mechanisms. The formation of zwitterionic hydrogel blends is attractive approach for several reasons. It is a relatively simple and versatile method for improving the performance of hydrogels under boundary lubrication conditions and provides a reservoir of lubricant which can be eluted to the surface. Blending PVA with PMEDSAH was also shown to result in improved interstitial fluid load support. The shortcoming of this method is that the boundary lubricant is not bound physically bound to the hydrogel and may be depleted over time through diffusion.



The advantage of zwitterionic polymer brush functionalized hydrogels is that the boundary lubricant is chemically bound to the surface of the hydrogel and may be present at a higher concentration than what would be attainable in a blend. Brush functionalized hydrogels also provide the option of stimuli responsive coefficient of friction depending on the surface chemistry. The shortcoming of the brush functionalized gel approach is that there is no replenishment of boundary lubricant following removal of the brush layer following surface wear.

Given the unique benefits of both the blend and brush methods described in Chapters 2-4, combination of the two is expected to result in tribological performance superior to that of blending or grafting alone. Preparation of this material would be relatively straightforward. Following the preparation of a zwitterionic blend using the methods described in Chapters 2 and 3, the sample would be dehydrated and then subjected to brush functionalization via a similar method to what was described in Chapter 4.

In addition to being a self-replenishing boundary lubrication system benefiting from having boundary lubricant chemically bonded to the surface of the hydrogel, the resulting material is also expected to display superior interstitial fluid load support due to the combined effects of the blend and brush functionality. Experiments which would provide valuable insights include: (1) comparison of compressive properties between the three sample types within the context of Hertzian biphasic theory, (2) assessment of the effects of the zwitterionic brush layer on the diffusive kinetics of the solubilized boundary lubricant, and (3) investigation into the effectiveness of the hypothesized lubrication mechanism through pin on disk friction tests (monitoring changes in coefficient of friction and surface wear over time).

All friction testing described in this dissertation was performed with a modified rheometer. This is not an ideal platform for characterizing the hypothesized self-replenishing lubrication

mechanism. For this reason, a custom electromechanical pin on disc tribometer was designed and manufactured. The device design and validation are described in Appendix A. Instructions for motion control and friction force data acquisition is provided in Appendix C. The insights gained from the investigations described in this section are expected to be of great interest to the readership of *Advanced Materials*.

#### 6.2.4 Characterization of Hydrogel Performance Under Physiologically Relevant Conditions

As noted in Chapter 1, there is a need for a comprehensive solution for the repair of articulating joints. The material described in this investigation shows great potential for this application from a tribological perspective. One shortcoming of the characterization methods described thus far is that they fail to capture the complex kinematics observed in the knee joint. The effects of more physiologically relevant loading involving simultaneous rolling and sliding motion, as well as the use of more physiologically relevant lubricating fluids such as phosphate buffered saline (PBS) are expected to provide a more applicable sense of the benefits of the tribological enhancements described in this investigation. To address these concerns a custom electromechanical device with six degrees of freedom has been design and manufactured. The design, operation instructions and validation of this device are described in Appendix B.

As noted previously, in addition to minimizing hydrogel surface wear, it is important that hydrogels used for the repair of focal chondral defects do not damage the opposing cartilage surface. Given the hydration lubrication mechanism that is understood to be at work in the zwitterionic blends and brush functionalized hydrogels these are expected to reduce surface wear of the opposing cartilage surfaces compared to neat PVA-H. This result would be attributed to hindrance of adhesive wear due to hydration lubrication. This hypothesis could be investigated by testing osteochondral plugs against hydrogels using a pin on disc test configuration such as the one

described in Appendix A. Preliminary method development was achieved with osteochondral plugs harvested from tibial plateau's and femoral condyles harvested from bovine specimens obtained from a local butcher (E & M Custom Slaughterhouse, Rome, NY). Given the rigidity of the bone tissue and the size of the specimens, a Dremel 3.5 amp oscillating saw was used to extract rectangular sections which could easily be fastened in a vice clamp. 12 mm diameter osteochondral plugs each about 10 – 15 mm long were subsequently harvested using a coring drill bit. Following extraction osteochondral plugs can be soaked in PBS and stored in vacuum sealed bags in a -20 °C freezer until use.

As noted in Chapter 1, collagen is one of the primary structural constituents of articular cartilage. Hydroxyproline is one of the three main amino acid constituents of collagen and can be measured with femtomole resolution via high performance liquid chromatography (HPLC) [245]. In HPLC, pressurized liquid mixtures are pumped through a column containing a solid absorbent material. The velocity at which of each compound passes through the column depends on the degree of its interaction with the absorbent solid. The time at which a given analyte emerges from the column is referred to as the retention time. The emergence of a given analyte is detected via an UV absorbance detector. Compounds of interest can be chemically “marked” through a process known as derivatization. Figure 6.4 illustrates the processes involved in HPLC. Additional details regarding the measurement of cartilage wear via HPLC is detailed in Appendix C.

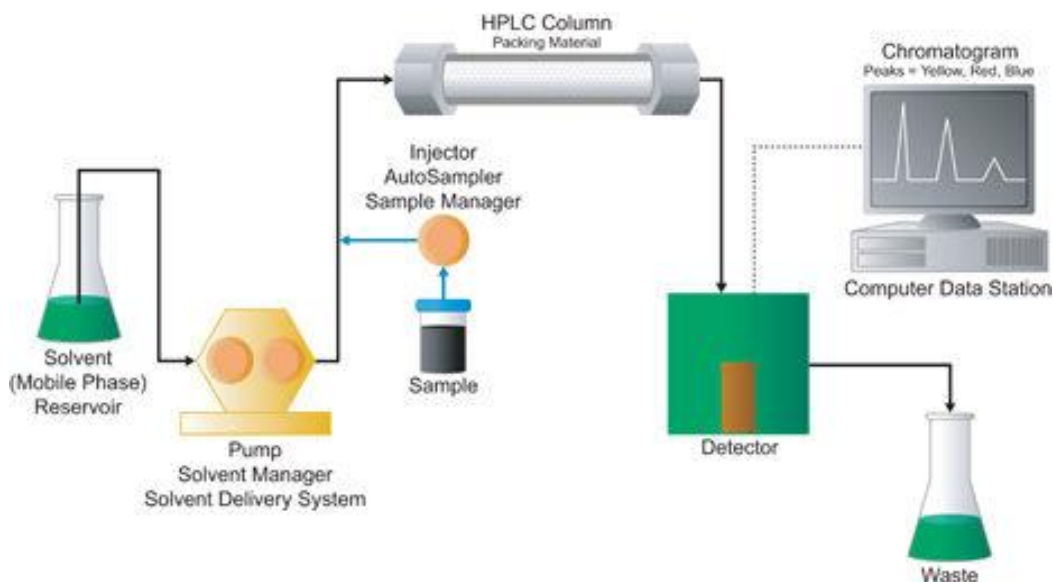


**Figure 6.4** – Schematic illustration of the primary components of an HPLC system

### 6.2.5 Multiscale Modelling of Hydrogel Tribological Performance

This dissertation relied on a combination of theoretical and experimental approaches to examine links between material structure, properties, and function. Analytical models are valuable tools for defining constitutive relations which allow investigators to predict mechanical/tribological behavior given measurable material properties. The use of analytical models with complementary experiments is often necessary to validate a mechanistic postulate or examine a hypothesis that is either impractical or impossible to investigate solely with experimental measures. An example is the use of indentation tests and Hertzian biphasic theory to determine the effect of the boundary lubricant on the hydrogel's ability to provide interstitial fluid load support. Given the geometric complexity of in vivo conditions, biphasic materials such as articular cartilage and hydrogels are often modelled using finite element analysis.

Accurate characterization of experimentally measured material properties such as permeability, contact modulus, boundary lubricant diffusive kinetics, and coefficient of friction is expected to enhance the development and validation of more accurate biphasic constitutive laws

and finite element models. These analytical tools would allow investigators to validate many of the hypotheses developed in this dissertation and would also be a valuable tool for the design and optimization of self-replenishing lubrication systems. Such an investigation would be of great interest to the readership of the *Journal of the Mechanics and Physics of Solids* or the *Journal of Applied Mechanics*.

#### *6.2.6 Mechanically and Tribologically Enhanced Low Friction, Low Fouling Nanofibrous Composites*

As noted in Chapter 5, in addition to being an excellent boundary lubricant, zwitterionic polymers also have low fouling and antimicrobial properties due to their superhydrophilicity. PMEDSAH inherently does not have suitable mechanical properties for most practical applications. A recent report by Lalani and Liu demonstrated that water stable electrospun PMEDSAH could be prepared via a relatively labor-intensive process relying on UV crosslinking following electrospinning. The resulting materials showed great potential for use as a superabsorbent, low fouling, antimicrobial wound dressing.

The investigation described in Chapter 5 demonstrated that mechanical properties of a neat TPU and enhanced toughness can be achieved through the fabrication of composite fiber mat consisting of boundary lubricant and TPU. These fiber mats also displayed the effects of surface bound PMEDSAH as evidenced by the significant reduction in coefficient of friction compared to the neat TPU. This motivates investigation into the effectiveness of these fabrication methods on improving resistance TPU's towards biofouling. Such investigations could support the design of novel wound dressings and cardiovascular stent coatings and would be of great interest to the readership of *Biomacromolecules*

### *6.2.7 Continuum Modelling of Low Friction, Low Fouling Nanofibrous Composites*

The composite material fabrication method described in Chapter 5 shows great potential for use in the repair of low friction fibrous tissue such as the Achilles tendon or rotator cuff. While Pellethane lacks suitable mechanical strength for such applications, the versatile fabrication method developed in Chapter 5 is compatible with alternative TPU's with higher Young's modulus such as PCL. Tensile strength could be improved further through the addition of more rigid thermoplastics such as PLA. Although analysis of experimental results within the context of linear models such as Young's modulus are often suitable for characterizing the effects of processing parameters on material performance, the finite deformation, anisotropy and nonlinearity of natural tissue can be more accurately described through the implementation of continuum models. Use of exact models is also ideal for comparison between composite fibermats and natural tissue benchmarks. Such models are also expected to be useful for optimizing mechanical properties as well as predicting time dependent properties of biodegradable scaffolds. Such an investigation could be achieved through the integration tensile experiments involving measurement of longitudinal and transverse deformation with a hyperelastic constrained mixture model.

## APPENDIX A: DESIGN OF A PIN ON DISC TRIBOMETER FOR SURFACE WEAR CHARACTERIZATION

### A.1 Introduction

A custom tribometer capable of measuring friction in a pin on disc test configuration was designed and fabricated to support characterization of the self-replenishing boundary lubrication mechanism described in Chapters 2, 3, and 6. The design was subject to four specific design requirements: (1) force controlled loading, (2) 1D reciprocating motion, (3) supports testing in a fluid bath, and (4) accurate measurement of coefficient of friction. The resulting design is illustrated in Figure A.1.

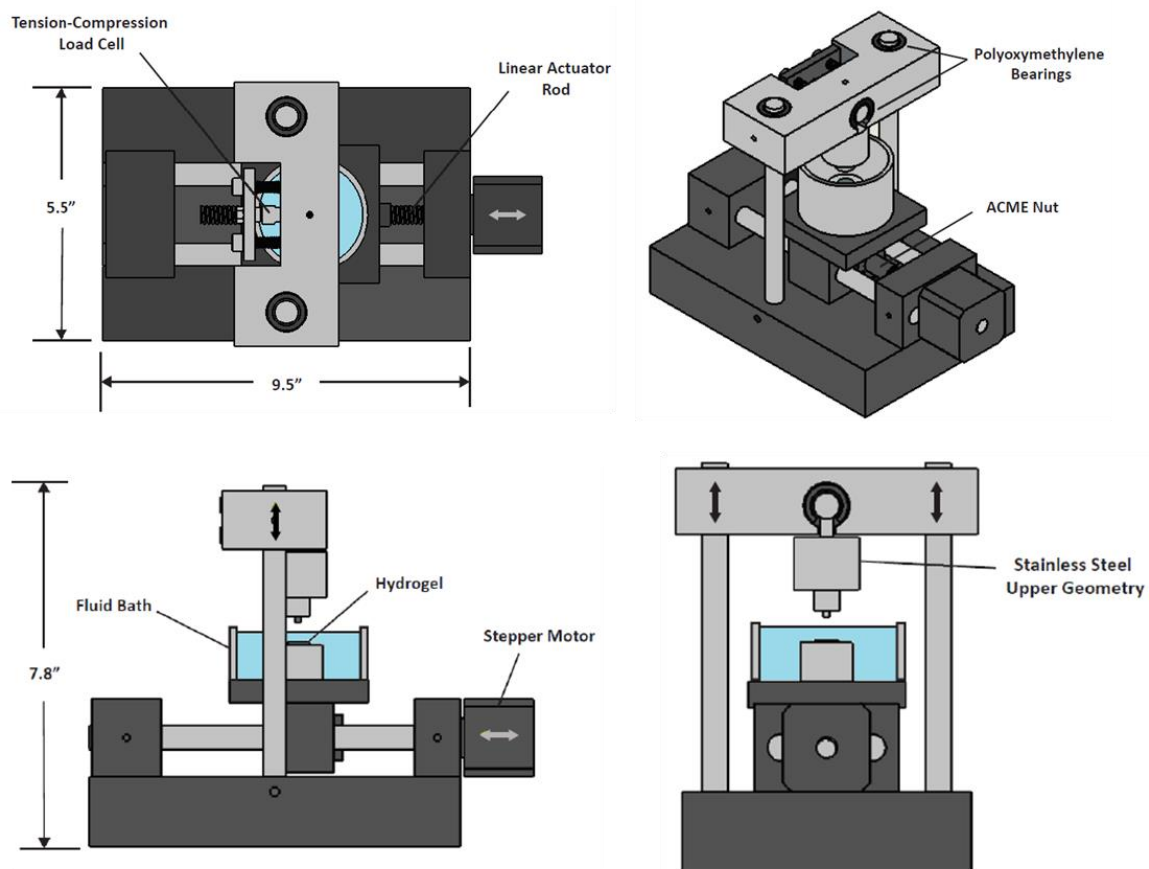


Figure A.1 – Custom designed electromechanical 1D reciprocating pin on disc tribometer

## A.2 Position Control

Reciprocating motion is driven with a Nanotec linear actuator driven by a stepper motor (Nanotec Inc, Stoneham, MA). Control of the stepper motor was achieved with a BeagleBone Black single board microcomputer (Texas Instruments Inc., Dallas, TX) running MachineKit on a Linux-based OS. MachineKit is an open-source platform designed for control of CNC machines. The G code used to control reciprocating motion is provided below:

```
#1 = 0; Defines initial value for counter variable
G21; Defines coordinates in millimeters
G90; Enables absolute position comands instead of relative
G40; Cut radius compensation off
G64; Constant velocity
G94; Feed rate units [mm/min]
F100; Feed rate = 100 mm/min
O101 WHILE [#1 LT 100]; While #1 < 100...
G1 X 4; Move to X = 4
G1 X-4; Move to X = -4
#1 = [#1+1]; Increases counter variable by 1
O101 ENDWHILE; End while loop
M2; End program
```

The upper geometry illustrated in Figure A.1 provides force controlled loading as a dead weight. The applied load can be increased by placing weights on top of the support block which is attached to upper geometry. The interface between the upper geometry and the support block is threaded to support a variety up test configurations including stainless steel on hydrogel, hydrogel on hydrogel, or cartilage on hydrogel experiments (Figure A.2). The fluid bath was prepared with a transparent polycarbonate tube so that surface wear could be monitored throughout a given experiment. Vertical position can be monitored with an I-series laser displacement sensor



(Keyence Corp, Osaka, Japan) mounted on the support block. The addition of a vertical displacement sensor allows for measurement of creep and surface wear.

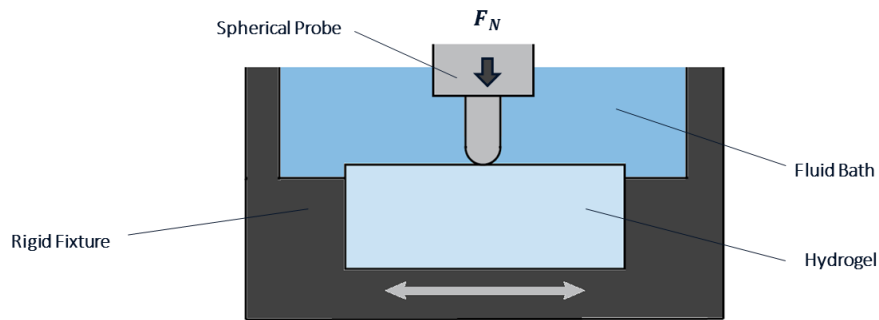


**Figure A.2** – Example pin on disc test configuration supported by the tribometer

### A.3 Force Transduction

To monitor coefficient of friction, measurement of the tangential force between the upper and lower geometry was necessary. This was achieved by coupling the upper geometry with a 20N XFTC300 tension-compression load cell (TE Connectivity Ltd., Schaffhausen, Switzerland). The coupling was designed to isolate the load cell from normal forces. The load cell is designed to operate as a 1D displacement transducer. When the load cell is subjected to an axial load, the change in distance between an opposing set of electrodes changes resulting in a change in resistance which is reflected in the measured voltage. Full scale loading corresponds to a voltage of 5 V.

#### A.4 Load Cell Calibration

Friction force calibration was achieved by rotating the tribometer by 90° and suspending weights from the upper geometry (Figure A.3). Results revealed that tangential forces lower than 1 N go undetected by the load cell due to static friction (Figure A.4). The force transduction assembly also displayed a linear relationship between measured force and applied force ( $R^2 = 0.985$ ). The effects of cross talk were assessed by placing weights on the upper support block while monitoring the measured force under static conditions. Results indicate that cross talk accounts for about 6% of the force read by the load cell.

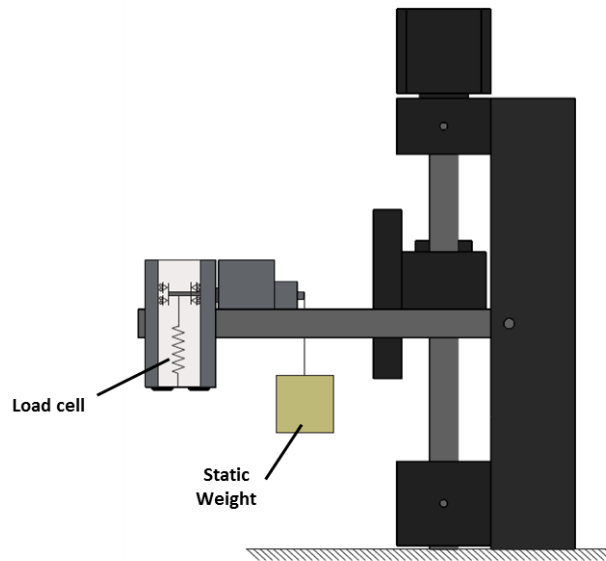


**Figure A.3** – Test configuration used for friction force load cell calibration

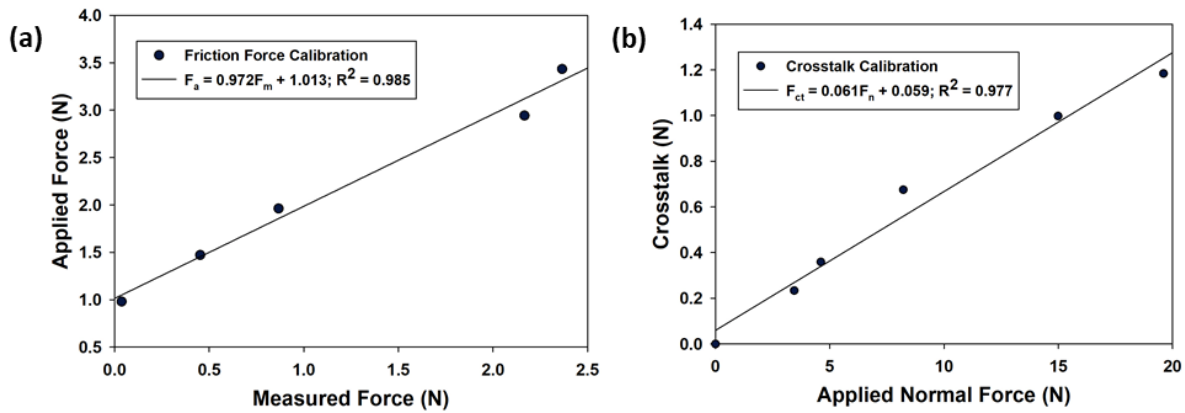


**Figure A.4** – Representative results from (a) friction force and (b) crosstalk calibration

### A.5 Friction Force Measurement

Once friction force transduction and crosstalk have been calibrated, friction force measurements can be performed by loading a sample and running the position control script assuming a given wear track length, sliding speed, and number of cycles. A representative friction force versus time trace for a spherical stainless-steel tip against a 40 wt% neat PVA hydrogel is provided in Figure A.5.

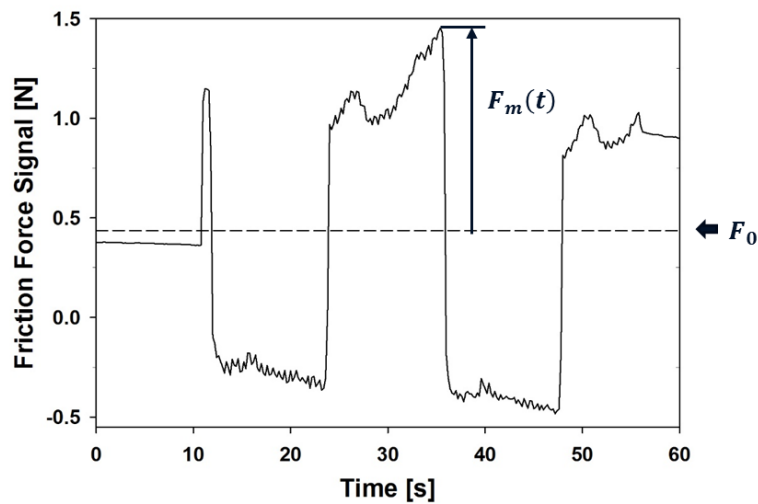


**Figure A.5** – Representative friction force vs time trace for a stainless steel spherical indenter tip articulating against a neat PVA hydrogel in DI water

Given  $F_a$ , obtained through the friction force calibration, and  $F_{ct}$ , obtained through crosstalk calibration friction force,  $F_f$ , can be measured using equation A.1. The average friction force for a given period of time can be calculated using equation A.2.

$$F_f = F_a - F_{ct} \quad (\text{A.1})$$

$$\bar{F}_f = \frac{1}{n} \sum_{t=0}^n \sqrt{(F_f(t) - F_0)^2} \quad (\text{A.2})$$

## APPENDIX B: DESIGN OF A SIX DEGREE OF FREEDOM TRIBOMETER FOR SURFACE WEAR CHARACTERIZATION

### B.1 Introduction

The hydrogels described in this dissertation show great potential for the repair of focal chondral defects in the tibiofemoral (knee) joint. One shortcoming of the experimental test methods described in this investigation is that they fail to capture the complex kinematic of *in vivo* articulating surfaces. Previous investigations have demonstrated that biomimetic rolling and sliding motions observed in *vivo* result in unique wear characteristic which are not observed in 1D experiments [246,247]. This section describes the design of a versatile & relatively simple device capable of replicating the kinematics of the human tibiofemoral joint in a physiologically relevant environment. The tribometer has been designed to support characterization of the tribological response of natural and synthetic constructs, such as articular cartilage, synthetic hydrogels, and tissue engineering scaffolds.

### B.2 Description of Motion

The three-dimensional range of motion of the tibiofemoral joint has previously been characterized by LaFortune et al [248]. Their study of on kinematics of human tibiofemoral joint during walking provides position vs. time data for six degrees of freedom (three translational axes of motion, and three rotational axes of motion). The subjects were reported to have walked at a mean speed of 1.2 m/s. Graphical results from their gait analysis were inputted into SolidWorks so that the position, velocity and acceleration range could be calculated via interpolation. The

calculated position, velocity, and acceleration ranges of the tibiofemoral joint are presented in Table B.1.

Motion of the custom designed tribometer is driven by a combination of stepper motors, linear actuators, optical encoders, and digital controllers. The remainder of this section will describe the mechanisms which provide control over the six degrees of freedom.

**Table B.1** - Calculated position, velocity, and acceleration range of the tibiofemoral joint during walking

Axis	Position Range		Velocity Range		Acceleration Range		Anatomical Motion
	deg	mm	rad/s	mm/s	rad/s <sup>2</sup>	mm/s <sup>2</sup>	
Xr	25		1.41		16.4		Adduction/Abduction
Yr	68		7.16		55.3		Extension/Flexion
Zr	18		1.16		10.7		Internal/External
Xt		19		111.3		840	Anterior/Posterior
Yt		12		78.6		1100	Lateral/Medial
Zt		18		51.6		560	Compression/Distractio

### *B2.1 Anterior-posterior and medial-lateral displacement*

Figure B.1 illustrates the upper assembly supporting anterior-posterior and medial-lateral displacement control (x-y translation). The upper portion of the machine was mounted to a set of rails which were attached to a support frame such that the upper test material can translate across the surface of the lower test material along two orthogonal axes. For each axis, a single stepper motor was mounted to the support frame and coupled with a 5mm pitch linear actuator. The device was designed to have a 25 mm range of translation along both axes.

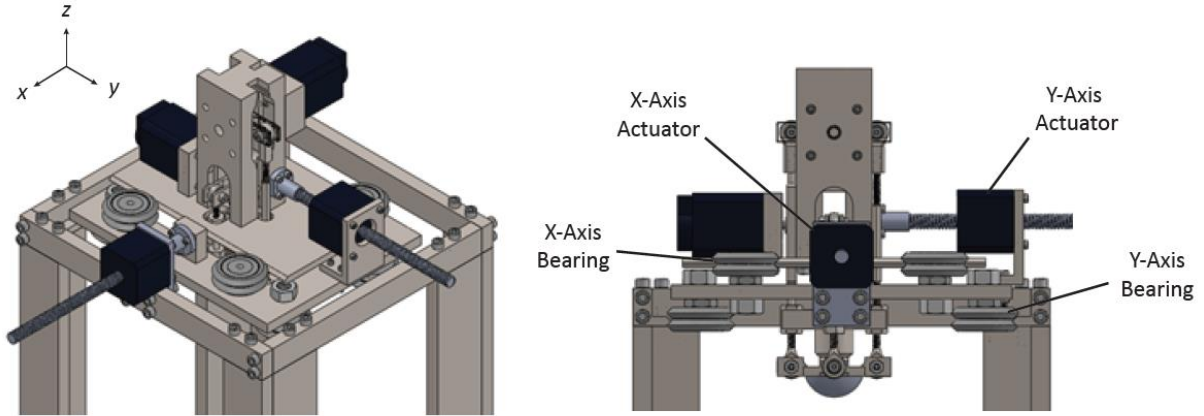


**Figure B.1** - Upper assembly supporting anterior-posterior and medial-lateral displacement control

### *B2.2 Flexion-extension and adduction-abduction*

Figure B.2 illustrates a detail of the assembly which provides control over flexion-extension and valgus-varus motion (rotation about the x and y axes). The upper articulating geometry is attached to a rotator plate which is held against a spherical bearing via two pairs of control arms. Each pair of control arms was coupled with a single stepper motor. This configuration allows the stepper motors mounted on the upper tower to drive rotation about their respective axis. This design supports rotation as high as  $35^\circ$  relative to the x-y plane.

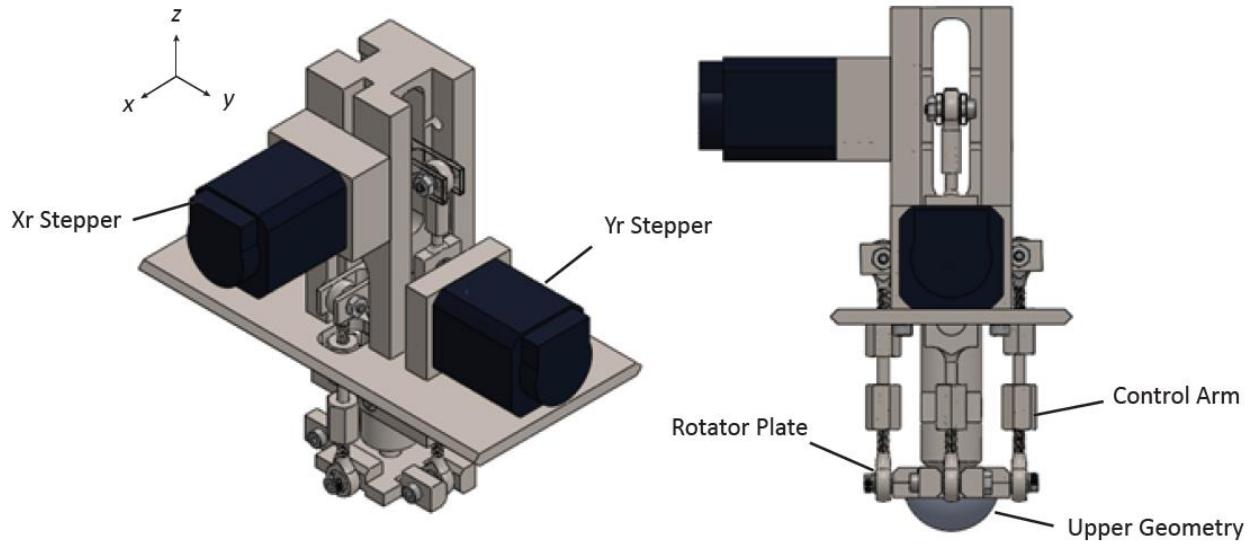


**Figure B.2** - Detail of flexion-extension and valgus-varus motion control assembly

### *B2.3 Distraction-compression*

As illustrated in Figure B.3, the base of the test material tray rests on two pairs of inclined planes. These opposing units are denoted as the upper wedge set and the lower wedge plates. The inclines on these wedge plates were each machined to 45 degrees. Each sliding surface of the vertical slider assembly was lined with strips of PTFE to minimize friction. As the lower wedge plate is driven by the z-axis actuator, the upper wedge plate is driven along the z axis providing distraction and compression motion. The absolute range of motion for this degree of freedom is 30 mm. Actuation of the base with this method provides lateral stability as the opposing surface translates across it and a mechanical advantage of 1.4.



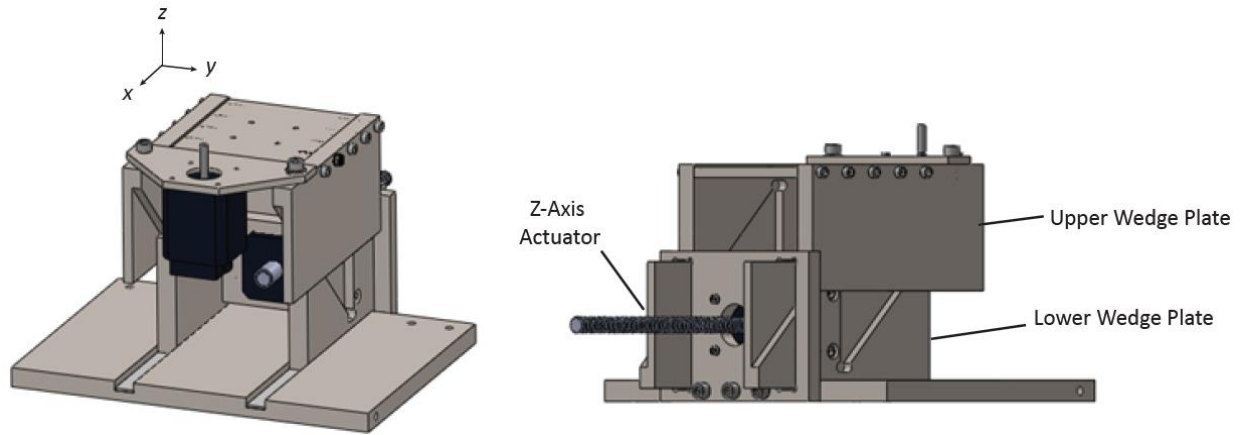


**Figure B.3** - Detail of vertical displacement control system

#### B2.4 Internal-external rotation

Internal-external rotation is driven by a gear train as shown in Figure B.4. Smooth motion with minimal friction is achieved via a slewing ring bearing assembly as illustrated in the exploded view in Figure B.4. The use of a gear train provides a mechanical advantage of 1.9.

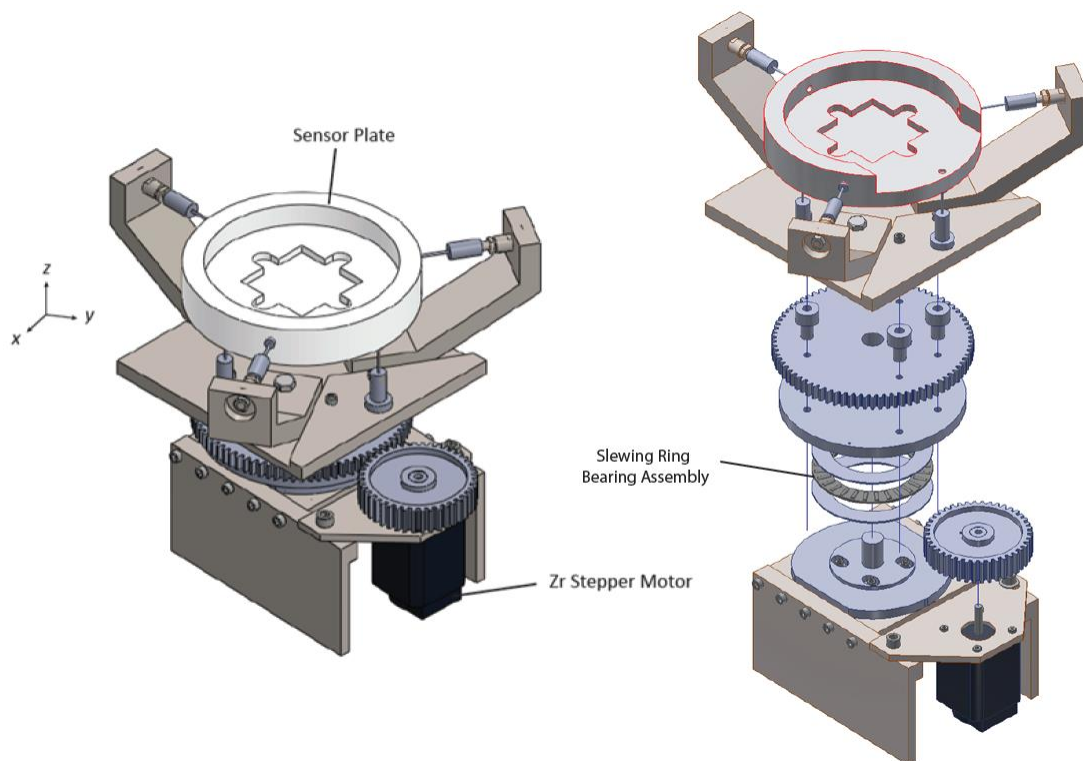


**Figure B.4** - Assembled and exploded view of the internal-external rotation system

### B2.6 Stepper Motor Selection.

The stepper motors and linear actuators were sized based on component inertia and the anticipated normal and tangential forces. SolidWorks was used to compute the moment of inertia for rotating parts, and the weight of translating parts. The software enables simple computation of moments of inertia and component mass based on the geometry and material properties. Given the equivalent rotational inertia and maximum angular acceleration for each of the axes, a torque value needed to actuate the device with zero friction force was calculated. Datasheets for the stepper motor include the maximum holding torque, the dynamic torque as a function of rotational speed, and power consumed allowing us to select the appropriate stepper motor for each motion axis. A maximum friction coefficient was then calculated assuming the stepper motor met performance standards set by the manufacturer.

**Table B.2** – Stepper motor capacity and Nanotec part number for each degree of freedom

Axis	Max COF	Actuator	Capacity
Xr	0.392	ST4118D1804	0.8 Nm
Yr	0.34	ST4118D1804	0.8 Nm
Zr	0.165	ST4118D1804	0.8 Nm
Xt	>1	LS4118S1404-T5x5	120 N
Yt	>1	LS4118S1404-T5x5	120 N
Zt	N/A	L4118L1804-T6x1	450 N

### B.3 Digital Motion Control

A block diagram of the custom designed and fabricated digital and power electronics for the tribometer is provided in Figure B.5. Control of stepper motors and motion was accomplished with a BeagleBone Black single board microcomputer (Texas Instruments Inc., Dallas, TX) running MachineKit on a Linux-based OS. MachineKit is an open-source platform designed for control of CNC machines with up to 9 axes of motion.

Given the cyclic nature of the motion profiles associated with the kinematic of the tibiofemoral joint, functions describing the interpolated motion profiles for each degree of freedom were obtained via Fourier series approximations given by:

$$f(t) = \frac{1}{2}a_0 + \sum_{n=1}^{\infty} a_n \cos(nwt) + b_n \sin(nwt) \quad (B.1)$$

Fourier series representation of the motion profile for each degree of freedom are illustrated in Figure B.6 and the Fourier coefficients are presented in Table B.3. The position of each axis was recorded via 4000 count-per-revolution optical encoders. Non-contact infrared limit switches were used as a safety feature as well as a means for calibrating the zero-location of each axis prior to running an experiment. The entire motion control system was powered by a CX500 Power supply (Corsair Components, Inc, Fremont, CA).

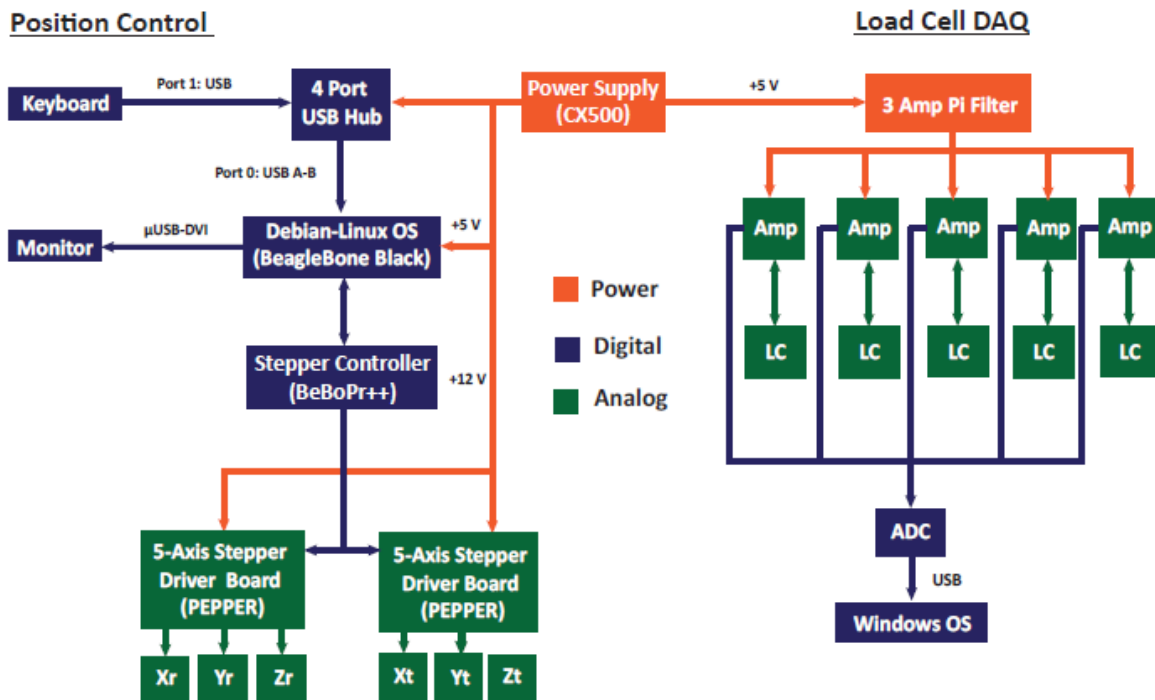


**Figure B.5** - Block diagram illustrating component involved in position control and load cell data acquisition

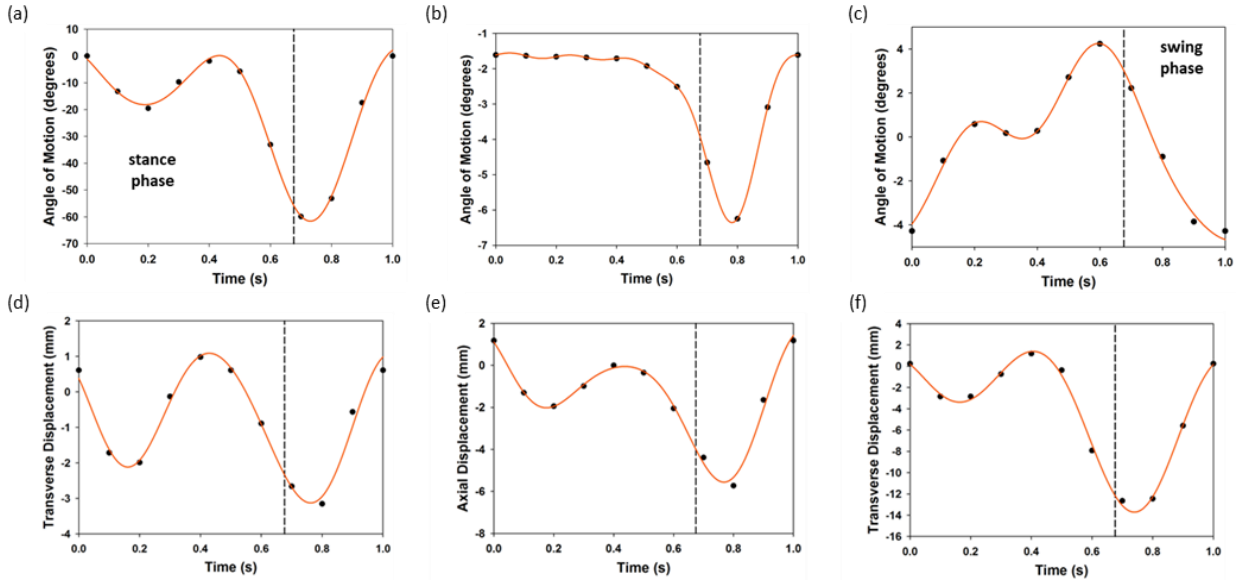


**Figure B.6** - Interpolated experimental data and Fourier series representation of the kinematics of the human tibiofemoral joint during a single gait cycle for (a) flexion-extension, (b) abduction-adduction, (c) internal-external rotation, (d) medial-lateral displacement, (e) compression-distraction, and (f) anterior-posterior displacement

**Table B.3** - Calculated position, velocity, and acceleration range of the tibiofemoral joint during walking

Anatomical Motion	Fourier Coefficients											
	$a_0$	$a_1$	$b_1$	$a_2$	$b_2$	$a_3$	$b_3$	$a_4$	$b_4$	$a_5$	$b_5$	$w$
Abduction/Adduction	-2.576	0.588	1.49	0.8975	-0.6285	-0.4243	-0.4619	-0.2211	0.2414	0.1246	0.1039	5.712
Internal/External	-0.3777	-3.338	0.8862	0.3229	1.586	-0.5661	-0.2322	0	0	0	0	5.714
Flexion/Extension	-19.42	10.85	15.61	10.18	-17.74	-2.782	-0.05416	0	0	0	0	5.715
Medial/Lateral	-0.7558	0.06616	0.6616	0.9457	-1.51	0.1248	-0.2818	0	0	0	0	5.721
Anterior/Posterior	-3.972	2.17	4.543	2.167	-3.975	-0.1805	-0.2336	0	0	0	0	5.711
Compression/Distraction	-1.458	1.027	1.259	1.572	-1.628	-0.03653	-0.5537	0	0	0	0	5.716

## B.4 Force Transduction

Force transduction was achieved through an array of model XFTC300 series tension-compression load cells (TE Connectivity Ltd., Schaffhausen, Switzerland). Accurate measurement of forces in three orthogonal directions requires a total of five load cells, three arranged symmetrically around the diameter of the sensing platform, and two below the base of the platform.

These units support accurate measurement of normal and tangential forces between a pair of articulating surfaces.

The manufacturers provide two measures of accuracy for the model XFTC300 load cells, linearity and hysteresis, both of which have a specified accuracy of  $\leq \pm 0.5\%$  full scale (F.S.). Articular cartilage in the human tibiofemoral joint has been reported to be subjected to an average pressure of about 700 kPa with peak pressures reaching just over 2 MPa and coefficient of friction as low as 0.001 [10-12]. To replicate the pressures experienced in the knee joint, 50 N capacity load cells were selected for measurement of normal force. 20 N capacity load cells were selected for tangential force measurement. A lower capacity load cell may also be used in place of 20 N capacity load cells for increased resolution with very low friction interfaces.

#### *B4.1 Load Cell Platform*

The load cell platform as shown in Figures B.7 uses three load cells laterally spaced at  $120^\circ$  to measure both X and Y forces, as well as two load cells and a dummy cell on the bottom to measure Z force. Each load cell is mounted in such a way as to prevent off-axis loading, and to allow zeroing of force under unloaded conditions.

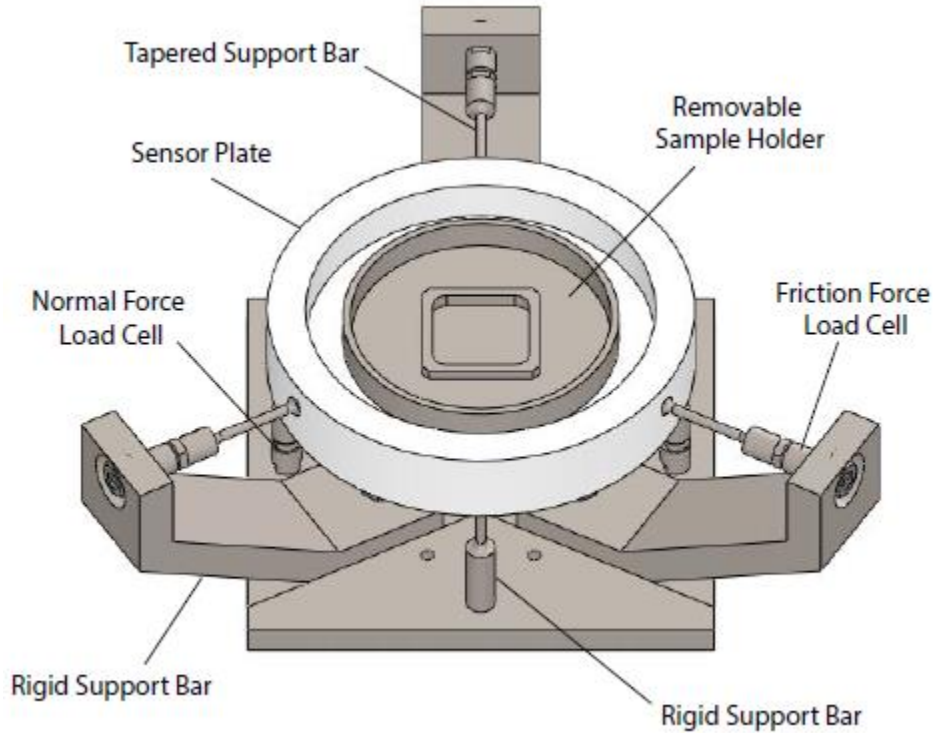


**Figure B.7** – Sensor plate design

#### *B4.2 Load Cell Data Acquisition*

Load cells were connected to Dataforth SCM5B modules (Dataforth Corp. Tucson, AZ), which received power from a custom-designed pi filter designed to improve signal integrity. The output of each module was connected to a Measurement Computing USB-1608FS DAQ unit (Measurement Computing Corp., Norton, MA), containing 8 separate SAR ADCs for simultaneous sampling at up to 250kHz and 16 bits. Data logging was achieved through a LabVIEW virtual instrument which records the data in TDMS format to reduce file size. While data is typically captured at around 100Hz, the ADCs are capable of much higher speed operation; this allows for super-sampling which increases the resolution to an effective 20 bits and significantly decreases noise.

### B4.3 Load Cell Calibration

A portion of the applied forces act to strain the support structure of the system in addition to the load cells themselves. Calibration of the normal force measurement system was achieved with proof masses and static force analysis. To do this, proof masses were balanced on a rigid pin which was fastened to center of the sensor plate (Figure B.8). This method allows us to easily align the center of mass with the center of the sensor plate. Masses ranging from 700 – 2150 g were used to create a calibration curve for the sensor plate.

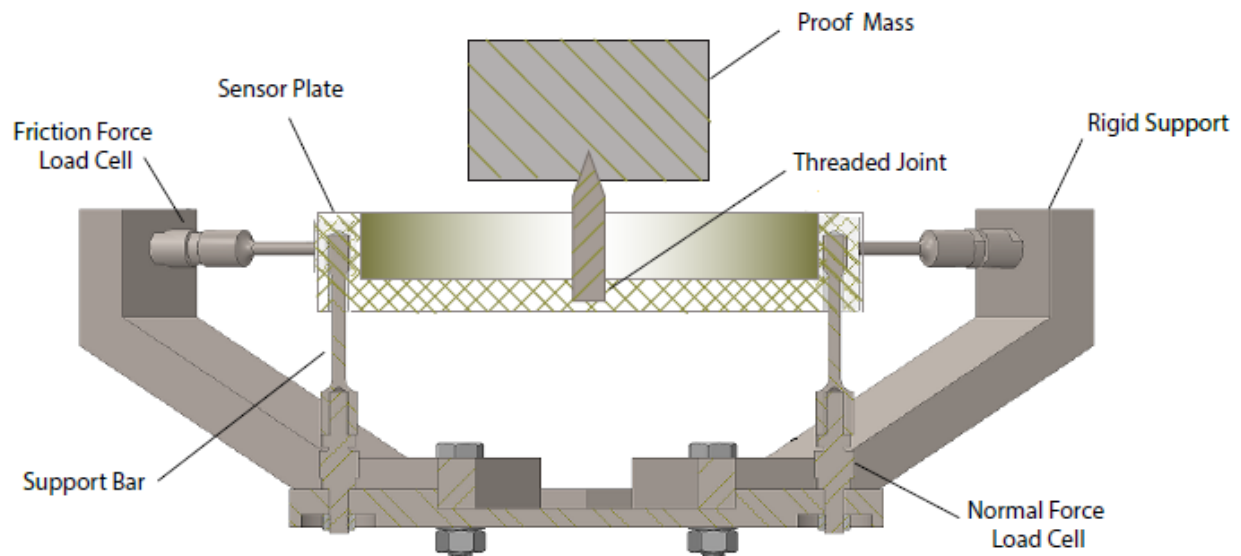


**Figure B.8** - Normal force load cell calibration detail

Calibration of the tangential load cells was achieved via a similar method, shown in Figure B.9. An external load cell was used to apply a known force on the sensor platform coincident with the line of action of the installed load cell. The force readout of the external load cell was then plotted against the force readout of the load cell connected to the sensor plate and a calibration curve was formulated.

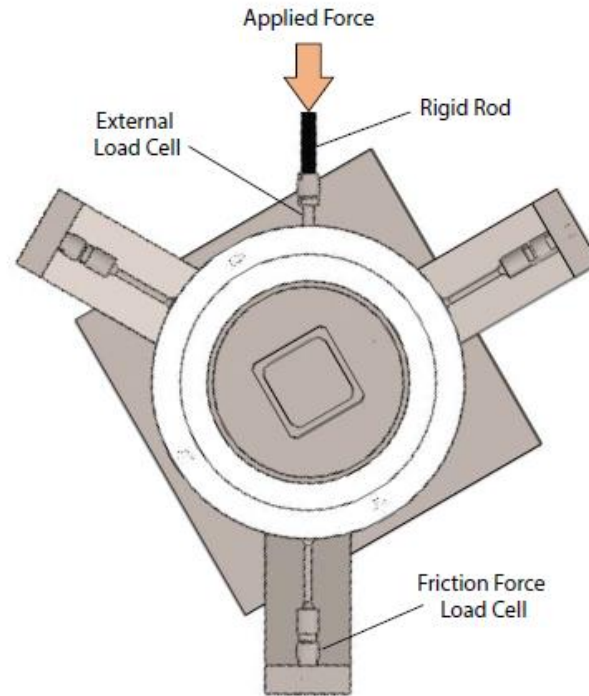


**Figure B.9** - Friction force load cell calibration detail

Crosstalk between multiple-axis sensor measurements occurs when the two or more sensors are not completely mechanically isolated from one another. Thus, a change in one sensor corresponds with a false change in the other. To address this concern, crosstalk was quantified between the normal and friction force load cell output.

#### *B4.4 Force Transduction Characterization Results*

The response of the normal force load cells was quite linear. The linear curve fit with of both loads cells yielded  $R^2 \cong 1$ . Figure B.10a provides a representative calibration curve. Tangential load response was also quite linear with  $R^2 = 0.980$ . A representative calibration curve is illustrated in Figure B.10b. Crosstalk was found to cause a false change in the friction force



reading by about 7% of the applied normal force. A representative calibration curve is illustrated in Figure B.10c.

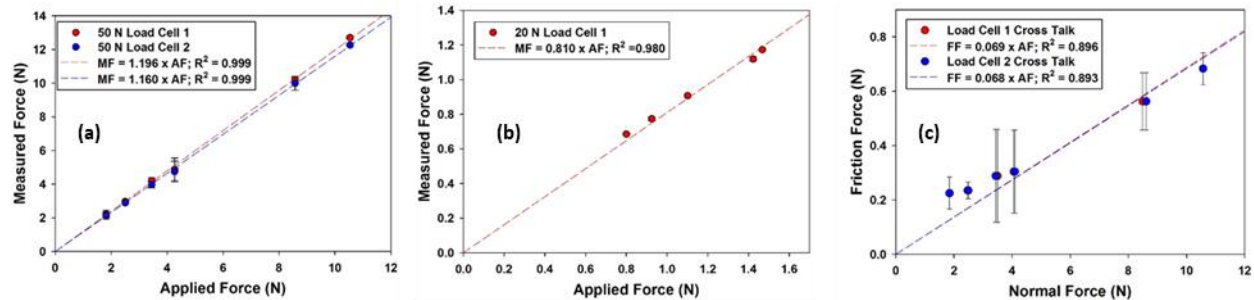


**Figure B.10** – Representative results from (a) normal, (b) tangential, and (c) crosstalk characterization

## B.5 Conclusion

A six axis tribometer was designed to replicate the kinematics of articulating surfaces in human tibiofemoral joints. CNC software coupled with stepper motors were used to control motion. An embedded control system supports control of all six degrees of freedom. Motion tracking can be achieved via optical encoder outputs. Measurement of force in three orthogonal axes is provided using tension compression load cells and LabVIEW software. The load cells were calibrated individually and with respect to each other.

The design is such that a variety of tests configurations are supported, using any combination of axes and arbitrary motion profiles. Preliminary characterization of the system reveals precise motion control as well as linear force response characteristics. This tribometer supports more physiologically relevant tribological characterization of synthetic joint materials than single or dual axis tribometers. The compact nature of the tribometer and length of the motion and force transduction cables allows it to be easily transported and stored in conventional incubators. In addition, to tribological testing this device would also be useful for mechano-stimulation of tissue engineering scaffolds such as those intend for use in articular cartilage repair.

## APPENDIX C: CHARACTERIZATION OF CARTILAGE SURFACE WEAR USING HIGH PERFORMANCE LIQUID CHROMATOGRAPHY

### C.1 Introduction

Hydroxyproline is one of the three main amino acid constituents of collagen and can be measured with femtomole resolution via high performance liquid chromatography (HPLC). This technique requires the use of a pump to pass pressurized liquid mixtures through a column containing a solid absorbent material. The velocity at which of each compound passes through the column depends on the degree of its interaction with the absorbent solid. The time at which a given analyte emerges from the column is referred to as the retention time. The emergence of a given analyte is detected via an UV absorbance detector. Compounds of interest can be chemically “marked” through a process known as derivatization. The method outlined in this section is inspired by previously described methods presented by Hustson et al [245] and McGann et al [249].

### C.2 Materials

Hydroxyproline, sarcosine, hydrogen chloride, sodium acetate, sodium monophosphate, o-phthalaldehyde, iodocetamide, 9-fluorenylmethylchloroformate (FMOC), boric acid, sodium hydroxide,  $\beta$ -mercaptoethanol, ethyl ether, acetonitrile, and glacial acetic acid all reagent grade were obtained from Sigma Aldrich, (Milwaukee, WI, USA). Acetone was obtained from Fisher scientific (Hampton, NH, USA).

### C.3 Calibration Curve

1. Prepare stock solution of 2 mM hydroxyproline then dilute to get 25, 50, 100, 250, 500, 750, and 1000  $\mu\text{M}$  standards in water (total volume for each level = 900  $\mu\text{L}$ )
2. Add 11.3  $\mu\text{L}$  of 2 mM sarcosine to each 900  $\mu\text{L}$  sample of hydroxyproline standard
3. Run standards in triplicate

### C.4 Wear Particle Extraction:

1. Following wear tests, place hydrating fluid in  $-80\text{ }^{\circ}\text{C}$  freezer for 24 h and then lyophilize at  $-40\text{ }^{\circ}\text{C}$  for 48 h
2. Seal resulting material in glass vial with 6 M HCl and hydrolyze for 18 h at  $110\text{ }^{\circ}\text{C}$  and then dry via rotovap.
3. Dissolve dried hydrolystates in water and then filter through 0.22  $\mu\text{m}$  pore size syringe filter
4. Add 11.3  $\mu\text{L}$  of 2mM sarcosine to each 900  $\mu\text{L}$  aliquot of filtered solution

### C.5 Derivatization

1. Transfer 900  $\mu\text{L}$  aliquots to 5 mL glass vials followed by addition of 200  $\mu\text{L}$  of borate buffer (0.7 M boric acid, pH 9.5, with NaOH)
2. Add 100  $\mu\text{L}$  of OPA solution (50 mg o-phthalaldehyde dissolved in 1 mL acetonitrile containing 26  $\mu\text{L}$  of  $\beta$ -mercaptoethanol)
3. 60 s later add 100  $\mu\text{L}$  iodoacetamide reagent (140 mg/mL of iodoacetamide in acetonitrile)
4. One minute later add 300  $\mu\text{L}$  of 5 mM FMOC in acetone
5. Cap and vortex reaction vial between each addition of reagent.
6. One minute after addition of FMOC reagent add 2 mL ethyl ether
7. Shake vial vigorously for 30 s to wash the contents of the vial
8. Discard organic layer and repeat wash twice more for a total of three washes

## C.6 High-Performance Liquid Chromatography Measurement

1. Inject 50  $\mu\text{L}$  of remaining aqueous phase into HPLC
2. Injections should be made every 30 min without an intervening wash
3. Separation can be achieved with a C-18 column
4. Pump mobile phase at a constant rate of 1 mL/min
5. Degree of cartilage wear can be estimated from the concentration of hydroxyproline

## APPENDIX D: USE OF TRIBOLOGICALLY ENHANCED HYDROGELS FOR REPAIR OF FOCAL CHONDRAL DEFECTS

### D.1 Introduction

Review of current treatment modalities for articular cartilage repair reveals the need for improved solutions, especially for younger more active patients. It was postulated that tribologically enhanced hydrogels such as the ones described in this investigation display great potential for the repair of focal chondral defects in the tibiofemoral (knee) joint. In addition to characterizing the tribological behavior of these hydrogels, it is important to investigate their ability to maintain biomechanical stability within the joint following implantation. It was postulated that PVA hydrogels with compressive properties on the order of what has been reported for natural tissue would successfully fulfil this function. To investigate this hypothesis, 15 mm tall freeze thaw PVA hydrogel plugs with an average compressive modulus of  $1.95 \pm 0.12$  MPa and a 3.5 cm radius of curvature were prepared. Samples were subsequently subjected to biomechanical characterization in human tibiofemoral joints. Hydrogel implantation and biomechanical testing were performed by Ronnie Sismondo, MD, Nat Ordway, MS, PE, and Fred Werner, MME, PE. from the Musculoskeletal Science Research Center (MSRC) at SUNY Upstate Medical University.

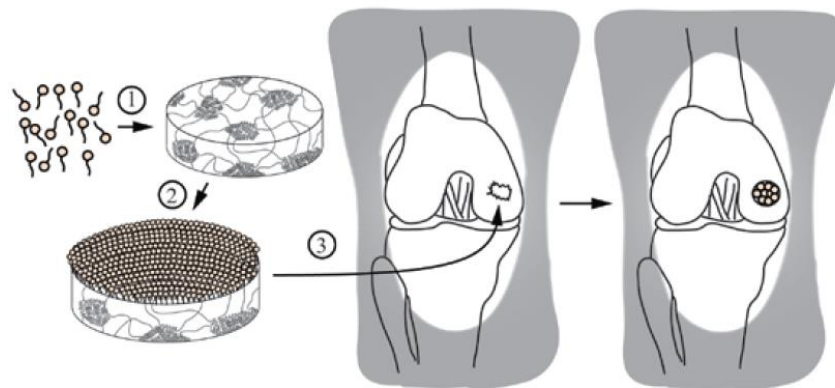


**Figure D.1** – Illustration of the proposed surgical procedure where (1) zwitterionic boundary lubricant molecules are grafted on to a hydrogel blend resulting in a (2) self-replenishing boundary lubricant enhanced material which (3) following implantation restores mechanical and tribological performance of an intact joint.

## D.2 Experimental Methods

A total of six cadaver knees were characterized in a test frame previously developed and validated by Van Valkenburg et al [250]. This device, illustrated in Figure D.2a, supports application of axial load, torque, anterior-posterior loading and knee flexion load profiles. Contact pressures between the articulating surfaces were measured with a Tekscan 4400 dynamic pressure sensor (Tekscan Inc., Boston, MA) connected to the medial tibial plateau. Contact pressures were measured during six cycles of a dynamic gait cycle as well as static axial loading at 30 degrees of flexion. Contact pressure measurements were recorded with intact knees, following coring of the medial femoral condyle, and after implantation of the hydrogel plug. Hydrogels were designed to be oversized in diameter so that they could be implanted via a press fit. The surface of the gel typically protruded by about 1 mm relative to the surrounding cartilage as illustrated in Figure D.2b. Following contact pressure measurements, the sensor was removed and knees were subjected to 1,000 cycles of the dynamic gait to qualitatively characterize hydrogel plug fixation.

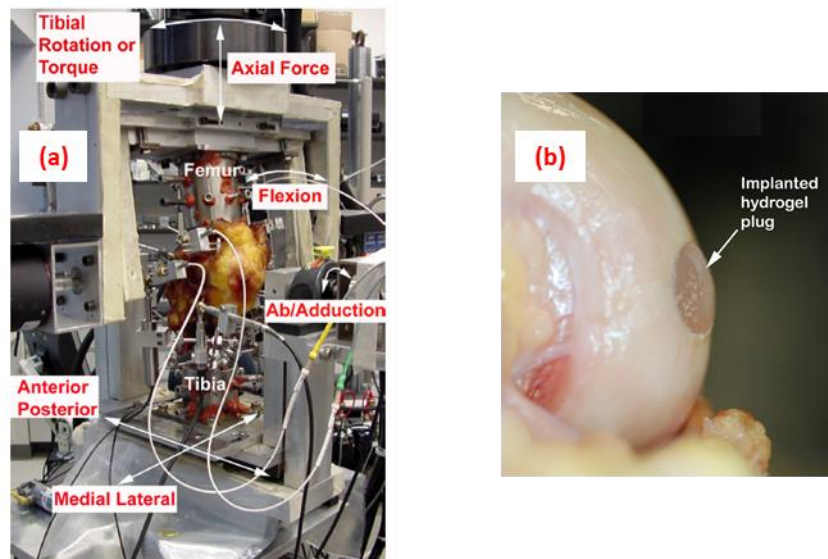


**Figure D.2** – Photograph of (a) the experimental test setup used for gait simulation [250] and (b) a hydrogel plug implanted in a human femoral condyle

### D.3 Results

No significant difference in the peak and average contact pressures at the implant site was observed between the intact knee and following plug implantation. The average pressure at the implant site was  $1.0 \pm 0.9$  MPa in the intact knee and  $0.8 \pm 0.3$  MPa following implantation of the hydrogel plug. The peak pressure at the hole location was  $2.0 \pm 1.5$  MPa in the intact knee and  $1.0 \pm 0.4$  MPa following plug insertion. Peak pressure over the entire contact area of the pressure sensor was  $2.0 \pm 1.4$  MPa in the intact knee,  $1.8 \pm 0.5$  MPa following osteochondral plug removal and  $1.2 \pm 0.3$  MPa after plug insertion. Following 100 cycles, the hydrogel was observed to be flush with the surrounding tissue. No surface damage or hydrogel plug loosening was observed following 1,000 cycles.

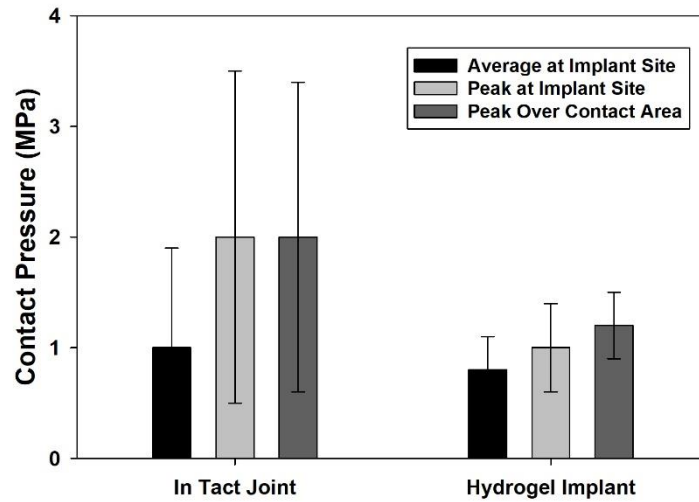


**Figure D.3** – Average contact pressures from various areas within the knee joint in intact joints compared to joints containing a hydrogel plug implant

#### **D.4 Conclusion & Future Directions**

The findings reported in this investigation support the hypothesis that tribologically enhanced hydrogel plugs can restore biomechanical function in human tibiofemoral joints. There are many challenges which need to be addressed before such approaches can become clinically viable. Additional considerations which were not addressed in this investigation include optimization of the surgical procedure *in vivo*, successful biological integration and long-term performance through fatigue testing and quantitative wear measurements. It would also be interesting to investigate the effects of hydrogel plug mechanics on joint contact pressures. While this treatment method resembles OATS, it benefits from not requiring removal of tissue from a lesser load bearing section of the joint. Overall this investigation supports the potential use of tribologically enhanced hydrogels for articular cartilage repair.



## **APPENDIX E: DESIGN OF A DEVICE FOR IN SITU CHARACTERIZATION OF DEFORMATION INDUCED CHANGES TO POLYMER MICROSTRUCTURE UNDER UNIAXIAL TENSION**

### **E.1 Introduction**

In typical engineering analysis and design solid materials are often treated as a continuum, with constitutive laws based on bulk parameters such as modulus. Material scientists are often interested in studies related to material crystal structure which describes how the atoms which make up a given material are organized. The sort and long-range order or crystal structure is typically characterized with x-ray scattering as demonstrated in this dissertation. Investigations involving material structure are of interest since these metrics are directly related to bulk material properties providing valuable fundamental structure to function relationships.

In addition to being influenced by parameters such as molecular weight and chemical structure, the molecular organization of polymers, specifically semicrystalline polymers, is understood to be influenced by deformation. For example, uniaxial stretching has been shown to induce anisotropy due to the change in polymer chain orientation [251]. Strain induced crystallization has also been shown to significantly enhance the mechanical properties of due to strain hardening. These methods are often applied when thermoplastic polymers are drawn [252,253]. Because of the unique behavior, this class of materials, there is great interest in in situ characterization of x-ray diffraction while materials are subjected to deformation induced structure transitions. This interest motivated the design of a custom device capable of supporting in situ characterization of strain induced changes in polymer crystallinity.

## E.2 Device Design

In the design of any mechanical system, simplicity is paramount. The x-ray stretcher device design described in this section was inspired by that of a turnbuckle. The design requires thin strips of polymer to be mounted on a pair of polyoxymethylene (Delrin®) blocks constrained to a pair of guide rods which support uniaxial motion. The support blocks are coupled with a shaft constructed from a left handed threaded rod bonded to a right handed threaded rod. The threaded rod is connected to an external handle which drives adduction and abduction of the blocks. The evacuated x-ray chamber is equipped with tapped holes allowing the stretcher to be easily mounted within the spectrometer. The device was also designed to have adjustable height, allowing investigators to manually position the centerline of their sample in line with the x-ray beam. Figure E.1 illustrates the device design. For remote operation of the stretcher, the external knob could be coupled with a stepper motor equipped with a digital control system like what was described in Appendix A and B.

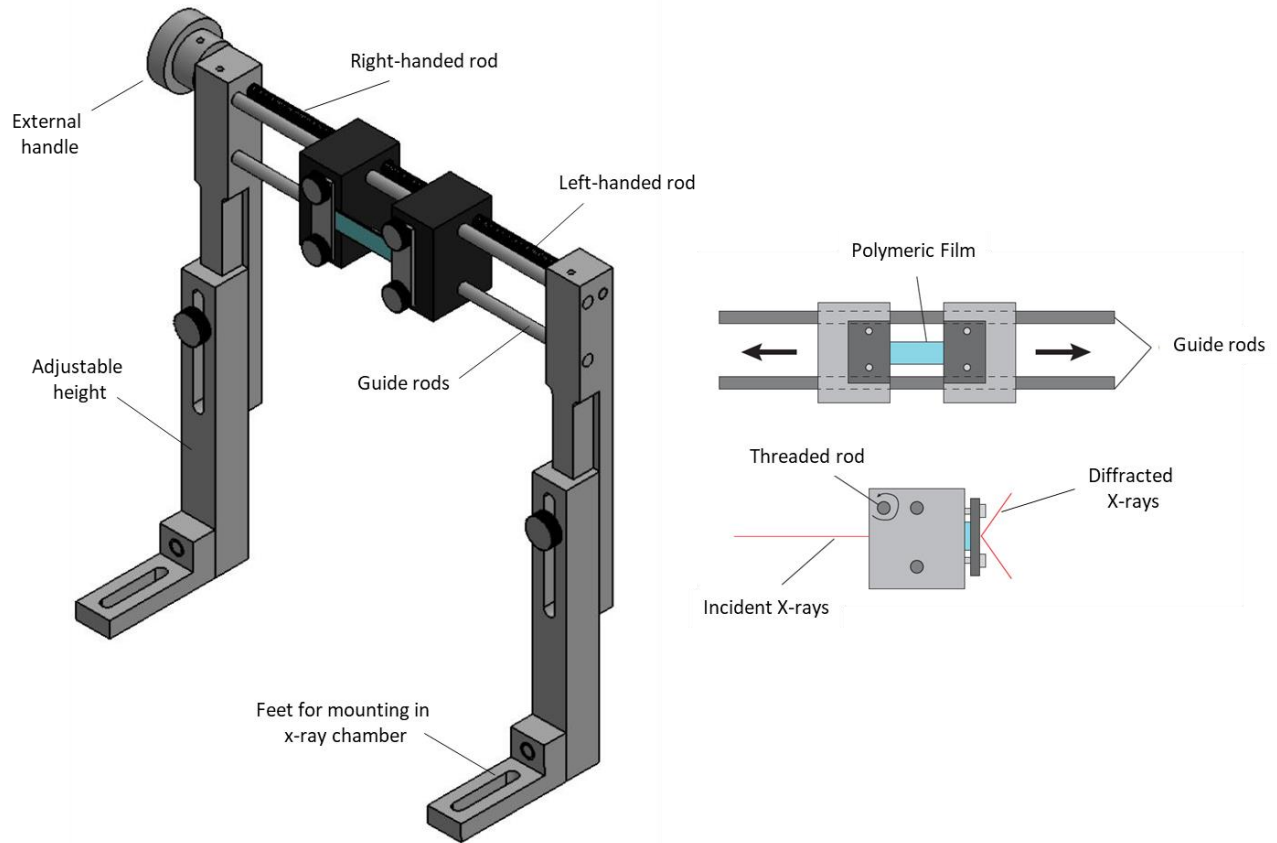


**Figure E.1** – Schematic illustration of the x-ray stretcher design

### E.3 Conclusion

This section details the design of a device suitable for in situ characterization of deformation induced crystallization. Investigations using this device are expected to be of interest to the readership of Polymer in characterization of the unique properties of novel semicrystalline polymers, polymer blends, and composites.

## REFERENCES

- [1] Bhushan B. Principles and applications of tribology. : John Wiley & Sons, 2013.
- [2] Dowson D. Bio-tribology. Faraday Discuss 2012;156:9-30.
- [3] Seror J, Zhu L, Goldberg R, Day AJ, Klein J. Supramolecular synergy in the boundary lubrication of synovial joints. Nat Commun 2015;6:6497.
- [4] Klein J. Hydration lubrication. 2013;1:1-23.
- [5] Wojnar R. Bone and cartilage—its structure and physical properties. 2010;:1-75.
- [6] Mansour JM. Biomechanics of cartilage. 2003;:66-79.
- [7] Parkes M, Myant C, Dini D, Cann P. Tribology-optimised silk protein hydrogels for articular cartilage repair. Tribol Int 2015;89:9-18.
- [8] Collagen and Your Skin's Health. 2015;2016.
- [9] Ethier CR, Simmons CA. Introductory biomechanics: from cells to organisms. : Cambridge University Press, 2007.
- [10] Buckwalter JA, Mow VC, Ratcliffe A. Restoration of injured or degenerated articular cartilage. J Am Acad Orthop Surg 1994;2:192-201.
- [11] Esko JD, Kimata K, Lindahl U. Proteoglycans and Sulfated Glycosaminoglycans. In: Varki A, Cummings RD, Esko JD, Freeze HH, Stanley P, Bertozzi CR, Hart GW, et al, editors.

Essentials of Glycobiology. 2nd ed. Cold Spring Harbor (NY): The Consortium of Glycobiology Editors, La Jolla, California, 2009.

[12] Klein TJ, Rizzi SC, Schrobback K, Reichert JC, Jeon JE, Crawford RW, Hutmacher DW. Long-term effects of hydrogel properties on human chondrocyte behavior. 2010;6:5175-5183.

[13] Ng KW, Ateshian GA, Hung CT. Zonal chondrocytes seeded in a layered agarose hydrogel create engineered cartilage with depth-dependent cellular and mechanical inhomogeneity. 2009;15:2315-2324.

[14] Mauck RL, Soltz MA, Wang CC, Wong DD, Chao PG, Valhmu WB, Hung CT, et al. Functional tissue engineering of articular cartilage through dynamic loading of chondrocyte-seeded agarose gels. J Biomech Eng 2000;122:252-260.

[15] Buckwalter JA, Mankin HJ. Articular cartilage: degeneration and osteoarthritis, repair, regeneration, and transplantation. Instr Course Lect 1998;47:487-504.

[16] Ateshian GA. The role of interstitial fluid pressurization in articular cartilage lubrication. J Biomech 2009;42:1163-1176.

[17] Hamrock BJ, Schmid SR, Jacobson BO. Fundamentals of fluid film lubrication. : CRC press, 2004.

[18] Chester VL, Calhoun M. Gait symmetry in children with autism. 2012;2012.

[19] Mow VC, Ateshian G. Lubrication and wear of diarthrodial joints. 1997;2:275-315.

- [20] Moore A, Burris D. Tribological rehydration of cartilage and its potential role in preserving joint health. 2017;25:99-107.
- [21] Mow VC, Kuei S, Lai WM, Armstrong CG. Biphasic creep and stress relaxation of articular cartilage in compression: theory and experiments. J Biomech Eng 1980;102:73-84.
- [22] McCutchen C. Animal joints and weeping lubrication. New Sci 1962;15:928-930.
- [23] Soltz MA, Ateshian GA. Experimental verification and theoretical prediction of cartilage interstitial fluid pressurization at an impermeable contact interface in confined compression. J Biomech 1998;31:927-934.
- [24] Mow VC, Ateshian GA, Spilker RL. Biomechanics of diarthrodial joints: a review of twenty years of progress. J Biomech Eng 1993;115:460-467.
- [25] Mow MC, Ling FF. On weeping lubrication theory. 1969;20:156-166.
- [26] Dowson D, Wright V, Longfield MD. Human joint lubrication. Biomed Eng 1969;4:160-165.
- [27] Walker PS, Dowson D, Longfield MD, Wright V. Lubrication of human joints. Ann Rheum Dis 1969;28:194.
- [28] Hlaváček M. The role of synovial fluid filtration by cartilage in lubrication of synovial joints—II. Squeeze-film lubrication: homogeneous filtration. J Biomech 1993;26:1151-1160.
- [29] Hlaváček M. The role of synovial fluid filtration by cartilage in lubrication of synovial joints—IV. Squeeze-film lubrication: the central film thickness for normal and inflammatory

synovial fluids for axial symmetry under high loading conditions. J Biomech 1995;28:1199-1205.

[30] Hlaváček M. Lubrication of the human ankle joint in walking with the synovial fluid filtrated by the cartilage with the surface zone worn out: steady pure sliding motion. J Biomech 1999;32:1059-1069.

[31] Hou J, Holmes M, Lai W, Mow V. Boundary conditions at the cartilage-synovial fluid interface for joint lubrication and theoretical verifications. J Biomech Eng 1989;111:78-87.

[32] Soltz MA, Basalo IM, Ateshian GA. Hydrostatic pressurization and depletion of trapped lubricant pool during creep contact of a rippled indenter against a biphasic articular cartilage layer. J Biomech Eng 2003;125:585-593.

[33] Longfield MD, Dowson D, Walker PS, Wright V. "Boosted lubrication" of human joints by fluid enrichment and entrapment. Biomed Eng 1969;4:517-522.

[34] Maroudas A. Research Report 2: Hyaluronic Acid Films. 1966;181:122-124.

[35] Walker PS, Dowson D, Longfield MD, Wright V. "Boosted lubrication" in synovial joints by fluid entrapment and enrichment. Ann Rheum Dis 1968;27:512-520.

[36] Coles JM, Blum JJ, Jay GD, Darling EM, Guilak F, Zauscher S. In situ friction measurement on murine cartilage by atomic force microscopy. J Biomech 2008;41:541-548.

[37] Raviv U, Laurat P, Klein J. Fluidity of water confined to subnanometre films. Nature 2001;413:51.

- [38] Klein J, Kumacheva E. Confinement-induced phase transitions in simple liquids. 1995;;816-816.
- [39] Ma L, Gaisinskaya-Kipnis A, Kampf N, Klein J. Origins of hydration lubrication. 2015;6:6060.
- [40] Klein J. Surface Force Balances. 2001;2016.
- [41] Ogston A, Stanier J. The physiological function of hyaluronic acid in synovial fluid; viscous, elastic and lubricant properties. J Physiol (Lond ) 1953;119:244-252.
- [42] Laurent TC, Laurent UB, Fraser JR. Functions of hyaluronan. Ann Rheum Dis 1995;54:429-432.
- [43] Singh A, Corvelli M, Unterman SA, Wepasnick KA, McDonnell P, Elisseeff JH. Enhanced lubrication on tissue and biomaterial surfaces through peptide-mediated binding of hyaluronic acid. 2014;13:988-995.
- [44] Jay GD. Lubricin and surfacing of articular joints. 2004;15:355-359.
- [45] Swann DA, Silver FH, Slayter HS, Stafford W, Shore E. The molecular structure and lubricating activity of lubricin isolated from bovine and human synovial fluids. Biochem J 1985;225:195-201.
- [46] Das S, Banquy X, Zappone B, Greene GW, Jay GD, Israelachvili JN. Synergistic interactions between grafted hyaluronic acid and lubricin provide enhanced wear protection and lubrication. 2013;14:1669-1677.



- [47] Schmidt TA, Gastelum NS, Nguyen QT, Schumacher BL, Sah RL. Boundary lubrication of articular cartilage: role of synovial fluid constituents. 2007;56:882-891.
- [48] Hills BA. Identity of the joint lubricant. J Rheumatol 2002;29:200-201.
- [49] Hills BA, Butler BD. Surfactants identified in synovial fluid and their ability to act as boundary lubricants. Ann Rheum Dis 1984;43:641-648.
- [50] Mazzucco D, Scott R, Spector M. Composition of joint fluid in patients undergoing total knee replacement and revision arthroplasty: correlation with flow properties. Biomaterials 2004;25:4433-4445.
- [51] Sarma A, Powell G, LaBerge M. Phospholipid composition of articular cartilage boundary lubricant. 2001;19:671-676.
- [52] Seror J, Merkher Y, Kampf N, Collinson L, Day AJ, Maroudas A, Klein J. Normal and shear interactions between hyaluronan–aggrecan complexes mimicking possible boundary lubricants in articular cartilage in synovial joints. 2012;13:3823-3832.
- [53] Benz M, Chen N, Israelachvili J. Lubrication and wear properties of grafted polyelectrolytes, hyaluronan and hylan, measured in the surface forces apparatus. 2004;71:6-15.
- [54] Schwarz IM, Hills BA. Surface-active phospholipid as the lubricating component of lubricin. Br J Rheumatol 1998;37:21-26.
- [55] Dethloff LA, Gilmore LB, Brody AR, Hook GE. Induction of intra- and extra-cellular phospholipids in the lungs of rats exposed to silica. Biochem J 1986;233:111-118.

- [56] Dethloff LA, Gilmore LB, Hook GE. The relationship between intra- and extra-cellular surfactant phospholipids in the lungs of rabbits and the effects of silica-induced lung injury. *Biochem J* 1986;239:59-67.
- [57] Hills B. Boundary lubrication in vivo. *Proc Inst Mech Eng Part H J Eng Med* 2000;214:83-94.
- [58] Chen M, Briscoe WH, Armes SP, Cohen H, Klein J. Polyzwitterionic brushes: Extreme lubrication by design. 2011;47:511-523.
- [59] Liu C, Wang M, An J, Thormann E, Dédinaité A. Hyaluronan and phospholipids in boundary lubrication. 2012;8:10241-10244.
- [60] Wang M, Liu C, Thormann E, Dédinaité A. Hyaluronan and phospholipid association in biolubrication. 2013;14:4198-4206.
- [61] Seror J, Merkher Y, Kampf N, Collinson L, Day AJ, Maroudas A, Klein J. Articular cartilage proteoglycans as boundary lubricants: structure and frictional interaction of surface-attached hyaluronan and hyaluronan–aggrecan complexes. 2011;12:3432-3443.
- [62] Reinholz G, Lu L, Saris D, Yaszemski MJ, O’driscoll S. Animal models for cartilage reconstruction. *Biomaterials* 2004;25:1511-1521.
- [63] Hunziker EB, Lippuner K, Keel M, Shintani N. An educational review of cartilage repair: precepts & practice–myths & misconceptions–progress & prospects. 2015;23:334-350.

- [64] Musumeci G, Castrogiovanni P, Leonardi R, Trovato FM, Szychlinska MA, Di Giunta A, Loreto C, et al. New perspectives for articular cartilage repair treatment through tissue engineering: A contemporary review. *World J Orthop* 2014;5:80-88.
- [65] Minas T. A primer in cartilage repair. *J Bone Joint Surg Br* 2012;94:141-146.
- [66] Insall J. The Pridie debridement operation for osteoarthritis of the knee. *Clin Orthop* 1974;101:61-67.
- [67] Muller B, Kohn D. Indication for and performance of articular cartilage drilling using the Pridie method. *Orthopade* 1999;28:4-10.
- [68] Insall JN. Intra-articular surgery for degenerative arthritis of the knee. A report of the work of the late K. H. Pridie. *J Bone Joint Surg Br* 1967;49:211-228.
- [69] Kreuz PC, Erggelet C, Steinwachs MR, Krause SJ, Lahm A, Niemeyer P, Ghanem N, et al. Is microfracture of chondral defects in the knee associated with different results in patients aged 40 years or younger? 2006;22:1180-1186.
- [70] Sledge SL. Microfracture techniques in the treatment of osteochondral injuries. *Clin Sports Med* 2001;20:365-378.
- [71] Steadman JR, Briggs KK, Rodrigo JJ, Kocher MS, Gill TJ, Rodkey WG. Outcomes of microfracture for traumatic chondral defects of the knee: average 11-year follow-up. 2003;19:477-484.

[72] Asik M, Ciftci F, Sen C, Erdil M, Atalar A. The microfracture technique for the treatment of full-thickness articular cartilage lesions of the knee: midterm results. 2008;24:1214-1220.

[73] Mithoefer K, Williams RJ,3rd, Warren RF, Potter HG, Spock CR, Jones EC, Wickiewicz TL, et al. The microfracture technique for the treatment of articular cartilage lesions in the knee. A prospective cohort study. J Bone Joint Surg Am 2005;87:1911-1920.

[74] Schmidt H, Hasse E. Arthroscopic surgical treatment of circumscribed cartilage damage with spongiolization or Pridie drilling. Beitr Orthop Traumatol 1989;36:35-37.

[75] Mithoefer K, Williams RJ, Warren RF, Potter HG, Spock CR, Jones EC, Wickiewicz TL, et al. Chondral resurfacing of articular cartilage defects in the knee with the microfracture technique. J Bone Joint Surg Am 2006;;294-304.

[76] Beresford WA. Chondroid bone, secondary cartilage, and metaplasia. : Urban & Schwarzenberg, 1981.

[77] Lexer E. Substitution of whole or half joints from freshly amputated extremities by free plastic operation. 1908;6:601-607.

[78] Axhausen G. Die histologischen und klinischen Gesetze der freien Osteoplastik auf Grund von Tierversuchen. 1909;88:23-145.

[79] Zheng H, Martin JA, Duwayri Y, Falcon G, Buckwalter JA. Impact of aging on rat bone marrow-derived stem cell chondrogenesis. 2007;62:136-148.

- [80] Sherman SL, Garrity J, Bauer K, Cook J, Stannard J, Bugbee W. Fresh osteochondral allograft transplantation for the knee: current concepts. *J Am Acad Orthop Surg* 2014;22:121-133.
- [81] Brittberg M, Lindahl A, Nilsson A, Ohlsson C, Isaksson O, Peterson L. Treatment of deep cartilage defects in the knee with autologous chondrocyte transplantation. *N Engl J Med* 1994;331:889-895.
- [82] Saris DB, Vanlauwe J, Victor J, Haspl M, Bohnsack M, Fortems Y, Vandekerckhove B, et al. Characterized chondrocyte implantation results in better structural repair when treating symptomatic cartilage defects of the knee in a randomized controlled trial versus microfracture. *Am J Sports Med* 2008;36:235-246.
- [83] Richter W. Cell-based cartilage repair: illusion or solution for osteoarthritis. *Curr Opin Rheumatol* 2007;19:451-456.
- [84] Chen FH, Rousche KT, Tuan RS. Technology Insight: adult stem cells in cartilage regeneration and tissue engineering. *2006;2:373-382.*
- [85] Ahmed N, Stanford WL, Kandel RA. Mesenchymal stem and progenitor cells for cartilage repair. *Skeletal Radiol* 2007;36:909-912.
- [86] Arthur A, Zannettino A, Gronthos S. The therapeutic applications of multipotential mesenchymal/stromal stem cells in skeletal tissue repair. *J Cell Physiol* 2009;218:237-245.
- [87] Grande DA, Singh IJ, Pugh J. Healing of experimentally produced lesions in articular cartilage following chondrocyte transplantation. *Anat Rec* 1987;218:142-148.

- [88] Reddi AH. Morphogenesis and tissue engineering of bone and cartilage: inductive signals, stem cells, and biomimetic biomaterials. *Tissue Eng* 2000;6:351-359.
- [89] Reddi AH. Cartilage morphogenetic proteins: role in joint development, homeostasis, and regeneration. *Ann Rheum Dis* 2003;62 Suppl 2:ii73-8.
- [90] Glowacki J. In vitro engineering of cartilage. 2000;37:171-178.
- [91] Chesterman PJ, Smith AU. Homotransplantation of articular cartilage and isolated chondrocytes. An experimental study in rabbits. *J Bone Joint Surg Br* 1968;50:184-197.
- [92] Iwasa J, Engebretsen L, Shima Y, Ochi M. Clinical application of scaffolds for cartilage tissue engineering. 2009;17:561-577.
- [93] O'Shea TM, Miao X. Bilayered scaffolds for osteochondral tissue engineering. 2008;14:447-464.
- [94] Lu HH, Subramony SD, Boushell MK, Zhang X. Tissue engineering strategies for the regeneration of orthopedic interfaces. *Ann Biomed Eng* 2010;38:2142-2154.
- [95] Chao PG, Yodmuang S, Wang X, Sun L, Kaplan DL, Vunjak-Novakovic G. Silk hydrogel for cartilage tissue engineering. 2010;95:84-90.
- [96] Lee CS, Gleghorn JP, Choi NW, Cabodi M, Stroock AD, Bonassar LJ. Integration of layered chondrocyte-seeded alginate hydrogel scaffolds. *Biomaterials* 2007;28:2987-2993.

- [97] Park Y, Sugimoto M, Watrin A, Chiquet M, Hunziker EB. BMP-2 induces the expression of chondrocyte-specific genes in bovine synovium-derived progenitor cells cultured in three-dimensional alginate hydrogel. 2005;13:527-536.
- [98] Toh WS, Lee EH, Guo X, Chan JK, Yeow CH, Choo AB, Cao T. Cartilage repair using hyaluronan hydrogel-encapsulated human embryonic stem cell-derived chondrogenic cells. Biomaterials 2010;31:6968-6980.
- [99] Tan H, Chu CR, Payne KA, Marra KG. Injectable in situ forming biodegradable chitosan–hyaluronic acid based hydrogels for cartilage tissue engineering. Biomaterials 2009;30:2499-2506.
- [100] Baker MI, Walsh SP, Schwartz Z, Boyan BD. A review of polyvinyl alcohol and its uses in cartilage and orthopedic applications. 2012;100:1451-1457.
- [101] Kon M, de Visser AC. A poly (HEMA) sponge for restoration of articular cartilage defects. Plast Reconstr Surg 1981;67:289-293.
- [102] Ma R, Xiong D, Miao F, Zhang J, Peng Y. Novel PVP/PVA hydrogels for articular cartilage replacement. 2009;29:1979-1983.
- [103] Hung K, Tseng C, Dai L, Hsu S. Water-based polyurethane 3D printed scaffolds with controlled release function for customized cartilage tissue engineering. Biomaterials 2016;83:156-168.
- [104] Bray JC, Merrill EW. Poly (vinyl alcohol) hydrogels for synthetic articular cartilage material. 1973;7:431-443.

- [105] Bray JC, Merrill EW. Poly (vinyl alcohol) hydrogels. Formation by electron beam irradiation of aqueous solutions and subsequent crystallization. *J Appl Polym Sci* 1973;17:3779-3794.
- [106] Mawad D, Anne Boughton E, Boughton P, Lauto A. Advances in hydrogels applied to degenerative diseases. *Curr Pharm Des* 2012;18:2558-2575.
- [107] Bader RA. Synthesis and viscoelastic characterization of novel hydrogels generated via photopolymerization of 1, 2-epoxy-5-hexene modified poly (vinyl alcohol) for use in tissue replacement. 2008;4:967-975.
- [108] Lee KY, Mooney DJ. Hydrogels for tissue engineering. *Chem Rev* 2001;101:1869-1880.
- [109] Corkhill P, Trevett A, Tighe B. The potential of hydrogels as synthetic articular cartilage. *Proc Inst Mech Eng Part H J Eng Med* 1990;204:147-155.
- [110] Freeman ME, Furey MJ, Love BJ, Hampton JM. Friction, wear, and lubrication of hydrogels as synthetic articular cartilage. *Wear* 2000;241:129-135.
- [111] Yodmuang S, McNamara SL, Nover AB, Mandal BB, Agarwal M, Kelly TN, Chao PG, et al. Silk microfiber-reinforced silk hydrogel composites for functional cartilage tissue repair. 2015;11:27-36.
- [112] Li W, Wang D, Yang W, Song Y. Compressive mechanical properties and microstructure of PVA–HA hydrogels for cartilage repair. 2016;6:20166-20172.



- [113] Murakami T, Yarimitsu S, Nakashima K, Yamaguchi T, Sawae Y, Sakai N, Suzuki A. Superior lubricity in articular cartilage and artificial hydrogel cartilage. Proc Inst Mech Eng Part J 2014;228:1099-1111.
- [114] Blum MM, Ovaert TC. A novel polyvinyl alcohol hydrogel functionalized with organic boundary lubricant for use as low-friction cartilage substitute: Synthesis, physical/chemical, mechanical, and friction characterization. 2012;100:1755-1763.
- [115] Bryant SJ, Anseth KS. Controlling the spatial distribution of ECM components in degradable PEG hydrogels for tissue engineering cartilage. 2003;64:70-79.
- [116] Yarimitsu S, Sasaki S, Murakami T, Suzuki A. Evaluation of lubrication properties of hydrogel artificial cartilage materials for joint prosthesis. 2016;2:40-47.
- [117] Blum MM, Ovaert TC. Investigation of friction and surface degradation of innovative boundary lubricant functionalized hydrogel material for use as artificial articular cartilage. Wear 2013;301:201-209.
- [118] Hassan CM, Peppas NA. Structure and morphology of freeze/thawed PVA hydrogels. Macromolecules 2000;33:2472-2479.
- [119] Hassan C, Peppas N. Structure and applications of poly (vinyl alcohol) hydrogels produced by conventional crosslinking or by freezing/thawing methods. 2000;:37-65.
- [120] Oka M, Ushio K, Kumar P, Ikeuchi K, Hyon S, Nakamura T, Fujita H. Development of artificial articular cartilage. Proc Inst Mech Eng Part H J Eng Med 2000;214:59-68.

- [121] Xu P, Du M, Zheng Q. Influence of Preparation Parameters on the Frictional Behavior of PVA Hydrogel Against Glass Substrate. 2014;:708-714.
- [122] Klenin V, Klenina O, Galaktionov V. Study of supermolecular particles in aqueous solutions of polyvinyl alcohol. 1966;8:1734-1741.
- [123] Murakami T, Sakai N, Yamaguchi T, Yarimitsu S, Nakashima K, Sawae Y, Suzuki A. Evaluation of a superior lubrication mechanism with biphasic hydrogels for artificial cartilage. Tribol Int 2015;89:19-26.
- [124] Kuster MS, Wood GA, Stachowiak GW, Gachter A. Joint load considerations in total knee replacement. J Bone Joint Surg Br 1997;79:109-113.
- [125] Holloway JL, Lowman AM, Palmese GR. Mechanical evaluation of poly (vinyl alcohol)-based fibrous composites as biomaterials for meniscal tissue replacement. 2010;6:4716-4724.
- [126] Holloway JL, Lowman AM, VanLandingham MR, Palmese GR. Chemical grafting for improved interfacial shear strength in UHMWPE/PVA-hydrogel fiber-based composites used as soft fibrous tissue replacements. Composites Sci Technol 2013;85:118-125.
- [127] Chen K, Zhang D, Wang S. Start-up friction properties of poly (vinyl alcohol)/nano-hydroxyapatite/silk composite hydrogel. 2013;3:265-272.
- [128] Wu G, Zhao C, Wang C, Zhang W. The effect of preparation methods on tribological properties of PVA-H/HA composites. 2008;17:811-819.

- [129] Gonzalez JS, Alvarez VA. Mechanical properties of polyvinylalcohol/hydroxyapatite cryogel as potential artificial cartilage. 2014;34:47-56.
- [130] Ma R, Xiong D, Miao F, Zhang J, Peng Y. Friction properties of novel PVP/PVA blend hydrogels as artificial cartilage. 2010;93:1016-1019.
- [131] Park KR, Nho YC. Synthesis of PVA/PVP hydrogels having two-layer by radiation and their physical properties. Radiat Phys Chem 2003;67:361-365.
- [132] Joshi A, Fussell G, Thomas J, Hsuan A, Lowman A, Karduna A, Vresilovic E, et al. Functional compressive mechanics of a PVA/PVP nucleus pulposus replacement. Biomaterials 2006;27:176-184.
- [133] Yanez F, Concheiro A, Alvarez-Lorenzo C. Macromolecule release and smoothness of semi-interpenetrating PVP-pHEMA networks for comfortable soft contact lenses. 2008;69:1094-1103.
- [134] Maolin Z, Hongfei H, Yoshii F, Makuuchi K. Effect of kappa-carrageenan on the properties of poly (N-vinyl pyrrolidone)/kappa-carrageenan blend hydrogel synthesized by  $\gamma$ -radiation technology. Radiat Phys Chem 2000;57:459-464.
- [135] Kao F, Manivannan G, Sawan SP. UV curable bioadhesives: copolymers of N-vinyl pyrrolidone. 1997;38:191-196.
- [136] Katta JK, Marcolongo M, Lowman A, Mansmann KA. Friction and wear behavior of poly (vinyl alcohol)/poly (vinyl pyrrolidone) hydrogels for articular cartilage replacement. 2007;83:471-479.

- [137] Thomas J, Lowman A, Marcolongo M. Novel associated hydrogels for nucleus pulposus replacement. 2003;67:1329-1337.
- [138] Mouritsen OG. Life-as a matter of fat. : Springer, 2005.
- [139] Blum MM, Ovaert TC. Low friction hydrogel for articular cartilage repair: evaluation of mechanical and tribological properties in comparison with natural cartilage tissue. 2013;33:4377-4383.
- [140] Laschewsky A. Structures and synthesis of zwitterionic polymers. 2014;6:1544-1601.
- [141] Azzaroni O, Brown AA, Huck WT. UCST Wetting Transitions of Polyzwitterionic Brushes Driven by Self-Association. 2006;118:1802-1806.
- [142] Carr LR, Krause JE, Ella-Menye J, Jiang S. Single nonfouling hydrogels with mechanical and chemical functionality gradients. Biomaterials 2011;32:8456-8461.
- [143] Yang W, Bai T, Carr LR, Keefe AJ, Xu J, Xue H, Irvin CA, et al. The effect of lightly crosslinked poly (carboxybetaine) hydrogel coating on the performance of sensors in whole blood. Biomaterials 2012;33:7945-7951.
- [144] Zhang L, Cao Z, Bai T, Carr L, Ella-Menye J, Irvin C, Ratner BD, et al. Zwitterionic hydrogels implanted in mice resist the foreign-body reaction. Nat Biotechnol 2013;31:553-556.
- [145] Hu W, Haddad PR. Electrostatic ion chromatography. 1998;17:73-79.

- [146] Chen S, Zheng J, Li L, Jiang S. Strong resistance of phosphorylcholine self-assembled monolayers to protein adsorption: insights into nonfouling properties of zwitterionic materials. *J Am Chem Soc* 2005;127:14473-14478.
- [147] Holmlin RE, Chen X, Chapman RG, Takayama S, Whitesides GM. Zwitterionic SAMs that resist nonspecific adsorption of protein from aqueous buffer. *Langmuir* 2001;17:2841-2850.
- [148] Vaisocherova H, Yang W, Zhang Z, Cao Z, Cheng G, Piliarik M, Homola J, et al. Ultralow fouling and functionalizable surface chemistry based on a zwitterionic polymer enabling sensitive and specific protein detection in undiluted blood plasma. *Anal Chem* 2008;80:7894-7901.
- [149] Jiang W, Awasum JN, Irgum K. Control of electroosmotic flow and wall interactions in capillary electrophoresis capillaries by photografted zwitterionic polymer surface layers. *Anal Chem* 2003;75:2768-2774.
- [150] Gaisinskaya A, Ma L, Silbert G, Sorkin R, Tairy O, Goldberg R, Kampf N, et al. Hydration lubrication: exploring a new paradigm. *Faraday Discuss* 2012;156:217-233.
- [151] Stauffer SR, Peppast NA. Poly (vinyl alcohol) hydrogels prepared by freezing-thawing cyclic processing. *Polymer* 1992;33:3932-3936.
- [152] Ramer G, Lendl B. Attenuated total reflection Fourier transform infrared spectroscopy. 2013;.
- [153] Poon CY, Bhushan B. Comparison of surface roughness measurements by stylus profiler, AFM and non-contact optical profiler. *Wear* 1995;190:76-88.

- [154] Giraldez MJ, García-Resúa C, Lira M, Oliveira MEC, Yebra-Pimentel E. White light interferometry to characterize the hydrogel contact lens surface. 2010;30:289-297.
- [155] Ling D, Bodugoz-Senturk H, Nanda S, Braithwaite G, Muratoglu OK. Quantifying the lubricity of mechanically tough polyvinyl alcohol hydrogels for cartilage repair. Proc Inst Mech Eng Part H J Eng Med 2015;229:845-852.
- [156] Hoffman RV. Organic chemistry: an intermediate text. : John Wiley & Sons, 2004.
- [157] Radu A, Eleonora C, Lucian A, Georgeta C, Virginia V, Cristiana T. In vitro biocompatibility testing of implantable biomaterials. 2008;13:3863-3872.
- [158] Thongphud A, Paosawatyanong B, Visal-Athaphand P, Supaphol P. Improvement of hydrophobic properties of the electrospun PVA fabrics by SF6 plasma treatment. 2008;55:625-628.
- [159] Bunn C. Crystal structure of polyvinyl alcohol. Nature 1948;161:929-930.
- [160] Mikołajczyk T, Rabiej S, Boguń M, Szparaga G, Draczyński Z. Nanocomposite polyvinyl alcohol fibers for medical applications. J Appl Polym Sci 2011;120:1234-1244.
- [161] Fujii K. Stereochemistry of poly (vinyl alcohol). 1971;5:431-540.
- [162] Zheng Y, Huang X, Wang Y, Xu H, Chen X. Performance and characterization of irradiated poly (vinyl alcohol)/polyvinylpyrrolidone composite hydrogels used as cartilages replacement. J Appl Polym Sci 2009;113:736-741.

- [163] Jiang H, Zuo Y, Zhang L, Li J, Zhang A, Li Y, Yang X. Property-based design: optimization and characterization of polyvinyl alcohol (PVA) hydrogel and PVA-matrix composite for artificial cornea. *J Mater Sci Mater Med* 2014;25:941-952.
- [164] Alexandre N, Ribeiro J, Gärtner A, Pereira T, Amorim I, Fragoso J, Lopes A, et al. Biocompatibility and hemocompatibility of polyvinyl alcohol hydrogel used for vascular grafting—in vitro and in vivo studies. 2014;102:4262-4275.
- [165] Israelachvili J. *Intermolecular and Surface Forces: Revised Third Edition*. Intermolecular and Surface Forces. 2011;.
- [166] Grubin A, Vinogradova IE. *Investigation of the contact of machine components*. : Central Scientific Research Institute for Technology and Mechanical Engineering (TsNIITMASH), 1949.
- [167] Zhang Y. New film thickness equation for elastohydrodynamic lubrication of isothermal smooth line contacts under heavy loads for Newtonian fluids. 2013;5:182-186.
- [168] Morales-Espejel GE, Wemekamp A. Ertel—Grubin methods in elastohydrodynamic lubrication—a review. *Proc Inst Mech Eng Part J* 2008;222:15-34.
- [169] Stachowiak G, Batchelor AW. *Experimental methods in tribology*. : Elsevier, 2004.
- [170] Stammen JA, Williams S, Ku DN, Guldborg RE. Mechanical properties of a novel PVA hydrogel in shear and unconfined compression. *Biomaterials* 2001;22:799-806.
- [171] Bodugoz-Senturk H, Macias CE, Kung JH, Muratoglu OK. Poly (vinyl alcohol)—acrylamide hydrogels as load-bearing cartilage substitute. *Biomaterials* 2009;30:589-596.

- [172] Curley C, Hayes JC, Rowan NJ, Kennedy JE. An evaluation of the thermal and mechanical properties of a salt-modified polyvinyl alcohol hydrogel for a knee meniscus application. 2014;40:13-22.
- [173] Lee S, Pereira BP, Yusof N, Selvaratnam L, Yu Z, Abbas A, Kamarul T. Unconfined compression properties of a porous poly (vinyl alcohol)–chitosan-based hydrogel after hydration. 2009;5:1919-1925.
- [174] Gong JP. Friction and lubrication of hydrogels—its richness and complexity. 2006;2:544-552.
- [175] Pan Y, Xiong D, Ma R. A study on the friction properties of poly (vinyl alcohol) hydrogel as articular cartilage against titanium alloy. *Wear* 2007;262:1021-1025.
- [176] Pramanick AK, Gupta S, Mishra T, Sinha A. Topographical heterogeneity in transparent PVA hydrogels studied by AFM. 2012;32:222-227.
- [177] Tominaga T, Kurokawa T, Furukawa H, Osada Y, Gong JP. Friction of a soft hydrogel on rough solid substrates. 2008;4:1645-1652.
- [178] Jin Z, Dowson D, Fisher J. Fluid film lubrication in natural hip joints. 1993;25:545-555.
- [179] Osaheni AO, Finkelstein EB, Mather PT, Blum MM. Synthesis and characterization of a zwitterionic hydrogel blend with low coefficient of friction. 2016;46:245-255.
- [180] Lalani R, Liu L. Synthesis, characterization, and electrospinning of zwitterionic poly (sulfobetaine methacrylate). *Polymer* 2011;52:5344-5354.



- [181] Sperling LH. Introduction to physical polymer science. : John Wiley & Sons, 2005.
- [182] Peppas N, Bures P, Leobandung W, Ichikawa H. Hydrogels in pharmaceutical formulations. 2000;50:27-46.
- [183] Siepmann J, Peppas N. Modeling of drug release from delivery systems based on hydroxypropyl methylcellulose (HPMC). Adv Drug Deliv Rev 2001;48:139-157.
- [184] Moore A, Burris D. An analytical model to predict interstitial lubrication of cartilage in migrating contact areas. J Biomech 2014;47:148-153.
- [185] Moore A, Zimmerman B, Chen X, Lu X, Burris D. Experimental characterization of biphasic materials using rate-controlled Hertzian indentation. Tribol Int 2015;89:2-8.
- [186] Mattice JM, Lau AG, Oyen ML, Kent RW. Spherical indentation load-relaxation of soft biological tissues. J Mater Res 2006;21:2003-2010.
- [187] Willcox PJ, Howie DW, Schmidt-Rohr K, Hoagland DA, Gido SP, Pudjijanto S, Kleiner LW, et al. Microstructure of poly (vinyl alcohol) hydrogels produced by freeze/thaw cycling. 1999;37:3438-3454.
- [188] Mark JE. Physical properties of polymers handbook. : Springer, 2007.
- [189] Hickey AS, Peppas NA. Mesh size and diffusive characteristics of semicrystalline poly (vinyl alcohol) membranes prepared by freezing/thawing techniques. J Membr Sci 1995;107:229-237.

- [190] Accardi MA, Dini D, Cann PM. Experimental and numerical investigation of the behaviour of articular cartilage under shear loading—interstitial fluid pressurisation and lubrication mechanisms. *Tribol Int* 2011;44:565-578.
- [191] Ruberti JW, Braithwaite GJ. 2009;.
- [192] Choi J, Bodugoz-Senturk H, Kung HJ, Malhi AS, Muratoglu OK. Effects of solvent dehydration on creep resistance of poly (vinyl alcohol) hydrogel. *Biomaterials* 2007;28:772-780.
- [193] Gong J, Iwasaki Y, Osada Y, Kurihara K, Hamai Y. Friction of gels. 3. Friction on solid surfaces. 1999;103:6001-6006.
- [194] Taunton HJ, Toprakcioglu C, Fetters LJ, Klein J. Forces between surfaces bearing terminally anchored polymer chains in good solvents. *Nature* 1988;332:712-714.
- [195] Klein J, Perahia D, Warburg S. Forces between polymer-bearing surfaces undergoing shear. *Nature* 1991;352:143.
- [196] Klein J, Kumacheva E, Mahalu D, Perahia D, Fetters LJ. Reduction of frictional forces between solid surfaces bearing polymer brushes. *Nature* 1994;370:634-636.
- [197] De Gennes P. Polymers at an interface; a simplified view. *Adv Colloid Interface Sci* 1987;27:189-209.
- [198] Klein J. Shear, friction, and lubrication forces between polymer-bearing surfaces. 1996;26:581-612.

- [199] Chen M, Briscoe WH, Armes SP, Klein J. Lubrication at physiological pressures by polyzwitterionic brushes. *Science* 2009;323:1698-1701.
- [200] Charrault E, Lee T, Easton CD, Neto C. Boundary flow on end-grafted PEG brushes. 2016;12:1906-1914.
- [201] Secomb T, Hsu R, Pries A. Tribology of capillary blood flow. *Proc Inst Mech Eng Part J* 2006;220:767-774.
- [202] Cheng N, Brown AA, Azzaroni O, Huck WT. Thickness-dependent properties of polyzwitterionic brushes. *Macromolecules* 2008;41:6317-6321.
- [203] Yang J, Chen H, Xiao S, Shen M, Chen F, Fan P, Zhong M, et al. Salt-responsive zwitterionic polymer brushes with tunable friction and antifouling properties. *Langmuir* 2015;31:9125-9133.
- [204] Gong J, Higa M, Iwasaki Y, Katsuyama Y, Osada Y. Friction of gels. 1997;101:5487-5489.
- [205] Gong JP, Kagata G, Osada Y. Friction of gels. 4. Friction on charged gels. 1999;103:6007-6014.
- [206] Li X, Wu C, Yang Q, Long S, Wu C. Low-velocity super-lubrication of sodium-alginate/polyacrylamide ionic-covalent hybrid double-network hydrogels. 2015;11:3022-3033.

- [207] Nakano Y, Kurokawa T, Du M, Liu J, Tominaga T, Osada Y, Gong JP. Effect of hyaluronan solution on dynamic friction of PVA gel sliding on weakly adhesive glass substrate. *Macromolecules* 2011;44:8908-8915.
- [208] Kobayashi M, Terayama Y, Kikuchi M, Takahara A. Chain dimensions and surface characterization of superhydrophilic polymer brushes with zwitterion side groups. 2013;9:5138-5148.
- [209] Matsuda Y, Kobayashi M, Annaka M, Ishihara K, Takahara A. Dimensions of a free linear polymer and polymer immobilized on silica nanoparticles of a zwitterionic polymer in aqueous solutions with various ionic strengths. *Langmuir* 2008;24:8772-8778.
- [210] Zhang Z, Moxey M, Alswieleh A, Morse AJ, Lewis AL, Geoghegan M, Leggett GJ. Effect of salt on phosphorylcholine-based zwitterionic polymer brushes. *Langmuir* 2016;32:5048-5057.
- [211] Wei Q, Cai M, Zhou F, Liu W. Dramatically tuning friction using responsive polyelectrolyte brushes. *Macromolecules* 2013;46:9368-9379.
- [212] Ricciardi R, Auriemma F, Gaillet C, De Rosa C, Lauprêtre F. Investigation of the crystallinity of freeze/thaw poly (vinyl alcohol) hydrogels by different techniques. *Macromolecules* 2004;37:9510-9516.
- [213] Ricciardi R, Auriemma F, De Rosa C, Lauprêtre F. X-ray diffraction analysis of poly (vinyl alcohol) hydrogels, obtained by freezing and thawing techniques. *Macromolecules* 2004;37:1921-1927.

- [214] Leach MK, Feng Z, Tuck SJ, Corey JM. Electrospinning fundamentals: optimizing solution and apparatus parameters. 2011;;e2494-e2494.
- [215] Anton F. 1934;.
- [216] Orr SB, Chainani A, Hippensteel KJ, Kishan A, Gilchrist C, Garrigues NW, Ruch DS, et al. Aligned multilayered electrospun scaffolds for rotator cuff tendon tissue engineering. 2015;24:117-126.
- [217] Walmsley GG, McArdle A, Tevlin R, Momeni A, Atashroo D, Hu MS, Feroze AH, et al. Nanotechnology in bone tissue engineering. 2015;11:1253-1263.
- [218] Lalani R, Liu L. Electrospun zwitterionic poly (sulfobetaine methacrylate) for nonadherent, superabsorbent, and antimicrobial wound dressing applications. 2012;13:1853-1863.
- [219] Ballengee JB, Pintauro PN. Composite fuel cell membranes from dual-nanofiber electrospun mats. *Macromolecules* 2011;44:7307-7314.
- [220] Zhang S, Shim WS, Kim J. Design of ultra-fine nonwovens via electrospinning of Nylon 6: Spinning parameters and filtration efficiency. *Mater Des* 2009;30:3659-3666.
- [221] Ladd J, Zhang Z, Chen S, Hower JC, Jiang S. Zwitterionic polymers exhibiting high resistance to nonspecific protein adsorption from human serum and plasma. 2008;9:1357-1361.
- [222] Brash JL. Exploiting the current paradigm of blood–material interactions for the rational design of blood-compatible materials. 2000;11:1135-1146.

- [223] Greiner A, Wendorff JH. Electrospinning: a fascinating method for the preparation of ultrathin fibers. 2007;46:5670-5703.
- [224] Shenoy SL, Bates WD, Frisch HL, Wnek GE. Role of chain entanglements on fiber formation during electrospinning of polymer solutions: good solvent, non-specific polymer–polymer interaction limit. Polymer 2005;46:3372-3384.
- [225] Fong H, Chun I, Reneker D. Beaded nanofibers formed during electrospinning. Polymer 1999;40:4585-4592.
- [226] Zahedi P, Rezaeian I, Ranaei-Siadat S, Jafari S, Supaphol P. A review on wound dressings with an emphasis on electrospun nanofibrous polymeric bandages. Polym Adv Technol 2010;21:77-95.
- [227] Weller C, Sussman G. Wound dressings update. 2006;36:318-324.
- [228] Winter GD. Formation of the scab and the rate of epithelization of superficial wounds in the skin of the young domestic pig. Nature 1962;193:293-294.
- [229] Jahn S, Klein J. Hydration lubrication: the macromolecular domain. Macromolecules 2015;48:5059-5075.
- [230] Sun Y, Wei Z, Zhao C, Jay GD, Schmid TM, Amadio PC, An K. Lubricin in human achilles tendon: The evidence of intratendinous sliding motion and shear force in achilles tendon. 2015;33:932-937.

[231] Lee SY, Niikura T, Reddi AH. Superficial zone protein (lubricin) in the different tissue compartments of the knee joint: modulation by transforming growth factor beta 1 and interleukin-1 beta. 2008;14:1799-1808.

[232] Itoi E, Berglund LJ, Grabowski JJ, Schultz FM, Growney ES, Morrey BF, An K. Tensile properties of the supraspinatus tendon. 1995;13:578-584.

[233] Siegler S, Block J, Schneck CD. The mechanical characteristics of the collateral ligaments of the human ankle joint. Foot Ankle 1988;8:234-242.

[234] Wren TA, Yerby SA, Beaupré GS, Carter DR. Mechanical properties of the human achilles tendon. Clin Biomech 2001;16:245-251.

[235] Huang Z, Zhang Y, Kotaki M, Ramakrishna S. A review on polymer nanofibers by electrospinning and their applications in nanocomposites. Composites Sci Technol 2003;63:2223-2253.

[236] Kim GH. Electrospun PCL nanofibers with anisotropic mechanical properties as a biomedical scaffold. 2008;3:025010.

[237] Lynch HA, Johannessen W, Wu JP, Jawa A, Elliott DM. Effect of fiber orientation and strain rate on the nonlinear uniaxial tensile material properties of tendon. J Biomech Eng 2003;125:726-731.

[238] Lee CH, Shin HJ, Cho IH, Kang Y, Kim IA, Park K, Shin J. Nanofiber alignment and direction of mechanical strain affect the ECM production of human ACL fibroblast. Biomaterials 2005;26:1261-1270.

- [239] Yin Z, Chen X, Chen JL, Shen WL, Nguyen TMH, Gao L, Ouyang HW. The regulation of tendon stem cell differentiation by the alignment of nanofibers. *Biomaterials* 2010;31:2163-2175.
- [240] Tumbic J, Romo-Urbe A, Boden M, Mather PT. Hot-compacted interwoven webs of biodegradable polymers. *Polymer* 2016;101:127-138.
- [241] Lin C, Wang Y, Lin C, Wang S, Chien H, Cheng N, Tsai W, et al. Peptide-modified zwitterionic porous hydrogels for endothelial cell and vascular engineering. 2014;3:297-310.
- [242] Venault A, Subarja A, Chang Y. Zwitterionic Polyhydroxybutyrate Electrospun Fibrous Membranes with a Compromise of Bioinert Control and Tissue-Cell Growth. *Langmuir* 2017;33:2460-2471.
- [243] Bhattacharjee J. *Atomic Force Microscope: Fundamental Principles*. 2015;2016.
- [244] Benetti EM, Zapotoczny S, Vancso GJ. Tunable Thermoresponsive Polymeric Platforms on Gold by “Photoiniferter”-Based Surface Grafting. *Adv Mater* 2007;19:268-271.
- [245] Hutson PR, Crawford ME, Sorkness RL. Liquid chromatographic determination of hydroxyproline in tissue samples. 2003;791:427-430.
- [246] Bragdon C, O'Connor D, Lowenstein J, Jasty M, Syniuta W. The importance of multidirectional motion on the wear of polyethylene. *Proc Inst Mech Eng Part H J Eng Med* 1996;210:157-165.



[247] Wang A, Stark C, Dumbleton J. Mechanistic and morphological origins of ultra-high molecular weight polyethylene wear debris in total joint replacement prostheses. Proc Inst Mech Eng Part H J Eng Med 1996;210:141-155.

[248] Lafortune M, Cavanagh P, Sommer H, Kalenak A. Three-dimensional kinematics of the human knee during walking. J Biomech 1992;25:347-357.

[249] McGann ME, Vahdati A, Wagner DR. Methods to assess in vitro wear of articular cartilage. Proc Inst Mech Eng Part H J Eng Med 2012;226:612-622.

[250] Van Valkenburg SM, Werner FW, Bhimji S, White BF, Asseman FB. Assessment of Physiological Load Testing of Total Knee Implants. 2014;44:258-267.

[251] Jolly L, Tidu A, Heizmann J, Bolle B. Microstructure evolution in polyamide PA11 under small uniaxial extension. Polymer 2002;43:6839-6851.

[252] Stoclet G, Seguela R, Vanmansart C, Rochas C, Lefebvre J. WAXS study of the structural reorganization of semi-crystalline polylactide under tensile drawing. Polymer 2012;53:519-528.

[253] Stoclet G, Lefebvre J, Séguéla R, Vanmansart C. In-situ SAXS study of the plastic deformation behavior of polylactide upon cold-drawing. Polymer 2014;55:1817-1828.

## VITA

**Name of Author:** Allen O. Osaheni

**Place of Birth:** Rochester, New York, USA

**Date of Birth:** November 14, 1991

### Education:

BS, Mechanical Engineering, Clarkson University, 2013

MS, Mechanical & Engineering, Syracuse University, 2015

PhD, Mechanical & Aerospace Engineering, Syracuse University, 2017

### Publications:

Osaheni A.O., Mather P.T., Blum M.M. "Mechanics & Tribology of Electrospun Low Friction Polyurethane Fibermats". *Journal of the Mechanical Behavior of Biomedical Materials* (in preparation)

Osaheni A.O., Mather P.T., Blum M.M. "Effect of Lubricant Chain Length on the Mechanics, Tribology, and Diffusive Properties of Zwitterionic Hydrogel Blends" *Materials Science and Engineering C: Materials for Biological Applications* (in preparation).

Osaheni A.O., Ash-Shakoor A.A, Finkelstein, E.B, Gitsov I., Mather P.T., Blum M.M. "Synthesis and Characterization of Zwitterionic Polymer Brush Functionalized Hydrogels with Ionic Responsive Coefficient of Friction". *Soft Matter* (in preparation).

Osaheni A.O., Olson R.M., Smolnycki, G.J., Blum M.M. "Design of a Six-Axis CNC Tribological Bioreactor Capable of Replicating the Three-Dimensional Kinematics of Human Tibiofemoral Joints". *Journal of Mechanical Design* (in preparation).

Osaheni, Allen O., et al. "Synthesis and Characterization of a Zwitterionic Hydrogel Blend with Low Coefficient of Friction." *Acta Biomaterialia* 46 (2016): 245-255.

Amell, J.M., Griffin R.W., Malfa M.B., Nycz C.J., Osaheni A.O., Erath B.D., Fite K.B., Kuxhaus L. "Cost Effective Electrolarynx: A Feasibility Study." *ASME 2013 Summer Bioengineering Conference Proceedings*, pp. V01BT63A001-V01BT63A001. American Society of Mechanical Engineers, 2013.

## Conference Presentations

Sismondo R.A, Werner F.W., Ordway N.R., Osaheni A.O., Blum M.M, Scuderi M.G., “The Use of a Hydrogel Plug in the Repair of Osteochondral Defects of the Knee: A biomechanical Evaluation of Restoration of Native Contact Pressures in Cadaver Knees”. *ORS Annual Meeting*, New Orleans, LA (abstract under review)

Osaheni A.O., Gitsov I., Mather P.T., Blum M.M. “Synthesis and Characterization of Zwitterionic Polymer Brush Functionalized Hydrogels”. Oral Presentation. *2017 MRS Spring Meeting & Exhibit*, Phoenix, AZ, April 2017

Osaheni A.O., O’Connor K.A., Mather P.T., Blum M.M. "Electrospinning and Characterization of Low Friction Zwitterionic Polyurethane Fiber-mat Composites", Poster Presentation. *Society for Biomaterials 2017 Annual Meeting & Exposition*, Minneapolis, MN, April 2017.

Osaheni A.O., Lindberg E.D., Mather P.T., Blum M.M. “Characterization of the Viscoelastic and Diffusive Properties of Low Friction Zwitterionic Hydrogel Blends”, Poster Presentation. *Society for Biomaterials 2017 Annual Meeting & Exposition*, Minneapolis, MN, April 2017.

Osaheni A.O., Finkelstein E.B, Gitsov I., Mather P.T., Blum M.M. “Synthesis and characterization of zwitterionic brush functionalized poly (vinyl alcohol) hydrogels”. Oral Presentation. *3rd International Conference on BioTribology*, London, UK, September 2016.

Osaheni A.O., Finkelstein E.B., Mather P.T., Blum M.M. “Synthesis & Characterization of a Novel, Biomimetic, Tribologically Enhanced Hydrogel for Biomedical Applications”. Poster Presentation *10th World Biomaterials Congress*, Montreal, Canada, May 2016.

Osaheni A.O., Mather P.T., Blum M.M. “Design & Characterization of a Tribologically Enhanced Hydrogel for Use as an Articular Cartilage Replacement”. Oral Presentation. *ASME International Mechanical Engineering Congress & Exposition*, Houston, TX, November 2015.

Osaheni A.O. , Bader R.A, Mather P.T., Blum M.M. “Design & Characterization of a Low Friction Zwitterionic Hydrogel for use as an Articular Cartilage Replacement”. Oral Presentation. *New York State Biotechnology Symposium*, Upton, NY, May 2015.

Ramos R.D., Osaheni A.O., Blum M.M. “Cell viability studies of boundary lubricant enhanced poly-vinyl alcohol hydrogels”. Poster Presentation. *41st Annual Northeast Biomedical Engineering Conference*, Rensselaer, NY April 2015

Osaheni A.O., Blum M.M. “Design & Characterization of Low-Friction Zwitterionic Boundary Lubricant Hydrogels for use as Articular Cartilage Replacement”. Oral Presentation. *STLE Tribology Frontiers Conference*, Chicaco, IL, October 2014.

Amell, J.M., Griffin R.W., Malfa M.B., Nycz C.J., Osaheni A.O., Erath B.D., Fite K.B., Kuxhaus L. "Cost Effective Electrolarynx: A Feasibility Study." Oral Presentation. *ASME Summer Bioengineering Conference*, Sunriver, OR. June 2013

**Patents:**

Blum MM, Mather PT, Osaheni A, inventors; Syracuse University, assignee. "Self-replenishing boundary lubrication in hydrogels using zwitterionic polymers". United States patent application US 15/335,361. 2016 Oct 26.

Mather P.T. Blum M.M., Osaheni A.O., "Functionally Graded Webs for Lubricious, Low Fouling Films (invention disclosure in preparation)